Advanced Structured Materials

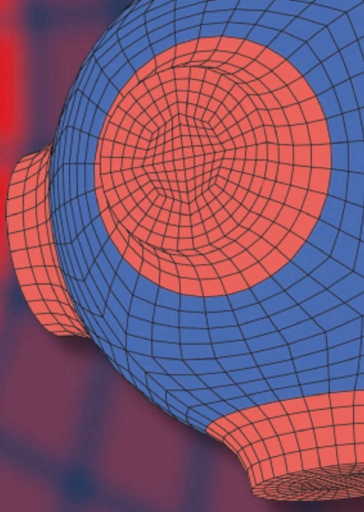

Lucas F. M. da Silva
Paulo A. F. Martins
Mohamad S. El-Zein *Editors*

Advanced Joining Processes

Springer

Advanced Structured Materials

Volume 125

Common engineering materials reach in many applications their limits and new developments are required to fulfil increasing demands on engineering materials. The performance of materials can be increased by combining different materials to achieve better properties than a single constituent or by shaping the material or constituents in a specific structure. The interaction between material and structure may arise on different length scales, such as micro-, meso- or macroscale, and offers possible applications in quite diverse fields.

This book series addresses the fundamental relationship between materials and their structure on the overall properties (e.g. mechanical, thermal, chemical or magnetic etc) and applications.

The topics of *Advanced Structured Materials* include but are not limited to

- classical fibre-reinforced composites (e.g. glass, carbon or Aramid reinforced plastics)
- metal matrix composites (MMCs)
- micro porous composites
- micro channel materials
- multilayered materials
- cellular materials (e.g., metallic or polymer foams, sponges, hollow sphere structures)
- porous materials
- truss structures
- nanocomposite materials
- biomaterials
- nanoporous metals
- concrete
- coated materials
- smart materials

Advanced Structured Materials is indexed in Google Scholar and Scopus.

More information about this series at http://www.springer.com/series/8611

Lucas F. M. da Silva · Paulo A. F. Martins ·
Mohamad S. El-Zein
Editors

Advanced Joining Processes

Springer

Editors
Lucas F. M. da Silva
Department of Mechanical Engineering
Faculty of Engineering
University of Porto
Porto, Portugal

Paulo A. F. Martins
Department of Mechanical Engineering
University of Lisbon
Lisbon, Portugal

Mohamad S. El-Zein
Moline Technology Innovation Center
John Deere
Moline, IL, USA

ISSN 1869-8433 ISSN 1869-8441 (electronic)
Advanced Structured Materials
ISBN 978-981-15-2956-6 ISBN 978-981-15-2957-3 (eBook)
https://doi.org/10.1007/978-981-15-2957-3

© Springer Nature Singapore Pte Ltd. 2020
This work is subject to copyright. All rights are reserved by the Publisher, whether the whole or part of the material is concerned, specifically the rights of translation, reprinting, reuse of illustrations, recitation, broadcasting, reproduction on microfilms or in any other physical way, and transmission or information storage and retrieval, electronic adaptation, computer software, or by similar or dissimilar methodology now known or hereafter developed.
The use of general descriptive names, registered names, trademarks, service marks, etc. in this publication does not imply, even in the absence of a specific statement, that such names are exempt from the relevant protective laws and regulations and therefore free for general use.
The publisher, the authors and the editors are safe to assume that the advice and information in this book are believed to be true and accurate at the date of publication. Neither the publisher nor the authors or the editors give a warranty, expressed or implied, with respect to the material contained herein or for any errors or omissions that may have been made. The publisher remains neutral with regard to jurisdictional claims in published maps and institutional affiliations.

This Springer imprint is published by the registered company Springer Nature Singapore Pte Ltd.
The registered company address is: 152 Beach Road, #21-01/04 Gateway East, Singapore 189721, Singapore

Editorial

This volume of *Advanced Structured Materials* contains selected papers presented at the 1st International Conference on Advanced Joining Processes 2019 (AJP 2019), held in Ponta Delgada, Azores (Portugal), during October 24–25, 2019 (www.fe.up.pt/ajp2019).

The goal of the conference was to provide a unique opportunity to exchange information, present the latest results as well as discuss issues relevant to advanced methods of joining such as friction stir welding, joining by plastic deformation, laser welding, advanced mechanical joining, adhesive bonding and hybrid joining. The focus is on process optimization in experimental and simulation terms, metallurgical and material behavior associated with joining, engineering properties and assessment of joints, health and safety aspects of joining, durability of joints in service, industrial applications and education.

Approximately, 160 papers were presented by researchers from more than 20 countries. In order to disseminate the work presented in AJP 2019, selected papers were prepared which resulted in the present volume dedicated to *Advanced Joining Processes*. A wide range of topics are covered resulting in 11 chapters dealing with the most recent research topics concerning mechanical joining (first part), welding (second part) and adhesive bonding (third part). The book is a state of the art of advanced methods of joining and also serves as a reference volume for researchers and graduate students working with advanced joining processes.

The organizer and editor wish to thank all the authors for their participation and cooperation, which made this volume possible. Finally, I would like to thank the team of Springer-Verlag, especially Dr. Christoph Baumann, for the excellent cooperation during the preparation of this volume.

Porto, Portugal	Lucas F. M. da Silva
Lisbon, Portugal	Paulo A. F. Martins
Moline, USA	Mohamad S. El-Zein
December 2019	

Contents

Mechanical Joining

Welding

Adhesive Bonding

Mechanical Joining

Investigation on Clinching with Additional Local Material Bond by Thermal Joining

V. Wesling, H. Wiche and C. Koch

Abstract In the investigation, point-shaped connections were created by combining a clinching process with laser beam welding and resistance spot welding. The connection, which was generated, unites the form-fitting joint of clinching operations with the material bond of thermal joining processes. The objective was to use the advantages of both types of joints with respect to the mechanical properties. For joints made by clinching, these are high cyclic strengths. For joints made by welding, these are high static strengths. A sheet metal combination consisting of two EN AW-5754 sheets, each with a thickness of 1 mm, was assembled. In addition to the strengths under different load types, the respective failure behavior of the individual compounds was investigated. It is proven that the combination of the methods shows both a change in strengths and new failure mechanisms. In conclusion, it is presented that an increase in strength can be realized by additional local material bond of a clinched joint in the static case without causing a reduction in strength in the cyclic load case. Furthermore, it is shown that a local material bond at the undercut or outside a clinching joint has no increased notch effect through the thermal joining process, even though the material bond is only in the periphery of the clinching joint.

Keywords Hybrid joining · Laser beam welding · Clinching · Resistance spot welding · Static strength · Wohler lines · Notch effect · Shear tension · Cross tension

1 Introduction

The aim of the investigation is to create a punctual joint to compete with established punctual joining technics like resistance spot welding and self-piercing riveting, commonly used in automotive sector [1]. The joining point is based on a clinching process, which is characterized by high cyclic strength and a low static strength.

V. Wesling · H. Wiche · C. Koch (✉)
Clausthal University of Technology, 38678 Clausthal-Zellerfeld, Germany
e-mail: ck10@tu-clausthal.de

Clausthal Centre of Material Technology, Leibnizstraße 9, 38678 Clausthal-Zellerfeld, Germany

L. F. M. da Silva et al. (eds.), *Advanced Joining Processes*,
Advanced Structured Materials 125, https://doi.org/10.1007/978-981-15-2957-3_1

Opposite characteristics are typical for welded joints with high static strength and low cyclic strength [2]. The target is to improve the static strength by the combination of clinching and additional material bonding while retaining the high cyclic strength of the joint. The possibility of improving a clinching process by material bond or additional thermal treatment is reported in various investigations [2–8]. Mostly, the thermal treatment is used to increase formability of the joining partners and therefore increasing the process range, which is limited by formability and strength of the joining materials [8, 9]. A combination of clinching and friction stir welding leads to a material bond, which is limited to the bottom of the joint [6, 10]. A similar material bond is created by combining the clinching process with cold press welding, which is also limited to the bottom area of the clinching joint [4]. An investigation of the combination of resistance spot welding and clinching leads to a material bond in the whole deformation zone [5]. The combination of clinching and brazing or adhesive is done by a major material bond, whereas the clinching joint works as an auxiliary and the large-scale material bond is responsible for strength [2, 3, 7]. The aim of this investigation is to adapt the local material bond and the clinching process to create a load-specific optimal joining point. The purpose is to create a custom local material bond, which is not restricted to geometrical elements of the joining point to influence the strength of the joint. The joint should not need additional joining elements like adhesive or rivets, which shows additionally lightweight potential.

2 Procedure

During the investigation, EN AW-5754 with 1-mm thickness was processed. The process routes contained a clinching process and a resistance spot welding process or a laser beam welding process. The clinching was done on a universal electromechanical press with an effective stroke of 6 mm and a maximum force of 150 kN. The clinching tool R-DF 8 was used to create a round joining point with a diameter of 8 mm without a cutting element and an extensible die. The resistance spot welding was done with a servopneumatic C50 spot welding gun with a maximum direct current of 25 kA and a maximum force of 5 kN. The CuCr1Zr electrodes had a geometry F1 according to DIN EN ISO 5821 with a work diameter of 8 mm. For the modified RSW, an electrode geometry with a work diameter of 4.5 mm was used. For laser beam welding, a HAAS HL4006 with 4 kW and an optic with 300-μm spot diameter were used. The created specimens were tested under cross-tension and shear tension load. The different process routes of the hybrid joints are shown in Figs. 1, 2, 3 and 4. At the process route clinch(CL) + resistance spot welding with modified electrode (RSW(mod.)), a resistance spot weld with the electrode modified to fit inside an clinch joint was performed after the clinching process. The RSW process after the clinching caused deformation and cracks at the bottom area of the joint; therefore, a process route with a thermal joining after the clinching process is not suitable. The process route RSW(mod.)+CL created only a material bond at the bottom area of the clinching joint, while the material bond from the RSW+CL

Fig. 1 CL+RSW(mod.)

Fig. 2 RSW(mod.)+CL

Fig. 3 RSW+CL

Fig. 4 Laser D6+CL

process includes the bottom and also the undercut area. Creating hybrid connections with laser welds allows even more complex geometries as shown in Fig. 4, where only the undercut is locally bonded.

Figure 5 shows different laser weld geometries, which were tested. The diameters used for circular welds were 3, 5, 6 and 15 mm, to create a material bond at different areas of the clinching joint. Besides circular welds, also linear welds with a length of 10 mm and different orientations were done (0° and 90° to force direction).

Fig. 5 Laser–hybrid geometries

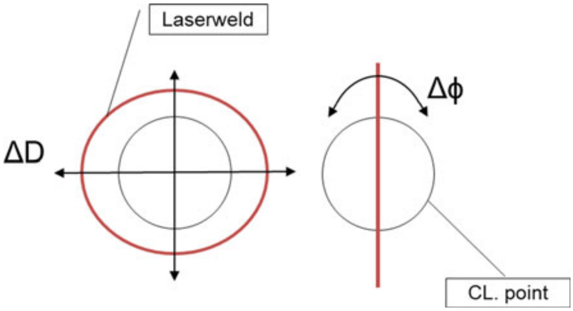

3 Investigation on Combination Clinch + Resistance Spot Welding

The results of the static testing of the reference and RSW–hybrid specimen are shown in Fig. 6. It is visible that the clinch joint has both lower cross-tension and shear tension strengths than the RSW joint. The material bond at the bottom area increases

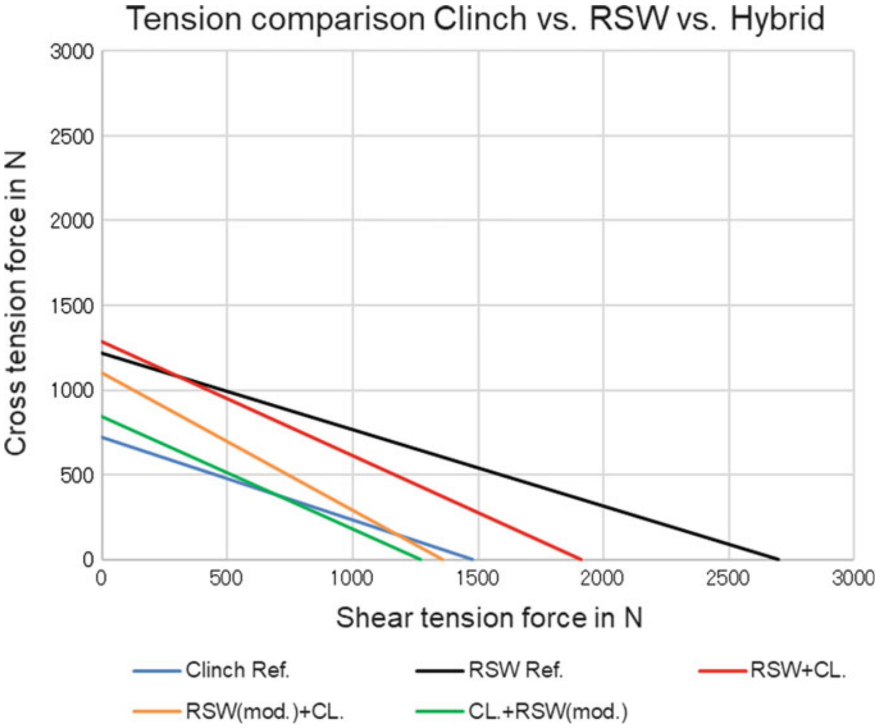

Fig. 6 Static shear tension RSW and CL

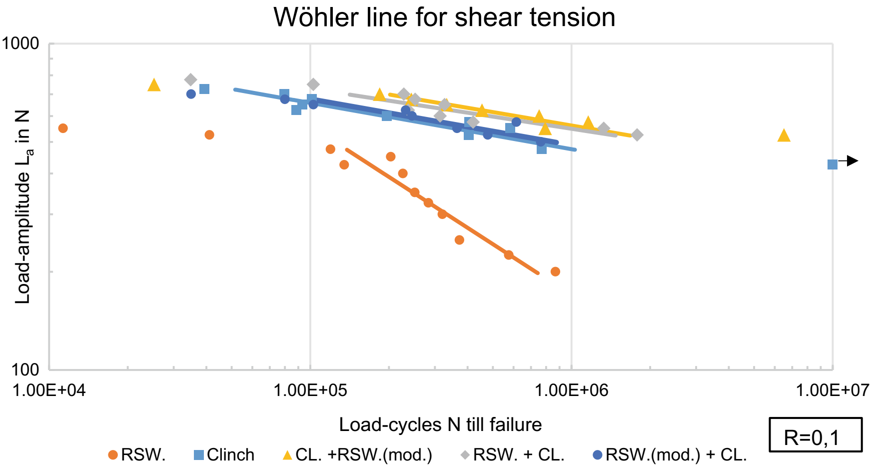

Fig. 7 Wöhler line RSW/CL

the cross-tension but decreases shear tension strength; see RSW(mod.)+CL and CL+RSW(mod). A material bond overlapping the undercut as done with RSW+CL increases both strengths in cross-tension and shear tension, but fails to exceed the reference RSW joint.

Under cyclic load and shear tension, RSW sustains a higher notch effect than the clinching joint, as it is shown in Fig. 7. The clinching joint has a higher load level than the RSW connection. It is also shown that all hybrid connections have nearly the same load level as the clinching joint and do not have a notch effect as high as those of the RSW connection.

The results from the combination of clinching and resistance spot welding show that it is possible to improve the static strength of the joint without having a negative influence by the local material bond on the notch effect of a hybrid connection under cyclic load. A disadvantage of a local material bond by RSW is that it is limited by circular symmetry and the additional high tool wear during the welding of aluminum [11].

4 Investigation on Combination Clinch + Laser Beam Welding

Two linear material bonds with a length of 10 mm through the clinching point have been tested under shear stress. The force application was under 0° and 90° to the weld direction. The results in Fig. 8 show that the orientation of the weld in relation to the load direction has no influence on the strength and no further improvement of strength is reached. By the use of circular welds with different diameters, various

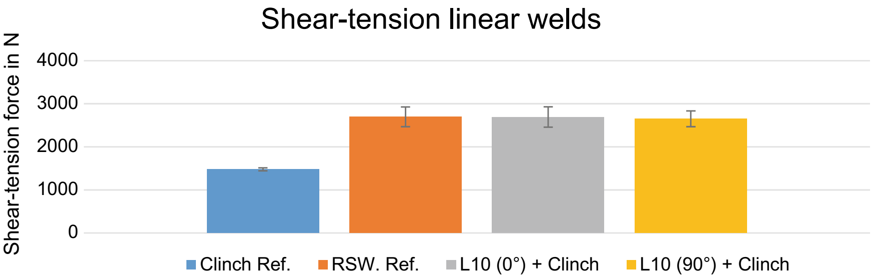

Fig. 8 Linear material bond shear tension

Fig. 9 Comparison of circular material bond

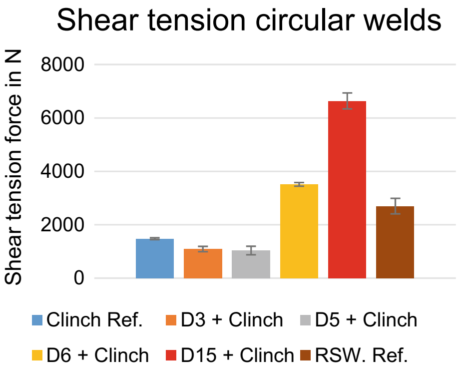

areas of the clinching joint were locally bonded. The diameters of 3 and 5 mm create a local material bond in the bottom area of the joint, the diameter of 6 mm creates a material bond directly in the undercut area as shown in Fig. 4, and the diameter of 15 mm creates a material bond in the periphery of the clinch joint, without contacting it.

Figure 9 shows all circular welds under shear tension. It depicts that a local material bond in the bottom area of a clinch joint leads to a decrease in strength under shear tension. Material bond in the undercut and region around the clinchpoint increases the strength under shear tension.

The hybrid connection with the 15-mm diameter material bond offers the highest increase of strength but also uses up the biggest area for the joining point. Therefore, the achieved strength is set in proportion to the joining point size in Fig. 10, which shows that the joining point with a weld diameter of 6 mm has the highest utilization rate per area. A comparison with the results from the RSW and hybrid connections under different tensions in Fig. 11 shows that through the local material bond by the laser beam welding an increase in both force directions is accomplished. Compared to the reference clinching joint, there is an increase of 85% in strength for cross-tension and an increase of 140% in strength for shear tension. Furthermore, the hybrid connection exceeds the strength of the reference RSW connection.

Fig. 10 Comparison of strength per joint size

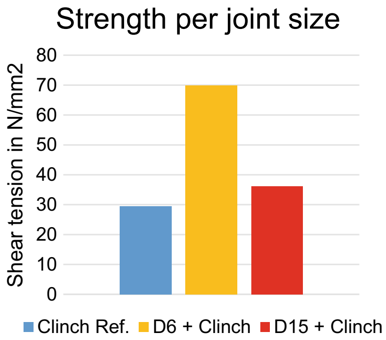

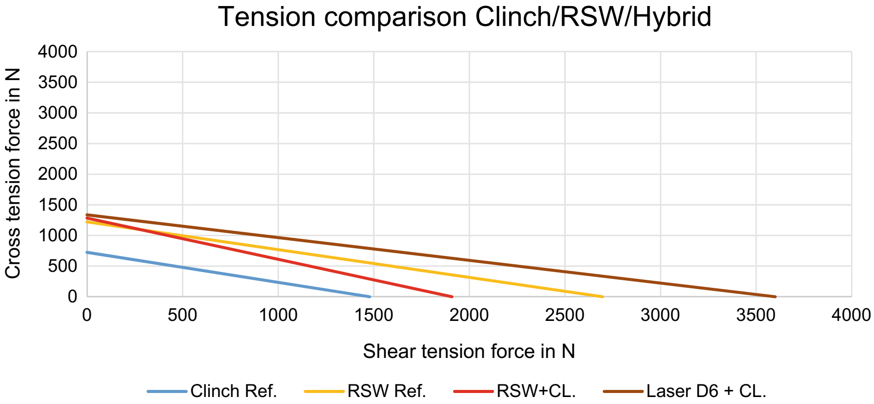

Fig. 11 Tension comparison of CL/RSW/laser

The Wöhler lines for shear tension in Fig. 12 show that both the RSW specimen and the laser-welded specimen are placed under those which are clinched or joined through a hybrid process. This is confirmed through a comparison of the notch effect and the load amplitude for 5×10^5 load circles in Fig. 13. It shows that the welded specimens have a low *k*-factor as well as a low load amplitude. The clinch and hybrid joints have a high *k*-factor as well as a high load amplitude, which nearly level for both the clinch and hybrid joints. Furthermore, the notch effect of the clinch connection is slightly lower than those of the hybrid connections. One can see an increase of load amplitude with an increased local material bond area, while retaining the *k*-factor. This is valid for both the hybrid and laser-welded specimens. The results of the laser–hybrid specimens are similar to the results of the RSW–hybrids and show that the notch effect is compensated completely through the additional clinching process, which means there is no negative effect by the material bond in the undercut and periphery of the clinching joint. This is especially important, as it seems that even a local material bond at the periphery of a clinching joint has no negative effect on

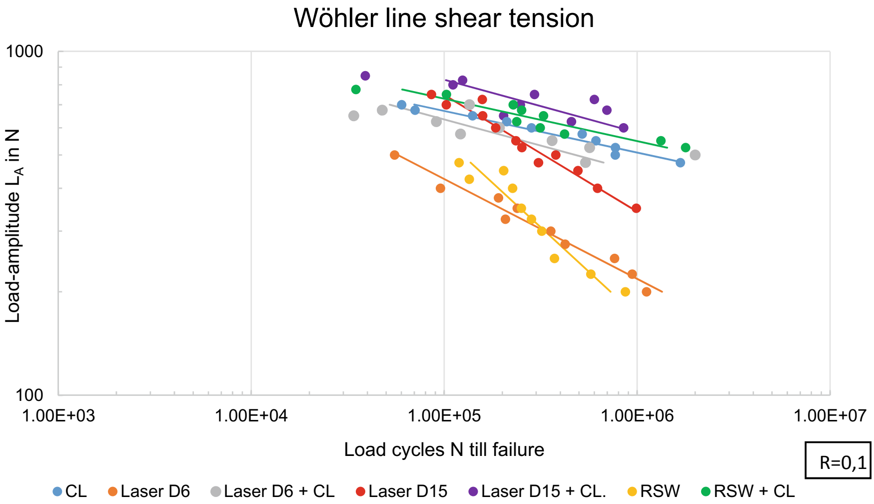

Fig. 12 Wöhler lines

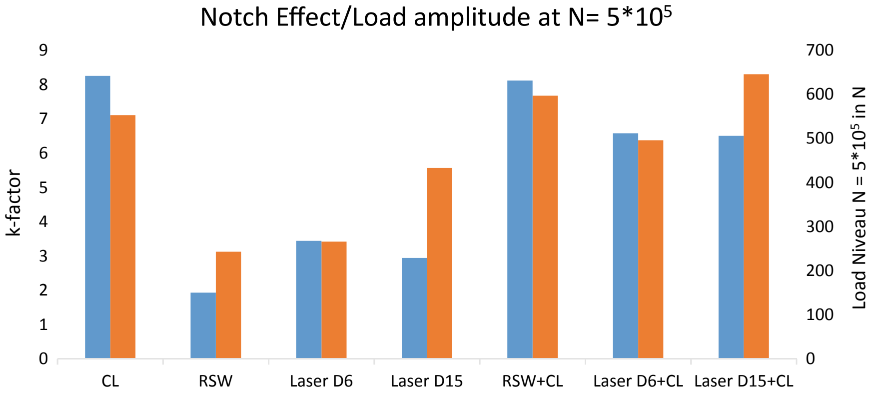

Fig. 13 Notch effect/load amplitude comparison

the fatigue strength. This allows material bond geometries to be tested, which have no contact to the clinching point.

5 Failure Mechanisms

The failure of a clinching joint is strongly dependent on the applied force direction. For example, under shear tension neck failure occurs and under cross-tension button peel appears. Due to the additional material bond, a change of failure mechanism

Fig. 14 Two-step failure

occurred, which depends on the location of these bonds. A material bond at the bottom area of a clinching joint leads to a neck failure as well as the reference clinching joint. At cross-tension, a two-step failure occurs as shown in Fig. 14. In the first step, a button peel occurs, which is caused by the undercut. The second step is cracking of the bottom area, which leads to a total failure of the connection and is caused by the material bond at the bottom area.

Specimens with a material bond at the undercut fail through neck failure, which is independent of force direction. The increase in shear tension and cross-tension strength is due to the increase of neck wideness, which is responsible for the failure mechanism of both force directions, because of the lack of an undercut. Specimens with a material bond in the periphery fail through button peel. In that case, the clinch joint has no influence on the failing mechanism. The failing under cyclic load is identical with those under static load and shear tension. With a decrease of load amplitude, the failure occurs through a crack starting tangential to the joining point and moving to the edge of the specimen.

6 Conclusion and Further Investigations

The results show that due to the combination of a clinching process and a local material bond an increase of the static strength under shear tension as well as cross-tension is possible. The creation of a material bond at the bottom area of a clinching joint leads to an increase of cross-tension only, due to the two-step failure mechanism. A material bond at the undercut or beyond increases the static strength in both force directions. The combination of clinching and laser beam welding has more potential due to the higher strength, the possibility of creating complex geometries as well as no tool wear. If a joint consists of a material bond, the notch effect is completely negated under shear stress, through an extra clinch process regardless of the location of the material bond (bottom, undercut, periphery). The fatigue strength of the hybrid connections levels with those joined by clinching. Further investigations should be done for load directions of 30° and 60° to represent a load with different proportions of shear tension and cross-tension. Next to the static and cyclic load case, the dynamic load case will be tested to see the joint behavior under crash conditions. The local material bond through laser beam welding should be further adapted to achieve best results in strength depending on load directions by, e.g., non-continuous welds or other complex weld geometries. The clinchpoint geometry is to be customized adjusting to the material bond. For example, it is possible to become obsolete for the undercut of the clinching joint, due to the material bond and therefore it is easier to create a joint with one-sided flat geometry.

References

1. Friedrich, H.E.: Leichtbau in der Fahrzeugtechnik, p. 2013. Springer Fachmedien Wiesbaden, Wiesbaden; s.l. (2013)
2. Reinstettel, M.: Laboruntersuchung zur Prozessstabilität beim Niet-Clinchen, vol. 47, p. 2008. Verl. Wiss. Scripten, Zwickau (2008)
3. Wittke, K., Riedel, F.: Hochfeste Durchsetzfüge-Weichlot-Verbindungen. Blech Rohre Profile, Nr. **10**, 798–800 (1992)
4. Riedel, F., Matthes, K.J.: Die Kombination Clinchen - Kaltpressschweißen erzeugt hochfeste und einseitig ebene Verbindungen. DVS Berichte: Schweißen und Schneiden 2000: Vorträge der gleichnamigen Großen Schweißtechnischen Tagung in Nürnberg 27. bis 29, pp. 73–77 (2000)
5. Zhang, Y., Shan, H., Li, Y., Guo, J., Luo, Z., Ma, C.Y.: Joining aluminum alloy 5052 sheets via novel hybrid resistance spot clinching process. Mater. Des. **118**, 36–43 (2017)
6. Lin, P.C., Lo, S.M., Wu, S.P.: Fatigue life estimations of alclad AA2024-T3 friction stir clinch joints. Int. J. Fatigue **107**, 13–26 (2018)
7. Hahn, O., Budde, L.: Quasi-formschlüssige Fügeverfahren kombinieren mit stoffschlüssigen. Bänder Bleche Rohre, Nr. **8**, 82–94 (1989)
8. Osten, J.: Werkstoffstrukturen und Eigenschaften beim laserunterstützten Clinchen von hochfesten Stahl/Aluminium Mischverbindungen. Shaker Verlag GmbH (2018)
9. Doege, E.: Thermisch unterstütztes Clinchen von Blechen und Bauteilen aus Magnesium-Knetlegierungen. Hannover: EFB-Forschungsbericht **203** (2003)
10. Lin, P.C., Chen, W.: Fatigue analysis of swept friction stir clinch joints between aluminum and steel sheets. SAE Int. J. Mater. Manuf. **10**(2), 2017 (2017)
11. Ostermann, F.: Anwendungstechnologie aluminium. Springer, Berlin/Heidelberg (2014)

Development of Semi-analytical Models for Aircraft Wheel Assembly Design

Ahmed Haddar, Louis Augustins, Alain Daidie, Emannuel Rodriguez and Jean-Frédéric Diebold

Abstract This article is devoted to the development of a calculation macro-model for the sizing of aircraft wheel fasteners. By their design, airliners tires are too rigid to be mounted on the wheel like car or motorcycle tires. Therefore, it is necessary to design a wheel in two separate parts so as to plug the tire on a first half-wheel and then "close" the assembly with the second. Therefore, the two half-wheels must be held together. In most cases, a bolted joint plays this essential role. The aim of this work is to develop a methodology related to the generation of semi-analytical model representative of the assembly. The tool is designed with a local approach that models an angular wheel sector including the most solicited bolt. It makes possible to evaluate tensile and bending stresses in the bolt, taking into account the roundness effect of the wheel. The objective is to obtain results close to finite element 3D modeling but with a very limited computation time. To achieve this goal, the principle of this model is to represent all parts of the wheel by 1D axisymmetric elements such as plate and shell elements, beam, tube, and spring elements (to model the contact) ensuring a description close to the actual wheel. Contact between the two half-wheels is also taken into account in order to detect the location of any unsticking after application of external loads. Different cases will be simulated (inflation case, straight line, and cornering

---

A. Haddar (✉) · L. Augustins · J.-F. Diebold
Safran Landing Systems-Velizy, 78140 Vélizy-Villacoublay, France
e-mail: ahmed.haddar@safrangroup.com

L. Augustins
e-mail: Louis.augustins@safrangroup.com

J.-F. Diebold
e-mail: jean-frederic.diebold@safrangroup.com

A. Haddar · A. Daidie · E. Rodriguez
Institut Clement Ader-Toulouse, 31400 Toulouse, France
e-mail: alain.daidie@insa-toulouse.fr

E. Rodriguez
e-mail: Emmanuel.rodriguez@icam.fr

E. Rodriguez
ICAM-Toulouse, 31076 Toulouse, France

L. F. M. da Silva et al. (eds.), *Advanced Joining Processes*,
Advanced Structured Materials 125, https://doi.org/10.1007/978-981-15-2957-3_2

case). The mechanical strength of the most solicited bolt will be analyzed for these different configurations. The results in tensile and bending stresses will be observed at the screw level. A comparison of the results from the proposed digital macro-model and the 3D digital simulations will be analyzed. The developed tool will be used in the early design phase which allows the design engineer to define the mechanical and geometric properties of the wheel and bolts to find the optimal assembly.

Keywords Bolted assembly · Aircraft wheel · Semi-analytical model · Roundness · Non-linear contact

1 Introduction

To ensure a good static stability of an assembly done with fasteners like bolts, the designer is often satisfied with approximate calculations which, combined with an appropriate safety coefficient, make it possible to design these elements with sufficient safety. Unfortunately, this solution does not always guarantee good fatigue resistance, which is essential to ensure the proper functioning of the various elements of a structure and more particularly of the assemblies and to allow a sufficient service life. Indeed, a fatigue calculation is strongly linked not only to the permissible fatigue limits of the metals constituting the parts which are generally defined from the experimental tests, but also to the accuracy of calculations of alternating stresses in the elements to be designed.

Several authors have addressed the problem of the dimensioning of fasteners in both static and fatigue: Jaspart [1] has focused, through its models, on the failure of the assembly while taking into account the plastification of the screw and the assembled parts. Schauman [2] treated the assembly of eccentric symmetrical flanges to provide an expression of bolt deformation based on the geometric data of the assembly.

The most commonly used works in the industry are those of the German recommendations VDI [3]. They have proposed analytical models to calculate the stresses in the screw, when it is a centered or slightly eccentric assembly under certain assumptions. Agatonovic [4], Guillot [5, 6], Bakhiet [7] have developed and perfected the “Bent Beam” model, which treats highly eccentric joints with good precision, taking into account the pretension installed in the screw, and the gapping between the assembled parts. On the other hand, for a geometry such as an aircraft wheel and for high loads, these models do not give precise results, which lead us to choose a new approach that remains within the pre-sizing logic.

Several semi-analytical models have been developed to study the behavior of a bolted assembly in several complex cases. Indeed, semi-analytical models are finite element-based models, reduced to a minimum number of specific elements in order to best describe the behavior of a screwed connection for the shortest possible calculation time. These calculation approaches allow us to model more complex cases, but on the other hand, these models are often specific and restricted to a limited number of configurations. The case of axial loading is not included in this type of model since the analytical models for these configurations are sufficiently efficient. On the other hand, other types of solicitations are studied using simplified numerical models.

Daidie and Chakari [8] modeled two prismatic parts fixed by two screws or two identical bolts. The model consists of discretizing the assembly into one-dimensional finite elements to form a mesh of beam elements with three degrees of freedom per node. The contact between the two assembled parts is modeled by spring elements with two nodes, and each bolt is represented by a beam whose support plane of the head adheres to the upper face of the part. Its results are very satisfactory, unfortunately its field of application remains limited to a rather specific assembly configuration.

Vadean and Leray [9] have developed an advanced model for sizing screwed connections of a roller-bearing slewing ring. The main objective of the model is to calculate the physical quantities loading the crown fixing elements (normal force, bending moment, and alternating stress) which will be used to dimension them in static and fatigue. It models a single-bolt connection element. It therefore assumes that there is no significant variation in load around the sector studied, which is generally the sector relating to the most solicited element. It is made of finite elements at two nodes. Each node has three degrees of freedom.

The objective of Soule de Lafont [10], as part of the CARAB project [11], is to design a finite element connector allowing a better description of the actual behavior of the bolted connection. The objective is the replacement of a 3D calculation model for bolted joints by a 2D calculation model where the bolt would be modeled by a connector taking into account the nonlinearities of the behavior due to play, friction, contact, etc. Consequently, the volume of a case study will be replaced by a model plate or shell. In commercial FE calculation codes, the developed connector implementation is done through a FORTRAN program interpreted by the code. Thus, the tool developed is exportable to different calculation codes. The principle of the connector finite element is to model the overall behavior of a bolted joint without discretization of the fastener. The developed connector model makes it possible to model all phenomena such as bolt–plate interactions and plate–plate contacts. Thus, the bolt is modeled by the connector and the parts by a mesh through plate elements.

Dericquebourg [12] has been interested in modeling assemblies made of volume parts, such as engine mounts. For these assemblies, the tightened part is characterized by a body that is quite voluminous and more rigid than the ends of the part, which have more flexible parts, and this family of assemblies is very diverse in terms of shapes and forces and requires, as interface parts, to be pre-dimensioned very early in the project.

This article focuses on the study of a semi-analytical tool that model the assembly between the two parts that make up an aircraft wheel. First of all, some specific elements of a wheel geometry are presented. Then, the proposed semi-analytical model is described. The process of solving the numerical problem and the procedure chosen to model the contact between the two parts of the wheel in order to detect a possible unsticking are proposed. Thereafter, a comparison study between the results of the developed tool and the results of the 3D finite element models [13–15] is carried out in order to assess the precision and reliability of our results.

Finally, new ideas and approaches will be proposed to improve our model to get as close as possible to reality.

2 Model Description

The tool is designed with a local approach that models an angular wheel sector including the most solicited bolt as shown in Fig. 1.

It makes possible to evaluate tensile and bending stresses in the bolt, taking into account the roundness effect of the wheel. The objective is to obtain results close to finite element 3D modeling considered as reference but with a very limited computation time.

To achieve this goal, the principle of this model is to represent all parts of the wheel by 1D axisymmetric elements such as plate elements, beam, tube, and spring elements (to model the contact) ensuring a description close to the actual wheel. Contact between the two half-wheels is also taken into account in order to detect the location of any gaping after the application of external loads. The local model must take into consideration all the possible loads: inflating, rolling in a straight line, and turning.

The first step is to enter the input parameters that correspond to the geometry of the wheel (dimension of the beads, rims, assembled parts, the stick, and the hubs), the geometry of the bolt (nominal diameter, head diameter, length of the threaded and unthreaded part, the diameter of passage), and the mechanical properties of the wheel and the bolt (Young's modulus and Poisson's ratios). The tool also makes

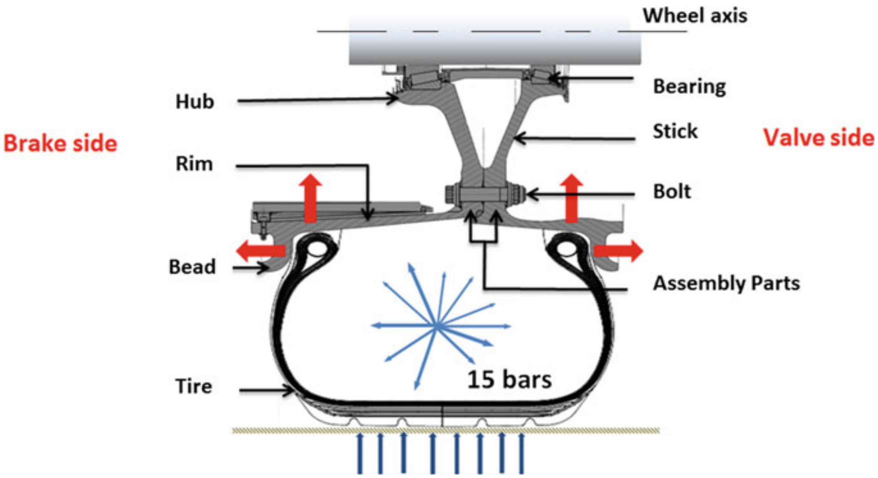

Fig. 1 General description of the aircraft wheel

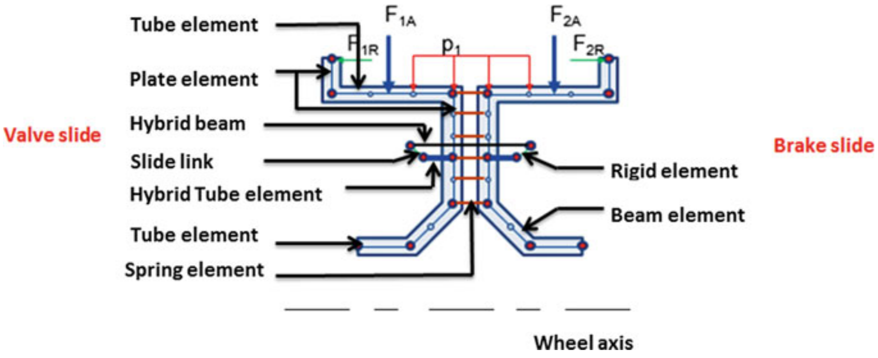

Fig. 2 Semi-analytical model of the aircraft wheel

possible to vary the bolt implantation diameter in order to find the ideal position to size the assembly.

The modeling of the assembly is carried out using 1D elements as presented in Fig. 2.

Indeed, the assembled parts and the beads are presented by axisymmetric plate elements, the rim and the hub by tube elements, the stick by beam elements. To model the stiffness in tension and compression of the bolt, it will be modeled by a hybrid beam element. In order to model the local behavior of the bolt with the wheel, the assembly part is also modeled by a hybrid tube element. The contact between assembled parts is modeled by spring elements.

A detailed description of some elements will be presented in the following paragraphs.

2.1 Plate Element

During the discretization of the assembled part, the weakening caused by the presence of the hole of the passage of the bolt should be taken into account. So a new equivalent thickness at the through hole is calculated. The elementary stiffness matrix is modified to take into account the decrease of rigidity by the presence of the hole.

ϕ is the length of the arc corresponding to the material removed, and ψ is the length of the arc of the remaining material at the hole of the bolt as shown in Fig. 3.

An equivalent thickness is defined from a corrective coefficient ϵ to take into account the attenuation related to the presence of the hole. The lengths are also subtracted from the average radius of the element (a + b)/2.

Assuming that $\sin(\frac{\pi}{z}) < 1$, an approximate value of the multiplier coefficient $\epsilon = \frac{\psi}{(\psi+\phi)}$ as a function of geometry of the structure and the position of nodes of the axisymmetric plate element is obtained.

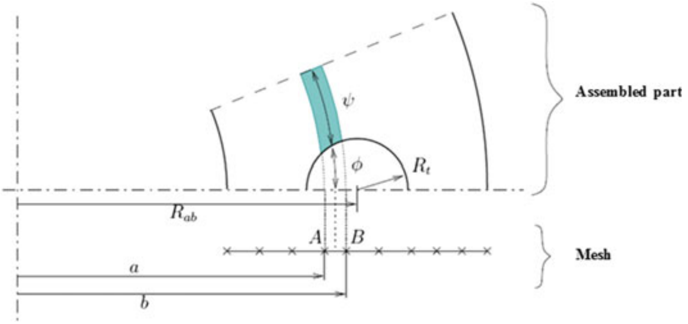

Fig. 3 Taking into account the drilling in the assembly part

$$\varepsilon = 1 - \frac{\sqrt{R_t^2 - (\frac{a+b}{2} - R_{ab})^2}}{\frac{\pi}{Z}\frac{a+b}{2}} \tag{1}$$

where R_t is the hole radius, R_{ab} is the implantation radius of the bolt, a and b are lengths at the radius of axisymmetric plate element, and Z the number of bolts used.

Noticing that the cube of the thickness of the element h^3 is a factor in each term of the stiffness matrix of the plate elements. The equivalent thickness could be calculated with the formula below:

$$h_{eq} = h.\epsilon^{1/3} \tag{2}$$

By knowing the equivalent thickness, the procedure of calculating the elementary matrix of a standard plate element is applied.

2.2 Hybrid Beam Element

The hybrid beam element makes possible to model the threaded element, taking into account its tension stiffness and also bending stiffness. In order to obtain the behavior of the bolt, it is modeled with two beams of different lengths L_0 et L_1, respectively, representing the unthreaded and threaded lengths in the tight length. The global stiffness of the bolt is the sum of the stiffness of the two beams previously mentioned and the rigidity of two fictive beams which represent the screw head and the nut (Fig. 4).

The screw head and the nut act as additional lengths of the bolt. These additional lengths can be expressed using correction coefficients α_0 and α_1 to take into account, respectively, the screw head stiffness of the threaded portion and the screw stiffness. Coefficients α_0 and α_1 vary according to the types of assemblies.

To calculate the tensile flexibility of the bolt S_B, the following equation is used:

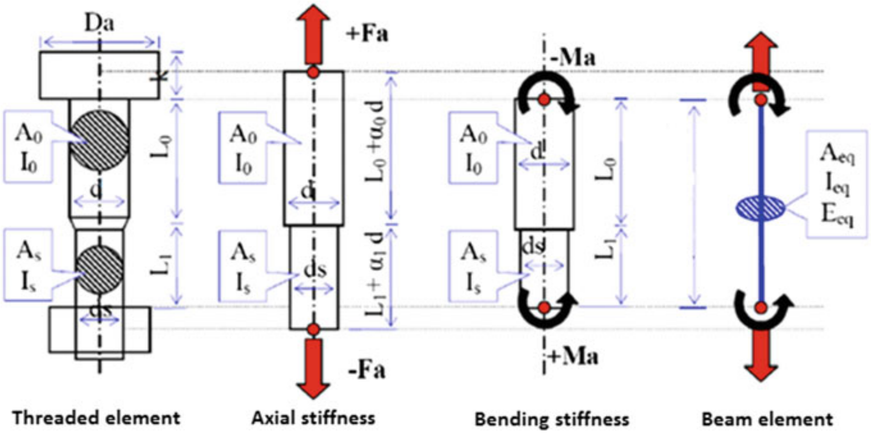

Fig. 4 Reduction of a threaded element to a hybrid beam element

$$S_B = \frac{1}{E_B}[\frac{L_0 + \alpha_0.d}{A_0} + \frac{L_1 + \alpha_1.d}{A_S}] \tag{3}$$

where E_B is Young's modulus of the bolt, A_0 is the surface of the smoothed part of the bolt, A_s is the surface of the threaded part of the bolt.

The bending flexibility S_{FB} is calculated by neglecting the deformations at the screw head and between the nut and the engaged part. The flexibility thus calculated is reduced, and the calculation is conservative. The flexibility is calculated by using the following equation.

$$S_{FB} = \frac{1}{E_B}[\frac{L_0}{I_0} + \frac{L_1}{I_S}] \tag{4}$$

In order to model the exact behavior of the bolt by a beam element, the equivalent surface A_{eq} and the equivalent second moment of area I_{eq} should be founded by using these formulas:

$$A_{eq} = \frac{L_0 + L_1}{\frac{L_0+\alpha_0.d}{A_0} + \frac{L_1+\alpha_1.d}{A_S}} \tag{5}$$

$$I_{eq} = \frac{L_0 + L_1}{\frac{L_0}{I_0} + \frac{L_1}{I_S}} \tag{6}$$

These equivalent properties are then integrated into the stiffness matrix of a conventional beam element, thus making it possible to physically represent the behavior of the element in tension and bending. The bolt head is linked to the half-wheel brake side by a rigid element and a hybrid tube element. The nut is connected to the half-wheel valve side by a slide link and a hybrid tube element.

This slide connection allows us to model the tightening of the bolt by applying a pretension between the center of this connection and the end of the bolt.

2.3 Hybrid Tube Element

In order to model the compression and bending behavior locally in the assembled part of the wheel under the screw head and nut, a new element called hybrid tube element is used.

The stiffness matrix of a hybrid tube element corresponds to a tube element but with axial rigidity. Indeed, it is necessary to build a model whose flexibility in compression of the assembled parts corresponds perfectly. This equivalent axial stiffness can be determined by combining a tube element with a bar element.

The stiffness matrix of an axisymmetric hybrid tube element is illustrated in Fig. 5. The terms "H" and "−H" correspond to the element axial stiffness.

We know that an axial stiffness of a bar element K_p can be found using this formula:

$$K_p = \frac{E.A_p}{L} \tag{7}$$

where L is the length of the element, A_p is the area of the equivalent section, E is Young's modulus of the wheel, and r is the position of the element in relation to the wheel axis. For a tube element, H is equal to $H = \frac{r}{L}$ but for a hybrid element:

$$K_p = \frac{\frac{E.A_p}{L}}{C} \tag{8}$$

where C is equal to $C = \frac{2\pi}{Z} \cdot \frac{E.t}{1-\nu^2}$.

The eccentricity, between the implantation radius of the hybrid beam element, modeling the fixation, and the implantation radius of the hybrid tube elements relative to the two parts of the wheel, is an important parameter for the bending stress of the beam.

This location is determined using the discretization approach of a n-sector face, then determining the position of the center of gravity of these different sectors relative to the location radius of the fasteners as shown in Fig. 6.

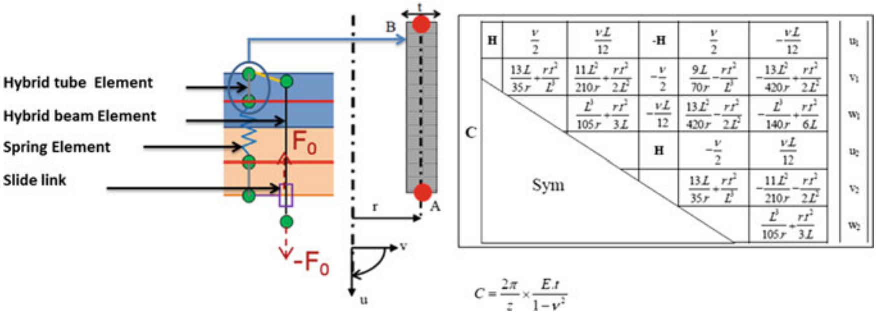

$$C\begin{array}{|cccccc|c}
H & \frac{\nu}{2} & \frac{\nu L}{12} & -H & \frac{\nu}{2} & -\frac{\nu L}{12} & u_1 \\
 & \frac{13L}{35r}+\frac{rt^2}{L^3} & \frac{11L^2}{210r}+\frac{rt^2}{2L^2} & -\frac{\nu}{2} & \frac{9L}{70r}-\frac{rt^2}{L^3} & -\frac{13L^2}{420r}+\frac{rt^2}{2L^2} & v_1 \\
 & & \frac{L^3}{105r}+\frac{rt^2}{3L} & -\frac{\nu L}{12} & \frac{13L^2}{420r}-\frac{rt^2}{2L^2} & -\frac{L^3}{140r}+\frac{rt^2}{6L} & w_1 \\
 & & & H & -\frac{\nu}{2} & \frac{\nu L}{12} & u_2 \\
 & \text{Sym} & & & \frac{13L}{35r}+\frac{rt^2}{L^3} & -\frac{11L^2}{210r}-\frac{rt^2}{2L^2} & v_2 \\
 & & & & & \frac{L^3}{105r}+\frac{rt^2}{3L} & w_2
\end{array}$$

$$C = \frac{2\pi}{z} \times \frac{E.t}{1-\nu^2}$$

Fig. 5 Hybrid tube element

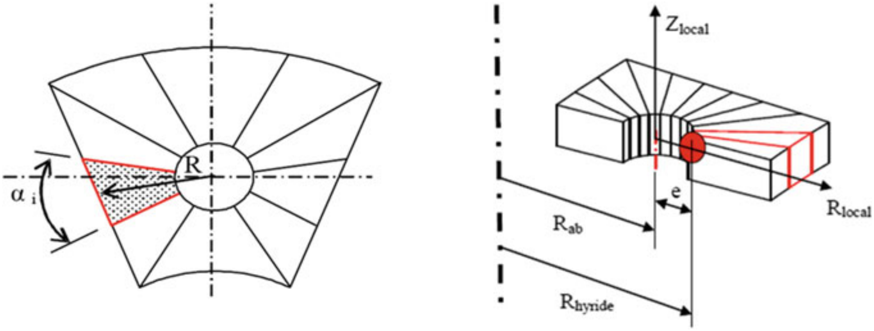

Fig. 6 Location of hybrid tube element

2.4 *Spring Element*

Contact is modeled by springs whose properties are linear. Indeed, these springs are modeled by bar elements that work only in tension–compression. The flexibility of the contact is calculated from the axial flexibility of the assembly multiplying it by a calibration coefficient: $S_{contact} = S_{total} C_{ref}$. C_{ref} is the repair coefficient and represents the proportion of the flexibility of the assembly attributed to the contact element. Subsequently, each spring stiffness is deduced using the following formula:

$$K_i = \frac{(S_{i-1} + S_i)}{(2S_{total} S_{contact})} \tag{9}$$

Indeed, the stiffness of a spring is a fraction of the overall stiffness, and each fraction is proportional to the average of the two mesh surfaces adjacent to the spring.

3 Model Construction

The first step of the code is to calculate the bolt flexibility and those of the assembled parts using the methods described in the previous paragraphs. Subsequently, the structure is meshed; in this part of the code, one can define the size of the element of each part of the geometry can be denied. Then all the elements are built, and their types are defined in order to get as close as possible to reality. Indeed the rim and the hub will be modeled by tube elements, the stick by beam elements, parts assembled by axisymmetric plate elements and hybrid tube elements, and finally, the bolt will be modeled by a hybrid beam element.

The next step is to calculate the spring stiffness of each spring using the method described in 2–4.

At this point, all the necessary elements exist to build the K global stiffness matrix. Then, we apply the preload Q to ensure the tightening of the bolt. Subsequently, we calculate the external force according to the cases of loads (inflation, rolling). These functions allow us to have the force vector F. The final step is to calculate the displacement vector applying the following relation:

$$U = K^{-1}F \tag{10}$$

This displacement vector U allows us to find the tensile and bending stresses in the various positions of the bolt and also the gapping position.

3.1 Global Stiffness Matrix

The global stiffness matrix aims to assemble local stiffness matrices of all elements. These elementary matrices are calculated in the local coordinate system of the element, so they must be transformed into the global coordinate system according to the orientation of the element using a transformation matrix.

Each node has 3 degrees of freedom (U, V, W), so the global matrix will have dimension (3 NbNodes, 3 NbNodes). Once the global matrix is assembled, it is necessary to integrate kinetic relations, linking the bolt to the wheel. Indeed, the bolt head is linked to the wheel by a rigid element. It should be noted that the introduction of a rigid element requires the addition of the kinematic relations between the two nodes concerned. In addition to introduce the pretension of the screw, it is necessary to make a sliding connection between the end of the bolt and the 1/2 wheel.

The contact is only modeled by springs; the friction between the 1/2 wheels is not taken into account so far; we define a kinematic relation on the two most off-center nodes toward the outside of the wheel imposing an identical radial displacement is defined.

The integration of kinematic relationships in the rigidity matrix is operated according CHAIB [16].

A kinematic relation between a master node and a slave node is an equation linking the degrees of freedom of each slave node to those of the master node. Physically, any addition of a kinematic relationship reduces the kinematic unknowns (displacements) and increases static unknowns (reaction forces).

The integration of the kinematic relation that couples the displacement u_m to the displacement u_l reduces the number of kinematic unknowns but it will add a static unknown.

$$\begin{pmatrix} K_{1,1} & \cdots & \cdots & \cdots & \cdots & K_{1,n} \\ \vdots & K_{l,l} & \cdots & \cdots & K_{l,m} & \vdots \\ \vdots & \cdots & K_{i,i} & K_{i,j} & \cdots & \vdots \\ \vdots & \cdots & K_{j,i} & K_{j,j} & \cdots & \vdots \\ \vdots & K_{m,l} & \cdots & \cdots & K_{m,m} & \vdots \\ K_{n,1} & \cdots & \cdots & \cdots & \cdots & K_{n,n} \end{pmatrix} \begin{pmatrix} u_1 \\ u_l \\ u_i \\ \vdots \\ \\ u_m \\ u_n \end{pmatrix} = \begin{pmatrix} F_1 \\ F_l \\ F_i \\ \vdots \\ \\ F_m \\ F_n \end{pmatrix} + \begin{pmatrix} 0 \\ +F^r \\ 0 \\ \vdots \\ \\ -F^r \\ 0 \end{pmatrix} \tag{11}$$

let us take the flowing kinematic relationship $u_m = a - \frac{C_l}{C_m} u_l$. By introducing this relation into stiffness matrix K, the following relations are obtained:

$$\sum_{i,j \neq m,l} K_{i,j} u_j + (K_{i,l} - \frac{C_l}{C_m} K_{i,m}) u_l + 0 \times u_m = F_i - aK_{i,m} \tag{12}$$

$$\sum_{j \neq m,l} K_{l,j} u_j + (K_{l,l} - \frac{C_l}{C_m} K_{l,m}) u_l + 0 \times u_m = F_l - a.K_{l,m} + F^r \tag{13}$$

$$\sum_{j \neq m,l} K_{m,j} u_j + (K_{l,l} - \frac{C_l}{C_m} K_{m,m}) u_l + 0 \times u_m = F_m - a.K_{m,m} - F^r \tag{14}$$

To solve this system of equations, it is necessary to reduce the dimension of the global stiffness matrix dimension to (n −1), in other words, to delete the row and the column “m” and to use a classical linear method.

To avoid the reduction of the matrix and keep the same rank “n”, the kinetic relationship (13) is added to (14), and the new system is then given by:

$$\begin{pmatrix} K_{1,1} & (K_{1,l} - \frac{C_l}{C_m} K_{1,m}) & . & . & 0 & K_{1,n} \\ K_{l,1} + K_{m,1} & B & K_{l,i} + K_{m,i} & K_{l,i} + K_{m,i} & 0 & K_{l,n} + K_{m,n} \\ . & (K_{i,l} - \frac{C_l}{C_m} K_{i,m}) & K_{i,i} & K_{i,j} & 0 & . \\ . & (K_{j,l} - \frac{C_l}{C_m} K_{j,m}) & K_{j,i} & K_{j,j} & 0 & . \\ 0 & A.C_l & 0 & 0 & A.C_m & 0 \\ K_{n,1} & (K_{n,l} - \frac{C_l}{C_m} K_{n,m}) & . & . & 0 & K_{nn} \end{pmatrix} \begin{pmatrix} u_1 \\ u_l \\ u_i \\ \vdots \\ \\ u_m \\ u_n \end{pmatrix}$$

$$= \begin{pmatrix} F_1 - a.K_{1,m} \\ F_l + F_m - 2a.K_{1,m} \\ F_i - a.K_{i,m} \\ \vdots \\ A.a \\ F_n - a.K_{n,m} \end{pmatrix} \tag{15}$$

where $B = K_{l,l} - \frac{C_l}{C_m} K_{1,m} + K_{l,l} - \frac{C_l}{C_m} K_{m,m}$ and A is a non-perturbing constant of the conditioning of the global stiffness matrix K. Our tool assigns to "A" the maximum of diagonal terms relating to degrees of freedom coupled (u_l and u_m), that is the maximum of "$K_{l,l}$" and "$K_{m,m}$".

3.2 Problem Solving

For each load case, the problem is solved in two steps.

The first step is the application of the pretension load to ensure the tightening of the bolt, and the second step is to apply the case of external load cases (inflation, rolling).

First of all, the pretension is applied to both nodes of the element that represents the bolt. To create the slide link, it is necessary to add a fictitious node. It is connected with the bottom of the hybrid tube element, and a positive pretension +Q is applied. And for the node of the bottom of the bolt, a negative pretension −Q is applied. With these two values, the effort vector F is created.

Then, and in order to avoid the global stiffness matrix K singularity and to be able to invert it, it is necessary to define suitable boundary conditions. These boundary conditions consist of clamping all the nodes that represent the bearings. To apply the clamping conditions, the global stiffness matrix K should be modified with the displacement vector U and the external forces vector F by eliminating the rows and columns corresponding to the degrees of freedom clamped for the nodes concerned. Indeed, a smaller system is obtained.

In order to check whether there is a gaping or not between the two parts of the wheel, a linear resolution is impossible. It will be necessary to know in advance the final state of the contact after tightening of the bolt to take only in consideration springs that work in compression and modify the global stiffness matrix.

The idea is to consider; as a first step, the contact is total, meaning that all the springs are taken into account, and thus, their elementary rigidity is included in the global matrix K.

Once the first iteration carried out, springs that work in traction are deactivated. On the other hand, if all the springs work in compression, it means that the solution is valid. if not, the calculation is repeated but this time only the stiffness of the springs in compression are injected, meaning that the global stiffness matrix is recalculated. The operation is repeated until two successive iterations have the same contact state (the same springs working in compression) (Fig. 7).

Once the displacement vector of all the nodes is obtained after tightening, it is possible to assess the relative displacement δ_0 between the two points of applications of the pretension.

This information will be used to substitute the initial loading condition "Q" by its initial relative displacement δ_0 for further calculation under loadings.

To do this, a kinematic relationship is applied between the two link nodes, in order to preserve the initial clamping when computing with an external load.

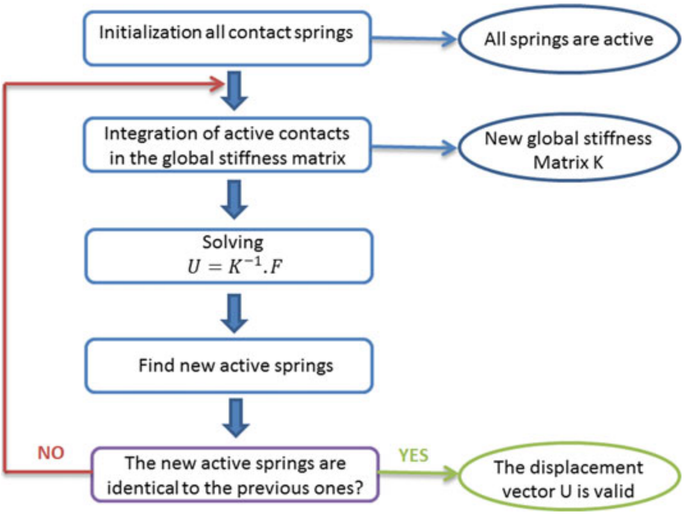

Fig. 7 Contact resolution algorithm

The displacement of the two extreme nodes of the bolt is obtained and makes it possible to calculate the normal force and the bending moment.

The tension and bending stresses in the bolt will subsequently be evaluated. Knowing that no stress is applied to the beam element modeling: the bolt outside the concentrated forces at the nodes, an uniform tension force, and a linear bending moment along with the elements are obtained.

4 Results

Results given by the developed tool using the semi-analytical model and the results of the reference finite elements model in different configurations are presented and compared.

In order to be able to compare the results properly, a finite element model taking into account only one sector (20° for a 23 in. wheel) which contains a single bolt is realized, that is to say, a finite element model that fits our tool is developed.

Subsequently, these tool results are compared with the results of a complete element model which takes into account the whole wheel with all the bolts to valid axisymmetric hypothesis .

Figures 8 and 9 show that the semi-analytical model gives the results of quite close to numerical simulations. The bolt supports normal tensile and bending stresses. The distinction of these solicitations shows a good concordance between the semi-analytical and numerical models (especially in inflation load). Note that the design of the rims offers good rigidity to the wheel. Under severe or even extreme stress,

Fig. 8 Tensile stress in the bolt

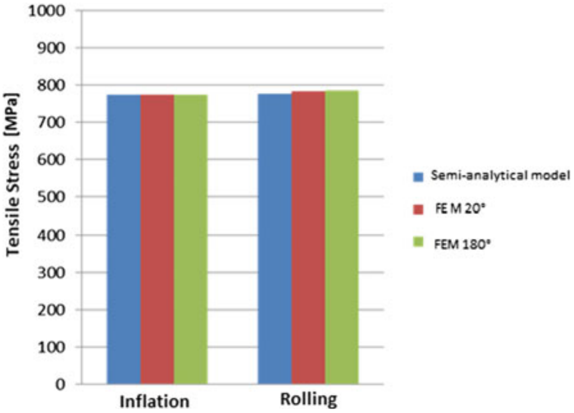

Fig. 9 Bending stress in the bolt

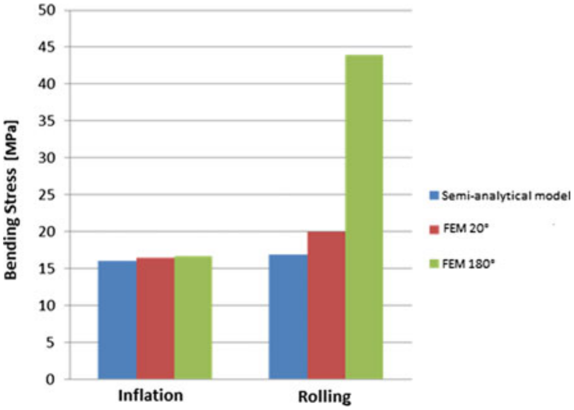

the bending stress existing in the bolt remains low in front of the tensile stress which represents more than 70 % of the total normal stress.

For rolling load, the tool gives very good results concerning the tensile stress. However, concerning the bending stress, it cannot approach the stress calculated by a complete finite element model. Indeed the difference between these stresses (more than 50%) may be explained by the roundness of the wheel due to the weight of the aircraft.

Our model does not represent the forces applied on the wheel accurately, indeed the elements used are all axisymmetric elements which imply that the tool considers the forces as axisymmetric. But, the weight of the aircraft only applies to a well-defined sector of the wheel, which results in its ovalization, which increases bending stresses in the bolts.

5 Conclusion and Prospects

This research work was based on a bibliographical study and more particularly on the semi-analytical models existing in the literature for the pre-dimensioning of fasteners submitted to highly off-centered loads. Several analytical models for the calculation of tensile stress and bending moment in bolts were analyzed to find the most appropriate model for the configuration of an aircraft wheel assembly.

The objective is to properly quantify the tensile and bending stresses in bolts for different loading configurations. Following this bibliographical study, a calculation tool was developed to calculate the tensile and bending stresses in the most stressed bolt located at the lower part of the wheel. The calculation is based on very specific axisymmetric 1D elements that can adequately describe the geometry of a wheel.

From each elemental stiffness matrix of each element, a global stiffness matrix is built, which leads to find the displacements of all the nodes of the system and more precisely the displacements in the nodes that constitute the bolt. These deflections allow to find the tensile and bending stresses in all the positions of the bolt.

Comparison of the results of this semi-analytical model with the reference numerical results shows a good correlation of the tensile stress results calculated at the screw level for the two loading cases applied (inflation and rolling).

However, for the rolling case, the model underestimates the bending stress compared to the 3D finite element model. The proposed model has been tested with several types of wheels of different sizes, and for each case, the same type of results was obtained.

This difference may be explained by the roundness of the wheel that the model does not take into account since it is built by axisymmetric elements.

In order to improve our model, wheel-scale perturbation such as roundness, clamp dispersion, and interaction between different fasteners shall be taken into account. A global-local approach should be developed. Indeed with such an approach a complete system could be performed, not limited to the wheel sector only. This obviously implies knowing the elastic interaction between all bolts. Several research works in the literature [17–20] propose analytical and numerical solutions that can efficiently quantify the elastic interactions between the fasteners of a cylindrical flange.

References

1. Bursi, O., Jaspart, J.P.: Benchmarks for finite element modelling of bolted steel connections. J. Constr. Steel Res. **43**(1–3), 17–42 (1997)
2. Schaumann, P.: Global structural behaviour of ring flange joints. In: *NAFEMS Seminar, Modelling of Assemblies and Joints for Analyses*, 24–25 April 2002, Wiesbaden, Germany (2002)
3. Richtlinien, V.D.I.: VDI 2230. Systematic calculation of highly stressed bolted joints Joints with one cylindrical bolt (2015)
4. Agatonovic, P.: Beam model of beam flanged connections. In: Engineering Computation, vol. 2. Pineridge Press Ltd. (1985)

5. Guillot, J.: Assemblages par éléments filetés: calculs. In: B5560 à B5562, Techniques de l'ingénieur (1987)
6. Guillot, J.: Assemblages par éléments filetés: Modélisation et calcul. In: B5563, Techniques de l'ingénieur (1997)
7. Bakhiet, E.: An Etude des assemblages boulonns chargement fortement excentr soumis des sollicitations de fatigue. In: Thse N319, INSA de Toulouse France, pp. 1–264 (1994)
8. Daidié, A., Chakhari, J., Zghal, A.: Numerical model for bolted T-stubs with two bolt rows. In: *Structural Engineering and Mechanics, An International Journal*, vol. 26(3) 20 June 2007, pp. 343–361 (2007)
9. Vaden, A., Leray, D., Guillot, J.: Bolted joints for very large diameter bearings: numerical model development. Finite Elem. Anal. Des. **42**(4), 298–313 (2006). https://doi.org/10.1016/j.finel.2005.08.001
10. Soule De Lafont, M., Guidault, P., Boucard, P.: A finite element connector based on design parameters for the simulation of bolted assemblies. In: The Twelfth International Conference on Computational Structures Technology (2014)
11. CARAB. Projet FUI 13 CARAB, Conception Avancée Robuste pour les Assemblages Boulonnés, 2012–2016. In http://www.systematic-paris-region.org/fr/projets/carab
12. Dericquevourg, T., Daidie, A., Debarle, F., Sator, M.: An original global-local approach for predimensioning multi bolted joints. In: Proceedings of IDMME—Virtual Concept 2008 Beijing, China, 8–10 Oct 2008
13. Kim, J., Yoon, J.-C., Kang, B.-S.: An Finite element analysis and modelling of structure with bolted joints. Appl. Math. Model. **31**, 895–911 (2007)
14. Izumi, S., Yokoyama, T., Iwasaki, A., Sakai, S.: An Three-dimensional infinite element analysis of tightening and loosening mechanism of threaded fastener. Eng. Fail. Anal. **12**, 604–615 (2005)
15. Kapidzic, Z., Nilsson, L., Ansell, H.: An finite element modeling of mechanically fastened composite-aluminum joints in aircraft structures. Compos. Struct. **109**, 198–210 (2014)
16. Chaib, Z., Daidié, A., Leray, D.: Screw behavior in large diameter slewing bearing assemblies: numerical and experimental analyses. Int. J. Interact. Des. Manuf. **1**(1), 21–31 (2007)
17. Berot, M., Malrieu, J., Bay, F.: An An innovative strategy to create equivalent elements for modelling assembly points in joined structures. Eng. Comput. **31**(3), 453–466 (2014). https://doi.org/10.1108/EC-05-2012-0095
18. Liu, L., Chen, K.: An global-local finite element stress analysis of thick laminate multi-bolt joints in large-scale structures. Finite Elem. Anal. Des. **75**, 31–37 (2013)
19. Askti, R., Bois, C., Wargnier, H., Lecompe, J.: An a reduced fastener model using multi-connected rigid surfaces for the prediction of both local stress field and load distribution between fasteners. In: Finite Elem. Anal. Des. **110**, 32–42 (2016)
20. Nassar, S.A., Yang, X.J.: An novel formulation of bolt elastic interaction in gasketed joints. ASME J. Press. Vessel Technol. **131**(5), 051204 (2009)

Modeling the Effect of Nut Thread Profile Angle on the Vibration-Induced Loosening of Bolted Joint Systems

Sayed A. Nassar and Xianjie Yang

Abstract The effect of the nut thread profile angle is incorporated into a nonlinear friction model for investigating vibration-induced loosening preloaded bolt–nut system that is subjected to a harmonic transverse excitation. The proposed model also takes into account the effect of frictional characteristics of engaged threads and underhead contact surfaces, thread fit class, and hole clearance, as well as on the loosening performance. Correlation is established between the relative translational movement of the bolt–nut system and the relative bending rotation of the bolt–nut system. Critical bending angle is determined by the thread fit clearance. Model results show that as compared to standard nuts with a 60° thread profile angle, M10 × 1.5 nuts with a larger thread profile angle of 120° that are engaged with standard thread M10 × 1.5 bolts (i.e., with 60° thread profile angle) showed significantly higher resistance to loosening under a harmonic transverse load. Results show also that reducing thread fit clearance (i.e., thread fit class) and/or reducing the hole clearance would increase the resistance to vibration-induced loosening.

Keywords Bolt loosening · Thread profile angle

Nomenclature

A_b	Underhead bearing area
E	Young's modulus of bolt material
F_b	Bolt tension
F_{bs}	Transverse bearing friction shear force
F_{xM}	Bolt thread shear force component along x-direction caused by bending moment
$\overline{F}_{bs}$	Bearing friction shear force ratio $\lvert F_{bs}/\mu_b q_{b0}\rvert$
F_{ts}	Thread friction shear force component along x-direction

---

S. A. Nassar (✉) · X. Yang
Department of Mechanical Engineering, Fastening and Joining Research Institute (FAJRI), Oakland University, Rochester, MI 48309, USA
e-mail: nassar@oakland.edu

L. F. M. da Silva et al. (eds.), *Advanced Joining Processes*,
Advanced Structured Materials 125, https://doi.org/10.1007/978-981-15-2957-3_3

$\overline{F}_{\mathrm{ts}}$	Transverse thread friction shear force ratio $\lvert F_{\mathrm{ts}}/\mu_{\mathrm{b}}q_{\mathrm{b0}}\rvert$
h_0	Engaged thread length
I	Moment of inertia for the bolt cross-sectional area
k_{b}	Bolt tensile stiffness
k_{c}	Joint compressive stiffness
L	Bolt grip length
M_{b}	Bending moment on bolt underhead surface
M_{Ns}	Bending moment on nut bearing contact surface
M_{Nt}	Bending moment on thread surface
n	Number of fully engaged threads
p	Thread pitch
q_{b}	Underhead contact pressure
q_{b0}	Average underhead contact pressure
q_{t}	Thread contact pressure
$\boldsymbol{q}_{\mathrm{t}}$	Bolt thread pressure vector
q_{t0}	Average thread contact pressure on the whole engaged threads
q'_{t0}	Average thread contact pressure at the first engaged thread
r	Radius in the polar coordinate system
r_{b}	Equivalent bolt head bearing radius
r_{maj}	Major thread radius
r_{min}	Minor thread radius
r_{o}	Maximum contact radius under the bolt head
r_{i}	Minimum contact radius under the bolt head
T_{b}	Sliding bearing friction torque under transverse cyclic excitation
$\overline{T}_{\mathrm{b}}$	Bearing friction torque ratio $\lvert T_{\mathrm{b}}/\mu_{\mathrm{b}}q_{\mathrm{b0}}\rvert$
T_{p}	Pitch torque component
T_{t}	Sliding thread friction torque under transverse cyclic excitation
$\overline{T}_{\mathrm{t}}$	Thread friction torque ratio $\lvert T_{\mathrm{t}}/\mu_{\mathrm{t}}q_{\mathrm{t0}}\rvert$
v_{bx}	Relative translation velocity along x-direction between the bolt head and the joint bearing surface
$\boldsymbol{v}_{\mathrm{A}}$	Relative translation velocity vector at Point A between the bolt thread and the nut thread
v_{Ax}	Component of $\boldsymbol{v}_{\mathrm{A}}$ along x-direction
v_{Az}	Component of $\boldsymbol{v}_{\mathrm{A}}$ along z-direction
$\boldsymbol{v}_{\mathbf{t}}$	Relative velocity vector on the contact thread surface
v_{tx}	Component of $\boldsymbol{v}_{\mathbf{t}}$ along x-direction
v_{ty}	Component of $\boldsymbol{v}_{\mathbf{t}}$ along y-direction
v_{tz}	Component of $\boldsymbol{v}_{\mathbf{t}}$ along z-direction
$\boldsymbol{w}_1$	Outward unit vector normal to the thread surface
x, x'	Cartesian x-coordinate
z, z'	Cartesian z-coordinate
α	Half of thread profile angle
β	Lead helix angle
β'	Ratio of the transverse thread friction force to the bearing friction shear force
β_{b}	Bending stiffness on bolt underhead contact area

β'_{N}	Combined bending stiffness of the nut bearing surface and the engaged thread surface
β''_{N}	Combined bending stiffness of the nut bearing surface and the engaged thread surface when thread relative slippage occurs
β_{Ns}	Bending stiffness on nut bearing contact area
β_{Nt}	Bending stiffness on bolt thread contact area
χ'	Ratio $F_{\mathrm{ts}}/F_{\mathrm{bs}}$
χ''	Ratio $\Delta F_{\mathrm{ts}}/\Delta F_{\mathrm{bs}}$
δ_{b}	Bolt deflection
δ_{J}	External transverse displacement
δ_0	Amplitude of the transverse cyclic displacement
γ	Ratio of the major radius to the minor radius of the bolt thread: $\gamma = r_{\mathrm{maj}}/r_{\mathrm{min}}$
λ_{b}	Constant for bending stiffness of bolt head
λ_{Ns}	Constant for bending stiffness of nut
λ_{t}	Constant for thread contact pressure non-uniform distribution
η_{b}	Underhead bearing translation-to-rotational sliding speed ratio ($v_{\mathrm{bx}}/\omega_{\mathrm{t}}$)
η_{N}	Nut bearing translation-to-rotational sliding speed ratio ($v_{\mathrm{Nx}}/\omega_{\mathrm{t}}$)
η_{t}	Thread bending-to-torsional rotational sliding speed ratio ($\omega_{\mathrm{A}}/\omega_{\mathrm{t}}$)
ρ_{M}	Ratio ($\rho_{\mathrm{M}} = M_{\mathrm{Nt}}/F_{\mathrm{xM}}$), effective bending moment arm
μ_{b}	Bearing friction coefficient under bolt head
μ_{t}	Thread friction coefficient
θ	Angular coordinate
σ''	Ratio $\Delta\delta_{\mathrm{b}}/\Delta\phi_{\mathrm{Nt}}$
ω_{A}	Bending angular velocity of the bolt thread
φ_{b}	Bending angle at bolt underhead
φ'_{N}	Bending angle of bolt at nut threads
φ_{Ns}	Nut bending angle
φ_{Nt}	Relative bending angle between bolt threads and nut threads
ω_{t}	Relative angular velocity of the thread surfaces about bolt axis with respect to nut thread surface
ω'	Angular frequency of the transverse excitation (rad/s)
Δx	Translational displacement at point A along x-direction
Δz	Translational displacement at point A along z-direction
$\Delta\delta_{\mathrm{BJ}}$	Relative displacement between bolt underhead and joint
$\Delta\delta_{\mathrm{NJ}}$	Relative displacement between the nut and joint
$\Delta\varphi_{\mathrm{Nt}}$	Relative bending angle increment between the bolt threads and nut threads
$\Delta\theta_{\mathrm{A}}$	Rotation angle at point A

1 Introduction

Vibration-induced loosening of preloaded threaded fastener systems can lead to joint leakage at pressure boundaries, fatigue failure, or joint separation leading to significant warranty costs, catastrophic failure, safety risks, or loss of human life. Although there are some studies on the self-loosening of threaded fastener due to vibrations [1–13], none of the existing models has incorporated the thread profile angle as an independent variable that may have a significant effect on the vibration-induced loosening performance of preloaded threaded fastener systems. For example, Hess [7] provided a survey of some experimental and theoretical studies [4–8] on the vibration- and shock-induced loosening of threaded fasteners. The mechanism of vibration-induced loosening of threaded fasteners is primarily attributed to a reduction in the friction torque resistance, which is caused by the relative slippage between contact surfaces such as the interface between engaged threads and/or the interface between the bolt underhead and contacting joint surface [1–8]. Shoji and Sawa [13] proposed a three-dimensional finite element model to simulate the self-loosening of the threaded fastener under transverse cyclic loading. Their FEA simulation has been helpful to the understanding of the mechanics of the self-loosening process.

Nassar and Housari [14–16] developed an experimentally validated linear mathematical model for studying the loosening phenomenon in a preloaded threaded fastener system under a cyclic transverse load. The main variables in their model included the thread pitch, bolt preload, hole clearance, thread fit, bearing and thread friction coefficients, and the excitation amplitude of the cyclic transverse load. It was concluded that these parameters had a significant effect on the self-loosening of threaded fasteners. Their linear model has resulted in a linear correlation between the number of cycles-to-complete loss of bolt tension and the initial bolt preload. Subsequently, Nassar and Yang [17, 18] developed a more accurate nonlinear vibration-induced loosening model that was based on process, based on the relative slippage between two sets of contact surfaces, namely the contacting surfaces of the engaged bolt and nut threads (that had standard profile angles of 60°) and between the bearing contact between the bolt underhead and joint surfaces.

In this study, Nassar and Yang's model [17] is extended to incorporate the effect of the nut thread profile angle (as an independent design variable) on the loosening performance of a preloaded threaded joint model in which the engaged bolt threads have a standard 60° profile angle. Other variables investigated in this study include thread fit clearance, bolt hole clearance, frictional coefficients, and bolt preload level. An experimental procedure and test setup are developed for validating the proposed model.

2 Formulation of Frictional Torque and Shear Forces

This section is primarily dedicated to incorporating the engaged nut thread profile angle (as an independent variable) into the thread friction analysis of engaged bolt threads in a preloaded bolt–nut system that is subjected to a cyclic transverse load. However, frictional analysis of the bolt underhead contact surface with that of the joint surface, shown in Fig. 1, would be the same as that provided in Nassar and Yang model [17] as summarized in the following section.

2.1 Underhead Bearing Friction Analysis

Slippage and friction force illustrations on the underhead bearing contact surface are shown in Fig. 2. A transverse bearing friction shear force $\overline{F}_{\mathrm{bs}}$ and the corresponding bearing friction torque $\overline{T}_{\mathrm{b}}$ are given by Nassar and Yang [17] in terms of a newly defined speed ratio η_{b} as follows:

$$\overline{F}_{bs} = f_{3b}(\eta_b) = \left|\frac{F_{bs}}{\mu_b q_{b0}}\right| = \int_{r_i}^{r_o} r dr \int_0^{2\pi} \frac{(\eta_b + r\sin\theta)d\theta}{\sqrt{\eta_b^2 + r^2 + 2\eta_b r\sin\theta}} \tag{1}$$

$$\overline{T}_{\mathrm{b}} = f_{1\mathrm{b}}(\eta_{\mathrm{b}}) = \left|\frac{T_{\mathrm{b}}}{\mu_{\mathrm{b}} q_{\mathrm{b}0}}\right| = \int_{r_{\mathrm{i}}}^{r_{\mathrm{o}}} r^2 \mathrm{d}r \int_0^{2\pi} \frac{(\eta_{\mathrm{b}}\sin\theta + r)d\theta}{\sqrt{\eta_{\mathrm{b}}^2 + r^2 + 2\eta_{\mathrm{b}} r\sin\theta}} \tag{2}$$

$$\eta_{\mathrm{b}} = v_{\mathrm{bx}}/\omega_{\mathrm{t}} \tag{3}$$

where η_{b} is simply the ratio of the bolt underhead translational (sliding) speed $v_{1\mathrm{b}}$ in the x-direction to the bolt head angular (loosening) speed ω_{t}, T_{b} is the sliding

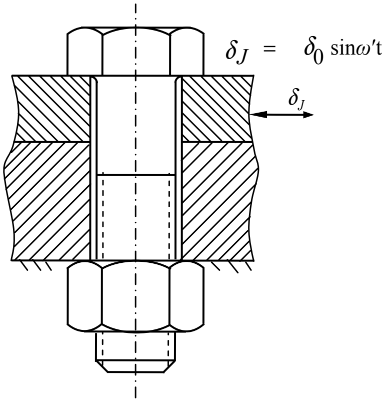

Fig. 1 Schematic of a bolt–nut model under harmonic transverse excitation

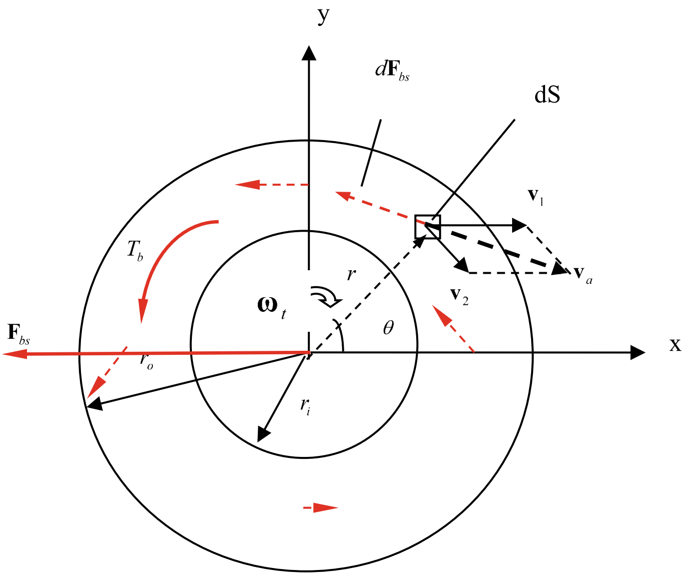

Fig. 2 Schematic diagram of underhead bearing sliding speeds bearing friction shear and torque

underhead bearing friction torque, F_{bs} is the underhead bearing friction shear force, μ_{b} is the underhead bearing friction coefficient, q_{b0} is the average underhead contact pressure, r_{i} and r_{o} are, respectively, the minimum and maximum underhead contact radii; r and θ are the polar coordinates within the underhead contact area.

Equations (1) and (2) are numerically solved for ratios $\overline{F}_{\mathrm{bs}}$ and $\overline{T}_{\mathrm{b}}$ in terms of the speed ratio η_{b} as a variable. Figure 3 shows that the bearing friction torque ratio $\overline{T}_{\mathrm{b}}$ (solid line) rapidly decreases with increasing η_{b} in the range $0 \leq \eta_{\mathrm{b}} \leq 75$, and it asymptotes to a nearzero value for $\eta_{\mathrm{b}} \geq 300$. However, the bearing shear force ratio $\overline{F}_{\mathrm{bs}}$ (dotted line) rises sharply from zero (at $\eta_{\mathrm{b}} = 0$) to a saturation value of $A_{\mathrm{b}} = \pi\left(r_{\mathrm{o}}^2 - r_{\mathrm{i}}^2\right)$ when $\eta_{\mathrm{b}} \geq 50$, approximately. The condition $\eta_{\mathrm{b}} = 0$ represents the case where the relative slippage is only due to bolt head rotation, as the force F_{bs} becomes zero in Eq. (1); the corresponding bearing friction torque in Eq. (2) is $T_{\mathrm{b}} = \mu_{\mathrm{b}} F_{\mathrm{b}} r_{\mathrm{b}}$, where F_{b} is the bolt tension and r_{b} is equivalent bearing friction radius. As $\eta_{\mathrm{b}} \to \infty$, however, the relative slippage becomes pure linear translational movement against the bearing friction force that peaks at $F_{\mathrm{bs}} = \mu_{\mathrm{b}} F_{\mathrm{b}}$ (with $T_{\mathrm{b}} = 0$).

2.2 Incorporation of Nut Thread Profile Angle into Frictional Analysis of Engaged Thread Surfaces

With reference to Fig. 4, since the (lead) helix angle is fairly small for standard threaded fastener products, its effect would be insignificant to the relationship

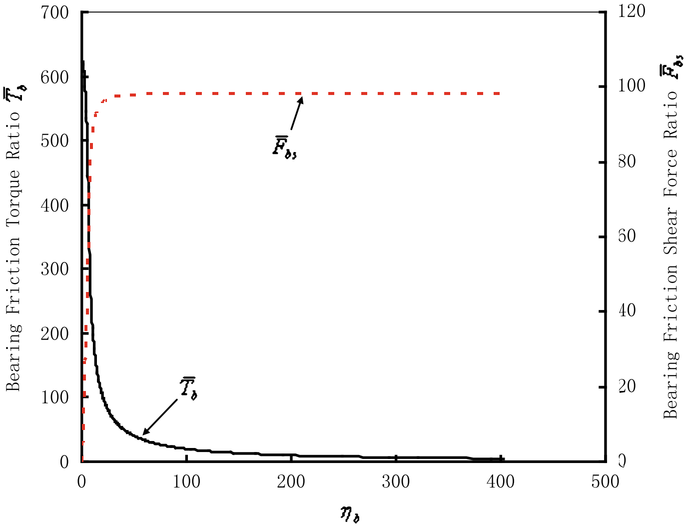

Fig. 3 Bearing friction ratios $\overline{T}_{\mathrm{b}}$ and $\overline{F}_{\mathrm{bs}}$ versus bearing speed ratio η_{b} for M10 × 1.5 bolt–nut model

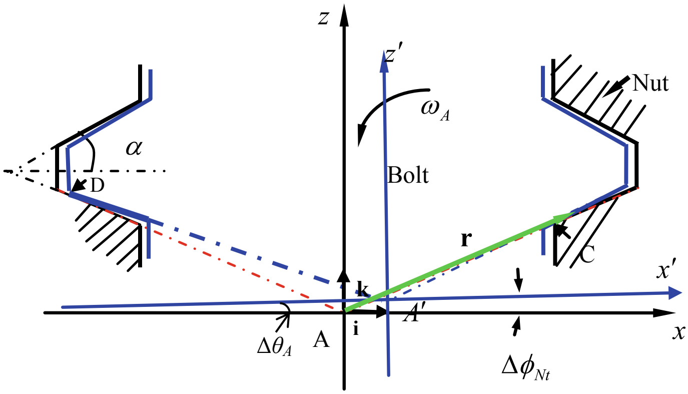

Fig. 4 Simplified 2-D schematic of local bolt and nut axes and relative slippage between engaged threads

between the x- and z-displacements at Point A and the bending angle of the thread flank. The kinetic relationship is hence established between the bending angle of the thread flank and the slippage of bolt threads with respect to the nut threads. At point A, the relative movements between the bolt and the nut are bending rotation angle $\Delta\theta_{\mathrm{A}}$, and linear x- and z-displacements Δx_{A} and Δz_{A}, respectively. The key parameter $\Delta\theta_{\mathrm{A}}$ for the effect of geometry clearance on the loosening performance is investigated in this study. The $x - z$ coordinate system is fixed on bolt thread while the $x' - z'$ system is fixed on nut thread. Before any relative bending rotation occurs between bolt and nut, the original two coordinate systems coincide and have the same original point A. When a bending rotation occurs, the $x' - z'$ coordinate system has a relative translational displacement and a relative bending rotation with respect to the $x - z$ system. The relationship between the two coordinate systems is given by

$$\begin{Bmatrix} x \\ z \end{Bmatrix} = \begin{Bmatrix} \Delta x_{\mathrm{A}} \\ \Delta z_{\mathrm{A}} \end{Bmatrix} + \begin{bmatrix} \cos \Delta\theta_{\mathrm{A}} & -\sin \Delta\theta_{\mathrm{A}} \\ \sin \Delta\theta_{\mathrm{A}} & \cos \Delta\theta_{\mathrm{A}} \end{bmatrix} \begin{Bmatrix} x' \\ z' \end{Bmatrix} \tag{4}$$

For the thread surface shown in Fig. 4, we have

$$z = \pm x \tan\alpha \tag{5}$$

$$z' = \pm x' \tan\alpha \tag{6}$$

where α is half of the thread profile angle.

Equation (4) gives the following values for x and z as follows:

$$x = \Delta x_{\mathrm{A}} + x' - \Delta\theta_{\mathrm{A}} z' \tag{7}$$

$$z = \Delta z_{\mathrm{A}} + \Delta\theta_{\mathrm{A}} x' + z' \tag{8}$$

For point C on the nut thread where $x = r_{\min}$, $z = r \tan\alpha_{\min}$, $z' = x' \tan\alpha$, we have

$$\Delta x_{\mathrm{A}} + x'(1 - \Delta\theta_{\mathrm{A}} \tan\alpha) = r_{\min} \tag{9}$$

$$r_{\min} \tan\alpha = \Delta z_{\mathrm{A}} + x'(\Delta\theta_{\mathrm{A}} + \tan\alpha) \tag{10}$$

where $r_{\min}$ is the minor thread radius of the nut.

Solving Eqs. (9) and (10) and ignoring higher order terms gives the kinematic equation for point A as follows:

$$\Delta z_{\mathrm{A}} - \Delta x_{\mathrm{A}} \tan\alpha = -\Delta\theta_{\mathrm{A}} \left[r_{\min} \left(1 + \tan^2\alpha \right) \right] \tag{11}$$

Similarly, for point D on the bolt thread (Fig. 4), using the geometric relations $x' = -r_{\mathrm{maj}}$, $z' = r_{\mathrm{maj}} \tan\alpha$, and $z = -x \tan\alpha$, where r_{maj} is the major thread radius and combing with Eq. (11) gives the x- and z-translational displacements Δx_{A} and Δz_{A} of point A and the corresponding translational velocity components v_{Ax} and v_{Az} as follows:

$$\Delta x_{\mathrm{A}} = \frac{(r_{\mathrm{maj}} + r_{\min})}{\sin 2\alpha_{\mathrm{A}}} \Delta\theta_{\mathrm{A}} \tag{12}$$

$$\Delta z_{\mathrm{A}} = \left(\frac{r_{\mathrm{maj}} - r_{\mathrm{min}}}{2} \sec^2 \alpha_{\mathrm{A}} \Delta\theta_{\mathrm{A}}\right) \tag{13}$$

$$v_{\mathrm{Ax}} = \frac{r_{\mathrm{maj}} + r_{\mathrm{min}}}{\sin 2\alpha} \Delta\theta_{\mathrm{A}} \tag{14}$$

$$v_{\mathrm{Az}} = \left(\frac{r_{\mathrm{maj}} - r_{\mathrm{min}}}{2}\right) \sec^2 \alpha \cdot \theta_{\mathrm{A}} \tag{15}$$

where ω_{A} is the time derivative $\mathrm{d}\theta_{\mathrm{A}}/\mathrm{d}t$ of the bending angle of the bolt thread.

Equations (14) and (15) characterize the relationship between the translational velocity components of point A and the bending angular speed of thread contact in x-z plane. However, the relative tangential velocity vector $\boldsymbol{v}_{\mathrm{t}}$ on the engaged threads would also include a relative rotational component about the bolt axis z. Thus, at any point on the bolt thread contact surface, the relative velocity $\boldsymbol{v}_{\mathrm{t}}$ with respect to the engaged nut threads is given by

$$\begin{aligned}\boldsymbol{v}_{\mathrm{t}} = \boldsymbol{v}_{\mathrm{A}} + (-\omega_{\mathrm{A}}\boldsymbol{j}) \times \boldsymbol{r} + (\omega_{\mathrm{t}}\boldsymbol{k}) \times \boldsymbol{r} = \left[v_{\mathrm{Ax}} - \omega_{\mathrm{A}}\left(\frac{p}{2\pi}\theta + r\tan\alpha\right) - \omega_{\mathrm{t}} r \sin\theta\right]\boldsymbol{i} \\ + \omega_{\mathrm{t}} r \cos\theta\, \boldsymbol{j} + (v_{\mathrm{Az}} + \omega_{\mathrm{A}} r \cos\theta)\boldsymbol{k}\end{aligned} \tag{16}$$

where p is the thread pitch, ω_{t} is the relative angular velocity of the thread surface about the z-axis with respect to nut thread surface.

The differential thread friction force vector $\mathrm{d}\boldsymbol{F}_{\mathrm{t}}$ on the representative area element of the engaged thread contact area is given by

$$\mathrm{d}\boldsymbol{F}_{\mathrm{t}} = \mu_{\mathrm{t}} q_{\mathrm{t}} \mathrm{d}S \frac{\boldsymbol{v}_{\mathrm{t}}}{|\boldsymbol{v}_{\mathrm{t}}|} \tag{17}$$

where μ_{t} is the thread friction coefficient, q_{t} is the thread contact pressure, and $\frac{\boldsymbol{v}_{\mathrm{t}}}{|\boldsymbol{v}_{\mathrm{t}}|}$ is a unit vector in the tangential direction. The corresponding transverse friction force component in the x-direction would be obtained from the dot product of an x-unit vector $\boldsymbol{i}$ with vector Eq. (17); the total transverse friction force F_{ts} on the thread surface would then be given by

$$\begin{aligned}F_{\mathrm{ts}} &= \iint\limits_{\Omega_{\mathrm{thread}}} \mu_{\mathrm{t}} q_{\mathrm{t}} \frac{\boldsymbol{v}_{\mathrm{t}} \cdot \boldsymbol{i}}{|\boldsymbol{v}_{\mathrm{t}}|} \mathrm{d}S \\ &= \int\limits_{r_{\mathrm{min}}}^{r_{\mathrm{maj}}} r\mathrm{d}r \int\limits_{0}^{2n\pi} \frac{\mu_{\mathrm{t}} q_{\mathrm{t0}} \left\{\frac{v_{\mathrm{Ax}}}{\omega_{\mathrm{t}}} - \frac{\omega_{\mathrm{A}}}{\omega_{\mathrm{t}}}\left(\frac{p}{2\pi}\theta + r\tan\alpha\right) - r\sin\theta\right\} \sqrt{\sec^2\alpha + \tan^2\beta}\,\mathrm{d}\theta}{\sqrt{\left[\frac{v_{\mathrm{Ax}}}{\omega_{\mathrm{t}}} - \frac{\omega_{\mathrm{A}}}{\omega_{\mathrm{t}}}\left(\frac{p}{2\pi}\theta + r\tan\alpha\right) - r\sin\theta\right]^2 + r^2\cos^2\theta + \left[\frac{v_{\mathrm{Az}}}{\omega_{\mathrm{t}}} + \frac{\omega_{\mathrm{A}}}{\omega_{\mathrm{t}}} r\cos\theta\right]^2}}\end{aligned} \tag{18}$$

where Ω_{thread} is the overall thread contact surface area between all engaged n threads, q_{t0} is average thread contact pressure, and β is the lead helix angle of the bolt and nut threads.

Additionally, using Eq. (17), the thread friction torque increment $\mathrm{d}T_{\mathrm{t}}$ would be given by

$$
\begin{aligned}
dT_{\mathrm{t}} &= (\boldsymbol{r} \times \mathrm{d}\boldsymbol{F}_{\mathrm{t}}) \cdot \boldsymbol{k} \\
&= \begin{vmatrix} \boldsymbol{i} & \boldsymbol{j} & \boldsymbol{k} \\ r\cos\theta & r\sin\theta & r\tan\alpha + \frac{p\theta}{2\pi} \\ v_{\mathrm{tx}} & v_{\mathrm{ty}} & v_{\mathrm{tz}} \end{vmatrix} \cdot \boldsymbol{k}\frac{\mu_{\mathrm{t}} q_{\mathrm{t0}}}{v_{\mathrm{t}}}\mathrm{d}S = \left(r\cos\theta v_{\mathrm{ty}} - r\sin\theta v_{\mathrm{tx}}\right)\frac{\mu_{\mathrm{t}} q_{\mathrm{t0}}}{v_{\mathrm{t}}}\mathrm{d}S
\end{aligned}
\tag{19}
$$

where v_{tx}, v_{ty}, and v_{tz} are the corresponding components of the sliding velocity vector $\boldsymbol{v}_t$ along x- , y- and z-directions, respectively. Taking the surface integral on the engaged thread surface Ω_{thread} gives the total thread friction torque T_{t} as follows:

$$
\begin{aligned}
T_{\mathrm{t}} &= \iint\limits_{\Omega_{\mathrm{thread}}} \mu_{\mathrm{t}} q_{\mathrm{t0}} \frac{\left(r\cos\theta v_{\mathrm{ty}} - r\sin\theta v_{\mathrm{tx}}\right)}{v_{\mathrm{t}}}\mathrm{d}S \\
&= \int\limits_{r_{\mathrm{min}}}^{r_{\mathrm{maj}}} r\mathrm{d}r \int\limits_{0}^{2n\pi} \frac{\mu_{\mathrm{t}} q_{\mathrm{t0}}\left\{r^2 - r\sin\theta\left[\frac{v_{\mathrm{Ax}}}{\omega_{\mathrm{t}}} - \frac{\omega_{\mathrm{A}}}{\omega_{\mathrm{t}}}\left(\frac{p}{2\pi}\theta + r\tan\alpha\right)\right]\right\}\sqrt{\sec^2\alpha + \tan^2\beta}\mathrm{d}\theta}{\sqrt{\left[\frac{v_{\mathrm{Ax}}}{\omega_{\mathrm{t}}} - \frac{\omega_{\mathrm{A}}}{\omega_{\mathrm{t}}}\left(\frac{p}{2\pi}\theta + r\tan\alpha\right) - r\sin\theta\right]^2 + r^2\cos^2\theta + \left[\frac{v_{\mathrm{Az}}}{\omega_{\mathrm{t}}} + \frac{\omega_{\mathrm{A}}}{\omega_{\mathrm{t}}} r\cos\theta\right]^2}}
\end{aligned}
\tag{20}
$$

Using Eqs. (18) and (20) and following a procedure similar to that employed in Sect. 2.1, the transverse thread force $\overline{F}_{\mathrm{ts}}$ and thread torque $\overline{T}_{\mathrm{t}}$ are obtained as follows:

$$
\overline{F}_{\mathrm{ts}} = \frac{F_{\mathrm{ts}}}{n\mu_{\mathrm{t}} q_{\mathrm{t0}}} = \int\limits_{r_{\mathrm{min}}}^{r_{\mathrm{maj}}} r\mathrm{d}r \int\limits_{0}^{2\pi} \frac{\left\{\left[\frac{r_{\mathrm{maj}} + r_{\mathrm{min}}}{\sin 2\alpha} - \left(\frac{p}{2\pi}\theta + r\tan\alpha\right)\right]\eta_{\mathrm{t}} - r\sin\theta\right\}\sqrt{\sec^2\alpha + \tan^2\beta}\mathrm{d}\theta}{\sqrt{\left\{\left[\frac{r_{\mathrm{maj}} + r_{\mathrm{min}}}{\sin 2\alpha} - \left(\frac{p}{2\pi}\theta + r\tan\alpha\right)\right]^2 + \left[\frac{r_{maj} - r_{\mathrm{min}}}{2}\sec^2\alpha + r\cos\theta\right]^2\right\}\eta_{\mathrm{t}}^2 + r^2 - 2\left[\frac{r_{\mathrm{maj}} + r_{\mathrm{min}}}{\sin 2\alpha} - \left(\frac{p}{2\pi}\theta + r\tan\alpha\right)\right]\eta_{\mathrm{t}} r\sin\theta}}
\tag{21}
$$

$$
\overline{T}_{\mathrm{t}} = \frac{T_{\mathrm{t}}}{n\mu_{\mathrm{t}} q_{\mathrm{t0}}} = \int\limits_{r_{\mathrm{min}}}^{r_{\mathrm{maj}}} r\mathrm{d}r \int\limits_{0}^{2\pi} \frac{\left\{r^2 + \eta_{\mathrm{t}}\left(\frac{p\theta}{2\pi} + r\tan\alpha - \frac{r_{\mathrm{maj}} + r_{\mathrm{min}}}{\sin 2\alpha}\right) r\sin\theta\right\}\sqrt{\sec^2\alpha + \tan^2\beta}\mathrm{d}\theta}{\sqrt{\left\{\left[\frac{r_{\mathrm{maj}} + r_{\mathrm{min}}}{\sin 2\alpha} - \left(\frac{p}{2\pi}\theta + r\tan\alpha\right)\right]^2 + \left[\frac{r_{\mathrm{maj}} - r_{\mathrm{min}}}{2}\sec^2\alpha + r\cos\theta\right]^2\right\}\eta_{\mathrm{t}}^2 + r^2 - 2\left[\frac{r_{\mathrm{maj}} + r_{\mathrm{min}}}{\sin 2\alpha} - \left(\frac{p}{2\pi}\theta + r\tan\alpha\right)\right]\eta_{\mathrm{t}} r\sin\theta}}
\tag{22}
$$

where the bending-to-torsional angular (sliding) speed ratio η_{t} on the threads is defined by

$$
\eta_{\mathrm{t}} = \frac{\omega_{\mathrm{A}}}{\omega_{\mathrm{t}}}
\tag{23}
$$

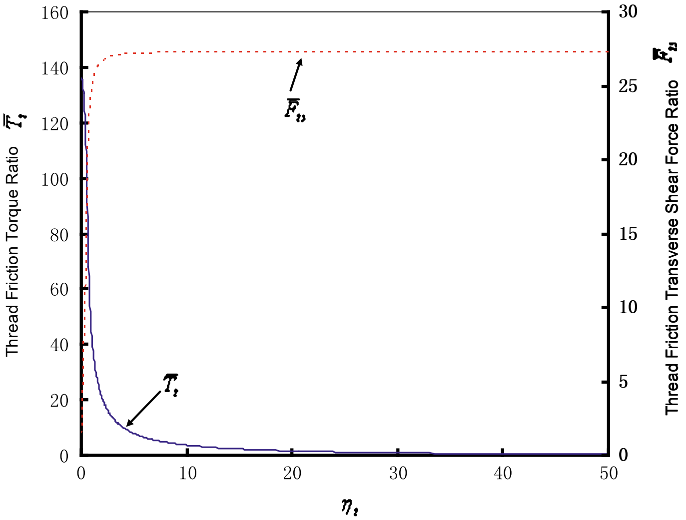

Fig. 5 Thread friction ratios $\overline{T}_t$ and $\overline{F}_{ts}$ versus thread speed ratio η_t for M10 × 1.5 bolt–nut model

Integral Eqs. (21) and (22) are numerically solved for $\overline{F}_{ts}(f_{3t}(\eta_t))$ and $\overline{T}_t(f_{1t}(\eta_t))$ in terms of the bending-to-torsional rotational sliding speed ratio η_t. Figure 5 shows that the (sliding) thread friction torque $\overline{T}_t$ (solid line) decreases rapidly in the range $0 \leq \eta_t \leq 20$; its value approaches zero for $\eta_t > 30$, although the limit of the right-hand side of Eq. (22) goes to zero as $\eta_t \to \infty$. The thread friction transverse shear force ratio $\overline{F}_{ts}$ (dotted line) rises rapidly from zero at $\eta_t = 0$ to its saturation value.

Under the transverse cyclic load (Fig. 1), intermittent vibration-induced loosening of the bolt would only occur when the value of system's pitch torque component $T_p = \frac{p}{2\pi} F_b$ from bolt–nut preloading [19] exceeds the sum of the sliding bearing friction torque component T_b and the sliding thread friction torque component T_t. From Eqs. (2) and (22), the condition for vibration-induced bolt loosening is given by

$$\left[T_p = \frac{p}{2\pi} F_b\right] > \left[\left(T_b = \mu_b n q_{b0} \overline{T}_b\right) + \left(T_t = \mu_t n q_{t0} \overline{T}_t\right)\right] \tag{24}$$

2.3 Transverse Shear Force on Bolt Thread Surface Due to Bending

The contact pressure distribution on preloaded engaged thread surfaces varies significantly along the bolt axis, with the highest contact pressure being on the first fully engaged thread near the face of the nut [20, 21]. Thread contact pressure rapidly

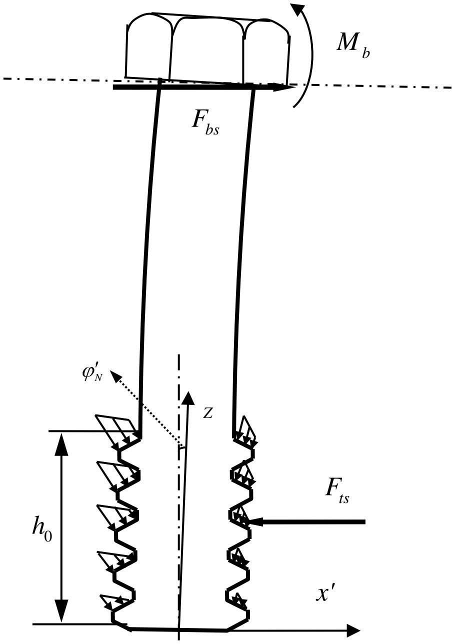

Fig. 6 Schematic of thread contact pressure distribution on threads

decreases with the distance from the first fully engaged thread. Bolt bending due to the externally applied transverse excitation would cause non-uniform distribution on each thread surface as illustrated by Fig. 6. A nonlinearly varying thread contact pressure vector $\boldsymbol{q}_{\mathrm{t}}$ is assumed as follows:

$$\boldsymbol{q}_{\mathrm{t}} = -\left[1 - \frac{p\theta}{3\pi h_0} - \frac{1}{3}\left(\frac{p\theta}{2\pi h_0}\right)^2\right]\left(q'_{\mathrm{t}0} + \lambda_{\mathrm{t}}\varphi_{\mathrm{Nt}}\frac{r\cos\theta}{r_{\mathrm{maj}}}\right)\boldsymbol{w}_1 \tag{25}$$

where $q'_{\mathrm{t}0}$ is the average thread contact pressure on the first engaged thread surface, z is the axial location, x is the transverse location, λ_{t} is a constant, φ_{Nt} is the bending angle at bolt threads, h_0 is the thread engagement length, $\boldsymbol{w}_1$ is the unit vector normal to the thread surface, which is given by

$$\boldsymbol{w}_1 = \frac{-(\tan\alpha\cos\theta + \tan\beta\sin\theta)\boldsymbol{i} - (\tan\alpha\sin\theta - \tan\beta\cos\theta)\boldsymbol{j} + \boldsymbol{k}}{\sqrt{\sec^2\alpha + \tan^2\beta}} \tag{26}$$

The bolt preload F_{b} is obtained by integrating the contact pressure overall engaged thread surfaces as follows:

$$F_b = \iint\limits_{\Omega_{\mathrm{thread}}} \left|\mathrm{q}_t \cdot \mathrm{k}\right| ds \approx \int\limits_{r_{\mathrm{maj}}}^{r_{\mathrm{min}}} r\,dr \int\limits_{0}^{2n\pi} q'_{t0}\left[1 - \frac{p\theta}{3\pi h_0} - \frac{1}{3}\left(\frac{p\theta}{2\pi h_0}\right)^2\right] d\theta$$

$$\approx q_t' 0 n\pi \left(r_{\mathrm{maj}}^2 - r_{\mathrm{min}}^2\right)\left\{1 - \frac{1}{3} - \frac{1}{9}\right\} = \frac{5}{9} q_t' 0 n\pi \left(r_{\mathrm{maj}}^2 - r_{\mathrm{min}}^2\right) \tag{27}$$

Thus, the average thread contact pressure $q_{\mathrm{t}0}'$ on the surface of the first engaged thread would be given by

$$q_{\mathrm{t}0}' = \frac{9F_{\mathrm{b}}}{5n\pi\left(r_{\mathrm{maj}}^2 - r_{\mathrm{min}}^2\right)} \tag{28}$$

The total transverse thread shear force component F_{xM} (along x-direction) caused by the non-uniform pressure distribution on all thread surfaces would be through dot product by the unit vector $\mathbf{i}$ as follows:

$$\begin{aligned}
F_{\mathrm{xM}} &= \iint\limits_{\Omega_{\mathrm{thread}}} \left|\boldsymbol{q}_{\mathrm{t}} \cdot \boldsymbol{i}\right| \mathrm{d}s \\
&\approx \int\limits_{r_{\mathrm{min}}}^{r_{\mathrm{maj}}} r\mathrm{d}r \int\limits_{0}^{2n\pi} (\tan\alpha\cos\theta \\
&+ \tan\beta\sin\theta)\left[1 - \frac{p\theta}{3\pi h_0} - \frac{1}{3}\left(\frac{p\theta}{2\pi h_0}\right)^2\right]\lambda_{\mathrm{t}}\varphi_{\mathrm{Nt}}\left(\frac{r\cos\theta}{r_{\mathrm{maj}}}\right) d\theta \\
&\approx \frac{5n\pi\tan\alpha\lambda_{\mathrm{t}}\varphi_{\mathrm{nt}}}{27r_{\mathrm{maj}}}\left(r_{\mathrm{maj}}^3 - r_{\mathrm{min}}^3\right)
\end{aligned} \tag{29}$$

The corresponding bending moment M_{Nt} caused by the non-uniform thread contact pressure $\boldsymbol{q}_{\mathrm{t}}$ about y-axis at the nut axis center is formulated as follows:

$$\begin{aligned}
M_{\mathrm{Nt}} = \iint\limits_{\Omega_{\mathrm{xy}}} &\left\{r\cos\theta + \left[r\tan\alpha + \tfrac{\theta}{2\pi}p\right](\tan\alpha\cos\theta + \tan\beta\sin\theta)\right\}\left[1 - \tfrac{p\theta}{3\pi h_0}\right. \\
&\left. -\tfrac{1}{3}\left(\tfrac{p\theta}{2\pi h_0}\right)^2\right]\lambda_{\mathrm{t}}\varphi_{\mathrm{Nt}}\tfrac{r\cos\theta}{r_{\mathrm{maj}}} r\mathrm{d}r\mathrm{d}\theta = \tfrac{\lambda_{\mathrm{t}}\varphi_{\mathrm{nt}}}{r_{\mathrm{mx}}} \\
\int_{r_{\mathrm{min}}}^{r_{\mathrm{maj}}} r^3\mathrm{d}r &\int\limits_{0}^{2n\pi} [\cos\theta - (\theta\tan\beta + \tan\alpha)(\tan\alpha\cos\theta + \tan\beta\sin\theta)]\cos\theta d\theta \\
&\approx \tfrac{n\pi\lambda_{\mathrm{t}}\varphi_{\mathrm{Nt}}}{r_{\mathrm{maj}}}\left(r_{\mathrm{maj}}^4 - r_{\mathrm{min}}^4\right)\left[\tfrac{5}{36}\sec^2\alpha + \tfrac{7n\pi}{72}\tan\alpha\tan\beta\right] = \beta_{\mathrm{Nt}}\varphi_{\mathrm{N}t}
\end{aligned} \tag{30}$$

where Ω_{xy} is the projected area of the thread contact area on x-y plane, and the bending stiffness β_{Nt} of the engaged threads is given by

$$\beta_{\mathrm{Nt}} \approx \frac{n\pi\lambda_{\mathrm{t}}}{r_{\mathrm{maj}}}\left(r_{\mathrm{maj}}^4 - r_{\mathrm{min}}^4\right)\left[\frac{5}{36}\sec^2\alpha + \frac{7n\pi}{72}\tan\alpha\tan\beta\right] \tag{31}$$

From Eqs. (29) and (30), the relationship between the thread shear force F_{xM} and the corresponding bending moment M_{Nt} on the thread surfaces may be expressed as follows:

$$F_{\mathrm{xM}} = \frac{M_{\mathrm{Nt}}}{\rho_{\mathrm{M}}}, \ \rho_{\mathrm{M}} = \frac{r_{min}\left(\gamma^4 - 1\right)\left(30\sec^2\alpha + 21n\pi\tan\alpha\tan\beta\right)}{40\tan\alpha\left(\gamma^3 - 1\right)} \tag{32}$$

where the effective bending moment arm ρ_{M} and the number of fully engaged threads in Fig. 6 is $n = h_0/p$.

As long as bolt bending (due to M_{Nt}) does not consume the hole clearance (to causes direct contact between the bolt shank and the internal surface of the hole), the thread friction shear force component F_{ts} in the x-direction would be given by

$$F_{\mathrm{ts}} = F_{\mathrm{bs}} + M_{\mathrm{Nt}}/\rho_{\mathrm{M}} \tag{33}$$

2.4 Rate of Bolt Loosening Due to Cyclic Transverse Load

In this section, various scenarios are used to formulate the rate of vibration-induced loosening per cycle in a preloaded bolt–nut model that incorporates the nut thread profile angle as an independent variable. Classical elastic beam theory is used in connection with the preceding formulation of the bearing shear force F_{bs}, bolt bending moment M_{b}, and twisting torque components T_{b} and T_{tp}.

Scenario I: No slippage on any contact surfaces (bolt underhead, nut face, or thread surfaces)

The bolt deflection δ_{b} and the bending angle φ_{b} at the junction with the bolt head (Fig. 6) are, respectively, given by

$$\delta_{\mathrm{b}} = \frac{F_{\mathrm{bs}}L^3}{3EI} - \frac{M_{\mathrm{b}}L^2}{2EI} + \varphi_{\mathrm{N}}'L \tag{34}$$

$$\varphi_{\mathrm{b}} = \frac{F_{\mathrm{bs}}L^2}{2EI} - \frac{M_{\mathrm{b}}L}{EI} + \varphi_{\mathrm{N}}' \tag{35}$$

where L is bolt grip length, E is Young's modulus of bolt material, I is moment of inertia of the bolt cross-sectional area, M_{b} is bending moment acting at the bolt underhead surface, the angle φ_{N}' is the sum of the nut rotational angle φ_{Ns} and the relative bending angle φ_{Nt} between the bolt threads and nut threads as follows:

$$\varphi_{\mathrm{N}}' = \varphi_{\mathrm{Ns}} + \varphi_{\mathrm{Nt}} \tag{36}$$

As the bolt and nut have small masses, when the transverse vibration frequency and excitation amplitude are not very high, the dynamic inertia force and moment can be ignored. The equilibrium conditions of the bolt–nut connection can make the following relationships

$$F_{\mathrm{bs}}L = M_{\mathrm{b}} + M_{\mathrm{Ns}}, \quad F_{\mathrm{bs}} = F_{\mathrm{N}s}, \quad M_{\mathrm{Ns}} = M_{\mathrm{Nt}} \tag{37}$$

where F_{Ns} is the shear force on the nut bearing contact surface along x-direction, and M_{Ns} is the bending moment on nut bearing contact surface.

The relationships between the bending moments and the corresponding rotations of the bolt underhead, nut bearing surface and the engaged threads are assumed to be expressed as follows:

$$M_{\mathrm{b}} = \beta_{\mathrm{b}}\varphi_{\mathrm{b}}, \quad M_{\mathrm{Ns}} = \beta_{\mathrm{Ns}}\varphi_{\mathrm{N}s}, \quad M_{\mathrm{Nt}} = \beta_{\mathrm{Nt}}\varphi_{\mathrm{Nt}} \tag{38}$$

where β_{b}, β_{Ns}, and β_{Nt} are, respectively, the bending stiffness of bolt underhead to joint, nut bearing-to-joint, and bolt threads-to-nut. The combined bending stiffness $\beta_{\mathrm{N}}^{'}$ of the nut bearing-to-joint and the engaged threads to nut is expressed as follows:

$$\frac{1}{\beta_{\mathrm{N}}^{'}} = \frac{1}{\beta_{\mathrm{Ns}}} + \frac{1}{\beta_{\mathrm{Nt}}} \tag{39}$$

From Eqs. (35) to (38), the following equations are also obtained

$$\delta_{\mathrm{b}} = \frac{F_{\mathrm{bs}}L^3}{3EI}\left\{1 + \frac{\frac{3EI}{L\beta_{\mathrm{N}}'} - \frac{3L}{4EI}\beta_{\mathrm{b}}}{1 + \frac{\beta_{\mathrm{b}}L}{EI} + \frac{\beta_{\mathrm{b}}}{\beta_{\mathrm{N}}'}}\right\}, \quad \varphi_{\mathrm{b}} = \frac{3EI\delta_{\mathrm{b}}}{L^2}\frac{\frac{L}{2EI} + \frac{1}{\beta_{\mathrm{N}}'}}{1 + \frac{3EI}{\beta_{\mathrm{N}}'L} + \frac{\beta_{\mathrm{b}}L}{4EI} + \frac{\beta_{\mathrm{b}}}{\beta_{\mathrm{N}}'}},$$
$$\varphi_{\mathrm{Nt}} = \frac{3EI\delta_{\mathrm{b}}}{\beta_{\mathrm{Nt}}L^2}\frac{1 + \frac{\beta_{\mathrm{b}}L}{2EI}}{1 + \frac{3EI}{\beta_{\mathrm{N}}'L} + \frac{\beta_{\mathrm{b}}L}{4EI} + \frac{\beta_{\mathrm{b}}}{\beta_{\mathrm{N}}'}} \tag{40}$$

If the bolt underhead and nut bearing contact pressures are assumed to vary linearly along the x-direction (Fig. 6), the bending moments M_{b} and M_{Ns} are given by

$$M_{\mathrm{b}} = \frac{\lambda_{\mathrm{b}}\pi}{4r_{\mathrm{e}}}\left(r_{\mathrm{e}}^4 - r_{\mathrm{i}}^4\right)\varphi_{\mathrm{b}} = \beta_{\mathrm{b}}\varphi_{\mathrm{b}}, \quad M_{\mathrm{Ns}} = \frac{\lambda_{\mathrm{Ns}}\pi}{4r_{\mathrm{Ne}}}\left(r_{\mathrm{Ne}}^4 - r_{\mathrm{Ni}}^4\right)\varphi_{\mathrm{Ns}} = \beta_{\mathrm{N}s}\varphi_{\mathrm{N}s} \tag{41}$$

where λ_{b} and λ_{Ns} are constants which affect β_{b} and β_{Ns}, respectively, and they are presented as follows:

$$\beta_{\mathrm{b}} = \frac{\lambda_{\mathrm{b}}\pi}{4r_{\mathrm{e}}}\left(r_{\mathrm{e}}^4 - r_{\mathrm{i}}^4\right), \quad \beta_{\mathrm{N}s} = \frac{\lambda_{\mathrm{Ns}}\pi}{4r_{\mathrm{Ne}}}\left(r_{\mathrm{Ne}}^4 - r_{\mathrm{Ni}}^4\right) \tag{42}$$

Equation (40) shows the linear relationship between the bolt deflection δ_{b} and the underhead friction shear force F_{bs} given by Eq. (1), which would also determine the value of the sliding underhead friction torque T_{b}. Similarly, Eqs. (34), (38), and (40) give the transverse shear force F_{ts} on the engaged threads in terms of F_{bs} as follows:

$$F_{\mathrm{ts}} = F_{\mathrm{bs}} + M_{\mathrm{Nt}}/\rho_{\mathrm{M}} = F_{\mathrm{bs}}\left[1 + \left(\frac{L}{\rho_{\mathrm{M}}}\right)\frac{1 + \frac{\beta_{\mathrm{b}}L}{2EI}}{1 + \frac{\beta_{\mathrm{b}}L}{EI} + \frac{\beta_{\mathrm{b}}}{\beta_{\mathrm{N}}'}}\right] = \chi' F_{\mathrm{bs}},$$

$$\chi' = \left[1 + \left(\frac{L}{\rho_{\mathrm{M}}}\right) \frac{1 + \frac{\beta_{\mathrm{b}} L}{2EI}}{1 + \frac{\beta_{\mathrm{b}} L}{EI} + \frac{\beta_{\mathrm{b}}}{\beta'_{\mathrm{N}}}}\right] \tag{43}$$

The expression for χ' in Eq. (43) represents the ratio of the thread friction force F_{ts} to the bearing friction shear force F_{bs}, which is obviously larger than 1.

Scenario II: Slippage only on the engaged thread surfaces (without slippage under the bolt head or the nut face)
When slippage occurs on the thread contact surface (as the contact friction force has reached its critical value), the increment $\Delta\delta_{\mathrm{b}}$ in bolt deflection and the corresponding bending angle increment $\Delta\varphi_{\mathrm{b}}$ of the bolt axis at the bolt head is, respectively, given by

$$\Delta\delta_{\mathrm{b}} = \frac{\Delta F_{\mathrm{bs}} L^3}{3EI} - \frac{\Delta M_{\mathrm{b}} L^2}{2EI} + \Delta\varphi'_{\mathrm{N}} L, \quad \Delta\varphi_{\mathrm{b}} = \frac{\Delta F_{\mathrm{bs}} L^2}{2EI} - \frac{\Delta M_{\mathrm{b}} L}{EI} + \Delta\varphi'_{\mathrm{N}} \tag{44}$$

Following the same procedure in scenario I, expressions for $\Delta\delta_{\mathrm{b}}$, $\Delta\varphi_{\mathrm{b}}$, φ_{Nt}, and F_{ts} are obtained as follows:

$$\begin{aligned}
\Delta\delta_{\mathrm{b}} &= \frac{\Delta F_{\mathrm{bs}} L^3}{3EI}\left\{1 + \frac{\frac{3EI}{L\beta''_{\mathrm{N}}} - \frac{3L}{4EI}\beta_{\mathrm{b}}}{1+\frac{\beta_{\mathrm{b}} L}{EI} + \frac{\beta_{\mathrm{b}}}{\beta''_{\mathrm{N}}}}\right\},\\
\Delta\varphi_{\mathrm{b}} &= \left(\frac{3EI\Delta\delta_{\mathrm{b}}}{L^2}\right)\frac{\frac{L}{2EI} + \frac{1}{\beta''_{\mathrm{N}}}}{1+\frac{3EI}{\beta''_{\mathrm{N}} L} + \frac{\beta_{\mathrm{b}} L}{4EI} + \frac{\beta_{\mathrm{b}}}{\beta''_{\mathrm{N}}}},\\
\Delta\varphi_{\mathrm{Nt}} &= \left(\frac{3EI\Delta\delta_{\mathrm{b}}}{\beta'_{\mathrm{Nt}} L^2}\right)\frac{1+\frac{\beta_{\mathrm{b}} L}{2EI}}{1+\frac{3EI}{\beta''_{\mathrm{N}} L} + \frac{\beta_{\mathrm{b}} L}{4EI} + \frac{\beta_{\mathrm{b}}}{\beta''_{\mathrm{N}}}} = \Delta\delta_{\mathrm{b}}/\sigma'',\\
\Delta F_{\mathrm{ts}} &= \Delta F_{\mathrm{bs}} + \frac{\Delta M_{\mathrm{Nt}}}{\rho_{\mathrm{M}}} = \Delta F_{\mathrm{bs}}\left[1 + \left(\frac{L}{\rho_{\mathrm{M}}}\right)\frac{1+\frac{\beta_{\mathrm{b}} L}{2EI}}{1+\frac{\beta_{\mathrm{b}} L}{EI} + \frac{\beta_{\mathrm{b}}}{\beta''_{\mathrm{N}}}}\right]\\
&= \chi'' \Delta F_{\mathrm{bs}}
\end{aligned} \tag{45}$$

where β'_{Nt} (which much less than β_{Nt} in Eq. (39)) is the contact bending stiffness of the bolt threads with respect to the nut threads as relative slippage between engaged threads occurs, and β''_{N} is the combined bending stiffness (bolt threads to nut and nut to clamped joint) during the slippage of the threads given by

$$\frac{1}{\beta''_{\mathrm{N}}} = \frac{1}{\beta_{\mathrm{Ns}}} + \frac{1}{\beta'_{\mathrm{Nt}}}, \tag{46}$$

and σ'' is given by

$$\sigma'' = \frac{1 + \frac{3EI}{\beta''_{\mathrm{N}} L} + \frac{\beta_{\mathrm{b}} L}{4EI} + \frac{\beta_{\mathrm{b}}}{\beta''_{\mathrm{N}}}}{1 + \frac{\beta_{\mathrm{b}} L}{2EI}}\left(\frac{\beta'_{\mathrm{Nt}} L^2}{3EI}\right) \tag{47}$$

A linear relationship exists in Eq. (45) between the incremental bolt deflection $\Delta\delta_{\mathrm{b}}$ and the incremental underhead shear force ΔF_{bs} . The total value of the bearing transverse friction shear force F'_{bs} would be

$$F'_{\mathrm{bs}} = F_{\mathrm{bs}} + \Delta F_{\mathrm{bs}} \tag{48}$$

Similar to Scenario 1, the value of the underhead friction shear force F'_{bs} will determine the value of the sliding underhead friction torque T_{b} by using Eqs. (1) and (2). Equation (45) also gives the relative bending angle increment $\Delta\varphi_{\mathrm{Nt}}$ between the bolt threads and nut threads in terms of bolt deflection increment $\Delta\delta_{\mathrm{b}}$. If the thread angle increment $\Delta\varphi_{\mathrm{Nt}}$ reaches its critical value $\Delta\varphi_{\mathrm{Ntcr}}$, which is determined by the thread geometry and the class of thread fit, slippage between the engaged threads would stop (i.e., loosening rotation would stop under this condition). Further increase of the transverse displacement of the joint would only cause relative transverse slippage between the nut face and the joint surface, which does not cause any loosening.

Scenario III: Relative slippage occurs simultaneously between all of the three sets of contact surfaces (bolt underhead–joint, nut face–joint, and engaged bolt–nut threads)

As outlined in Scenarios I and II, bolt loosening will only take place when each of the two surfaces is sliding against its respective contact. That requires the bolt underhead surface to be sliding against the contacting joint surface, which must also be simultaneous with relative sliding occurring between the contact surfaces of engaged threads. This is further explained in the following two sections:

(1) **Simultaneous slippage on the bolt underhead–joint and the engaged bolt–nut thread surfaces (without nut face slippage)**

The relative displacement $\Delta\delta_{\mathrm{BJ}}$ between bolt underhead and the fixed joint is given by

$$\Delta\delta_{\mathrm{BJ}} = \delta_{\mathrm{J}} - \Delta\delta_{\mathrm{b}} - \Delta x_{\mathrm{A}} = \delta_{\mathrm{J}} - \sigma''\Delta\varphi_{\mathrm{Nt}} - \Delta x_{\mathrm{A}} \tag{49}$$

$$\delta_{\mathrm{J}} = \delta_0 \sin\omega' t \tag{50}$$

where δ_{b} is the bolt deflection that corresponds to the relative displacement between the bolt underhead and its threaded end, δ_{J} is the cyclic joint transverse excitation, Δx_{A} is the relative displacement of the bolt threads, $\Delta\varphi_{\mathrm{Nt}}$ is the relative bolt thread bending angular increment with respect to nut, δ_0 is the amplitude of cyclic transverse excitation, and ω' is the angular frequency of the transverse excitation.

Differentiating Eq. (49) with respect to time, and the translational-to-angular speed ratios η_{b} and η_{t} as defined earlier (Sects. 2.1 and 2.2) gives bolt rotational speed ω_{t} of bolt threads relative to engaged nut threads as follows:

$$\omega_{\mathrm{t}} = \frac{\dot{\delta}_{\mathrm{J}}}{\eta_{\mathrm{b}} + \eta_{\mathrm{t}}\left(\frac{r_{\mathrm{maj}}+r_{\mathrm{min}}}{\sin 2\alpha} + \sigma''\right)} \tag{51}$$

The relative bending rotation increment $\Delta\varphi_{\mathrm{Nt}}$ with respect to the nut is obtained by integration as follows:

$$\Delta\varphi_{\mathrm{Nt}} = \int_{t_1}^{t} \omega_{\mathrm{A}}\mathrm{d}t = \int_{t_1}^{t} \eta_{\mathrm{t}}\omega_{\mathrm{t}}\mathrm{d}t \tag{52}$$

where t_1 indicated the start of loosening and t is current time (i.e., loosening duration $= t - t_1$).

The critical value $\Delta\varphi_{\mathrm{Ntcr}}$, which is the maximum bending angle between the bolt and the nut, is approximately determined by

$$\Delta\varphi_{\mathrm{Ntcr}} = \frac{\Delta d_{\mathrm{th}}}{\sqrt{d^2 + H^2}} \tag{53}$$

where Δd_{th} is the thread fit clearance between the bolt threads and nut threads (Fig. 7: based on pitch diameter), d is the bolt nominal diameter, H is the thread engagement length (Fig. 6). If $\Delta\varphi_{\mathrm{Nt}}$ reaches its critical value $\Delta\varphi_{\mathrm{Ntcr}}$, the bolt threads cannot have further relative bending angle increment with nut threads. The critical value $\Delta\varphi_{\mathrm{Ntcr}}$ is dependent on the thread clearance Δd_{th} (fit class), the thread engagement length H, and the thread major–minor diameters. As a result, $\Delta\varphi_{\mathrm{Ntcr}}$ would be proportional to the thread fit clearance, and it would decrease with the increasing the thread engagement length H and thread diameter. The horizontal resisting force would balance the external transverse shear force. The thread friction torque will increase significantly by the transverse resistant force. Under this scenario, the loosening condition is not satisfied and the loosening rotation of the bolt will stop.

On the other hand, if the absolute value $|\Delta\delta_{\mathrm{BJ}}|$ of the relative displacement reaches its critical value, which is equal to the joint hole diameter clearance Δd_{h}, the bolt shank will contact with the cylindrical surface of the hole. The contact pressure on the hole surface will produce additional friction torque resistance to the bolt loosening rotation. The additional friction torque can prevent the self-loosening of the threaded fastener.

If $\Delta\varphi_{\mathrm{Nt}} < \Delta\varphi_{\mathrm{Ntcr}}$ and $|\Delta\delta_{\mathrm{BJ}}| < \Delta d_{\mathrm{h}}$, the incremental clamp load loss $\mathrm{d}F_{\mathrm{b}}$ due to loosening caused by the transverse cyclic loading is given by

$$\mathrm{d}F_{\mathrm{b}} = \frac{k_{\mathrm{b}}k_{\mathrm{c}}}{k_{\mathrm{b}}+k_{\mathrm{c}}}\frac{p}{2\pi}\omega_{\mathrm{t}}\mathrm{d}t = \frac{k_{\mathrm{b}}k_{\mathrm{c}}}{k_{\mathrm{b}}+k_{\mathrm{c}}}\frac{p}{2\pi}\frac{\left|\dot{\delta}_{\mathrm{J}}\right|\mathrm{d}t}{\eta_{\mathrm{b}} + \eta_{\mathrm{t}}\left(\sigma'' + \frac{r_{\mathrm{maj}}+r_{\mathrm{min}}}{\sin 2\alpha}\right)} \tag{54}$$

(2) **Simultaneous slippage on the joint–nut face and bolt–nut engaged thread surfaces (without slippage on the bolt underhead surface)**

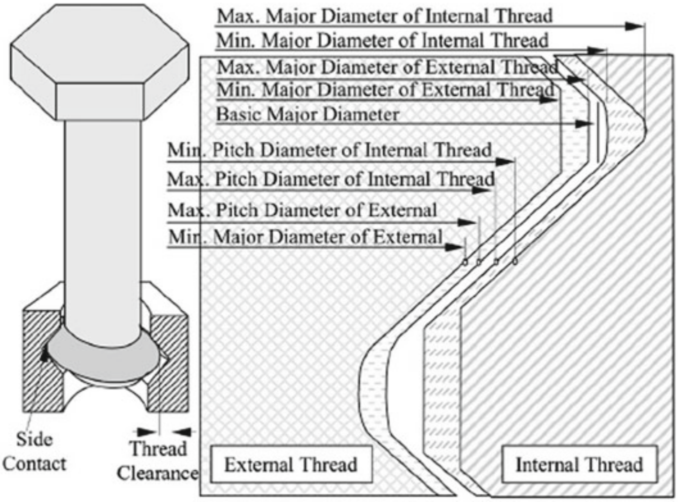

Fig. 7 Schematic of the thread clearance between engaged bolt and nut threads

The relative displacement $\Delta\delta_{\mathrm{NJ}}$ for the nut and the joint is given by Eq. (49). If $\Delta\varphi_{\mathrm{Nt}} < \Delta\varphi_{\mathrm{Ntcr}}$ and $|\Delta\delta_{\mathrm{NJ}}| < \Delta d_{\mathrm{h}}$, the incremental clamp load loss dF_{b} due to the loosening caused by the transverse cyclic loading would be given by

$$\begin{aligned} \mathrm{d}F_{\mathrm{b}} &= \frac{k_{\mathrm{b}}k_{\mathrm{c}}}{k_{\mathrm{b}}+k_{\mathrm{c}}}\left(\frac{p}{2\pi}\right)\omega_{\mathrm{t}}\mathrm{d}t \\ &= \frac{k_{\mathrm{b}}k_{\mathrm{c}}}{k_{\mathrm{b}}+k_{\mathrm{c}}}\left(\frac{p}{2\pi}\right)\frac{\left|\dot{\delta}_{\mathrm{J}}\right|\mathrm{d}t}{\eta_{\mathrm{N}}+\eta_{\mathrm{t}}\left(\sigma''+\frac{r_{\mathrm{maj}}+r_{\mathrm{min}}}{\sin 2\alpha}\right)}, \quad \text{with} \quad \eta_{\mathrm{N}} = \upsilon_{\mathrm{Nx}}/\omega_{\mathrm{t}} \end{aligned} \tag{55}$$

3 Results and Discussion

Figures 8, 9, 10, 11, 12, 13, and 14 show the proposed model prediction of loosening performance represented by Eq. (54), and the corresponding experimental validation, of a steel M10 × 1.5 Class 8 bolt–nut system (Fig. 1) that is subjected to harmonic transverse displacement with amplitude $\delta_0 = 0.71$ mm. Typical values of 200 MPa and 0.3 are, respectively, used for Young's modulus and Poisson's ratio. While the bolt thread profile angle is fixed in this study (at its standard 60° value), two different values are investigated for the engaged nut thread profile angle, namely the non-standard profile with $2\alpha = 120°$ and the standard nut thread are profile angle with $2\alpha = 60°$. Commercially available nuts with nonstandard profile angle $2\alpha = 120°$ are referred to as Spiralock nuts [7]. Coefficients of underhead bearing friction μ_{b}, thread friction μ_{t} were determined from separate precision torque-tension tests; their

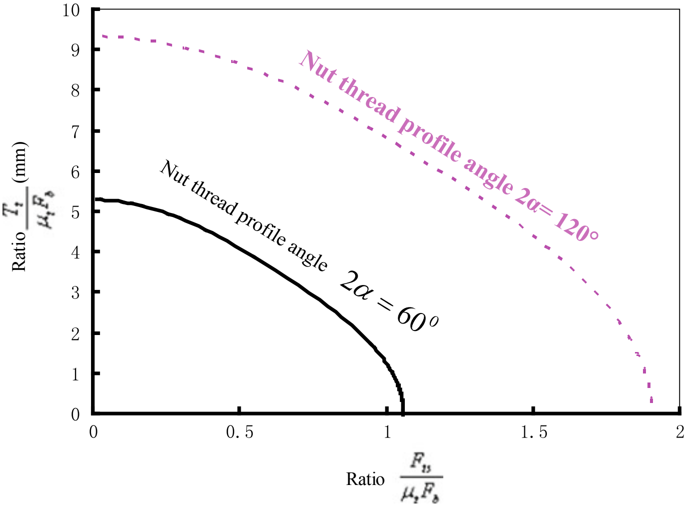

Fig. 8 Thread friction torque ratio $\overline{T}_t = \frac{T_t}{\mu_t F_b}$ versus thread friction transverse shear ratio $\overline{F}_{ts} = \frac{F_{ts}}{\mu_t F_b}$ (for nonstandard nut profile angle $2\alpha = 120°$ and standard nut profile angle $2\alpha = 60°$)

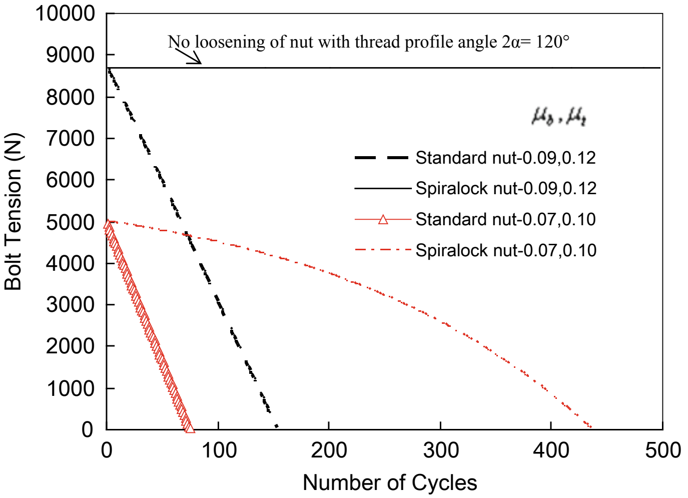

Fig. 9 Experimental validation of model prediction of nut loosening performance for two thread profile angles (standard nut with a thread profile angle $2\alpha = 60°$ versus nonstandard nut with $2\alpha = 120°$)

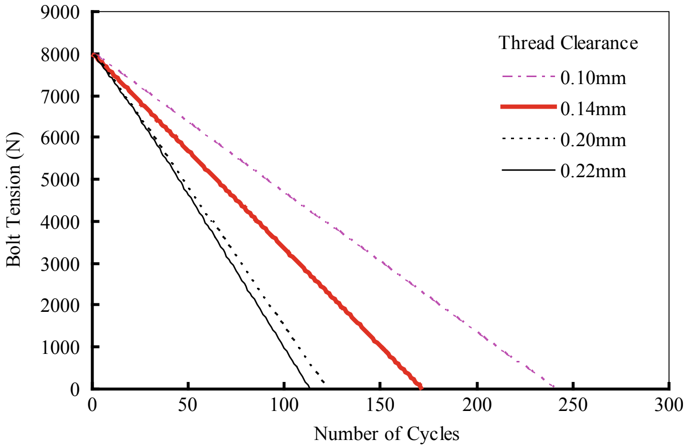

Fig. 10 Model prediction of the effect of thread clearance on the loosening performance of standard nut-bolt connection

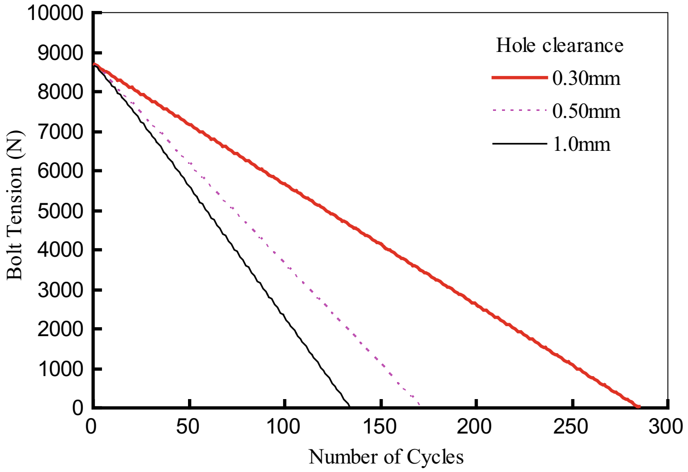

Fig. 11 Model prediction of the effect of hole diameter clearance on loosening performance of standard nuts

experimental values ranged from 0.065 to 0.13, for the various lubricity conditions between the underhead bearing and thread contact surfaces of test part. Bolt preload in this study is varied between 5 and 20.5 kN, which is 14–57% of the bolt proof load of 34.8 kN. Experimental validation of proposed model results on loosening performance was generated using a [modified] Junker vibration loosening test system [18] with a cyclic transverse displacement control.

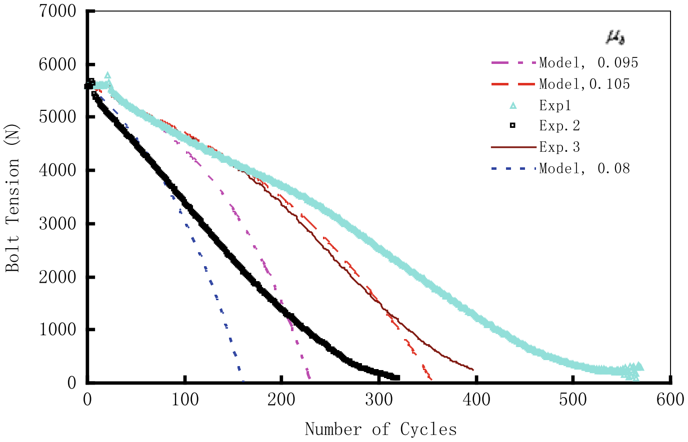

Fig. 12 Model validation of the loosening performance of nonstandard nut with thread profile angle $2\alpha = 120°$ (for bolt preload = 5600 N)

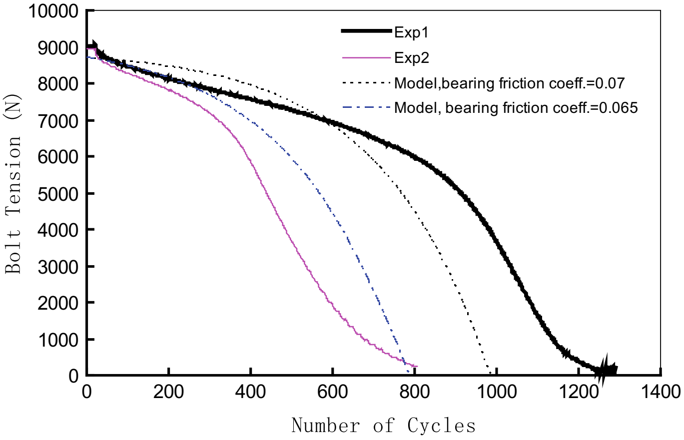

Fig. 13 Model validation of the loosening performance of nonstandard nut with thread profile angle $2\alpha = 120°$ (for bolt preload = 8,700 N)

3.1 Effect of Nut Thread Profile Angle 2α on the Loosening Performance

For the purpose of this study, two values of the nut thread profile angle $2\alpha = 120°$ and $2\alpha = 60°$ are used (Fig. 4) for engaging a standard bolt thread profile angle $2\alpha = 60°$. A commercially available specialty nut profile angle $2\alpha = 120°$ [7] is analytically and experimentally compared with standard female thread profile angle 600 [23] in terms of their respective loosening performance. For simplicity, it is

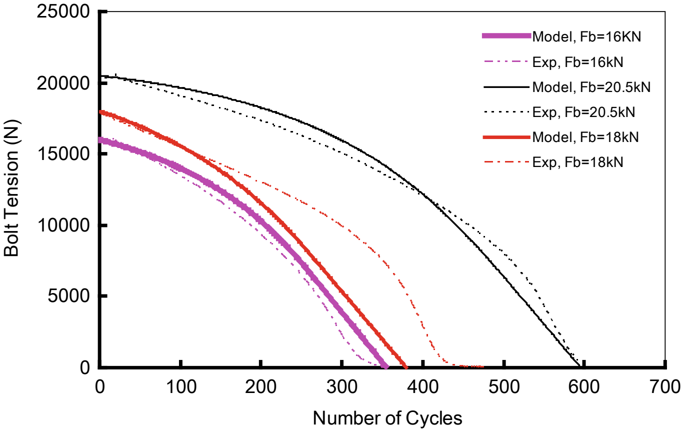

Fig. 14 Model validation of the effect of bolt preload on the loosening performance for standard nuts ($2\alpha = 60°$)

assumed that the thread friction coefficient μ_t would not be significantly affected by the thread profile angle, when test nuts have been cleaned.

Figure 8 displays the relationship between $\frac{T_t}{\mu_t F_b}$ and $\frac{F_{ts}}{\mu_t F_b}$ for the standard nut thread profile angle $2\alpha = 60°$ and nonstandard $2\alpha = 120°$ nuts when separately engaged with standard bolt threads. It is obvious that the ratio $\frac{F_{ts}}{\mu_t F_b}$ for critical transverse friction force of the larger thread profile angle nut ($2\alpha = 120°$) is much higher than that for the standard nut threads with $2\alpha = 60°$. If the transverse thread friction force F_{ts} is the same, the critical slipping thread friction torque T_t for $2\alpha = 120°$ would be much higher than that for standard nut. This means that the nut with larger thread profile angle is more resistant loosening as compared to nuts with standard thread profile angle $2\alpha = 60°$.

Figure 9 also shows better loosening performance of the nonstandard (larger) thread profile angle $2\alpha = 120°$, for various combinations of thread and bearing friction coefficients at two levels of bolt preload, namely 5000 and 8700 N. For an initial bolt preload of 8700 N the proposed model shows that the using a nut with a larger thread profile angle has completely prevented any loosening, while the standard nut $2\alpha = 60°$ has become completely loose (zero bolt tension) after only 150 vibration cycles. For a lower bolt preload of 5,000 N, the larger nut thread profile angle of $2\alpha = 120°$ has still out-performed the standard nut (with $2\alpha = 60°$) in terms of providing more resistance to loosening. The former withstood more than 400 vibration cycles before it became completely loose (with no residual bolt tension), as compared to less than 80 cycles for the latter.

3.2 Effect of Thread Fit

Figure 10 shows model prediction of the effect of thread fit clearance on the vibration loosening performance under harmonic transverse excitation. Thread fit class (tolerance) is often described as tight, medium, or loose fit [22]. An ISO designation of 6H/6g is assigned to a standard tolerance (fit) for commercially available metric nuts (6H)/bolts (6g). Since the nut thread clearance has already been directly incorporated as an independent variable in the proposed model, four arbitrary values of thread clearance are used, namely 0.10, 0.14, 0.20, and 0.22 mm. Results in Fig. 10 show that tighter thread fit would lower the rate of bolt loosing per cycle (i.e., increases the number of cycles to complete loosening). The number of the cycles until complete loosening is 240, 171, 121, and 113, for thread fit tolerance of 0.1 mm, 0.14 mm, 0.20 mm, and 0.22 mm, respectively.

3.3 Model Prediction of the Effect of Hole Clearance

Figure 11 shows loosening prediction of a of preloaded M10 × 1.5 bolt for hole diameter clearances of 0.3, 0.5, and 1.0 mm. A smaller hole clearance would reduce the vibration loosening rate, and the opposite is also true. For an initial bolt preload of 8700 N, the respective number of vibration cycles until complete loosening has been reached (i.e., zero bolt tension) for those three values of hole clearance are 285, 171, and 134.

3.4 Effect of Bearing Friction Coefficient on the Loosening Performance of Nuts with Nonstandard Thread Profile Angle ($2\alpha = 120°$)

Figures 12 and 13 show experimentally validated model prediction of the effect of bearing friction coefficient μ_b on the vibration loosening performance of a preloaded M10 × 1.5 bolt that is engaged with a nonstandard nut with a thread profile angle $2\alpha = 120°$ for two levels of bolt preload, namely 5600 and 8700 N. For both preload levels, the model prediction (solid lines) and experimental data (dotted lines) are in reasonable agreement in showing that increasing the bearing friction coefficient would reduce the bolt loosening rate per cycle. The difference between model prediction and the experimental data is lower for the higher preload level (Fig. 13).

3.5 Model Validation of the Effect of Bolt Preload

Finally, Fig. 14 shows experimental validation of the proposed model in terms of the effect of preload level on the loosening performance of a standard M10 × 1.5 bolt that is engaged with a standard nut ($2\alpha = 60°$). Three preload levels are used, namely 20, 18, and 16 kN; solid lines represent model prediction, while the dotted lines represent the corresponding experimental validation. Obviously, increasing the initial bolt tension would increase the number of vibration cycles-to-complete-loosening, in a nonlinear fashion. A reasonable agreement exists between the model prediction and test data.

4 Conclusion

This paper proposes an experimentally validated analytical model for investigating the effect of nut thread profile angle on the loosening performance of a preloaded bolt–nut system under a cyclic transverse excitation. Additional variables investigated include thread fit clearance, hole clearance, initial preload, and friction coefficients. Experimentally validated model prediction of the loosening performance shows that thread profile angle of the nut has significant effect on the loosening performance of a preloaded standard thread bolt. As compared to the standard nuts with 60° thread profile angle, nonstandard nuts with a larger thread profile angle of 120° (engaged with a preloaded standard M10 × 1.5 bolts) showed a significantly higher resistance to loosening under a harmonic transverse excitation. Results show also that reducing either of thread fit clearance (i.e., higher thread fit class) and/or reducing the clearance of bolt hole would increase the resistance to vibration-induced loosening of preloaded bolt–nut system. The opposite is also true; increasing either thread clearance (loose fit) and/or increasing the bolt hole clearance would reduce resistance to vibration-induced loosening of a preloaded bolt–nut system.

References

1. Ibrahim, R.A., Pettit, C.L.: Uncertainties and dynamic problems of bolted joints and other fasteners. J. Sound Vib. **279**, 857–936 (2005)
2. Harnchoowong, S.: Loosening of threaded fastenings by vibration, Ph.D. Dissertation. University of Wisconsin, Madison (1985)
3. Kasai, S., Matruoka, H.: Consideration of thread loosening by transverse impacts. ASME Press. Vessel. Pip. Div. PVP **367**, 117–123 (1998)
4. Kerley, J.J.: Dynamic and static testing of kaynar spiralock microdot nuts. Natl. Aeronaut. Space Adm. (NASA), Goddard Space Flight Cent. Eng. Serv. Div. Greenbelt MA (1984)
5. Junker, G.H.: New criteria for self-loosening of fasteners under vibration. SAE Trans. **78**, 314–335 (1969)
6. Finkelston, R.J.: How much shake can bolted joints take. Mach. Des. **44**, 122–125 (1972)

7. Hess, D.: Vibration and shock induced loosening. Handbook of bolts and bolted joints. In: Bickford, J.H., Nassar, S. (eds.) p. 911, pp. 757–824. Marcel Dekker, New York, NY (1998)
8. Sakai, T.: Investigations of bolt loosening mechanisms, 1st report: on bolts of transversely loaded joints. Bull. JSME **21**, 1385–1390 (1978)
9. Haviland, G.S.: Designing with threaded fasteners. Mech. Eng. **105**, 17–31 (1983)
10. Yamamoto, A., Kasei, S.: A solution for the self-loosening mechanism of threaded fasteners under transverse vibration. Bull. Jpn. Soc. Precis. Eng. **18**, 261–266 (1984)
11. Tanaka, M., Hongo, K., Asaba., E.: Finite element analysis of the threaded connections subjected to external loads. Bull. JSME **25**, 291–298 (1982)
12. Vinogradov, O., Huang, X.: On a high frequency mechanism of self-loosening of fasteners. In: Proceedings of 12th ASME Conference on Mechanical Vibration and Noise, Montreal, pp. 131–137. Quebec (1989)
13. Shoji, Y., Sawa, T.: Analytical research on mechanism of bolt loosening due to lateral loads. In: Proceedings of ASME Pressure Vessels and Piping Conference, Computer Technology, vol. 2, PVP2005–71333, pp. 59–65. Denver, Colorado, USA (2005)
14. Nassar, S.A., Housari, B.A.: Effect of thread pitch on the self-loosening of threaded fasteners due to cyclic transverse loads. ASME J. Press. Vessel. Technol. **128**, 590–598 (2006)
15. Nassar, S.A., Housari, B.A.: Study of the effect of hole clearance and thread fit on the self-loosening of threaded fasteners due to cyclic transverse loads. ASME J. Mech. Des. **128**, 586–594 (2006)
16. Housari, B.A., Nassar, S.A.: Effect of thread and bearing friction coefficients on the vibration-induced loosening of threaded fasteners under cyclic transverse loads. ASME J. Vib. Acoust. **129**, 1–9 (2007)
17. Nassar, S.A., Yang, X.: A mathematical model for vibration-induced loosening of preloaded threaded fasteners. ASME J. Vib. Acoust. **131**, 021009–1~13
18. Yang, X., Nassar, S.A.: Analytical and experimental investigation of self-loosening of preloaded cap screw fasteners. ASME J. Vib. Acoust. **133**, 031007–1~8
19. Motosh, N.: Development of design charts for bolts preloaded up to the plastic range. ASME J. Eng. Ind. **98**(3), 849–851 (1976)
20. Sopwith, D.G.: The distribution of load in screw threads. Proc. Inst. Mech. Eng. (G. B.) **159**(45), 373–383 (1948)
21. Englund, R.B., Johnson, D.H.: Finite element analysis of a threaded connection compared to experimental and theoretical research. J. Eng. Technol. **14**(2), 42–47 (1997)
22. Marks', L.S.: Standard handbook for mechanical engineers. In: Avallone, E.A., Baumeister, T. (eds.) III, 10th edn. pp. 8–21. McGraw-Hill, New York (1996)
23. Del, W.: From Earth to Saturn: getting a grip on vibration, shock and extreme temperature. Industrial and Utility Vehicle (January/February 2004)

Welding

Laser-Based Additive Manufacturing of Optical, Thermal and Structural Components

P. Neef, R. Bernhard, H. Wiche and V. Wesling

Abstract The joint project GROTESK which is funded by the European Regional Development Fund deals with the application of additive manufacturing for the generation of optical, thermal and structural components using the example of a laser system. This includes multi-material connection of metallic and nonmetallic materials with laser metal deposition (LMD), e.g., mountings for solid-state lasers like Nd:YAG, and the related material development for wire-based as well as powder-based processing. Primary requests for these contrary material groups aim at melting point, thermal expansion and thermal conductivity of the processed alloy. Especially, iron–nickel alloys are suitable for this field of application due to their precisely adjustable thermal expansion that is adapted over a wide range with the content of nickel. However, the adjustment of the processing of the metal represents another requirement for the selection of the alloy. Usually, the focus is on the process parameter settings. In this case, the specific admixture of alloy components based on the requirements for the respective application is identified as an integral process factor. Especially, reflectivity at a determined wavelength, thermal conductivity, diffusibility, density, heat capacity, viscosity and wetting behavior are elementary factors for the modification of the material processing. Furthermore, the particle size and density of powders affect the intensity of the absorbed laser radiation. Therefore, the adjustment of the wire-based processing results from thin-film coatings on metal wires generated with physical vapor deposition. Fractionation and admixture of additives lead to modified characteristics of the powders. Based on the requirements of the imprinted components, iron–nickel alloys are selected for the additive manufacturing process. These alloys are precisely adjustable in their properties due to the variation of the composition and show low thermal expansion at room temperature. However, measurements of the contact angle indicate an insufficient bonding of iron–nickel alloy and YAG. Therefore, a physical vapor deposition coating of titanium on

---

P. Neef (✉) · R. Bernhard · H. Wiche · V. Wesling
Clausthal Centre of Materials Technology, Clausthal University of Technology, Leibnizstrasse 9, 38678 Clausthal-Zellerfeld, Germany
e-mail: philipp.neef@tu-clausthal.de

V. Wesling
Institute of Welding and Machining, Clausthal University of Technology, Agricolastrasse 2, 38678 Clausthal-Zellerfeld, Germany

L. F. M. da Silva et al. (eds.), *Advanced Joining Processes*,
Advanced Structured Materials 125, https://doi.org/10.1007/978-981-15-2957-3_4

the YAG leads to a formation of an interface layer. This results in a significantly enhanced bonding, but also implies a time- and cost-intensive step. The development of an innovative in situ alloying due to direct admixture of titanium powder during additive manufacturing ensures precisely produced coatings between YAG and alloy. This process allows the generation of first multi-material connection of YAG and iron–nickel alloys in the laboratory scale.

Keywords Laser metal deposition · Multi-material connection · Material development · Thermal expansion · Wetting behavior

1 Introduction

The joint project "Generative Manufacturing of Optical, Thermal and Structural Components" (GROTESK) is an innovation network funded by the European Regional Development Fund (ERDF) and the Ministry for Science and Culture of Lower Saxony. The project partners Laser Zentrum Hannover e.V. (LZH), Leibniz University Hannover (LUH), Hochschule Hannover (HsH) and Clausthal Centre of Materials Technology (CZM) are researching the application of laser-based additive manufacturing for the production of laser components. This includes both optical components such as optical fibers and lenses but also structural and thermal components such as mountings for laser crystals and lenses. As part of the project, the CZM deals with material development as well as the conception of processing technology, taking into account the challenges of the present multi-material compound. The application of additive manufacturing for this purpose allows automation as well as functional integration.

Generative manufacturing processes have been the subject of research for about 25 years. Due to the technical progress in this area and the enormous potential in various fields of application, these manufacturing methods have been taking roots alongside the conventional manufacturing methods [1] and are no longer used only for the production of prototypes [2]. A considerable advantage of generative manufacturing arises from the possibility of generating geometrically complex structures that are either not or with great difficulty producible with conventional methods. This results in extended structural and design options as well as functional integration [3].

Additive manufacturing can be divided into processes that operate in the powder bed and systems that feed the material directly through a nozzle either powder-based or wire-based. While powder-based deposition offers greater precision, wire-based deposition can achieve significantly higher deposition rates and material yield [4]. The direct material feed offers the option to build on curved surfaces and 3D structures as well as to process several materials for the production of hybrid components [5, 6]. Such methods have the potential to build on partially finished products. This opens the possibility for the production of new components on conventionally manufactured components [2] like optical elements or laser crystals.

The current state of development of machines and processes enables the production of components made of various polymers, glasses and metallic materials, such as stainless steel and tool steel, as well as aluminum, titanium, cobalt-chromium and nickel-based alloys. In particular, polymer powders as starting materials have become very important for additive manufacturing in recent years and these powders are commercially available in many types and compositions for additive manufacturing processes. However, there are still deficiencies at metallic and ceramic powders with regard to the adaption of the properties during deposition.

In conjunction with the application of laser technology as an energy source for additive manufacturing, high purities and surface qualities can be achieved. In addition, the accuracy of the laser also allows filigree structures while maintaining small temperature frames [7, 8]. Moreover, the laser source covers a large working range depending on the physical properties of the applied material (melting point, electrical conductivity, thermal conductivity, etc.), in contrast to other available heat sources such as plasma, electric arc or infrared radiation.

In this paper, the consideration of properties of incompatible materials for multi-material connections is demonstrated. Regarding thermal expansion and wetting behavior of alloy and YAG substrate, the process steps of an application-specific problem definition are pointed out. The following chapters show the methods for the material selection and adaption as well as the process implementation.

2 Experimental Approach of wGROTESK

The subproject wGROTESK deals with the material and process development for laser-based additive manufacturing. Previous approaches in additive manufacturing were focused on an adaption of process parameters for given materials solely. Suitable settings allow a processability, but the options are underachieved. wGROTESK pursues a holistic approach. This also includes the adaptation of the applied filler material.

The built materials are essential process variables during additive manufacturing, which significantly influence the deposition speed and quality. In addition to the reflectivity at a certain wavelength, primary influencing factors are thermal conductivity, diffusibility, density, heat capacity and viscosity as well as the wetting behavior of the processed material. In the case of powders, the intensity of the emitted laser radiation additionally depends on the powder particle size, the particle density and the vertical position of the energy/laser input [9, 10].

The applied materials must also cover a diverse functional profile during the laser machining. The particular challenge for laser-based additive manufacturing lies in very high cooling rates to which the material is subjected after the sintering or melting process. The rapid solidification leads to changes in the resulting microstructures and precipitations as well as challenges regarding the stresses and distortion of the generated components. Porosity and component defects, for example, cannot be avoided entirely when using conventional metal powders.

Systematical adaption of properties of powdered materials begins by conventional fractionation via sieves in order to achieve uniform grain sizes. Further, powder preparation takes place via alloying and mixing with materials and additives by active milling. Due to high-energy input and suitable process control, particle or crystallite sizes in the range of a few nanometers can be generated. In addition, composites with nanoscale phase dispersion, so-called nanocomposites, can be synthesized and chemical reactions can be triggered in a targeted manner by grinding different materials simultaneously. Furthermore, it is possible by means of ball milling to produce metastable alloys which cannot be generated with conventional methods or only with difficulty [11]. In addition, there is the possibility of the targeted introduction of flux to affect the contact angle.

Another approach to the dedicated adaptation of materials for additive manufacturing is provided by thin-film coatings on wire-shaped materials. Thin-film coatings are currently used in many fields of engineering, including tool coating and corrosion protection (e.g., in the field of PEM fuel cells) [12–15]. These layers are usually applied by means of physical vapor deposition (PVD).

The challenge of the project is not only the process-reliable control of the laser metal deposition process, but also the connection of different material groups and the assurance of the operation of the imprinted laser system.

Thus, there is the requirement of a material that is both manageable additively in the LMD process and suitable for the join partners. First of all, the thermal properties must be taken into account. Thus, lenses and YAG must not be affected by too high melting point of the alloy, improper thermal expansion or thermal shock resistance. At the same time, it is relevant that the connection between metallic and nonmetallic materials is stable regarding mechanical and thermal loads.

Based on the demands, the analysis of the basic systems is concentrated on the compliance with thermal expansion, melting point and thermal conductivity. Iron–nickel alloys are suitable here in terms of thermal expansion, since these can be adjusted precisely by variation of the alloy composition, and moreover, very low expansion coefficients can be achieved. Most known is the invar alloy with about 36% nickel content, which has a thermal extension of less than 1.0 ppm in temperature ranges between 20 and 100 °C (see Fig. 1).

Only at higher temperatures, the expansion increases. Induced forces due to magnetic moments and magnetic frustration [17] lead to a lattice expansion, which interacts with the temperature-induced expansion. As the temperature rises, these magnetic effects diminish due to the change in magnetic properties counteracting the temperature-induced expansion. Upon reaching the Curie temperature, the expansion is drastically increasing. A comparison of the thermal expansion of various compositions of the iron–nickel alloys shows clearly the adaptation possibilities of the material. The variation of the nickel content from 36 to 48% leads to a significant increase of the expansion coefficient (see Fig. 1). The melting point of the iron–nickel alloy amounts about 1470 °C, which is below the critical temperature of the YAG.

The investigations aim simultaneously both on the process engineering and on the connection of the contrary materials and their properties. For the latter investigations, samples are generated in the oven in order to get an overview of the possibilities for

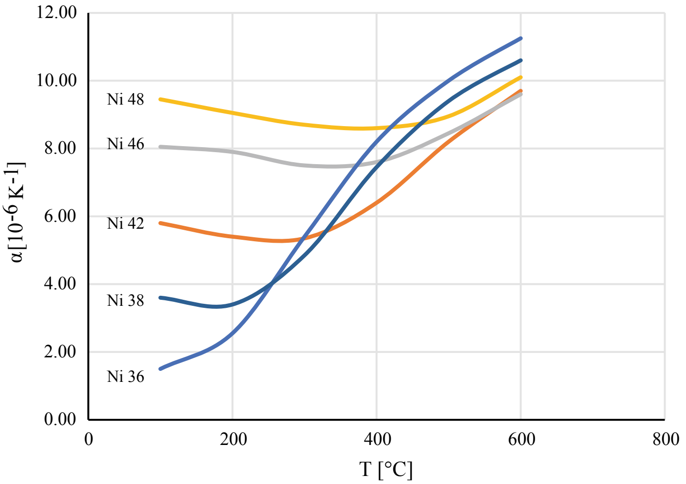

Fig. 1 Theoretical thermal expansion coefficient of iron–nickel alloys [16]

material adaption. Obviously, the additive manufacturing process differs significantly in terms of temperature gradients, so that, for example, diffusion mechanisms are far less pronounced and the risk of thermal shock is many times higher.

Consequently, only an ideal image can be worked out for the samples made in the oven, which is essential for the direction of the process engineering investigation of the additive deposition.

For this purpose, the metal powder is applied to a YAG crystal and molten in an optical contact angle measuring and contour analysis system allowing the measurement of the wetting contact angle. In addition, first dilatometer samples are generated in a furnace process to investigate the thermal expansion. Based on the results of these experiments, specimens are produced with laser metal deposition (LMD).

3 Results

Direct application of the metal alloy to the YAG crystal does not give promising results expectedly. Although a drop can be made on the crystal, Fig. 2a shows that the contact angle is about 95° and there is a clear evidence for improvement.

A first approach is a PVD coating of the crystal with an approximately 2-micron-thick titanium layer. Due to the high affinity for oxygen [18], the titanium coating leads to a metallization of the oxygen-rich YAG crystal, realizing a connection of the iron–nickel alloy via metallic bonds. The conducted experiments show a much lower contact angle (see Fig. 2b), but this solution has the decisive disadvantage of a time-consuming previous coating process.

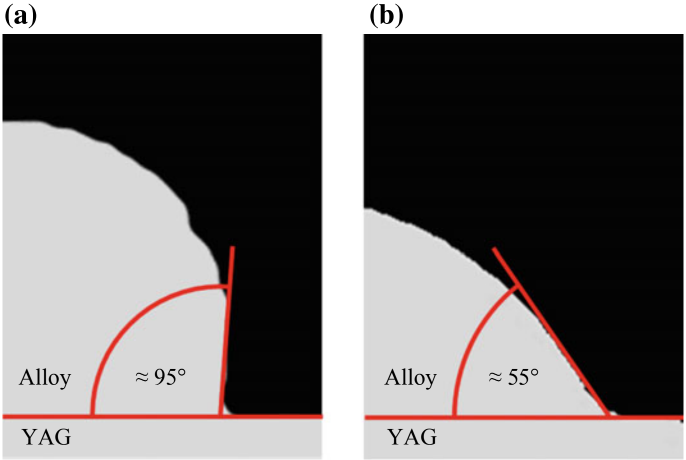

Fig. 2 Contact angle of iron–nickel alloy and YAG crystal, uncoated (**a**) and titanium coating (**b**)

Therefore, a further approach was to admix small amounts of titanium powder into the iron–nickel alloy. An admixture of 1 wt% titanium already leads to a layer between the two joining partners, which also achieves a contact angle that is comparable to the PVD layer. In addition, EDX measurements show that titanium can mostly be detected in the intermediate layer.

Figure 3 shows the layer between alloy and YAG which is between tenth of a micron and a few microns thick. The EDX measurement (see Table 1) indicates diffusion mechanism since the interlayer contains elements of Ti, FeNi and YAG.

The results of the EDX line scan (see Fig. 4) also show that diffusion processes take place between the two joining partners within the intermediate layer. Within the zone, all elements involved can be detected, with a gradual increase in the proportions.

However, the titanium admixture is required at the contact zone of alloy and YAG solely. Thus, there is the possibility of a gradual additive manufacturing, which means

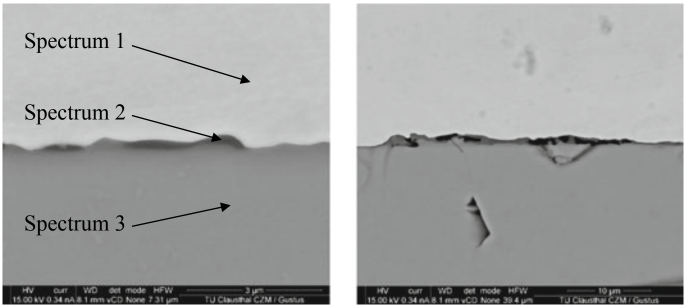

Fig. 3 EDX measurement of titanium-rich interlayer (see Table 1)

Table 1 Chemical compound [wt%] of interlayer (EDX measurement)

	Fe	Ni	Ti	Y	Al	O
Spectrum 1	57.16	42.05	0.78	–	–	–
Spectrum 2	18.60	13.00	18.96	16.66	8.49	24.27
Spectrum 3	–	–	–	45.20	21.74	33.07

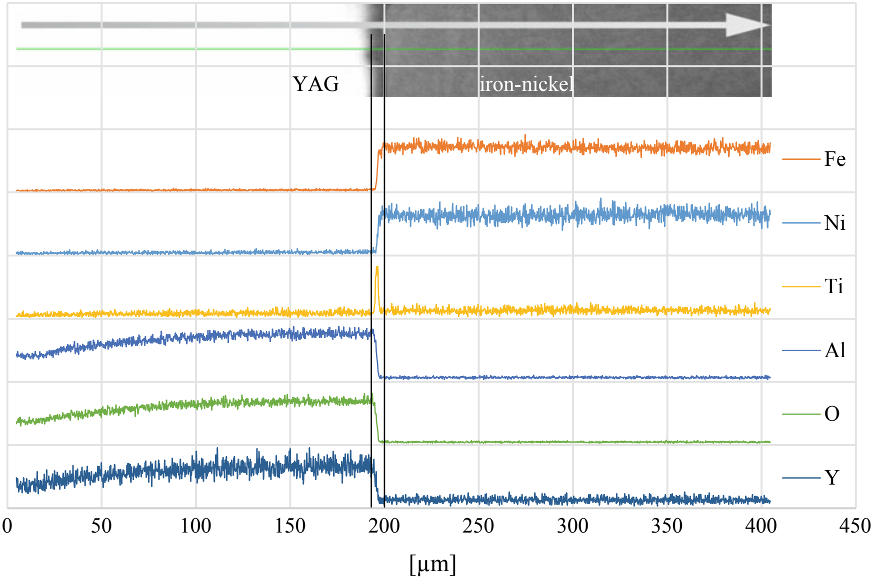

Fig. 4 EDX line scan of titanium-rich interlayer

that the admixture of the titanium powder is conducted in the areas close to the YAG exclusively.

With regard to the thermal expansion of the iron–nickel alloy, samples were produced by furnace as well as by additive manufacturing. In both variants, the previously described special behavior of the iron–nickel alloys can be seen. Figure 5 shows an additive manufactured sample and the eroded dilatometer specimen of about 40 mm in length.

The results of the additively made dilatometer samples show that the thermal expansion is in the expected range (see Fig. 6). Ideally, the composition is about 42–43% nickel. This means for temperatures below 500 °C that the expansion of the alloy is below the expansion of the YAG crystal. As a result, at these temperatures, the crystal would be interfered in expansion by compressive stresses. This is clearly preferable to induced tensile stresses.

The additive bonding of YAG and alloy represents a further challenge. Due to the comparatively low thermal shock resistance of the YAG crystal, preheating of the YAG is unavoidable. Consequently, the metal substrate in contact with the YAG

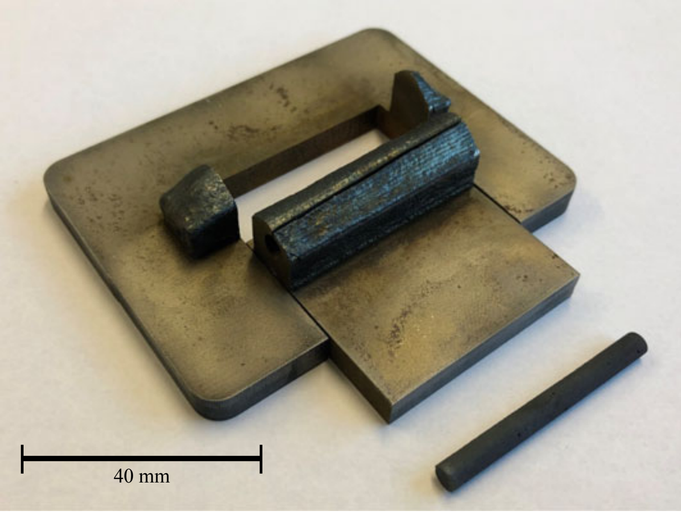

Fig. 5 Additive manufactured sample with eroded dilatometer specimen

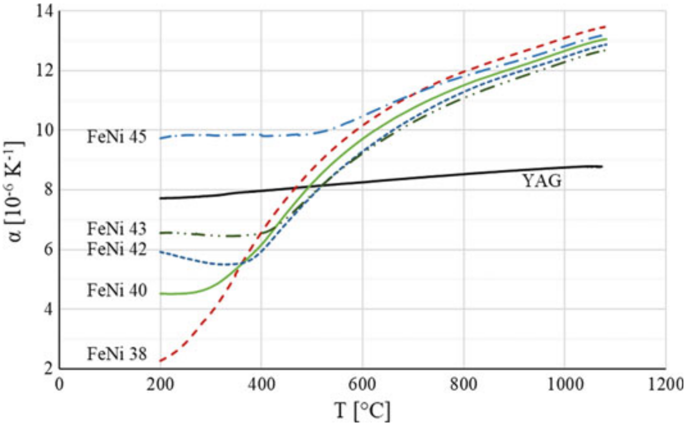

Fig. 6 Measured thermal expansion coefficients of additive manufactured iron–nickel samples

crystal is heated to temperatures of about 800 °C with an inductor, so that thermal damage is avoided. Experiments show the potential of the application of additive imprinting in the laboratory scale, but there are still more investigations required to transfer these results to large scale regarding welding sequence and structure strategy.

4 Conclusion

Additive manufacturing of multi-material connections of incompatible materials requires the consideration of a variety of properties. It is not just the setting of the process parameters but also the targeted adjustment of the alloy composition. Iron–nickel alloys demonstrate a sufficient thermal expansion at temperatures from room temperature to 500 °C, which is precisely adjustable with the composition. However, the bonding behavior of YAG is deficient. The application of a titanium coating on the YAG leads to improved bonding behavior of YAG and alloy, but the PVD process is time-consuming as well as expensive.

In this paper, it was shown that a direct admixture of titanium powder is an innovative step for in situ alloying resulting in an efficient titanium interlayer between YAG and alloy.

5 Perspective

The results of the applied iron–nickel alloy are satisfactory, but at the same time, there is still a great potential in terms of material selection. As a result, pseudo-alloys have also come under the spotlight for further investigations. Currently, the processing of copper–phosphorus–molybdenum pseudo-alloys is under investigation and initial promising results have been achieved (see Fig. 7).

Therefore, molybdenum grains are integrated into a copper–phosphorus matrix to combine the low thermal expansion of molybdenum with the high thermal conductivity of copper. The eutectic alloy of copper and phosphorus achieves lower melting point to avoid thermal loads. The influence of powder grinding on the resulting structure is analyzed at the same time.

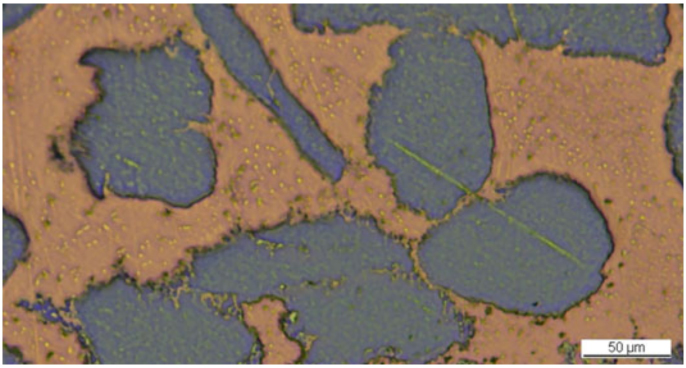

Fig. 7 Microstructure of additive manufactured copper–phosphorus–molybdenum pseudo-alloy

Acknowledgements We would like to thank the European Regional Development Fund (ERDF) and the Ministry for Science and Culture of Lower Saxony for funding and support (GROTESK, wGROTESK Project number: ZW6-8501 8048).

References

1. Gebhardt, A.: Generative Fertigungsverfahren: Additive Manufacturing und 3D Drucken für Prototyping—Tooling—Produktion. Carl Hanser Verlag, Munich (2013)
2. Levy, G.N., Schindel, R., Kruth, J.: Rapid manufacturing and rapid tooling with layer manufacturing (LM) technologies. CIRP Ann. Manuf. Technol. **52**(2), 589–609 (2003)
3. Functional Integration. EOS GmbH Electro Optical Systems. Cit. 29 Nov 2019. https://www.eos.info/functional-integration-39f837a0e69ec898
4. Smart processing module for wire-based laser deposition welding. Fraunhofer Institute for Production Technology IPT. Cit. 26 Nov 2019. https://www.ipt.fraunhofer.de/en/Competencies/processtechnology/non-conventional-manufacturing-processes-and-technology-integration/welding-head-lmd-w-20-l.html
5. Kaierle, S., Overmeyer, L., Alfred, I., Rottwinkel, B., Hermsdorf, J., Wesling, V., Weidlich, N.: Single-crystal turbine blade tip repair by laser cladding and remelting. CIRP J. Manuf. Sci. Technol. **19**, 196–199 (2017)
6. Lehmhus, D., Busse, M., von Hehl, A., Jägle, E.: State of the art and emerging trends in additive manufacturing: from multi-material processes to 3D printed electronics. MATEC Web Conf. **188**, 03013 (2018)
7. Glas-Metall-Verbindungen mit Lasertechnik. Laser Zentrum Hannover e.V. (LZH). Press release from 07.09.2007. Cit. 15 Oct 2019. https://www.lzh.de/de/node/2091
8. Metallische Werkstoffe—Pulvertechnologie. Fraunhofer-Allianz Generative Fertigung. Cit. 15 Oct 2018. https://www.generativ.fraunhofer.de/en/research/materials.html#tabpanel-3
9. Cyclone powder nozzle for lateral powder feed. Fraunhofer Institute for Material and Beam Technology IWS. Cit. 14 Oct 2019. https://www.iws.fraunhofer.de/en/business_fields/surface_treatment/laser_cladding/system_technology/cyclone_powder_nozzle.html
10. Kaierle, S., Barroi, A., Noelke, C., Hermsdorf, J., Overmeyer, L., Haferkamp, H.: Review on laser deposition welding: from micro to macro. Phys. Procedia **39**, 336–345 (2012)
11. Suryanarayana, C.: Process in material. Mater. Sci. **46**, 1–184 (2001)
12. Wesling, V., Kandelhardt, T., Hamje, J., Petsch, A.: Dünnfilmbeschichtung bei Korrosionsbeanspruchung von Aluminiumsubstrat. Bericht 2011–2012. Clausthaler Zentrum für Materialtechnik (2013)
13. Wesling, V., Petsch, A., Oppermann, C.: Untersuchung von Diamond-Like-Carbon PVD-Beschichtungen für Umformwerkzeuge von Aluminiumlegierungen. Bericht 2011–2012. Clausthaler Zentrum für Materialtechnik (2013)
14. Stallard, J., Teer, D.: A study of the tribological behaviour of CrN, Graphit-iC and Dymon-iC coatings under oil lubrication. Surf. Coat. Technol. 525–529 (2004)
15. Field, S., Jaratt, M., Teer, D.: Tribological properties of graphite-like and diamond-like carbon coatings. Tribol. Int. **37**, 949–956 (2004)
16. DIN 17745:2002-09: Wrought Alloys of Nickel and Iron—Chemical Composition
17. Rancourt, D., Dang, M.-Z.: Relation between anomalous magnetovolume behavior and magnetic frustration in Invar alloys. Phys. Rev. B **54**(17), 12225–12231 (1996)
18. Lütjering, G., Williams, J.C.: Titanium, pp. 50–52. Springer, Berlin (2003)

Welding Process for the Additive Manufacturing of Cantilevered Components with the WAAM

T. Feucht, J. Lange, B. Waldschmitt, A.-K. Schudlich, M. Klein and M. Oechsner

Abstract Wire + Arc Additive Manufacturing (WAAM) is widely used in both research and industry and is now also being studied in the building industry. The deposition rates are higher than those of other steel printing processes, such as selective laser melting (SLM). WAAM in combination with topology optimisation is therefore also of interest for standard applications. The Institute for Steel Construction and Materials Mechanics has two robots (Comau) with Fronius welding attachments. These are used to assess various applications for WAAM in the construction industry. The question of whether to produce not only vertical structures with neutral welding torch positions but also cantilevered components with overhangs but without supporting structures is a recurring issue. In this way, e.g., bridges with cantilever construction can be manufactured additively, as it was done on the Campus of the Technische Universität Darmstadt. The challenge in the additive manufacturing of structures with overhang is that the weld is not applied to a horizontal surface but sideways to the previous layer of weld. The molten pool then threatens to drop down before it hardens. Even without lateral dripping, clumps usually form in the vertical direction, making it difficult to produce the targeted geometry. Controlled solidification can be achieved by combining two welding process controls. On one hand, cold metal transfer (CMT) technology is used, which achieves controlled droplet separation by means of forward and backward movements. The process is supplemented by pauses in the welding process, which enables a defined partial solidification of the melt. The paper describes this new process in more detail and presents its use for the additive manufacturing of the world's first in situ additively manufactured steel bridge. It is shown that very good material properties can be achieved with the process. In addition, a new cooling process is presented with water spray cooling, which significantly reduces the manufacturing and cooling times and does not influence the material properties.

T. Feucht (✉) · J. Lange · B. Waldschmitt
Institute for Steel Construction and Materials Mechanics, Technische Universität Darmstadt, Darmstadt, Germany
e-mail: feucht@stahlbau.tu-darmstadt.de

A.-K. Schudlich · M. Klein · M. Oechsner
State Materials Testing Institute Darmstadt, Technische Universität Darmstadt, Darmstadt, Germany

L. F. M. da Silva et al. (eds.), *Advanced Joining Processes*,
Advanced Structured Materials 125, https://doi.org/10.1007/978-981-15-2957-3_5

Keywords Wire + Arc Additive Manufacturing · WAAM · Welding processes · Cantilevered components · Steel bridge · 3-D printing

1 Introduction

Additive manufacturing with steel is becoming more and more important. Many 3-D printing processes have been established in recent years [1, 2]. The promised advantages, e.g. individuality, freedom of design, innovative designs and rapid spare parts production, have led to increasing use in industrial applications. Wire-based arc welding with shielding gas (WAAM = Wire + Arc Additive Manufacturing) is very suitable for steel construction and the construction industry in general, as it enables high deposition rates (up to 5 kg/h) [3]. Many questions are still unsolved, but are also taken up and researched, which is made clear by the increasing number of publications [4]. A wide range of metallic materials can be used in this process—both the usual carbon steel welding wires, e.g. G3Si1/ER70S-6 [5], and various stainless steels [6, 7]. For the guidance of the welding device, there are portals whose workspace is limited [8] and robots [9] whose workspace can be considerably larger, especially if they work on rails. Research into the use of WAAM in the construction industry has intensified in recent years [10–13], although its implementation in construction has not yet been completed due to the lack of standardisation, which is essential.

An outstanding project in the field of civil engineering is the additive manufacturing of a bridge with the WAAM from the company MX3D (Amsterdam, Netherlands). The vision was to build bridges with robots on site; see Fig. 1a.

Finally, the bridge was built under laboratory conditions in a workshop [15]. The individual segments were manufactured in flat position, i.e. turned 90° to the final position, and then connected with manual welds; see Fig. 1b. A bridge manufacturing in the final position, respectively "midair" and in situ, has not yet been realised.

The TU Darmstadt has started a project in which a steel bridge is manufactured in situ; see Fig. 2. In the following, the process developed by the TU Darmstadt for this purpose is explained, and the manufacturing tests and experimental investigations are described.

a) MX3D Vision [14]　b) MX3D Bridge

Fig. 1 MX3D vision and bridge

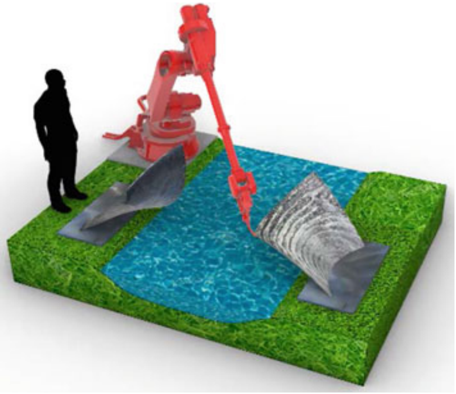

Fig. 2 Rendering of the in situ manufacturing

2 Cantilevered Structures

In situ manufacturing means that something has to be printed over and above something. The flat position is therefore no longer given. The material is applied in an almost liquid state and sideways, so that the weld metal threatens to flow downwards. Existing investigations show that a balance between the wire-feed-speed, the travel speed and the ratio of both is essential for consistent weld geometry without dripping [16, 17]. The geometry itself or the welding path has a further influence. In [18], it was found that in the case of tubular cross sections, the curvature of the weld seam in the longitudinal direction (and the resulting centrifugal force) leads to dripping. Conventional welding processes are therefore not suitable for this purpose. At the institute, welding parameters were found which can be used to manufacture structures with material properties, geometry prediction and geometry constancy equivalent to structures manufactured in flat position. The decisive welding parameters (travel speed and wire-feed-speed) and the CMT process control [19] were supplemented by an additional parameter, in particular a defined pause length. The right ratio of CMT cycles (welding time) and pause time in combination with the right travel speed allows the drop to harden to such an extent that it is no longer significantly influenced in its geometry by the following drop.

2.1 Process Parameters

The parameters used are listed in Table 1. The process parameters can be edited via a Fronius CMT Advanced 4000 R power source in the "CMT Cycle Step" characteristic.

Table 1 Process and input parameters "CMT Cycle Step"

Process and input parameters	Variable	Unit
Number of CMT cycles	15–25	–
Interval break	80–180	ms
Wire-feed-speed (set)	4.0	m/min
Travel speed	0.2–0.3	m/min
Gas set	15	l/min
Wire electrode	Weko 2 G3Si1 (ER 70 S-6) Ø 1.2 mm	–
Gas	Ferroline C18 (82% argon and 18% CO_2)	–

2.2 Manufacturing Examples

2.2.1 Bridge Segment

A manufacturing example can be seen in Fig. 3. The base plate was constantly in the same position. The welding torch was inclined by 45° during the entire manufacturing process.

The upper side shows a very high final near-net-shape surface; see Fig. 3a, b. The underside shows a higher surface waviness; see Fig. 3c. No weld metal has dripped down during production.

The width and height of a layer depend on the angle of the overhang. In the flat position, a width of approx. 6.0 mm and a height of approx. 1.6 mm are achieved. With horizontal application, a width of approx. 5.0 mm and a height of approx. 2.0 mm are achieved. The geometry of the weld seam is also influenced by whether the welding direction is upwards or downwards. The above-mentioned geometry values can therefore only be understood as reference values.

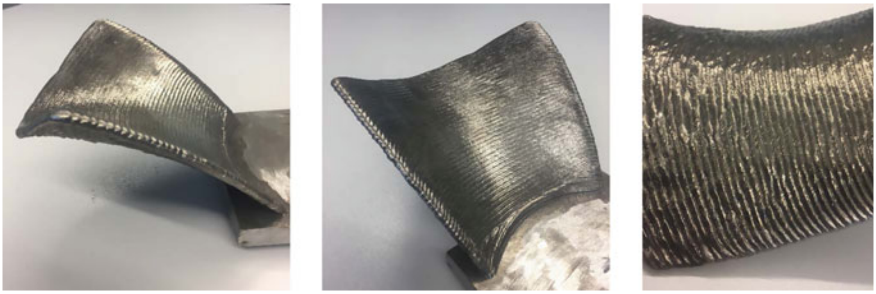

a) Upper Side b) Upper side c) Underside

Fig. 3 Additively manufactured bridge segment

Fig. 4 1:8 scale model

2.2.2 Complete Bridge (Scale 1:8)

In order to gain sufficient knowledge for the manufacturing of the true-to-scale bridge (see Sect. 2.2.3), a bridge was manufactured on a scale of 1:8; see [18] and Fig. 4. A special approach was used for the form finding of the bridge, and the robot programming was carried out parametrically because of the big advantages for additive manufacturing; see [20].

2.2.3 Complete Bridge (Scale 1:1)—In Situ

The bridge has a span of approx. 3 m and is approx. 1.5 m wide at its widest point. The base plates were fixed on Spinnaker foundations (concreteless foundation technology). To ensure conditions regardless of weather, the robot system including welding generator, filler material and gas was enclosed with a tent; see Fig. 5a. In addition, the enclosure also serves to ensure an undisturbed shielding gas flow in the arc area. At the end of October 2019, the two sides of the bridge were force-locked together.

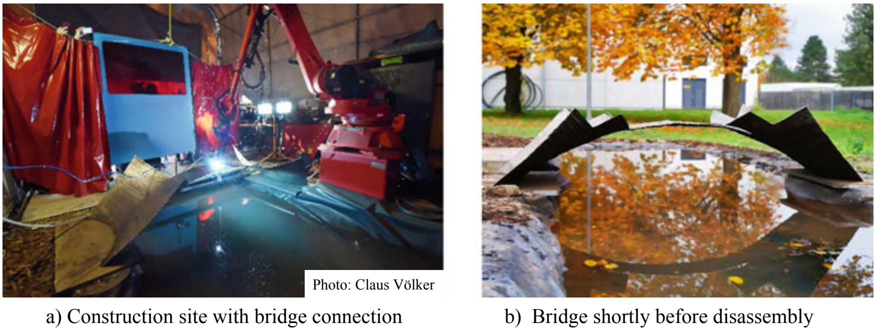

Photo: Claus Völker

a) Construction site with bridge connection

b) Bridge shortly before disassembly

Fig. 5 Pictures from construction site

3 Experimental Investigations

To determine the material properties of cantilevered structures, specimens were manufactured and experimentally investigated.

3.1 *Half-pipe*

In order to be able to produce tensile specimens, a half-pipe specimen was manufactured at an angle of 45°. The test set-up is shown schematically in Fig. 6.

Seven flat tensile specimens were milled out of the manufactured test specimen; see Fig. 7.

The results of the tensile tests are shown in Fig. 8. The yield strength shows an average of 403.0 N/mm^2 with a standard deviation of 7.4 N/mm^2. The manufacturer

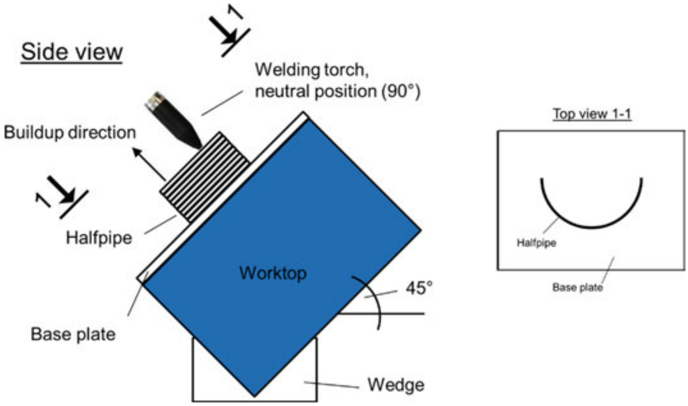

Fig. 6 Experimental set-up half-pipe

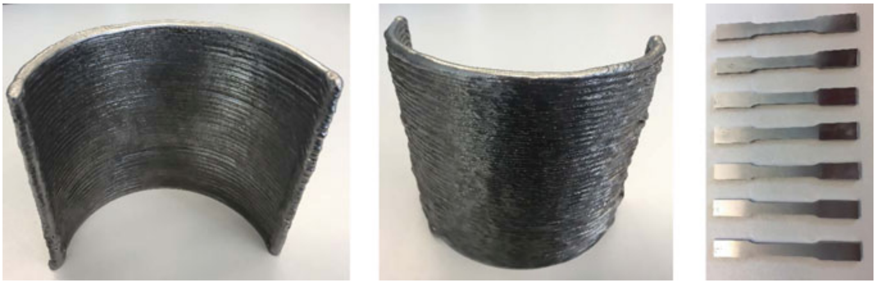

a) Upper side

b) Underside

c) Tensile spec.

Fig. 7 Half-pipe and tensile specimen

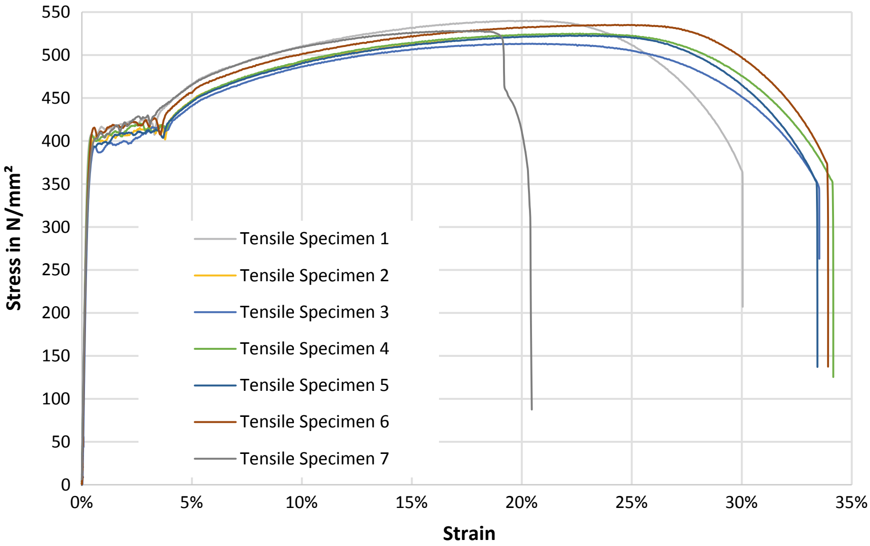

Fig. 8 Stress–strain curves for tensile tests on half-pipe

specifies a yield strength of at least 420 N/mm^2. This slight underrun in the tensile test specimens is common in additive manufacturing; see [21], among others. The strengths are usually higher in tensile test specimens stressed longitudinally to the layer path, so that the unfavourable direction was investigated here.

3.2 Walls to Determine the Influence of Spray Cooling

Not only the deposition rates, but also the cooling times are decisive for the manufacturing time in WAAM. Before the next weld layer can be applied, a certain and material-dependent temperature (interpass temperature) must be reached to prevent the weld metal from dripping down, which has a considerable influence on the manufacturing time. With smaller structures, the cooling time is even longer than the material deposition itself. An interpass temperature of 150 °C has been established for the G3Si1/ER70S-6 filler material used. Two cooling methods are compared in the following.

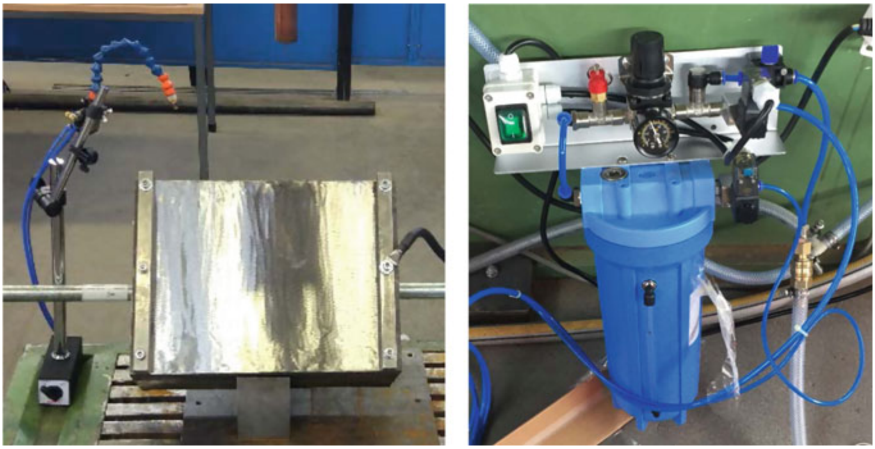

Fig. 9 Cooling with compressed air and sprayed water

3.2.1 Cooling Methods

Cooling with Compressed Air

With compressed air cooling, air is blown from a compressor onto the manufactured body after each layer is produced until the temperature falls below the desired interpass temperature. The high air flow accelerates the heat dissipation.

Cooling with Compressed Air and Sprayed Water

With spray cooling, water is added to the compressed air, creating a kind of water mist. The water evaporates on the surface of the test specimen and thus withdraws heat faster than with pure compressed air. Minimal quantity lubrication is used for this purpose; see Fig. 9.

3.2.2 Comparison of Manufacturing Time

To compare the two cooling methods, two identical wall-like structures were produced with the parameters from Table 1. Specimen 1 was cooled only with compressed air and specimen 2 with compressed air and sprayed water. In the air-cooled test, 186 s were cooled on average, whereas in the test specimen 2, only 93 s of water spray cooling were sufficient to fall below the target interpass temperature (Fig. 10).

	Compressed Air	Compressed air and sprayed water
Total manufacturing time for 112 Layers	405 min	230 min
Manufacturing time per layer	30.5 s/layer	30.5 s/layer
Average cooling time per layer	186 s	93 s

Fig. 10 Specimen (left) and comparison of manufacturing and cooling times (right)

3.2.3 Comparison of Material Properties

The resulting microstructures due to the different cooling procedures were investigated by means of light microscopy, hardness tests as well as tensile tests. Both cooling types lead to a ferritic–pearlitic microstructure, and the pearlite is spherical (Fig. 11). No pores were detected.

For each cooling procedure, tensile specimen was taken perpendicular to the building direction. Two specimens are in an “as-built” surface condition (Fig. 9, left), and two specimens are in a grinded “smooth” surface condition. The quasi-static properties and the hardness of the specimen manufactured with high and low cooling rates are more or less identical (Table 2). This shows that a further increase of the cooling rate and therefore a shortening of the building time is possible. The values of the “smooth” surface condition are increased, representing the influence of the surface condition.

4 Conclusion

This paper introduces the “CMT Cycle Step” process, which is particularly suitable for additive manufacturing of cantilevered structures. The TU Darmstadt uses the process to manufacture a steel bridge in situ. Various manufacturing experiments and experimental investigations are presented which show that the Cycle Step process can be used to produce geometrically error-free structures with good material properties. Furthermore, a cooling method with sprayed water is presented, with which the cooling times in additive manufacturing can be halved without negatively affecting the material properties or the microstructures.

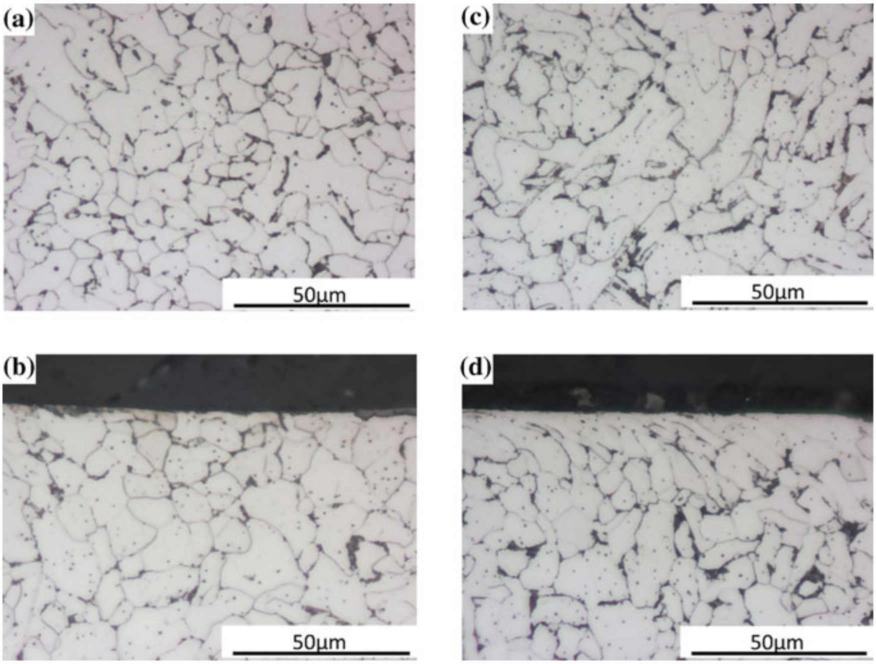

Compressed Air (CA)

Compressed air and sprayed water (CA+SW)

Fig. 11 Ferritic–pearlitic microstructure, core area (**a**, **c**) and near surface area (**b**, **d**)

Table 2 Quasi-static properties, hardness values

	Compressed air (CA)				Compressed air and sprayed water (CA + SW)			
	As built		Smooth		As built		Smooth	
	Mean value	Standard deviation	Mean value	Standard deviation	Mean value	Standard deviation	Mean value	Standard deviation
Yield strength in N/mm^2	362	3.5	397	2.8	358	19.8	414	0.7
Tensile strength in N/mm^2	458	0.7	498	0.7	459	2.1	506	1.4
	Mean value		Standard deviation		Mean value		Standard deviation	
Hardness [HV10]	161		3.5		163		3.5	

Acknowledgements We would like to thank the companies Fronius Deutschland GmbH, Messer Group GmbH, WDI Schweißtechnik GmbH, Comau Deutschland GmbH and Spinnaker GmbH for their support.

References

1. Frazier, W.E.: Metal additive manufacturing: a review. J. Mater. Eng. Perform. **23**(6), 1917–1928 (2014)
2. Gebhardt, A.: 3D-Drucken: Grundlagen und Anwendungen des Additive Manufacturing (AM). Carl Hanser, München (2014)
3. Ali, Y., Steinerstauch, K., Günther, K., Henckell, P., Bergmann, J.P.: Additive Fertigung von 3D-Verbundstrukturen mittels MSG-Schweißen. DVS-Bericht. **327**, 75–80 (2016)
4. Bergmann, J.P., Henckell, P., Reinmann, J., Hildebrand, J., Ali, Y.: Grundlegende wissenschaftliche Konzepterstellung zu bestehenden Herausforderungen und Perspektiven für die Additive Fertigung mit Lichtbogen. DVS Media GmbH, Düsseldorf (2018)
5. Williams, S.W., Martina, F., Addison, A.C., Ding, J., Pardal, G., Colegrove, P.: Wire + arc additive manufacturing. Mater. Sci. Technol. **32**(7), 641–647 (2016)
6. Laghi, V., Palermo, M., Gasparini, G., Girelli, A., Trombetti, T.: Geometrical characterization of wire-and-arc additive manufactured steel elements. Adv. Mater. Lett. **10**(10), 695–699 (2019)
7. Posch, G., Chladil, K., Chladil, H.: Material properties of CMT—metal additive manufactured duplex stainless steel blade-like geometries. Weld. World **61**(5), 873–882 (2017)
8. John, F., Fischer, G., Armatys, K., Riemann, A., Röhrich, T.: Potentiale von drahtbasierten Lichtbogenprozessen für die additive Fertigung. In: Mayr, P., Berger, M. (eds.) Füge- und Montagetechnik Chemnitz. Universitätsverlag Chemnitz, Chemnitz (2017)
9. Ding, D., Pan, Z., Cuiuri, D., Li, H.: A multi-bead overlapping model for robotic wire and arc additive manufacturing (WAAM). Robot. Comput. Integr. Manuf. **31**, 101–110 (2015)
10. Erven, M., Feucht, T., Lange, J., Eiber, M., Hildebrand, J., Bergmann, J.P.: Numerische und experimentelle Untersuchungen von Knoten im konstruktiven Stahlbau. DVS Congress, Rostock (2019)
11. Feldmann, M., Kühne, R., Citarelli, S., Reisgen, U., Sharma, R., Oster, L.: 3D-Drucken im Stahlbau mit dem automatisierten Wire Arc Additive Manufacturing. Stahlbau **88**(3), 203–213 (2019)
12. Feucht, T., Lange, J., Erven, M.: 3-D-printing with steel: additive manufacturing of connection elements and beam reinforcements. ce/papers Nordic Steel 2019 (Kopenhagen) **3**(3–4), 343–348 (2019)
13. Mechtcherine, V., Grafe, J., Nerella, V.N., Spaniol, E., Hertel, M., Füssel, U.: 3D-printed steel reinforcement for digital concrete construction—manufacture, mechanical properties and bond behaviour. Constr. Build. Mater. **179**(2018), 125–137 (2018)
14. MX3D: MX3D Vision. https://mx3d.com/about-2/. Access Date: 02.12.2019
15. Van der Velden, G.: MX3D: A 3D metal printing company. In: Knaack, U., Tessmann, O., Wibranek, B. (eds.) BE-AM | Built Environment Additive Manufacturing 2019. Technische Universität Darmstadt, Darmstadt (2019)
16. Hartke, M., Ali, Y., Günther, K., Bergmann, J.P.: Schweißtechnische Herstellung komplexer 3D-Freiformflächen mittels geregelter MSGKurzlichtbogentechnik. In: 4. Fachtagung „Schweißtechnische Verarbeitung von Stählen im Kraftwerksbau“, Duisburg (2014)
17. Kazanas, P., Deherkar, P., Almeida, P., Lockett, H., Williams, S.: Fabrication of geometrical features using wire and arc additive manufacture. Proc. Inst. Mech. Eng. Part B J. Eng. Manuf. **226**(6), 1042–1051 (2012)
18. Waldschmitt, B.: Additive manufacturing of a bridge. Master thesis, Technische Universität Darmstadt, Darmstadt (2019)

19. Fronius, Bruckner, J., Egerland, S., Himmelbauer, K., Millinger, A., Schörghuber, M., Söllinger, D., Waldhör, A.: Schweißpraxis aktuell: CMT-Technologie. Cold Metal Transfer—ein neuer Metall-Schutzgas-Schweißprozess. WEKA MEDIA GmbH & Co. KG, Kissing (2013)
20. Lange, J., Knaack, U., Feucht, T., Erven, M., Borg Costanzi, C.: Additive manufacturing by means of parametric programming of robots. In: Brell-Cokcan, S. (ed.) Construction Robotics. Springer, under review (2020)
21. Müller, J., Grabowski, M., Müller, C., Hensel, J., Unglaub, J., Thiele, K., Kloft, H., Dilger, K.: Design and parameter identification of wire and arc additively manufactured (WAAM) steel bars for use in construction. Metals **9**(7), 725 (2019)

Single-Sided Resistance Spot Welding of Steel–Aluminum Dissimilar Joints—Mechanical Characterization and Interface Formation

Konstantin Szallies, Moritz Zwicker and Jean Pierre Bergmann

Abstract Components made of aluminum–steel dissimilar joints show a high potential regarding to lightweight applications. In particular, due to their fundamental differences in chemical and physical properties, new approaches must be developed for common industrial joining processes. This study shows a new approach in order to characterize the joining zone formation using single-sided resistance welding. Based on the mechanical properties, the interface formation is investigated. Depending on the process variables, increasing mechanical tensile forces are shown with simultaneously increasing thickness of the diffusion zone. In this context, a significant porosity of the joint in the aluminum base material can be observed. For this purpose, a characterization method is developed.

Keywords Resistance welding · Single-sided resistance spot welding · Dissimilar materials · Lightweight design · Pore characterization · Dissimilar steel–aluminum joints

1 Introduction and State of the Art

Resistance spot welding is the most common joining technology in the sheet metal industry for welding steels. The main areas of application are the automotive and electrical industries. The major reasons are, in particular, the high automatability and flexibility as well as the high cost-effectiveness. The largest field of application for resistance spot welding is an automotive body shell construction, with about 5000 welding spots [6]. In this case, diverging welding requirements are such as multi-sheet joints, welding of deep-drawing, and high-strength steels as well as different sheet thicknesses with and without coating systems. Due to the current challenges of reducing emissions, multi-material construction methods in which steel and aluminum are used in combination are increasingly being pursued in these markets.

K. Szallies (✉) · M. Zwicker · J. P. Bergmann
Department of Production Technology, Technische Universität Ilmenau, Gustav-Kirchhoff-Platz 2, 98693 Ilmenau, Germany
e-mail: info.fertigungstechnik@tu-ilmenau.de; konstantin.szallies@tu-ilmenau.de

L. F. M. da Silva et al. (eds.), *Advanced Joining Processes*,
Advanced Structured Materials 125, https://doi.org/10.1007/978-981-15-2957-3_6

The use of aluminum–steel dissimilar joints requires adapted approaches and joining technologies, in particular due to the various physical and chemical properties which present major challenges in terms of joining technology. However, the thermal joining of aluminum with steel, respectively iron, is characterized by the formation of intermetallic phases at the interface. These exhibit a brittle hard mechanical behavior and minor fatigue strength. For this reason, technically complex mechanical joining processes and adhesives are currently used. These require additional joining elements. The elements are visible above the sheet thickness. Furthermore, additional process steps such as punching the element, hardening, and sealing the joint are necessary. This leads to longer production times and additional costs per component.

The requirement for a direct joint between aluminum and steel without the use of additional elements can be achieved by fusion welding and pressure welding. For fusion welding of aluminum–steel dissimilar joints, various publications can be determined [2, 7, 10]. An essential characteristic is the formation of cross-linked intermetallic phases (Fe_xAl_y) during solidification. These have a thickness of up to 500 µm and can cause to failure of the joint. Investigations of Achar [1] show the reduction of the joint strength for increasing phase thicknesses. Therefore, it is necessary to limit phase formation for practical applications.

At an aluminum concentration below 22 at.%, there is a solubility of aluminum in iron (Fig. 1), thus the formation of intermetallic phases can be prevented. Conversely, the technical process implementation, especially during welding, causes barriers. The reason for this is the temperature-dependent behavior of the diffusion coefficients of Fe in Al and of Al in Fe. The higher diffusion coefficient of Fe in Al leads to the fact that the formation of the ductility-reducing intermetallic phases cannot be prevented [8]. The propagation of these phases is based on diffusion of atoms and dependents on time and temperature during welding. For this reason, the expansion of the phases can only be influenced by the adjusted setting of the temperature–time profile in the welding process.

Therefore, it is necessary to reduce peak temperatures and welding times for practical applications. The process dynamics of resistance welding, with heating rates of up to 15,000 K/s, allows the formation of melts in short times. At this point, it can be assumed that the formation of the ductility-reducing phases can be strongly limited in comparison to other processes. Studies of Leuschen [5] show, however, that due to the insulating oxide layer on the one hand and the high electrical and thermal conductivity of the aluminum on the other hand, but also due to the higher heat capacity, a high welding current of up to 30 kA is necessary for welding aluminum with steels in order to produce an adequate joint. In comparison, the low thermal conductivity of the steel results in a high heat input also using short current times, which leads to a significant growth of the intermetallic phases and to brittle material behavior. Accordingly, the heat input during resistance spot welding of aluminum and steels must be adapted to the corresponding thermophysical properties in order to reduce the formation of intermetallic phases.

Neudel [6] shows in his work an approach to adapt the heat input during resistance spot welding of aluminum and steel directly to the material properties. Using an

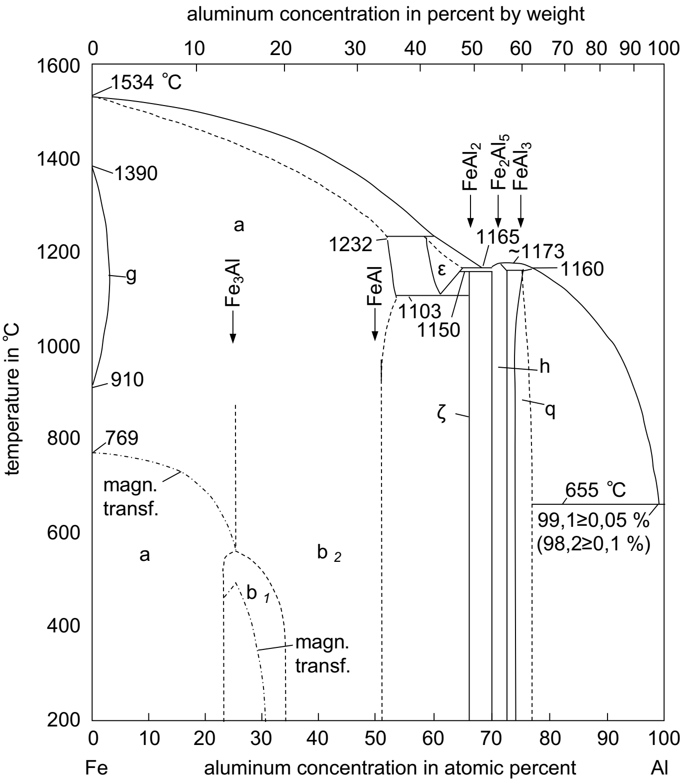

Fig. 1 Binary diagram of aluminum and iron with solubility of the materials for the state of equilibrium according to [3]

additional process tape with different electrical resistances, the heat input from the steel sheet into the aluminum sheet is influenced. For this purpose, a copper-coated steel tape with a low contact resistance is used in order to cause reduced heating in the steel. On the aluminum side, a process tape with a high resistance (e.g., chromium–nickel) is used to achieve an increasing heat input. This limits the diffusion of iron in aluminum and limits the thickness of the diffusion zone at the interface to 3–5 μm. Some failure risks prevent the application of this technology, for example, the time-consuming tape change, the tape break as well as the adhesion of the process tape after welding the sheet metal.

Own investigation shows a further possibility to join aluminum with steel directly without the use of additional joining elements by the resistance welding technology. With this method, the welding current is contacted single-sided in only one joining partner. Compared to the conventional two-sided electrode arrangement, the resistance heating is thus preferably carried out in only one joining partner, so that the total heat input is reduced and the formation of the intermetallic phases at the interface is limited.

2 Experimental Setup

The experimental investigations were carried out with a Dalex resistance welding machine with a combined 1000 Hz MFDC weld control and inverter Rexroth PSI 6300 and a welding transformer Rexroth PSG 6130. Electrode caps according to DIN EN ISO 5821 in F1 form with a diameter of 16 mm and an electrode working area of 5.5 mm were used.

The workspace configuration is shown in Fig. 2. In order to realize the single-sided current flow, both electrodes were arranged parallel. The total electrode force of the welding machine is equally divided by a spring arrangement of the welding tool. The current is conducted by a flexible connection from the bottom electrode to the welding electrodes of the tool. To prevent an electrical shunt, both electrodes are insulated from each other. The aluminum and steel joining partners are arranged below. A common automotive zinc-coated steel DX56D+Z100MB with a sheet thickness of 1.5 mm and the aluminum alloys EN AW-6082 and EN AW-5083 with a sheet thickness of 1.5 mm were used.

The investigations were carried out on overlap joints according to DVS/EFB 3480-1 with an overlap area of 20 × 45 mm^2 (Fig. 2). The electrodes, with a distance of 25 mm, were arranged centrally on the sheet. The current was always conducted as single-pulse welding regime.

To characterize the pores, metallographic cross sections were prepared, and the absolute area of the cavities and their distribution above the total aluminum sheet cross section were evaluated. The evaluation was carried out using the image processing program ImageJ. In addition, radiography investigations were carried out for the qualitative characterization of the cavity distribution.

For the investigations in the context to the half-section setup, a thermometry camera InfraTec Image IR 8300 was used to observe the temperature field distribution. The frame rate was 100 fps.

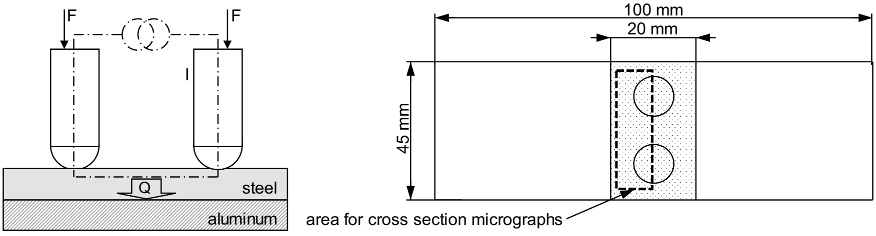

Fig. 2 Workspace configuration and specimen geometry

3 Results and Discussion

3.1 *Mechanical Properties*

First investigations of the mentioned approach show the mechanical properties of the joint for different material combinations as well as the selection of the process conditions [11]. In deviation to common test guidelines, the minimum process limit of the weldability is defined by a tensile force of at least 500 N in quasi-static shear tensile test, which allows a handling of the specimen. The maximum process limit of the weldability is defined by a spatter formation. To compare the joints depending on the welding current, the quasi-static load–strain curves were evaluated. Figure 3 shows exemplary for a constant current time of 400 ms the resulting tensile force–cross-head travel curves for three welding currents and the typical fracture behavior. For minor welding currents of 6 kA, the joints fail as shear fracture (Fig. 3a) and above as mixed fracture. From a welding current of 8 kA, the specimens fail with fracture of the aluminum base material. The respective fracture behavior thus results from the shear tensile forces; these depend on the process variables or rather the temperature–time profile.

Figure 4 shows the dependence of the maximum shear tensile forces and the maximum cross-head travel as function of the current time within the process limits. For increasing current times, the shear tensile force increases from about 0.5 kN to over 4.5 kN, whereby current times from 240 ms achieve such high tensile forces. This extends the cross-head travel to the maximum force from about 0.1 mm to over 0.6 mm. In addition, comparable cross-head travels result from comparable shear tensile forces, regardless of the current time.

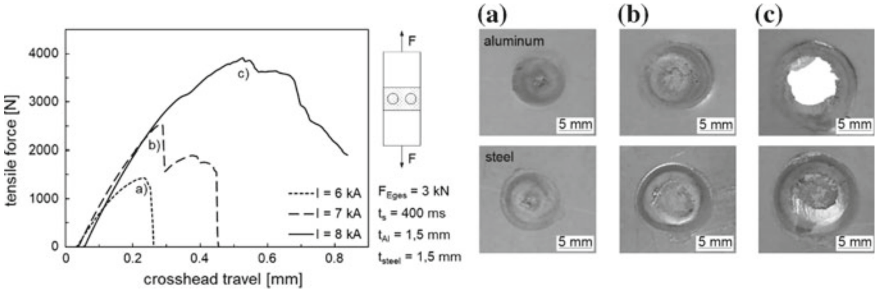

Fig. 3 Measured load–strain curves of the joints and the typical resulting fracture behavior: **a** shear fracture, **b** mixed fracture, and **c** fracture of the aluminum base material

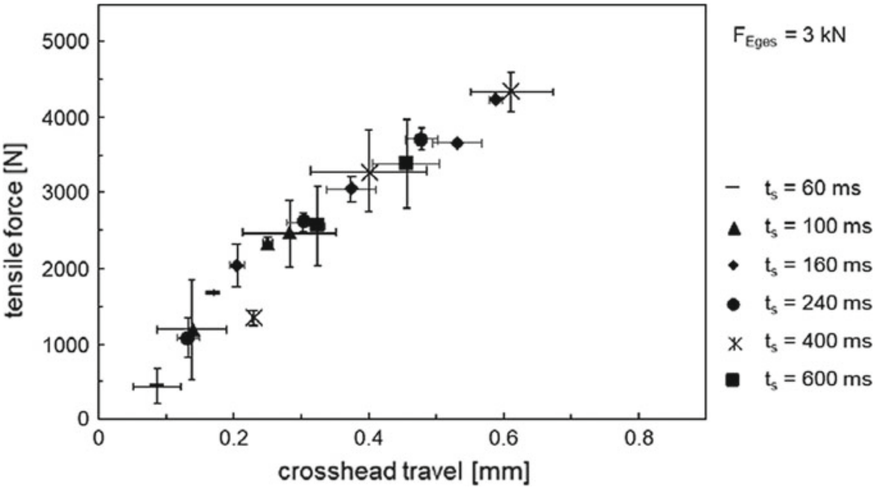

Fig. 4 Resulting tensile forces and cross-head travels depending on the current time

3.2 *Interface Formation*

As shown in the introduction, the mechanical properties of steel–aluminum dissimilar joints are mostly attributed to the thickness of the intermetallic phase. In order to determine the thickness of this diffusion zone, metallographic half sections were prepared. Figure 5 shows the resulting shear tensile force as a function of the dimension of the joining area, in particular the joint length. In particular, the resulting shear tensile forces depend on the joint length of the specimens. It can be seen that also for aluminum–steel dissimilar joints, increasing tensile forces results as a function of the joint length. In this context, the joint length represents the sum of both joint diameters. Figure 5 shows exemplary cross sections welded with a constant current time of 400 ms using currents of 6 kA (Fig. 5a) and 8 kA (Fig. 5b). Due to the

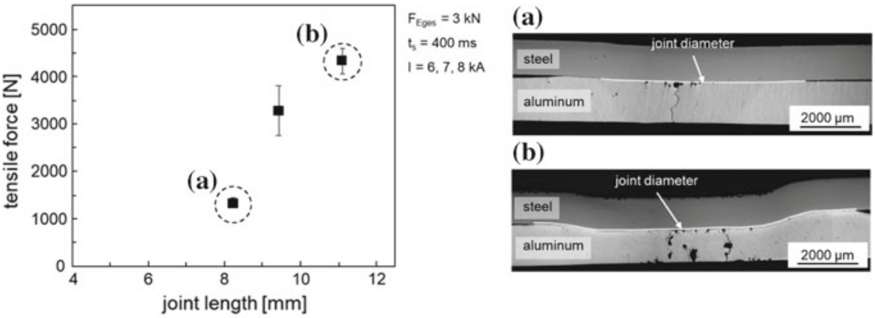

Fig. 5 Tensile forces depending on the joint diameter, cross sections depending on the welding current **a** 6 kA and **b** 8 kA

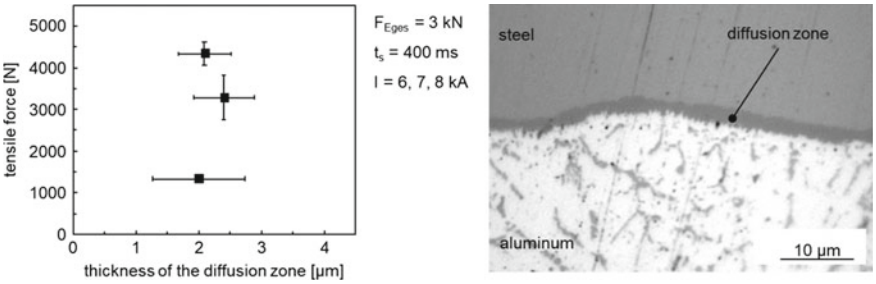

Fig. 6 Tensile forces depending on the thickness on the diffusion zone

higher heat input, an increasing deformation of the joining partners occurs below the electrodes, which leads to an influence on the sheet cross-sectional area. In addition, an increasing pore formation appears.

Figure 6 shows the quasi-static shear tensile forces as a function of the diffusion zone thickness. The thickness was measured in the center of both weld spots. In this context, using a constant current time of 400 ms and increasing welding currents, it can be seen that no clear influence on the thickness of the diffusion zone can be determined in this order of magnitude. The resulting thicknesses are in an average range of 1.2–3.0 µm.

In addition, the lateral expansion of the thickness of the diffusion zone was investigated. Therefore, the thickness was measured at a distance of 5 mm from the center of the weld spots. Shown in Fig. 7 the thickness of the diffusion zone is pronounced in the middle compared to the outer areas, which show a reduced thickness. This can be traced back to the temperature distribution during welding. In addition, the measured thicknesses of the diffusion zone are primarily in a comparable order of magnitude.

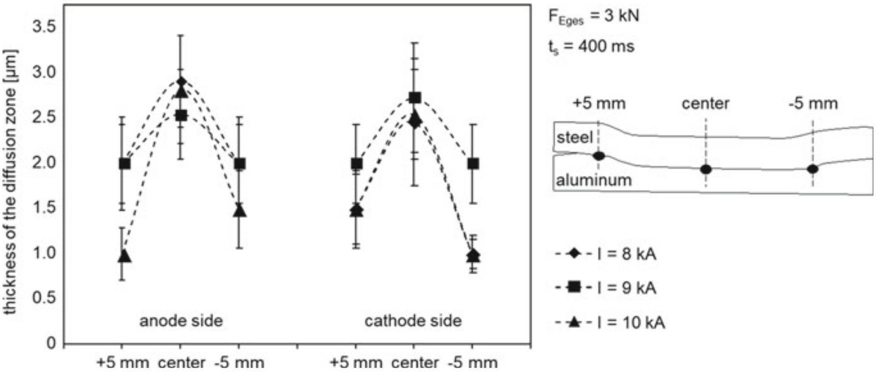

Fig. 7 Thickness of the diffusion zone depending on the distance from the center of the welding electrode

As shown, an increased joint diameter due to an increasing heating occurs. In addition, the tensile force of the joint depends on the joint diameter. Depending on the welding current, the thickness of the diffusion zone is about a comparable order of magnitude. Against this background, the increased tensile forces result from the increasing joint diameter.

3.3 Pores

A significant porosity of the joint results and propagates to the outer surface of the aluminum which is shown in Fig. 5. In order to investigate the influence of the process variables on the porosity, a method was developed to characterize the order of magnitude and distribution of the pores.

For this purpose, in each case, cross sections were prepared out of the specimen, in the middle of the welding spots. Subsequently, a gray value segmentation was carried out based on the cross-sectional images. Using an image processing system, the total pore areas of each welding spot were measured out. Figure 8 shows the total pore area of the anode side and cathode side in the aluminum cross-sectional area for the alloys EN AW-5083 and EN AW-6082. Regardless of the respective aluminum alloy, it shows that an increasing welding current is accompanied by an increase in the pore cross-sectional area. This results from the increased heat input and the increased heat-affected zone. The alloy EN AW-6082 shows a lower porosity compared to EN AW-5083. This could be traced back to the silicon of this aluminum alloy. The alloying element silicon has a diffusion-inhibiting effect for welding aluminum alloys [4, 12, 13]. In addition, the porosity of the welding spot on the anode side is more pronounced compared to the cathode side. This could be attributed to the Peltier effect.

The Peltier effect occurs in direct current circuits consisting of two dissimilar materials with different electrochemical voltages. This results in a voltage difference

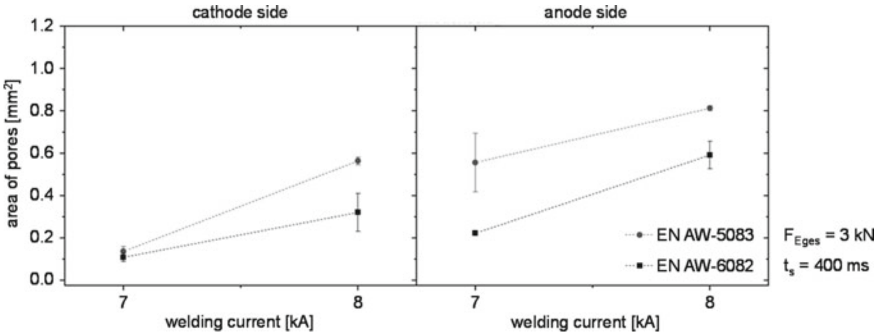

Fig. 8 Total area of pores depending on the welding current for the aluminum alloys EN AW-6082 and EN AW-5083

at the contact points. This difference causes that Peltier heat to be removed at the cathode-side transition and Peltier heat to be generated at the anode-side transition. This difference leads to an extraction of Peltier heat at the contact of the cathode side and to a generation of Peltier heat at the contact of the anode side.

This is shown in Fig. 9 for heating and cooling in the half-section model. The half-section model was carried out according to Schneemann [9]. In this context, it is necessary to reduce the electrode force and the welding current. The verification of the Peltier effect is carried out according to Neudel [6] by reversing the polarity of the electrodes. Figure 9 shows that between 60 ms and 100 ms current time, the anode-side interface (+) shows a more pronounced temperature field compared to the cathode-side interface (−) starting from the electrode–steel interface. During the hold time (500–600 ms), it can be also characterized that the temperature field on the aluminum side is reduced at a slower rate than in steel. This could be traced back to the actively cooled electrodes.

In order to characterize the pore distribution over the sheet cross section, the cross-sectional micrographs are divided into line segments. The lower aluminum sheet edge is defined as the reference line. Figure 10 shows the distribution of the anode-side area of pores over the cross section of the aluminum sheet for the aluminum alloys EN AW-6082 and EN AW-5083.

Using a welding current of 7 kA, the pronounced area of pores results at the aluminum–steel interface. The comparison of the pore distribution between welding currents of 7 and 8 kA shows that there are fewer pores at the aluminum–steel interface. It can be noted that the increasing welding current results in a significant redistribution of the area of pores. It can be determined that for an increasing welding current, the area of pores enhances with increasing distance from the aluminum–steel interface to the outer surface of the aluminum.

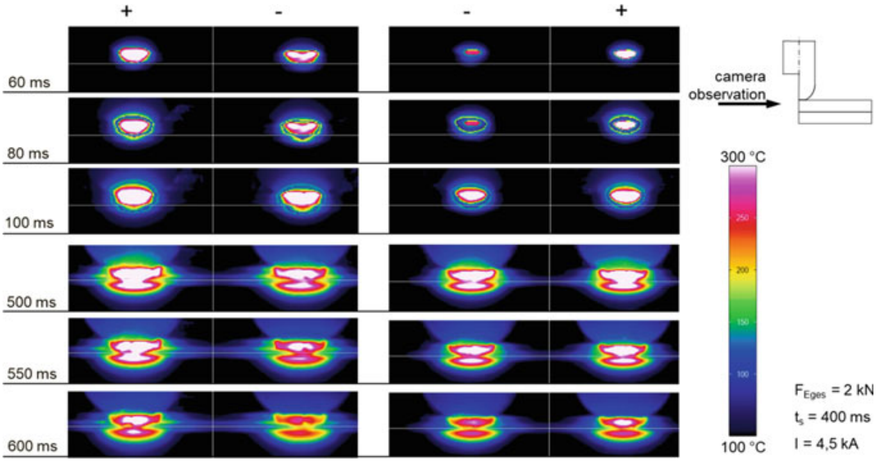

Fig. 9 Temperature distributions in half-section setup depending on the electrical polarity

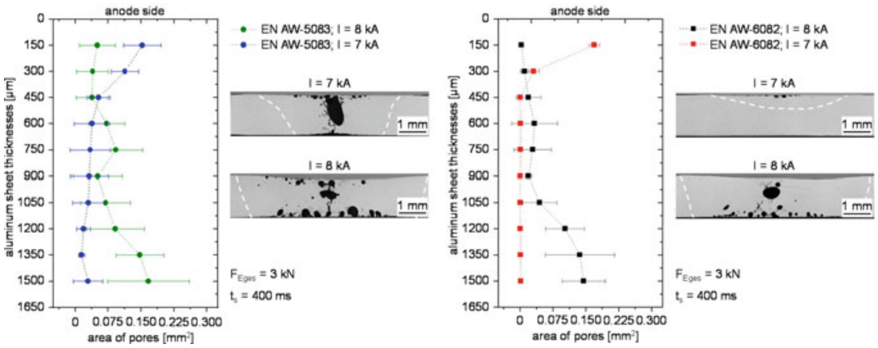

Fig. 10 Distribution of the area of pores depending on sheet thickness and the welding current for the aluminum alloys EN AW-5083 and EN AW-6082

Figure 11 shows the distribution of the pores for the aluminum alloy EN AW-5083 as a function of the current time. Using a current time of 300 ms, small pores result at the steel aluminum interface and a semi-lens-shaped melting zone is generated in the aluminum. As from a current time of 400 ms, a large central worm hole and a localized clustered porosity are generated at the interface and the outer surface of the aluminum. The melting zone spreads over the entire cross section of the aluminum sheet. As the current time increases, the melting zone still expands. This results in the formation of more widely distributed pores across the cross section of the aluminum sheet. This correlation has already been demonstrated as a function of the welding current. For this reason, it can be stated that the increase in thermal energy results in an increasing area of pores on the outer surface of the aluminum. In summary, the described relations lead to a mismatch between the mechanical load-bearing capacity and the reduction of pores.

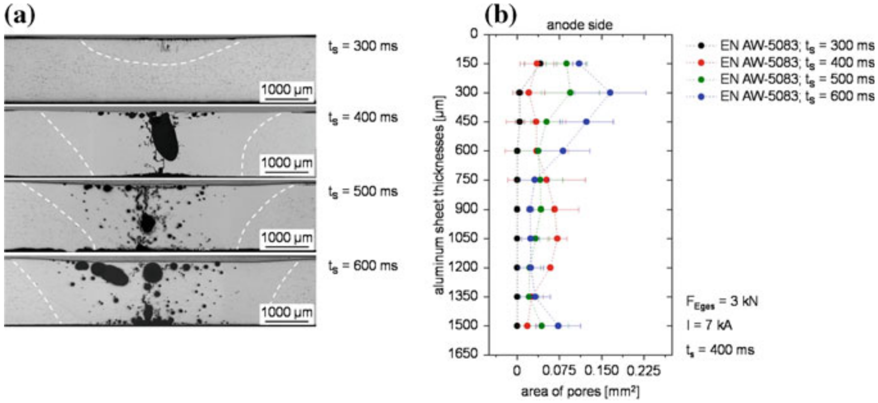

Fig. 11 **a** Cross sections of the joint zone depending on the current time and **b** distribution of the area of pores depending on sheet thickness and the current time

4 Conclusion

In this paper, novel results regarding single-sided resistance spot welding in parallel electrode arrangement of steel–aluminum dissimilar joints are shown. Compared to the mechanical properties, the interface formation is characterized. Moreover, the influence of process variables on the joint formation, especially welding current, was shown. It was pointed out that the interface is characterized by significant porosity, which depends on the process variables as well as the Peltier heating. A method to characterize the distribution of the porosity was shown. In this context, it was found that an increasing welding current results in a significant redistribution of the area of pores. In addition, the distribution of the area of pores was investigated depending on the aluminum alloy, the current time, and the welding current. This causes a mismatch between mechanical properties and concentration of the pores. The presented results regarding single-sided resistance spot welding of steel–aluminum dissimilar joints contribute to a better understanding of the joint formation.

References

1. Achar, G., Ruge, J.: Verbinden von aluminium mit Stahl, besonders durch Schweissen. Aluminium-Verlag, Düsseldorf (1981)
2. Atabaki, M., Nikodinovski, M., Chenier, P., Kovacevic, R.: Welding of aluminum alloys to steels: an overview. Conference presentation (2013)
3. Hamidreza, A.; Mahla, S.; Mostafa, M.; Kosar, A.: Effect of silicon and manganese on the kinetics and morphology of the intermetallic layer growth during hot-dip aluminizing. Surf. Coat. Technol. **357**, 483–496, 1 (2019)
4. Heumann, T., Dittrich, S.: Über die Kinetik der Reak-tionen von festem und flüssigem Aluminium mit Eisen. Zeitschrift für Metallkunde **50**, 617–635 (1959)
5. Leuschen, B.: Beitrag zum Tragverhalten von Aluminium- und Aluminium-Stahl Widerstandspunktschweißverbindungen bei verschiedenartiger Beanspruchung. Ph-Thesis, RWTH Aachen (1984)
6. Neudel, C.: Mikrostrukturelle und mechanisch-technologische Eigenschaften widerstandspunktgeschweißter Aluminium-Stahl Verbindungen für den Fahrzeugbau Ph.D. Thesis. Meisenbach, Erlangen (2014)
7. Radscheid, C.: Laserstrahlfügen von Aluminium mit Stahl, Ph.D. Thesis. Universität Bremen (1996)
8. Rathod, M.J.: Joining of aluminum alloys 5052 and low-carbon-steel by laser roll welding. Weld. J. 16s–26s (2004)
9. Schneemann, K.: Vorgänge beim Punktschweißen von Tiefziehstahl und ihr Einfluss auf das Schweißgut, Ph.D. Thesis. Universität Hannover (1967)
10. Schubert, E.: Untersuchungen zum Leichtbau mit Hilfelasergestützter Misch-bauweise. Universität Bremen, Habilitation (2002)
11. Springer, H., Szczepaniak, A., Raabe, D.: On the formation and growth of intermetallic phases during interdiffusion between low-carbon steel and aluminum alloys. In: Acta Materialia (2011)

12. Szallies, K., Pompe, T., Bergmann, J.P.: Grenzflächenausbildung beim einseitigen Widerstandspunktschweißen Stahl-Aluminium-Mischverbindungen; In: 24. DVS-Sondertagung Widerstandsschweißen (2019)
13. Windmann, M; Röttger, A., Theisen, W.: Formation of intermetallic phases in Al-coated hot-stamped 22MnB5 sheets in terms of coating thickness and Si content. Surf. Coat. Technol. **246**, 17–25, 5 (2014)

Investigations on the Influence of Beam Shaping in Laser Transmission Welding of Multi-layer Polymer Films with Wavelength-Adapted Diode Laser Beam Sources

Maximilian Brosda, Phong Nguyen, Alexander Olowinsky and Arnold Gillner

Abstract Multi-layer polymer films are used in a large number of technical areas. In many applications, a trend toward more flexible production and batch sizes down to one can be identified. Commercially available joining processes can only fulfill the requirements to a limited extent. The process principle of laser transmission welding with a wavelength-adapted laser beam source enables flexible and contour-independent welding of commercially available polymer films without material modification and therefore represents an alternative solution. In this method, the material-dependent intrinsic absorption bands of polymers in the wavelength range >1500 nm are addressed. Depending on the application, there are different specifications for the weld seam width but also for the available installation space. This results in different requirements such as distance between material surface and laser optics or required beam diameter. The requirements are highly variable depending on the application. In order to investigate the influences and effects of such beam shaping optical changes, laser welding experiments with different laser optical configurations on commercially available multi-layer polymer films are performed. The samples are analyzed using thin sections and *T*-peel tensile tests. In addition, the results will be discussed using raytracing models created in ZEMAX® Optic Studio 16. In particular, questions are discussed, whether a targeted energy input into a film layer is still possible or whether the entire film stack is melted.

Keywords Laser transmission welding · Multi-layer polymer films · Laser sealing · Laser polymer welding · Packaging

1 Introduction

The joining of polymer films with laser beam sources has a potential wide field of application. The requirements for the process result as well as for the process itself vary greatly depending on the application. For example, wide weld seams are

---

M. Brosda (✉) · P. Nguyen · A. Olowinsky · A. Gillner
Fraunhofer Institute for Laser Technology ILT, Steinbachstraße 15, 52074 Aachen, Germany
e-mail: Maximilian.Brosda@ilt.fraunhofer.de

L. F. M. da Silva et al. (eds.), *Advanced Joining Processes*,
Advanced Structured Materials 125, https://doi.org/10.1007/978-981-15-2957-3_7

required for gas-tight packaging, whereas very fine weld seams are required for welding laboratory on chip devices. For thicker film systems, on the other hand, it is necessary to use a high numerical aperture to prevent melting at the surface or the surrounding film layers. Molded components such as deep-drawn shells require a greater distance between the laser optics and the material surface. Another challenge is the so-called layer jump, in which the number of films to be joined increases, for example, from two to four. All the above-named examples result in different requirements for the laser transmission welding process. Previous work has been limited primarily to single-layer materials [1] or the selection of a suitable beam source [2]. Questions about the proper beam shaping have not yet been answered. In the following, it will therefore be examined to what extent these requirements can be fulfilled with a suitable beam shaping.

2 Fundamentals

In order to understand the following experimental investigations and above all the discussion of the results, some basic principles will first be presented. These include the basic principle of laser beam transmission welding of polymers with adapted wavelength as well as the physical relationships of beam shaping. A further section is dedicated to the optical properties of films which are of major importance for a successful welding process.

2.1 Laser Transmission Welding of Polymer Films

Most polymer films are transparent in the visible and near-infrared range (400–1500 nm). In order to achieve sufficient absorption in the material and hence melting, the classic approach is to modify the material to suit. This is associated with additional costs and is undesirable in many applications. In order to achieve sufficient absorption nevertheless, laser beam sources are used which address areas of higher absorption with their emission wavelength. The position of these intrinsic absorption bands (>1500 nm) depends on the polymer and the absorption capacity depends on the thickness of the polymer [3–6]. Polymer films usually consist of several different material layers. Each layer has its own specific absorption properties. The sum of all absorptions gives the total absorbency of the film [4]. In order to be able to weld the films together, they are positioned in an overlap arrangement and subjected with a joining pressure from the outside (Fig. 1).

The laser beam propagates into the stack of films from above and is focused on the contact layer of the two films. Through absorption processes and the resulting heat, the polymer is melted locally [7].

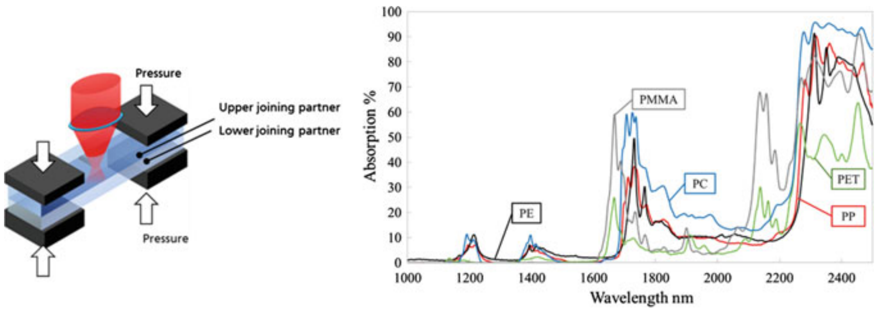

Fig. 1 Principle of laser transmission welding process

2.2 *Beam Shaping*

Laser focusing optics is used to shape the laser radiation for the process described above as required. A beam shaping optics usually consists of several lenses with a corresponding anti-reflective coating on the surface to reduce the loss of energy. Important parameters that can be set for beam shaping optics are the focal length of the last focusing lens, which influences the distance between the laser optics and the material surface, the beam diameter in the focus area and the numerical aperture. All these parameters are physically linked. A change of one parameter inevitably leads to a change of the others (Fig. 2).

In many processes, however, there is a conflict of objectives between the individual parameters. For example, it may be desirable to obtain a very narrow weld seam but still maintain a large distance between the material surface and the laser optics. Changes in the number of layers are also conceivable or a *Z* fluctuation caused by conveying technology is conceivable. Ideally, laser optics should be designed to compensate for these technical process influences. A beam shaping optic setup is

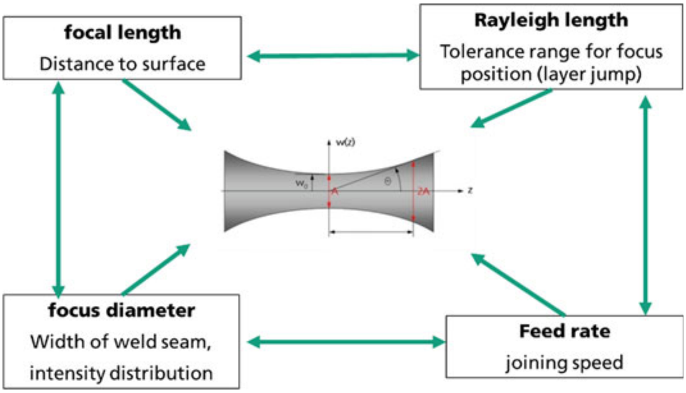

Fig. 2 Relationship of relevant parameters

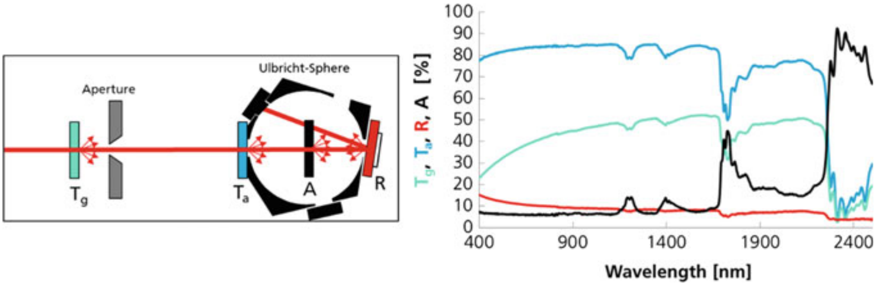

Fig. 3 Principle of optical measurement and corresponding measurement result

usually designed by using raytracing software. For the following investigations, the laser optics was designed, and the beam propagation is simulated with ZEMAX® Optic Studio 16.

2.3 Optical Properties of Polymer Films

The optical properties of polymer films can be determined with a suitable measurement setup. For the present investigations, a UV-Vis-NIR spectrometer with an integrating Ulbricht sphere is used. Figure 3 shows the measurement setup:

The measurement setup allows the determination of absolute transmission, reflection and absorption as well as the directional part of transmission. In this way, the scattering properties of a polymer can be determined. This is of particular interest if strongly scattering polymers are contained in a film system because this can also influence the beam propagation.

3 Experimental Setup

The experimental setup consists of an nLIGHT diode laser with a peak emission wavelength of 1685 nm and a maximum optical output power of 100 W at the fiber end. The laser beam is guided through a glass fiber with a core diameter of 600 μm from the laser beam source to the focusing optics. The laser optics consists of several lenses which can be exchanged modularly to realize different focal lengths and thus also focus diameters [7].

The used multi-layer polymer film is a two-layer film, consisting of a 12 μm polyethylene terephthalate (PET) on the outer side and a 90 μm linear low-density polyethylene (PE) on the inner side. The two layers are bonded with a pressure-sensitive adhesive with a thickness of a few μm. This type of multi-layer film is widely used in industry and is mainly used in food packaging. For the laser transmission

Fig. 4 Left: arrangement of the films, middle: experimental setup with diode laser and clamping device and right: CAD reproduction of the experimental setup including laser beam

welding process, the polymer films are positioned in an overlap arrangement so that PE is centered against PE. The joining pressure is applied on the upper side by a glass plate which is transparent to the laser beam. A sapphire glass is used as base. The more expensive sapphire glass plate is used to have the opportunity to measure the temperature while the welding process for further investigations. The focused laser beam propagates vertically from above into the experimental setup and is moved with an *XY* axis system along the desired contour.

To investigate the influence of the distance between the laser beam shaping optics and the material surface, modular laser optics is used. This laser optics can be modified in four steps to realize distances of 100, 200, 300 and 400 mm between optic and polymer film surface (see Fig. 5).

To reach these configurations, a change of different lenses is necessary. This exchange of the lenses also changes the overall transmission rate of the optics. In order to compensate this issue, a power measurement is performed for all laser optic variants, and the highest common power value is determined. This is 64 W at the workpiece surface and will be used in the following for the entire investigations as common and constant value. As already explained under fundamentals, the different configurations result in different beam caustics. These are visualized in Fig. 6 using a raytracing program.

It can be clearly seen with increasing focal length, on the one hand, the minimum beam diameter increases, and on the other hand, the divergence angle decreases. The right diagram also shows that the relative intensity distribution in the focus area changes with the focal length. If the focal length increases, the maximum relative intensity decreases and the width of the Gaussian curve increases.

4 Results and Discussion

Welding tests are now being carried out with the introduced experimental setup. The feed rate is varied with a constant optical power of 64 W. The welding process is carried out with the experimental setup. The entire process window is imaged, from the first slight adhesion to the first damage to the outer film layers. For evaluation,

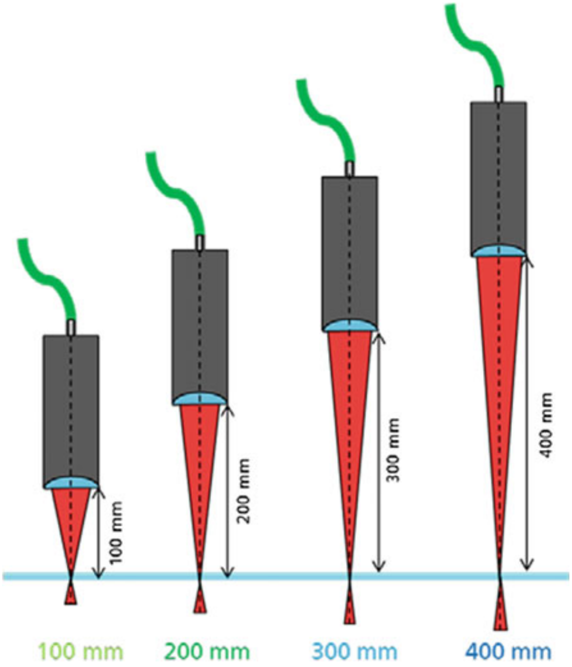

Fig. 5 Possible optical configurations in four steps

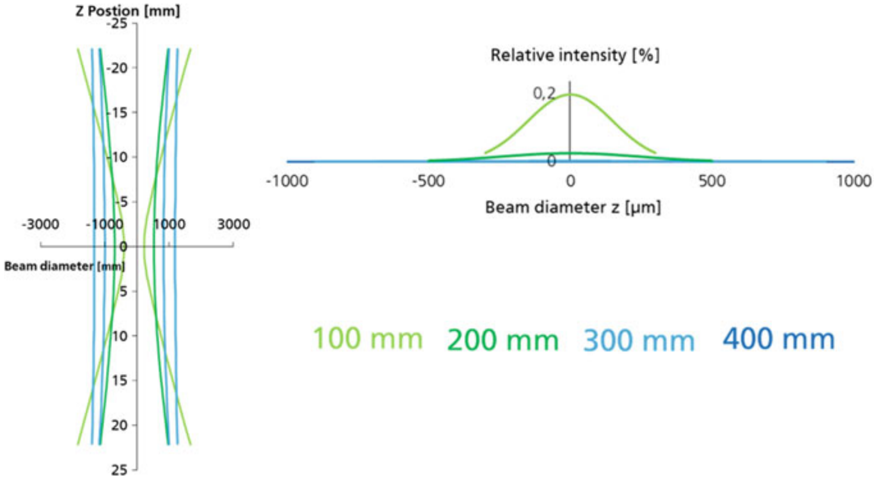

Fig. 6 Beam caustics and intensity distributions depending simulated with a raytracing approach

the samples are viewed from above with a light microscope, and cross section is performed which is analyzed by using a polarized microscope. This gives the opportunity to examine the heat-affected zone (HAZ) and also the weld seam width in detail (Figs. 7, 8, 9 and 10).

Already in the top view (graphic 7–11), it is clearly visible that the seam width increases as expected with increasing working distance. Furthermore, an increase in width can be observed when the feed rate is reduced. This can be traced back to the fact that the amount of the irradiated optical laser power remains the same and only acts over a larger area. This, however, reduces the power density, which in turn results in a longer interaction time required to achieve the necessary melting temperature in the polymer. Thin sections of the samples also reflect this. The entire process area is also well illustrated here.

For further analysis, tensile tests according to DIN EN 55529 T-Peel standard are carried out and the maximum peel forces evaluated. For each point, ten samples are evaluated (see Fig. 11).

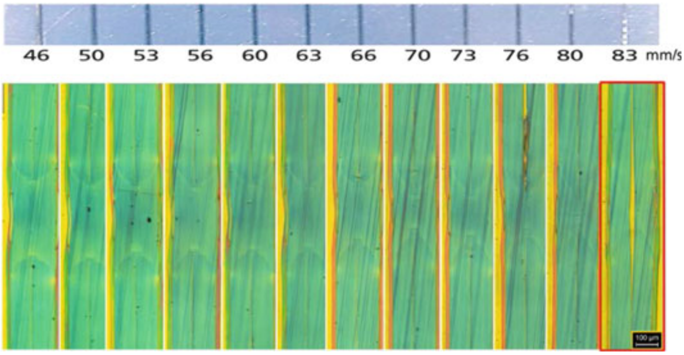

Fig. 7 Laser optics design—focal length (PET12/PE90, 64 W, 100 mm)

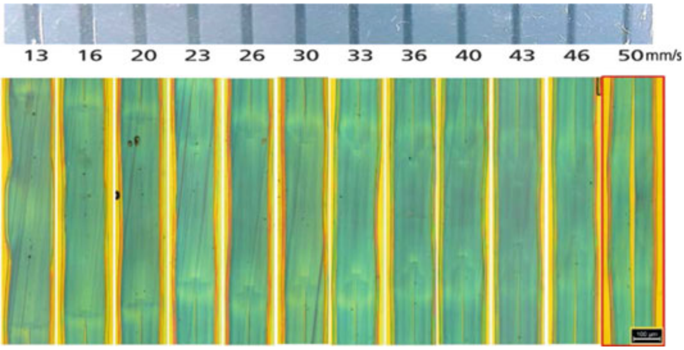

Fig. 8 Laser optics design—focal length (PET12/PE90, 64 W, 200 mm)

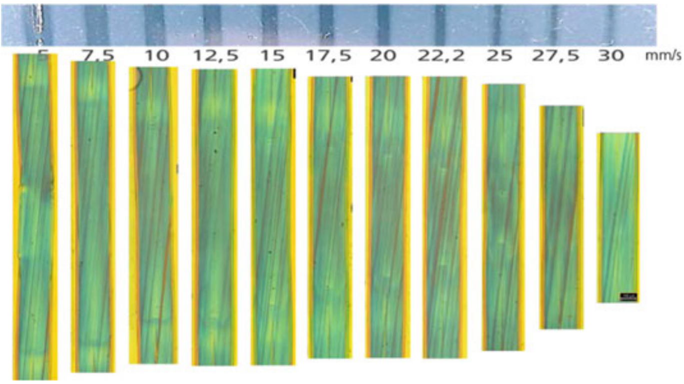

Fig. 9 Laser optics design—focal length (PET12/PE90, 64 W, 300 mm)

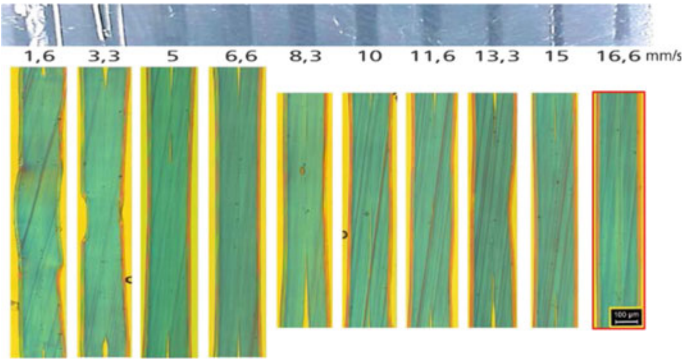

Fig. 10 Laser optics design—focal length (PET12/PE90, 64 W, 400 mm)

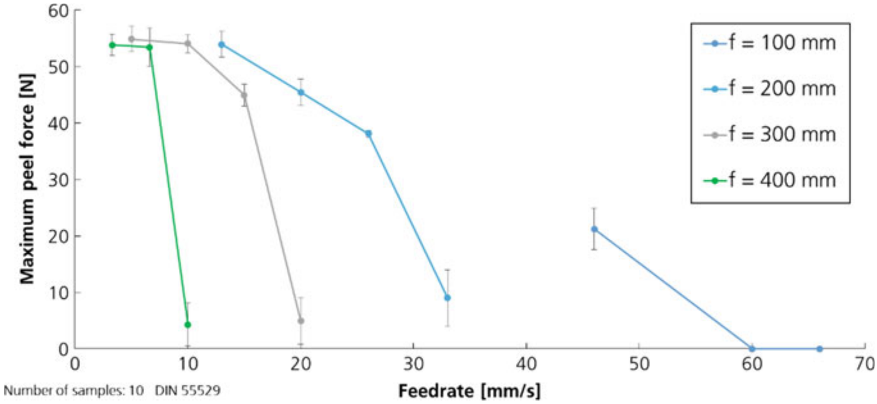

Fig. 11 Maximal peel force of investigated samples

The maximum peel forces achieved with the laser optic configurations of 200, 300 and 400 mm are all in the range of 50–60 N. The connection can therefore be classified as fixed. The maximum peel forces achieved with the laser optic configuration of 100 mm with 22 N are significantly lower than with the other configurations. As the feed rate increases, the maximum peel force decreases. While in the 300 and 400 configurations the decrease takes place over a similar feed rate range, this range is much more pronounced in the 200 mm configuration.

If typical influencing factors of a real process are considered, such as feed rate fluctuations, it can be seen that the 300 and 400 configurations, in particular, show a plateau. In this range, the feed rate can fluctuate without affecting the strength of the joint. On the other hand, a feed rate change in the 200 configuration leads directly to a change in the maximum strength.

If, on the other hand, it is desired to achieve a high as possible process speed, it becomes clear that a 400 configuration can achieve high maximum strengths and safety with regard to feed rate fluctuations, but that the feed rate is very low at 5 mm/s. In addition, only a very wide weld seam is possible cf. Fig. 10. Therefore, the use of a 200 laser optic configuration would be recommended, since the same maximum strengths can be achieved with 18 mm/s and a smaller weld seam width.

5 Conclusion

The investigated laser optics offers the possibility to react flexibly to different requirements of tool design and process control. For example, if a wide weld seam or a certain (large) minimum working distance to the foil surface is desired, as may be required for 3D-formed components, a long focal length optical configuration can be used. If, on the other hand, narrow joining seams are desired, the use of a short focal length configuration is the best solution. The physical interrelationships also mean that narrow seams with large working distances are technically only possible to a limited extent. The maximum peel forces achieved in three of the laser optic configurations investigated are at a similarly high level, but differ in the required feed rate. In summary, it can be said that, depending on the desired target size, compromises have to be made for other parameters. Therefore, it is necessary to first weight the requirements and then optimize them in the direction of the parameter with the highest weighting.

Acknowledgements Our thanks go to R. Jänchen from Fraunhofer Institute for Process Engineering and Packaging IVV Dresden, Germany, for providing the cross sections.

This IGF Project 19458 BG of the IVLV/DVS was supported via AiF within the program for promoting the Industrial Collective Research (IGF) of the German Ministry of Economic Affairs and Energy (BMWi), based on a resolution of the German Parliament.

References

1. Aden, M.: Influence of the laser-beam distribution on the seam dimensions for laser-transmission welding: a simulative approach. Laser Manufacturing. Springer Science + Business Media, New York (2016)
2. Brosda, M., Mamuschkin, V., Olowinsky, A.: Laserwelding of transparent polymer films. In: Proceedings LiM. Munich, Germany (2015)
3. Klein, R.: Laserwelding of Plastics, Wiley-VCH (2012)
4. Brosda, M., Mamuschkin, V., Olowinsky, A.: Laserwelding of transparent polymer films. In: Proceedings LiM 2015. Munich, Germany (2015)
5. Roesner, A., Abels, P., Olowinsky, A., Matsuo, N., Hin, S.: Absorber-free laser beam welding of transparent thermoplastics. In: Congress Proceedings: 27th International Congress on Applications of Lasers and Electronics Optics (ICALEO). Anaheim, USA (2008)
6. Devrient, M., Frick, T., Schmidt, M.: Laser transmission welding of optical transparent thermoplastics. In: Physics Procedia, vol. 12 (part A) (2011)
7. Brosda, M., Nguyen, P., Olowinsky, A., Gillner, A.: Analysis of the interaction process during laser transmission welding of multilayer polymer films with adapted laser wavelength by numerical simulation and thermography. In: Congress Proceedings: International Congress on Applications of Lasers and Electronics Optics (ICALEO). Orlando, USA (2019)

Connected, Digitalized Welding Production—Secure, Ubiquitous Utilization of Data Across Process Layers

S. Mann, J. Pennekamp, T. Brockhoff, A. Farhang, M. Pourbafrani, L. Oster, M. S. Uysal, R. Sharma, U. Reisgen, K. Wehrle and W. M. P. van der Aalst

Abstract A connected, digitalized welding production unlocks vast and dynamic potentials: from improving state-of-the-art welding to new business models in production. For this reason, offering frameworks, which are capable of addressing multiple layers of applications on the one hand and providing means of data security and privacy for ubiquitous dataflows on the other hand, is an important step to enable the envisioned advances. In this context, welding production has been introduced from the perspective of interlaced process layers connecting information sources across various entities. Each layer has its own distinct challenges from both a process view and a data perspective. Besides, investigating each layer promises to reveal insight into (currently unknown) process interconnections. This approach has been substantiated by methods for data security and privacy to draw a line between secure handling of data and the need of trustworthy dealing with sensitive data among different parties and therefore partners. In conclusion, the welding production has to develop itself from an accumulation of local and isolated data sources toward a secure industrial collaboration in an Internet of Production.

Keywords Welding production · Industrie 4.0 · Internet of Production · Data security · Data privacy

1 Introduction

Utilization of connected information sources has led to a paradigm shift in value chains and society, especially since the beginning of digitalization, but is not yet fully established in the industrial context. Initiatives, such as “Made in China 2015”

S. Mann (✉) · L. Oster · R. Sharma · U. Reisgen
Welding and Joining Institute (ISF), RWTH Aachen University, Aachen, Germany
e-mail: mann@isf.rwth-aachen.de

J. Pennekamp · K. Wehrle
Communication and Distributed Systems (COMSYS), RWTH Aachen University, Aachen, Germany

T. Brockhoff · A. Farhang · M. Pourbafrani · M. S. Uysal · W. M. P. van der Aalst
Process and Data Science Group (PADS), RWTH Aachen University, Aachen, Germany

L. F. M. da Silva et al. (eds.), *Advanced Joining Processes*,
Advanced Structured Materials 125, https://doi.org/10.1007/978-981-15-2957-3_8

from China, “Industrie 4.0” from Germany, or the “Industrial Internet Consortium” from the USA, are recent efforts to deliberately access and utilize information sources in industrial environments [1]. Corresponding concepts and platforms emerge therefore also in the field of production technology [2–6] and thus welding technology [7], but are difficult to implement comprehensively. Practical difficulties arise as soon as different subsystems, competencies, and parties join in a network of various information providers and stakeholders [8]. These challenges end up in confusion of different timescales in which data are acquired and required as well as in security and privacy concerns. Even though welding production is far from being fully digitalized, significant parts of measurable information are already available in forms of accessible data sources in the established welding production, e.g., in digital testing or welding process data. However, these data sources lack extensive networking while offering huge potential in improving welding production [7].

Core terms of connected, digitalized production systems in the sense of Industrie 4.0 are *cyber-physical systems (CPS)* and their interactions in *cyber-physical production systems (CPPS)* [9, 10], *vertical and horizontal networking* [3], *data analytics* [2], and *digital engineering* [11]. These elements are characteristic in connecting mechatronic systems to a connected infrastructure (CPS, CPPS), providing information across different levels of industrial production (vertical and horizontal networking), aggregating and interpreting data (data analytics), and providing a digital representation of real production systems (digital engineering).

In this work, potentials and methods shall be described, which utilize the networking of the established welding production among different entities. These potentials are discussed in the context of data security and privacy to ensure industrial application apart from secure, scientific boundary conditions. Deliberate attention given to data security and privacy provides the prerequisite to access extensive data sources that provide knowledge on the analyzed industrial production. This approach is mandatory for research in data-driven digital engineering. The foundation of this work lays in the understanding of welding production as a collection of different interlaced process layers to resolve the aforementioned potentials and challenges. This work does not focus on the welding process itself in the meaning of actual fusion of two workpieces since this part has already been subject to different studies [7] but rather in its superimposed process layers, namely weld seam process layer, assembly process layer, and product process layer.

2 Process Overview

Welding technology and its production environment should first of all be considered in their fundamental essence—and thus as a process. The classical welding process technology understands itself as the actual physical process of permanently joining two joining partners under the influence of pressure and/or heat. The welding process itself, however, is dependent on the process of the workpiece design in which the mechanical–technological requirements of the weld seam are defined. Following the welding process, the quality inspection and thus the assurance of the previously set requirement profile are found especially in the regulated welding production. Welding production in its industrial application is, yet, often part of a chain of other subprocesses such as machining or quality assurance. The focus is therefore no longer on the weld seam itself, but rather on the assembly. Within an even larger distance, the welding process is part of a product and part of the interaction between suppliers, production, service providers, and customers.

Current applications and concepts under the terms Internet of Production [12] or Industrie 4.0 often do not distinguish between these layers although they have essential peculiarities in the context of welding technology. The term “Internet of Production,” in general, describes the vision to establish an interconnected network for the production domain to utilize information across organizational borders and potentially, even across domains. A connected digitalized welding production opens up new potential in all process layers involved; however, continuous networking can only be achieved if all networked parties and competencies can communicate securely and accountable. Similar advances are also pursued for other production processes (e.g., stamping [13]).

Characteristic are the different time periods in which the respective process layers provide information (Fig. 1, left). Occurrences that have a significant influence on the quality of the weld seam can take place in the order of milliseconds, while the interaction between suppliers, production, and customers can reach multiple days. The distinction between different timescales has a particular effect on the technical requirements of networked systems w.r.t. latency, data volumes, and connectivity. Therefore, the methods for recording the respective processes differ considerably. Nonetheless, the data processing methods can be transferred to a large extent. Each process can be described by a sequence of different states that allow interpretation and ultimately process control in its common consideration.

Another representative challenge is the parties involved in the production process (Fig. 1, right). The welding process itself, and thus the weld seam, lies in the area of conflict between the technical requirements of the design and the downstream

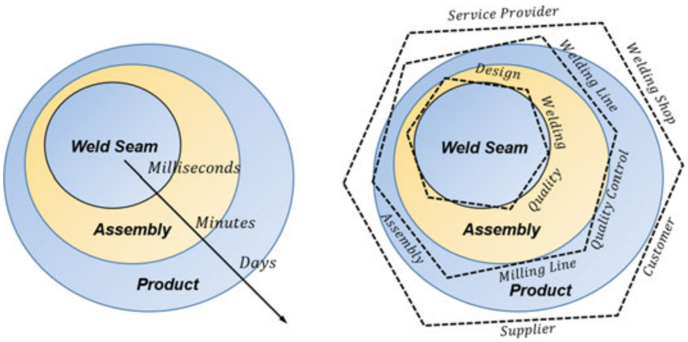

Fig. 1 A visualization of the different process layers of welding: the three process durations (left) range from milliseconds to days and the involved parties (right) differ with each layer

quality monitoring. As soon as the use of information across all parties is reliably guaranteed in accordance with the idea of Industrie 4.0 or an Internet of Production [7, 12], the question of responsibility and information security must inevitably be asked and answered. Especially when company borders are crossed as part of data exchanges, data security is a crucial aspect to protect sensitive business expertise and to protect the company's assets [8]. This paper only considers sensitive process data in the context of a welding production process and leaves the analysis of privacy implications of the workforce for future work.

In the following, technical potentials and methods are described for three process layers that motivate networking across all involved parties. In addition, however, decisive methods are presented that create the important basis for the possibilities described above in the sense of responsibilities, data security, and data protection.

3 Weld Seam Process Layer

On the lowest level, the weld seam process itself is described. Figure 2 visualizes three typical process steps that evolve around the weld seam and the essential form in which information on the substeps is available. First, the welding procedure specification (WPS) provides a defined requirement profile for all critical welding parameters (Fig. 2, upper bar). The WPS thus defines the mechanically technological weld seam properties and specifies the corresponding parameter spaces for the welding process. This step is followed by the actual welding process (Fig. 2, middle bar), which can be mapped using transient process data. The inspection of the weld seam with

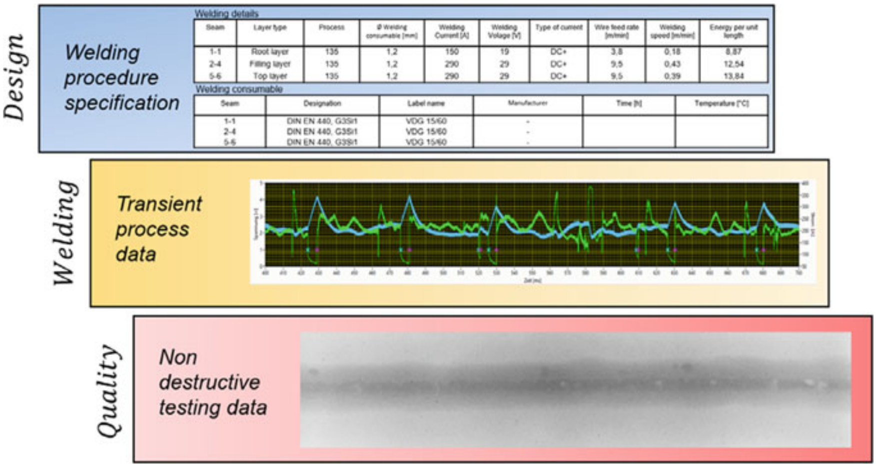

Welding details

Seam	Layer type	Process	Ø Welding consumable [mm]	Welding Current [A]	Welding Volage [V]	Type of current	Wire feed rate [m/min]	Welding speed [m/min]	Energy per unit length
1-1	Root layer	135	1,2	150	19	DC+	3,8	0,18	8,87
2-4	Filling layer	135	1,2	290	29	DC+	9,5	0,43	12,54
5-6	Top layer	135	1,2	290	29	DC+	9,5	0,39	13,84

Welding consumable

Seam	Designation	Label name	Manufacturer	Time [h]	Temperature [°C]
1-1	DIN EN 440, G3Si1	VDG 15/60	-		
2-4	DIN EN 440, G3Si1	VDG 15/60	-		
5-6	DIN EN 440, G3Si1	VDG 15/60	-		

Fig. 2 Weld seam process consists of three different substeps: (i) The requirements are set as part of the *Design*, (ii) the welding process is monitored as part of the *Welding*, and (iii) the result is tested as part of the *Quality* component

regard to its mechanical and technological properties is subsequently carried out in quality testing (Fig. 2, lower bar). Here, an example of a digitized X-ray is shown. This approach preserves the workpiece on the one hand and can store data in the form of digital images on the other hand. All described process steps can be linked as described in the following to gain a decisive added value. However, given that these three process steps are often assigned to different operational responsibilities, the issue of data security is already relevant to the lowest level of the production process.

3.1 Applications and Methods

The very basic type of data acquisition in arc welding is the transient recording of the electrical welding parameters, such as voltage and current. Those parameters need to be measured with a high sample rate (>50 kHz) as arc welding processes and GMA welding in particular are highly dynamic processes. A GMA welding process is presented in Fig. 3.

As the droplet detachment happens within a very short period of time, an evaluation of the process quality, as well as the detection of weld defects via the electrical signals, generates a high amount of time series data, which is hard to analyze in real time. The measurement data can be acquired using an industrial computer. Other very important welding parameters are, for example, the welding speed or the contact tip to workpiece distance of the welding torch. As those parameters are not changing rapidly, the data acquisition can be conducted with a significantly lower sample rate.

The example shows that for data mining in welding processes, different sets of time series data, acquired with different sample rates, need to be aggregated, labeled,

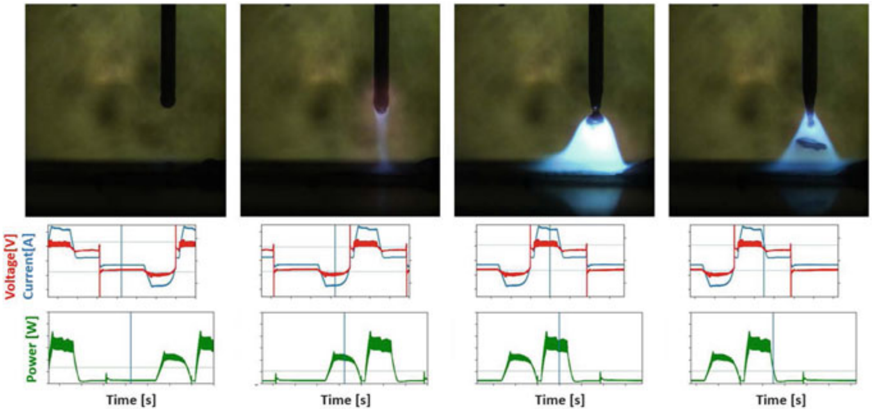

Fig. 3 GMA-AC process droplet detachment: The topside pictures show high-speed images of the process, and the bottom-side pictures detail the acquired electrical signals

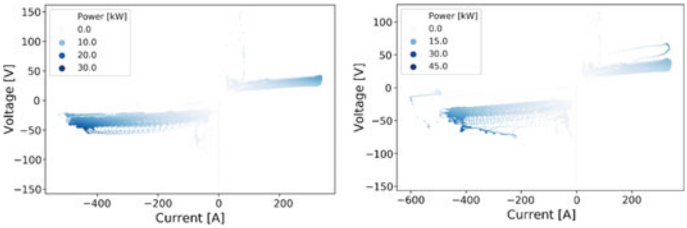

Fig. 4 Visualization of a GMA-AC welding process by plotting the process voltage over process current. The process power is indicated by the color intensity. Left: stable process, right: unstable process, followed by weld defects

and reduced to handable sizes. One possibility of analyzing the time series data may be the shape analysis of three-dimensional voltage–current process window as shown in Fig. 4.

Besides, Fig. 4 shows a possible visualization of a GMA weldment by plotting the transient current measurements over the voltage measurements. At the same time, the calculated process power is indicated by the color intensity. The analysis of the time signal could be reduced by extracting features out of the shape of the correlated voltage–current plot. This approach can give the possibility of describing a weldment by discrete features, aggregated out of a time series signal. The right side of Fig. 4 shows a weldment, which was followed by a formation of weld defects. By performing a simple cluster analysis, critical clusters can be identified, and the process can be quantified regarding the amount of data points that belong to a cluster, characterized by an increased chance of weld defects. Thereby the time series measurement of a welding process, recorded with a high sample rate, can be reduced to a simple set of quality key numbers to characterize the process. At that point, a compliance check with the defined WPS data may already hint to undue deviations.

To evaluate the acquired electric signal data and linking it to the weld seam quality, destructive as well as non-destructive testing is essential to generate a valid training dataset. For the initial generation of a usable dataset, the electrical welding data need to be linked to a quality criterion, generated by weld seam testing. The respective approach can be destructive testing, such as cross sections, as well as non-destructive tests, such as offline ultrasonic tests or online eddy current sensors. Here, anomalies in the electrical sensor signals may give a hint to possible weld defects. Destructive analysis can be conducted by taking cross sections of the weld seams. Automated image analysis can be used to extract features, such as penetration depth, aspect ratio, width and curvature of the weld seam, and the heat-affected zone, as illustrated in Fig. 5.

These tests are used to identify weld defects and therefore critical process parameter fields. Based on this information, labels can be generated for the clusters of the acquired electrical time series data. Similarly, every production step within the process chain emits data, which can be aggregated to a superordinate feature-based

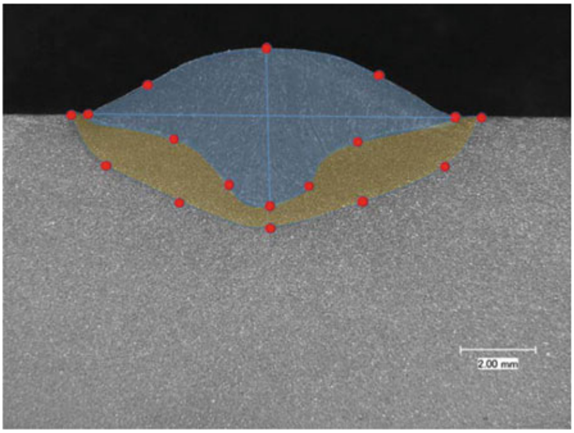

Fig. 5 Example of an automated feature extraction on a cross section. Features, such as penetration depth or weld seam width, can be used for labeling welding data

dataset, independent of the initial data types. As an aggregated dataset of the production process has been generated, predictive algorithms can be applied to investigate the influence of parameter changes to the efficiency of the process chain.

3.2 Data Security and Data Privacy

The three different substeps of the weld seam process are expected to exchange more information in the future. Consequentially, aspects of data security arise. This challenge is not only limited to company-internal scenarios where information is exchanged between departments as it is especially relevant in scenarios where substeps are outsourced to external parties, i.e., sensitive process information has to cross company borders multiple times [8]. As the data contain much detailed process information, external parties might obtain a deeper insight into the welding process. For example, the processed material or the area of application can be leaked. This scenario is further discussed as part of the product process layer.

In the context of interconnecting the three substeps of a weld seam process (design, welding, and quality), the previously described advances are already expected, based on data sharing between departments. However, concerns regarding accountability by the different departments challenge any adjustments of the process as departments do not want to be held responsible for issues resulting from improper data sharing or the underlying data quality. Hence, mechanisms must be in place to enable verifiability of the data exchanges and data retrieval in situations where deviations from the final workpiece occurred. For this layer, the requirements are less strict because usually no external parties are involved. Hence, each company internally has to agree how to implement accountability and determine the level of security which the respective implementation has to achieve. With such an approach in place, the weld seam process can be improved by utilizing data from other substeps to adjust production in the current substep accordingly without fearing blame or uncertainty in case of production errors.

Following the low-level analysis of the weld seam process layer with detailed process knowledge, the assembly process layer is analyzed in the next section to gain insight into the impact of an IoP-enabled assembly process layer.

4 Assembly Process Layer

The second introduced layer consists of the assembly process. Figure 6 describes the workpiece flow of a corresponding assembly process over different departments and individual steps until the assembly is finalized. All steps are defined according to operational departments and responsibilities with regard to their competence limits. The flow of information follows the workpieces to the assembly and is described by events. In addition to the quality optimization of the weld seam described before, process transparency and optimization are becoming increasingly important at this level. However, the challenges not only result from recording the corresponding events and corresponding workpieces, but also in the interfaces between the various competence limits.

4.1 Applications and Methods

At this process layer, data in form of event logs is put in the spotlight. Event logs are, in their simplest form, composed of case IDs (e.g., for weld seams, workpieces), events, which describe decisive occurrences during production and their according

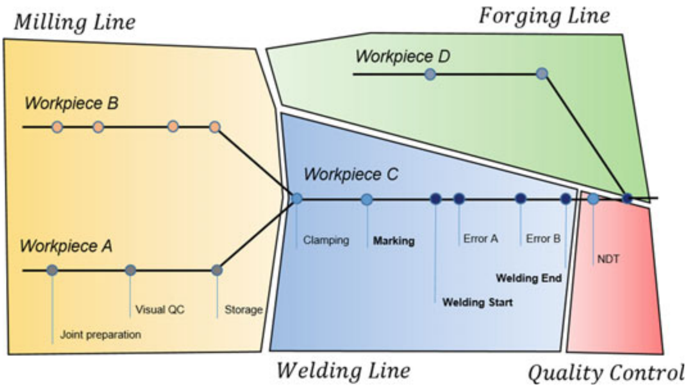

Fig. 6 Assembly process maps the workpiece flow to all departments (e.g., milling-, forging-, welding-line and quality control) that are involved during production from start to end

time stamp. This form of data opens up the door to process mining, which may not only be applied in this process layer but even in others due to its universal applications.

Process mining is a young research field which discovers, monitors, and improves real processes by applying techniques utilized to extract knowledge from so-called *event logs*. Basically, three fundamental types of process mining techniques exist: process discovery, conformance checking, and process enhancement [14], as presented in Fig. 7. Process discovery aims at extracting the real process models from underlying event logs, i.e., the real behavior of the processes is acquired, while conformance checking compares the observed behavior obtained from the underlying event log with the behavior recognized by the model. The goal of process enhancement is to improve the model at hand by exposing the information gathered from the event log. Discovering real processes and checking compliance between observed and allowed behavior, process mining uncovers and quantifies deviations, finds root causes for process variations and delays, and finds bottlenecks in the extracted process models. Furthermore, process mining provides the opportunity to predict process outcomes [15, 16], foresee deviations and bottlenecks, and compare processes w.r.t. various time periods, products, and organizations.

In the context of welding processes, process mining can be applied at different levels by utilizing various techniques applicable to the process layers *weld seam, assembly, and product*, as presented in Fig. 1 before. In a weld seam process, for example, operators and welding engineers specify the required parameters in the welding procedure specification which typically includes various important parameters, such as material specification (e.g., wall thickness, size/diameter, yield/tensile strength, metallurgical concerns), welding process type, welding direction, position, preheating temperature, filler, polarity, and process parameters (e.g., travel direction, polarity, wire welding transfer mode, number of passes, number of welders, and electrodes). The required parameter studies are time consuming, and revealing the relationships and correlations among the input parameter values of the welding process and the corresponding quality results is of high interest. For instance, decreasing the lapse time between passing and filling activities, and changing the number of passes may end up with better coating removal, affecting the overall quality assurance positively. Another example is to reveal the bottlenecks and failure of

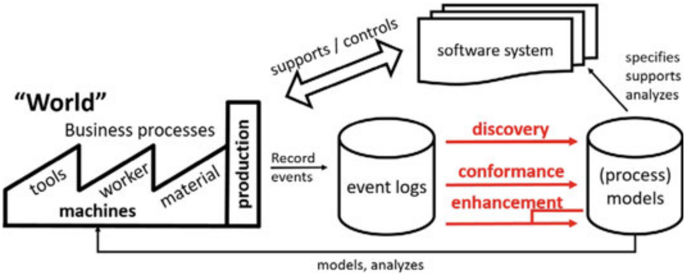

Fig. 7 Overview of the three types of process mining: process discovery, conformance checking, and process enhancement

the welding process, such as extracting the information about the circumstances (at which input parameters' values) in which the output material suffers lack of fusion and penetration, residing out of the tolerance range specified by the welding experts.

Process mining provides methods that are capable to create an integrated view of the welding production process based on data recorded in logs where each recording corresponds to an event. Each of these events comprises an activity, e.g., joint preparation for workpiece A (cf. Fig. 6), a timestamp, e.g., 15th February 2019, and optional resources, such as the worker involved in this production step. Furthermore, each event contains a unique case ID which identifies an associated case. In the context of the welding process, the assignment of case IDs might not be unique. Considering Fig. 6, on the one hand, each of the workpieces A and B might constitute its own unique case which spans its production until they are welded together yielding workpiece C. Thus, process mining would reveal models based on an independence assumption on the workpieces, therefore possibly lacking important dependencies. On the other hand, the ID of workpiece C could be used for all events related to the workpieces A and B introducing dependencies and relations between events which correspond to, until the timestamp of the event, unrelated workpieces. This relation might then distract the models from the important behavior. In this context, a hierarchical view on the process that enables investigation on different levels of granularity (workpieces A and B as different cases or summarized under the ID of workpiece C) would be an interesting opportunity.

The discovered models can further be a subject of conformance checking, i.e., a set of techniques which assess the compliance between the behavior described by the model and behavior comprised in the event log [17]. Therefore, conformance checking can be applied to discover deviations or anomalies of the production process, thus contributing to its transparency and efficiency.

Process comparison Any important characteristic of the underlying processes can be considered as an individual dimension for the process comparisons. In the context of welding production processes, there are different aspects, such as products, time, and resources. Based on these dimensions, a welding process cube can be built whose structure is similar to that of the Online Analytical Processing (OLAP). In a process cube, events are organized by using different dimensions [18]. The cells of a process cube can be analyzed by using different process mining techniques. Slicing and dicing are common operations in process cubes [18]. By slicing based on resources, the events related to a specific resource are removed. By dicing based on resource and time, the activities associated with a specific resource in the particular duration are filtered. Using correlation methods in different slices and dices allows companies to find correlations between the workload and performance. The comparison of these correlations in different slices and dices can provide beneficial information for process owners and engineers. This approach enables investigations of the effect of the workload on production performance of a specific user and also investigations of the impact of the workload on the performance of all users. This investigation can be performed in different slices or dices of the cube, depending on the focus.

Moreover, process mining may provide tools for detecting and monitoring changes in the assembly process termed *concept drift*. Aside from *concept drift* detection on the control flow level [19, 20], process specific attributes can also be incorporated [21] to gain insight into the assembly process development exploiting welding specific domain knowledge. This may further be a starting point for a following analysis, e.g., regarding causality detection or inter-process/intra-process comparison.

4.2 Data Security and Data Privacy

The field of responsible data science is concerned with the different issues regarding publishing, accessing, and using data in data science techniques. Process mining as a set of techniques that directly deals with the data of the organizations should also address these concerns. The information on the level of events including the resource information should be secured in a way that only responsible people would be able to access and perform analysis while preserving security and privacy issues. Recently, a general framework has been proposed [22] which ensures confidentiality in process mining techniques. In production processes, different stakeholders and levels of the event information, e.g., human resources working on the production processes, machines, and sensors, exist.

The framework shown in Fig. 8 provides the confidentiality in process mining techniques, especially in the context of our focus, i.e., production process. This framework can be customized in the production process context. Two (internal and

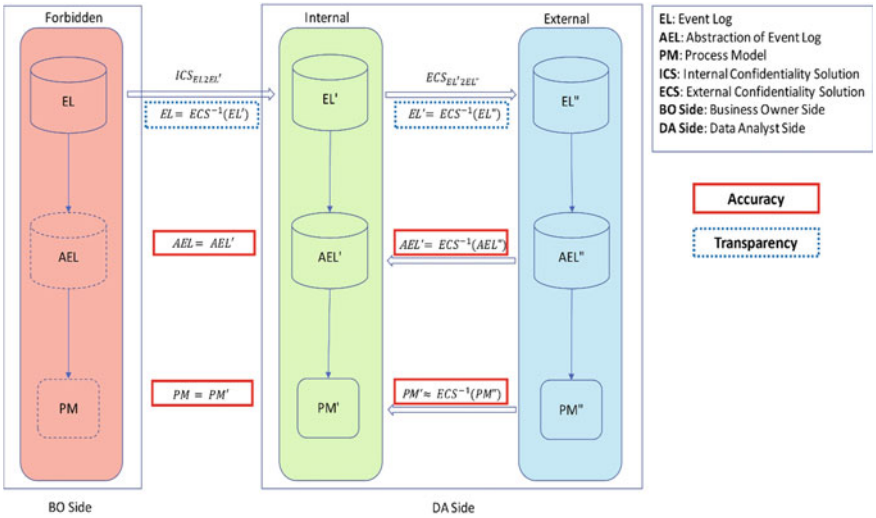

Fig. 8 Framework for confidentiality in process mining protects sensitive information during the analysis [22]

external) confidentiality solutions along with three different environments, namely the forbidden, internal, and external environment, exist. Therefore, event logs can be transformed using the abstraction technique. Moreover, based on the different users in different environments, either of the internal and external confidentiality solutions can be used.

Regardless of such a solution, all involved parties can also agree to collaboratively analyze the process. Unfortunately, sharing their process data can reveal a lot of inside information with other stakeholders. However, given that the different parties are (at least partially) in existing business relationships, a certain level of trust is already established. As an alternative, they can also appoint a trusted third party to conduct the analysis for them. From a security perspective, both of these approaches introduce at least a single point which has access to all data, i.e., a valuable target for data theft. Hence, process mining solutions which provide confidentiality are more beneficial in this context. Analyzing the process data without exchanging it is not a realistic option as most advances can only be achieved by collaboration between the different entities of the assembly process. Otherwise, changes to the process can only be implemented locally with a limited impact on the overall assembly layer.

Similar to the weld seam layer, the assembly layer also deals with internal departments in most cases. While an outsourcing of substeps to external parties is a potential future development for these two layers, it is already a reality in the context of the overall product process. Consequentially, as a next step we analyze this layer in the context of digitalized welding production. All security findings can also be applied to the previous two layers when external parties are involved.

5 Product Process Layer

The third layer defines the overall product process. Figure 9 describes the respective movement of different products from involved parties to a final good from the

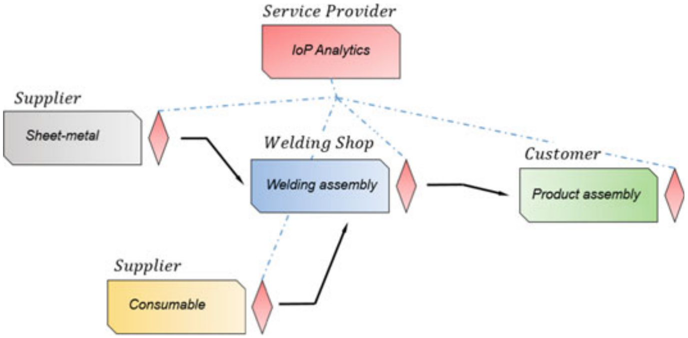

Fig. 9 Product process entails different parties (supplier, welding shop, service provider, and customer) and their products until the final good is produced

welding production point of view. In addition to the established interconnection of suppliers and customers, the IoP service provider also stands out, which will play an increasingly important role in a connected, digitalized welding production. The borders of different companies reveal the issues of data security and privacy more prominently than before. Nevertheless, the envisioned potential of data exchanges should make up for most of the associated risks as outlined in the following, i.e., the benefits should outweigh the risks perceived by the different companies. The flow of information follows the produced products. However, the result may be added value for any involved party due to insight gained at another party.

5.1 Applications and Methods

The concept of networked product quality was introduced [7] to show which information sources can be used directly to describe product quality in the context of welding. An essential component here is the acquisition of welding process data, but also the integration of decisive boundary conditions such as information about the workpiece material. The latter information is available to the supplier, but is not part of the inherent process data acquisition in welding production. If this information is utilized in the sense of the networked product quality, the welding shop is dependent on limited quality certificates on arrival or in need of dedicated in-house material analysis. In this context, accessing inherent process data from the material supplier directly in welding production is significantly more useful. The casting production is working toward comprehensive simulation and monitoring of the material microstructure [23, 24] which is a crucial property for welding. The competences and process data for extracting microstructural information of individual workpieces are therefore located at the production site rather than at the welding production. Nevertheless, knowledge about where and how microstructural properties are distributed in a casted workpiece is mandatory for successful welding. Adding spatially resolved data to the workpiece would eventually reduce testing efforts to find specific parameter settings and the overall weld quality.

Besides, in the interest of the welding shop customer, newly added value is opened up with correspondingly aggregated data on the welding assembly. The description of product quality between customer and supplier is often limited to two simple states: OK and NOK. The boundary between both states is defined by the violation of defined quality characteristics. However, as soon as the customer of the welding assembly has a reliable, higher-resolution quality description from the welding production, the products could be used more specifically according to their quality condition. Thus, assemblies that would otherwise fall below the NOK limit remain viable in less stressed products. This measure could especially benefit welding productions with an inherently high-quality fluctuation due to process uncertainties.

Apart from the established partners in welding production, a realistic assumption is that an IoP service provider will also have an increasingly important role in welding production. Cloud services for cross-location data communication are often considered a security risk in today's industry and therefore valuable data are commonly retained and processed locally [12]. If the service provider remains a pure infrastructure provider, without having access to the content of the data themselves, information security mandates properly implemented data confidentiality. However, the supported operations are limited in such a scenario and considering information from different parties is hard to achieve due to a challenging key management [8].

On the contrary, the methods described in the previous paragraphs can hardly be carried out locally by the welding manufacturer. IoP service providers and research institutions can make use of their information technology know-how as well as the corresponding powerful computing hardware, which is indispensable for data-based methods of machine learning. At this point, however, the question of how data can be abstracted to such an extent that sensitive information can be protected without decimating its content comes to the fore. The main challenge is that the value of specific process information is currently unknown as new process dependencies first have to be uncovered.

5.2 Data Security and Data Privacy

In contrast to the individual steps as discussed before, in this context, information of the manufacturing and production steps must be shared in detail to utilize further advances. Proposing a global solution is unlikely as the value of information differs between the different parties of the production process. Hence, the exact implementation must be defined depending on the use case. Furthermore, this categorization can only be made by domain experts, i.e., it requires joint efforts by computer scientists and mechanical engineers alike, to also protect intellectual properties and process know-how. Thus, the individual angles of improving the overall production process have to be analyzed in detail before abstracting too much or too little information. The access of external parties, who are part of the process, should be restricted to the minimum [25], i.e., they may only retrieve information that is required to (a) work on their subprocess and (b) improve the overall process. Respective measures must be taken to obfuscate sensitive data. Time series recordings of arc welding voltage and current can, e.g., not only tell which arc welding process is used. Such data can also describe process parameters and process variants or even reveal the deployed welding power source manufacturer.

In the future, newly collected information might become more valuable as it can be combined with a large stash of past production data [26], i.e., future data mining to improve the production process can rely on a large set of existing past process data. By integrating data sources of external parties, the significance of the available information can be further extended and improved. To still fulfill data security aspects that are mandated in today's production process, the respective information can be protected by different concepts, such as secure multiparty computation [8], secure offloading [27], privacy-preserving queries [28], or differential privacy [8]. The individual data collected during the weld seam process are utilized here again on a different level and by a larger set of different parties. Regardless, similar considerations regarding information security hold. In the following, the concepts are briefly put into perspective w.r.t. the considered welding process.

Secure multiparty computation In a setting with valuable process data that should not be shared with external parties, communication protocols based on secure multiparty computation can help to enable collaborations between distrusting parties. The general concept is to retain the input locally while the participants jointly compute a function. During the computation, no information is leaked and eventually both parties receive the result of the function. In the context of welding, participating parties could, for example, jointly compute whether offered material properties match the requirements of the weld seam process without revealing the respective properties and requirements.

Secure offloading To utilize (powerful) resources in the cloud obliviously, a welding assembly could encrypt their process data and conduct computations on the encrypted data. When designing a privacy-preserving protocol, the cloud cannot learn anything about the processed data. For example, a welding assembly can check whether they measured the same electrical subtraces in the past to then draw further conclusions about the expected quality of the weld seam. Depending on the level of established collaborations, even multiple parties could send their encrypted data to the cloud to receive the joint result. However, in this case, the cloud must be trusted to not share the input data with the other parties.

Privacy-preserving queries In scenarios with an IoP service provider, a welding assembly might be interested to receive insight into a certain welding operation without revealing the properties of the measured weld seam. Similarly, the IoP service providers want to keep their knowledge base private. In such a setting, privacy-preserving database queries can be used to allow a welding assembly to receive insights from a service provider without either party gaining access to the submitted query.

Differential privacy While individual data points are valuable from a business perspective, they might also help to identify the concrete order of a weld seam. Consequentially, parties of a product process have an incentive to hide these identifying characteristics. Differential privacy describes a concept how to protect private information in a larger set of data. After application, no private information can be identified as the data have been generalized, i.e., the individual privacy is protected. In the context of welding, process data could be processed before being handed over to the IoP service provider for further analysis.

Overall, the chosen concept depends on the concrete use case and the requirements w.r.t. information leakage. Unfortunately, the overhead for deploying them is far from negligible as they must be carefully tailored to the use case. Once approaches to improve the product process are widely established and collaborating with external parties is a usual part of production, further advances can be implemented by collaborating securely even with entities that have no direct influence on the production process [8] (this situation is not yet captured in Fig. 8). An easy approach is to rely on the IoP service provider to link the product processes of different welding-related processes with the previously considered welding process. However, such advances require trust into both the intermediate party and the utilized data sources underlying any propositions to improve the process.

6 Conclusion

Envisioned by advances, such as Industrie 4.0 or the IoP, process changes are likely to also affect the production of welding workpieces. In particular, companies hope to realize process improvements by connecting digitalized welding processes to utilize ubiquitous data securely even across entities. In this work, several applications have been presented which motivate to connect well-established welding production entities among different process layers while taking into account aspects of data security and privacy.

Weld seam process layer The connection of transient welding process data with testing data can be utilized to learn how to preemptively detect weld defects and improve the overall weld quality. In addition, simple compliance checks can be introduced by including WPS parameters to mentioned data sets. As currently no company borders are overstepped, each company internally has to agree how to implement accountability and determine the level of security the respective implementation has to achieve.

Assembly process layer The data shape of event logs has been introduced, opening up the door to process mining. Three established techniques, namely process discovery, conformance, and enhancement, have been described in the context of welding production to model, analyze, and improve corresponding processes. These methods are nevertheless not only applicable to the assembly process layer but even to other processes, describing their universal character. Security and privacy concerns have been addressed with a framework for confidentiality in process mining. This framework allows the secure access to event logs of data analysts by means of anonymizing and encryption without violating the privacy of the production site.

Product process layer Several use cases of interlinking data among different entities, here even companies, have been described, motivating advantages for each party involved. As security and privacy concerns rise especially to the fore, deliberate methods, namely secure multiparty computation, secure offloading, privacy-preserving queries and differential privacy, have been showcased.

Overall, an interconnection of different entities who are part of the production process can help to realize the envisioned welding advances in manifold ways. The structure of process layers is oriented toward the established welding production and prepares therefore the deliberate utilization of diverse information sources without confusing different applications and their stakeholders. To this end, the production landscape has to shift from a setting with locally retained data silos to a scenario with secure industrial collaboration as part of an Internet of Production.

Acknowledgements Funded by the Deutsche Forschungsgemeinschaft (DFG, German Research Foundation) under Germany's Excellence Strategy—EXC-2023 Internet of Production—390621612.

References

1. Kagermann, H., et al.: Industrie 4.0 in a Global Context: Strategies for Cooperating with International Partners. acatech STUDY, Munich (2016)
2. Jodlbauer, H.: Digitale Transformation der Wertschöpfung. Kohlhammer (2018)
3. Roth, A.: Einführung und Umsetzung von Industrie 4.0—Grundlagen, Vorgehensmodell und Use Cases aus der Praxis. Springer Gabler (2016)
4. Reinhart, G.: Handbuch Industrie 4.0. Carl Hanser Verlag (2017)
5. Schircks, A.D., et al.: Strategie für Industrie 4.0. Springer Gabler (2017)
6. Vogel-Heuser, B., et al.: Handbuch Industrie 4.0 Band 1. Springer Vieweg (2017)
7. Reisgen, U., et al.: Connected, digitalized welding production—Industrie 4.0 in gas metal arc welding. Weld. World **63**, 1121–1131 (2019). https://doi.org/10.1007/s40194-019-00723-2
8. Pennekamp, J., et al.: Dataflow challenges in an internet of production: a security & privacy perspective. In: ACM CPS-SPC (2019). https://doi.org/10.1145/3338499.3357357
9. DIN/DKE: Deutsche Normungs-Roadmap Industrie 4.0 (2015)
10. Pfeiffer, S.: Industrie 4.0 und die Digitalisierung der Produktion—Hype oder Megatrend. Aus Politik Zeitgeschichte 31–32 (2015)
11. WGP: WGP-Standpunkt Industrie 4.0. Wissenschaftliche Gesellschaft für Produktionstechnik (2016)
12. Pennekamp, J., et al.: Towards an infrastructure enabling the internet of production. In: IEEE ICPS (2019). https://doi.org/10.1109/ICPHYS.2019.8780276
13. Bergs, T., et al.: Stamping process modelling in an internet of production. In: CIRP TESConf (2019)
14. van der Aalst, W.M.P.: Data science in action. In: Process Mining, 2nd edn. Springer-Verlag, Berlin (2016)
15. Pourbafrani, M., et al.: Scenario-based prediction of business processes using system dynamics. In: On The Move to Meaningful Internet Systems, International Conference on Cooperative Information Systems (CoopIS 2019), vol. 11877, Lecture Notes in Computer Science, pp. 422–439 (2019)
16. Pourbafrani, M., et al.: Supporting decisions in production line processes by combining process mining and system dynamics. In: Intelligent Human Systems Integration 2020. Proceedings of the 3rd International Conference on Intelligent Human Systems Integration (IHSI 2020): Integrating People and Intelligent Systems, pp. 461–467 (2020)
17. van der Aalst, W.M.P., et al.: Replaying history on process models for conformance checking and performance analysis. Wiley Interdiscip. Rev. Data Min. Knowl. Discov. **2**(2), 182–192 (2012)
18. van der Aalst, W.M.P.: Process cubes: slicing, dicing, rolling up and drilling down event data for process mining. In: Song, M., Wynn, M.T., Liu, J. (eds.) Asia Pacific Business Process Management: First Asia Pacific Conference, AP-BPM 2013, Beijing, China, August 29–30, 2013. Selected Papers, pp. 1–22. Springer International Publishing, Cham (2013)

19. Jagadeesh Chandra Bose, R.P., et al.: Handling concept drift in process mining. In: Mouratidis, H., Rolland, C. (eds.) Advanced Information Systems Engineering, pp. 391–405. Springer Berlin Heidelberg, Berlin, Heidelberg (2011). ISBN 978-3-642-21640-4
20. Martjushev, J., et al.: Change point detection and dealing with gradual and multi-order dynamics in process mining. In: Matulevicius, R., Dumas, M. (eds.) Perspectives in Business Informatics Research. Lecture Notes in Business Information Processing, pp. 161–178. Springer, Germany (2015). ISBN 978-3-319-21914-1. https://doi.org/10.1007/978-3-319-21915-8_11
21. Hompes, B.F.A., et al.: Detecting change in processes using comparative trace clustering. In: CEUR Workshop Proceedings, vol. 1527, pp. 95–108 (2015)
22. Rafiei, M., et al.: Ensuring confidentiality in process mining. In: SIMPDA, pp. 3–17 (2018)
23. Liu, Z., et al.: Parameters determination of grain microstructure prediction for a single crystal casting simulation and its experimental validation. Int. J. Metalcast. **12**, 861 (2018). https://doi.org/10.1007/s40962-018-0220-9
24. Zhu, X., et al.: Influence of pouring methods on filling process, microstructure and mechanical properties of AZ91 Mg alloy pipe by horizontal centrifugal casting. China Foundry **15**, 196 (2018). https://doi.org/10.1007/s41230-018-7256-6
25. Pennekamp, J., et al.: Security considerations for collaborations in an industrial IoT-based lab of labs. In: IEEE GCIoT (2019)
26. Gleim, L., Bergs, T., Brecher, C., Decker, S., Lakemeyer, G., Wehrle, K., Pennekamp, J., Liebenberg, M., Buchsbaum, M., Niemietz, P., Knape, S., Epple, A., Storms, S., Trauth, D.: FactDAG: Formalizing data interoperability in an internet of production. IEEE Internet Things J, 1–1
27. Henrik, J., et al.: BLOOM: BLoom filter based oblivious outsourced matchings. BMC Med. Genomics **10**(Suppl 2) (2017). https://doi.org/10.1186/s12920-017-0277-y
28. Dahlmanns, M., et al.: Privacy-preserving remote knowledge system. In: IEEE ICNP (2019)

Adhesive Bonding

Structural Bonding of Single-Layer E-Coated Steel Structures in the Agricultural Sector

D. Estephan, S. Boehm and R. Nothhelfer-Richter

Abstract Mobile working machines usually have a welded frame structure which, due to its size, is commonly painted by spray application, which has a considerable influence on corrosion protection. An optimized corrosion protection could be achieved by electro-dip painting, but this is not economically legitimate due to the small lot sizes. This problem could be solved by shifting the joining process to the end of the process chain and using adhesive bonding technology. This means that smaller parts are dip-coated before the joining process. In order to achieve maximum corrosion protection, it is necessary not to damage the painted surface, so that only an adhesive joining process is possible. For successful implementation, it is therefore necessary to match both the adhesive system and the paint system to each other and additionally to the (steel) materials used and to qualify them with regard to the requirements. In the presented study, the main parameters of both coating properties and adhesive properties are investigated. The acrylate (AY) e-coats, which are scientifically analysed for the first time with regard to adhesiveness, showed good weather resistance, but inferior corrosion protection compared to epoxy-based (EP) e-coats. The adhesive strength of the joints has been investigated by lap shear tests. After stressing the bonds by corrosion tests (neutral salt spray, cyclic corrosion tests) and temperature changes, the failure changed in some cases from cohesive fracture of the adhesive to adhesive fracture in the coating–adhesive interface. Another critical point was detected: if the coating is injured near the bonded area, the corrosive under creepage can penetrate under the joint.

Keywords Structural bonding · Corrosion protection · Electro-coats · Adhesion · Weather resistance

---

D. Estephan (✉) · S. Boehm
Department of Cutting and Joining Manufacturing Processes, University of Kassel, Kassel, Germany
e-mail: d.estephan@uni-kassel.de

R. Nothhelfer-Richter
Fraunhofer Institute for Manufacturing Engineering and Automation IPA, Stuttgart, Germany

L. F. M. da Silva et al. (eds.), *Advanced Joining Processes*,
Advanced Structured Materials 125, https://doi.org/10.1007/978-981-15-2957-3_9

1 Introduction

In recent years, there is a great attention on the improvement of corrosion resistance of structural components. The World Corrosion Organization (WCO) estimates the annual global damage caused by corrosion at USD 2.2 trillion, which is equal to 3% of the gross domestic product [1]. According to the economic damage, an optimization of the corrosion protection is urgently necessary. To prevent corrosion of the welded frameworks of large body structures, especially in the agricultural sector, painting should be applied. The painting is performed as a wet paint or powder coating process. In the case of more complex structures with cavities and undercuts, due to the hard accessibility, an insufficient protection with the applied painting processes is expected. It is worthy to note that the cavities in these complex components are more sensitive to the corrosion initiation, and thus, they should be more protected [2].

In order to realize a complete protection, the cathodic dip coating (CDC) process is used in automotive engineering. In this process, the vehicle bodies are dipped into a bath, while the painting is carried out by electrolytic deposition. Using this method associated with a suitable pre-treatment, such as zinc phosphating [2], an efficient corrosion protection can be achieved on complex structures [3]. However, the costs of the CDC process depend on the components size, so that the process is only worthwhile for large quantities. But the chassis of mobile working machines, such as agricultural and construction machinery, in particular, are extremely larger than the bodies of passenger cars and are produced in significantly smaller quantities, so that the investment in dip coating technology is not economical for the manufacturers of these machines.

In order to enable an extended application range of the dip coating process in the field of agricultural and construction machinery, this process must become more economically attractive. One approach is to reduce the component size for the CDC process and the associated variation of the process chain. In other words, the entire body of agricultural machinery is not first joined by welding and then painted in the manufacturer's identification colour, as it was the case previously. The new idea is to first coat smaller assemblies in a dip bath and then join them to form the entire body. The dip coating of smaller assemblies implies lower investments in equipment, which makes this process more economically relevant. However, subsequent welding of the dip-coated components cannot be carried out, so that a different joining process has to be used. As an alternative to welding, adhesive bonding can be used as a joining process, as this process does not damage the coating during assembly.

Knowledge of the condition of the surfaces to be bonded is essential for adhesive bonding. This depends primarily on the paint system used. In the automotive industry, for example, car bodies are coated with a multi-layer system in order to meet the necessary requirements. For agricultural machinery, the requirements are less stringent, so that a single coat of paint is sufficient. For the approach of adhesive bonding, it is easier to deal with a single-layer coating, which additionally reduces the costs for the manufacturer. Due to their good UV stability, AY CDC coatings could be used for this purpose. Scientific studies on adhesion properties on these AY CDC systems have not yet been carried out.

Structural bonding on coated surfaces is becoming more important in the industry, as paint stripping or masking prior to bonding is expensive. Several studies on the subject of bonding to paint and single-layer EP-cathodic dip painting are available, but these are limited to paint systems and processes that are mainly used in automotive engineering. The large number of coating materials with different chemistry and different painting processes makes subsequent adhesion to these surfaces difficult without appropriate scientific investigation.

Schiel et al. [4] and Unger et al. [5] investigated adhesion properties of CDC and topcoat. Though, in this case, the adhesive was applied to a double-layer coating, instead of a single-layer coating. Such investigations on single-layer coatings do not exist yet. In combination with a preceding substrate pre-treatment in the form of zinc phosphating, this cathodic dip painting process currently offers the best corrosion protection and is state of the art in the automotive sector. It is even specified by some manufacturers as a primer coating against corrosion for steel material [6]. However, these EP-based standard CDC systems are not suitable as single-layer coatings for outdoor use, as the material is degradable by UV light, which is a major disadvantage. The components primed with EP CDC must therefore be protected with a UV-absorbing topcoat in a further painting process, which has the necessary light and weather stability. Figure 1 shows the typical coating structure in the automotive sector. Due to the multi-layer coating system, potential influencing factors such as layer thickness, paint composition and process parameters, which have a significant influence on the adhesive strength and adhesion of the individual paint layers to be achieved, are increasing [4, 7].

In addition to EP CDC, AY CDC systems are also used. Compared to EP CDC, these systems are particularly characterized by their improved UV stability. The required media resistance is also sufficient, so that they are already used in industry as single-layer coatings [8, 9]. It has applications in the agricultural and construction machinery sectors, which can produce large quantities and make the necessary investment for the systems economically reasonable [10]. This shows that AY CDC

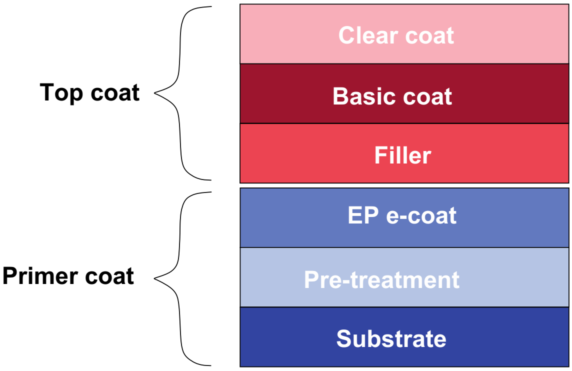

Fig. 1 Paint structure in the automotive sector

are suitable as single-layer systems. However, the suitability for adhesive joining has not yet been investigated.

In scientific papers on the subject of bonding on painted surfaces, the advantages and possibilities of bonding on topcoat are demonstrated. In Daniel et al. [11], two possibilities for bonding on topcoats are explained: bonding on cleaned and on primed topcoats. For the former, the coordination of the painting and bonding processes is essential. In the latter case, there is a certain independence from the coating system when the primer is used. That offers the possibility of unrestricted bonding to the coatings commonly used today. However, Daniel et al. also refers to a lack of scientific research on the subject of adhesion on painted surfaces.

In this work, tensile shear tests were carried out to investigate the bondability on AY CDC systems and the mechanical properties of the adhesive composites. These tests were performed both in aged and unaged condition. Subsequently, the results were compared with those of a commercially available EP CDC from corresponding tensile shear tests. In addition to the adhesiveness on painted surfaces, the adhesion of the paint to the steel substrates was also examined more closely.

2 Experiment

Agricultural machinery bodies are mainly made of simple structural steel, e.g. S235. Therefore, those steels should also be used for the investigations. The substrate thickness of 2 mm is sufficient for the substrate compliance to be negligible in the tensile shear test. Zinc phosphating is used to pre-treat the substrates before the painting process. The pre-treated steel specimens were coated with two different AY CDC coats: a blue CDC (CDC1) and a grey CDC (CDC2). The reference is a commercially available black EP CDC (reference), which is also used as a primer in automotive engineering. The selected adhesives for the joining process of the painted steel substrates differ with regard to the modulus of elasticity. The bondings were performed with 2C epoxy resin (2C-EP), 2C acrylate (2C-AY) and 2C silane-modified polymer (2C-MSP) adhesive. Before the bonding process, the surfaces of the coated specimens must be free of dust and grease, using, e.g. isopropanol.

The geometric specimen shape for the tensile shear test according to DIN EN ISO 1465 is 25×100 mm^2. The two parts are joined with an overlap length of 12.5 mm and an adhesive layer thickness of 0.5 mm that is suitable for all adhesives of the test series.

The test specimens are tested in their unaged state and after ageing. One possible ageing method is a climate change test (PV1200) from the automotive sector. This involves a four-week climate cycle (see Fig. 2), with varying humidity and temperature.

Other samples are kept in a chamber for 720 h under exposure to a neutral salt spray according to DIN EN ISO 9227. Some samples are scratched into the adjoining area of the bond so that the paint is damaged. So the adhesion properties of coating and adhesive depending on the influence of the corrosion infiltration can be

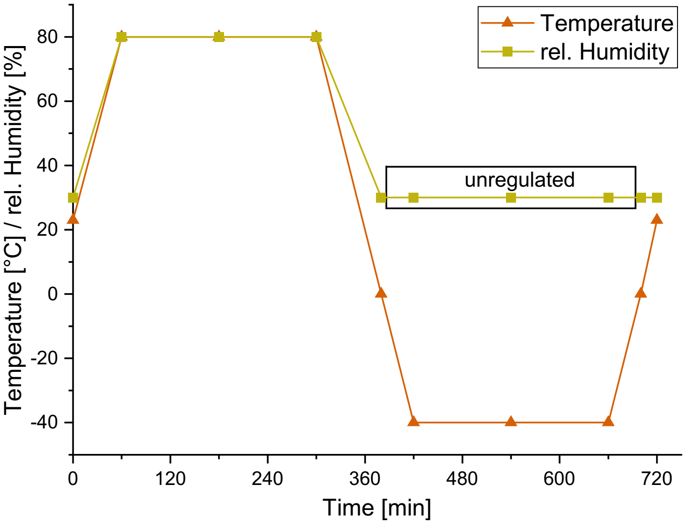

Fig. 2 Climate cycle PV1200 [according to VW PV1200]

investigated. Both the PV1200 and the salt spray test are common ageing methods in the automotive field. The third ageing method is the cyclic corrosion testing of materials and components in automotive construction according to VDA 233-102, which combines the previously mentioned tests. It consists of three different daily cycles A, B and C, as shown in Fig. 3. A test cycle consists of one week with the individual cycles as follows: B–A–C–A–B–B–A. The test duration here is 6 weeks.

It enables the simulation of practical stress in the laboratory and standardizes the test conditions for all multi-metal materials (coated and uncoated test sheets and components). Under the test conditions corrosion phenomena, such as filiform corrosion, are neither attenuated nor exaggerated and are therefore suitable as a reliable evaluation of corrosion protection. After the corresponding ageing, the test specimens are tested for tensile load according to DIN EN ISO 1465, the results are evaluated and the fracture patterns of the adhesive surfaces according to DIN EN ISO 10365 are examined. The same applies to the unaged test specimens.

3 Results and Discussion

The results for the tensile shear strength tests (Fig. 4) show a tensile shear strength of 28 MPa on all coatings CDC1, CDC2 and the reference coating for the adhesive 2C-EP in the unaged state. After 720 h salt spray loading, higher tensile shear strengths could be achieved with the adhesive bonds of the reference coating. The compounds with the AY coating CDC1 show no significant change in tensile shear strength after

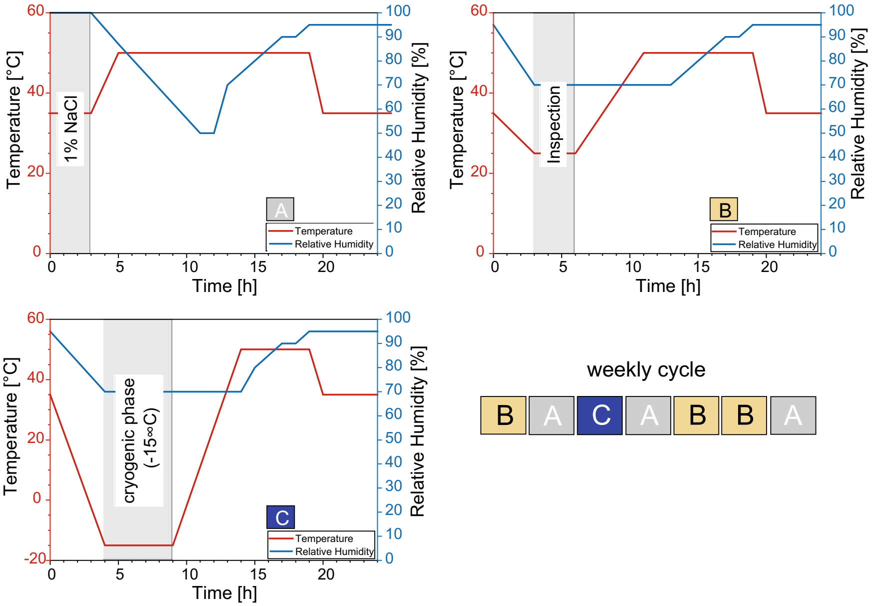

Fig. 3 VDA climate cycle [according to VDA 233-102]

Fig. 4 Tensile shear strength before and after ageing with the adhesive 2C-EP

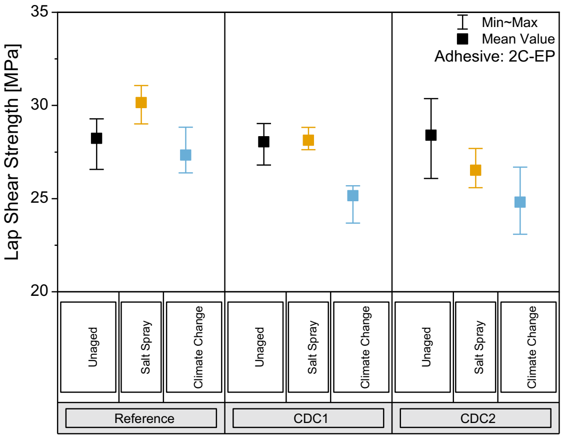

the salt spray test compared to the results of the unaged samples. A slight drop in the tensile shear strength to 26.5 MPa was observed in the test specimens of the CDC2 coating. The results after the climatic change test show a decrease in tensile shear strength for all coatings, while the decrease is greater for AY coatings than for the EP reference. By looking at the fracture patterns of the joining surfaces, it becomes clear that the weak point of the bond lies in the coating and not in the adhesive, which is able to detach the coating from the substrate (Fig. 8, left picture) before and after ageing. On the other hand, the shear strength was always higher than 20 MPa, with is a remarkable value.

The adhesive 2C-AY shows tensile shear strength of approx. 7 MPa on the reference and on the CDC1 coating and about 11 MPa on the CDC2 coating in the unaged state (Fig. 5). The respective ageing of the compounds with the reference and the CDC1 coating shows no serious differences compared to the unaged compounds of the same coating. Only the results of the samples coated with the CDC2 show a decrease in the tensile shear strength values to 8 MPa after salt spray test. The climate change test of the CDC2 coated composites also showed no change compared to the

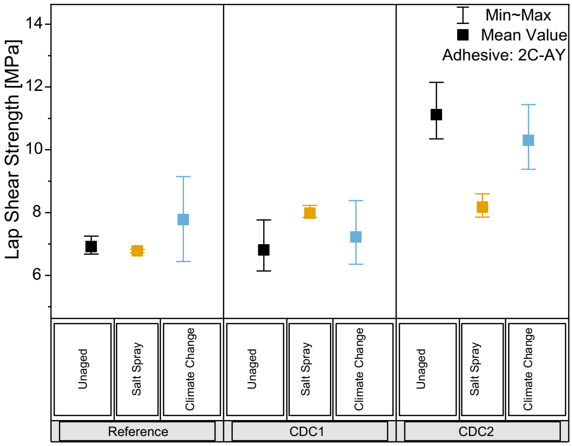

Fig. 5 Tensile shear strength before and after ageing with the adhesive 2C-AY

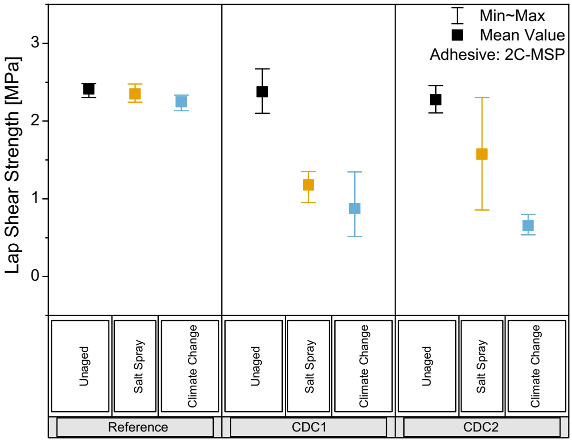

Fig. 6 Tensile shear strength before and after ageing with the adhesive 2C-MSP

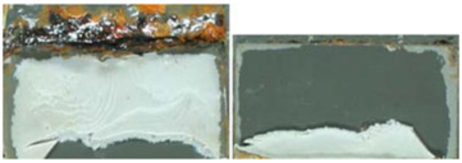

Fig. 7 Fracture pattern of injured specimen near bond line after ageing, CDC2, 2C-AY


2C-EP, CDC1, after 720h Salt Spray
2C-MSP, CDC1, without ageing
2C-MSP, CDC1, 4 weeks Climate Change
2C-AC, CDC2, without ageing
2C-AC, Reference, after 720h Salt Spray

Fig. 8 Fracture patterns of selected examples

values of the unaged composites. Regarding the fracture patterns in Fig. 8, there is always adhesive failure of the adhesive on the coating at all examined coatings.

The composites bonded with the adhesive 2C-MSP also show almost constant tensile shear strength of 2.4 MPa in the aged and unaged condition with the reference coating (Fig. 6). The same values are also achieved on the unaged test specimens coated with CDC1 and 2. However, the tensile shear strength of these coatings decreases significantly after ageing. The fracture patterns of the reference coatings show a cohesive failure in the adhesive aged and unaged. With AY CDC coatings, a cohesive fracture of the 2C-MSP can be observed without ageing, which shifts into an adhesive fracture in the interface CDC–2C-MSP after ageing (Fig. 8).

The VDA cyclic corrosion test has also an effect on the lap shear strength, which is shown in Figs. 9 and 10. The composites bonded with the adhesive 2C-AY have the same level on the reference coat before ageing and after the VDA test. With the

Fig. 9 Tensile shear strength with focus on VDA and salt spray injured specimens, 2C-AY

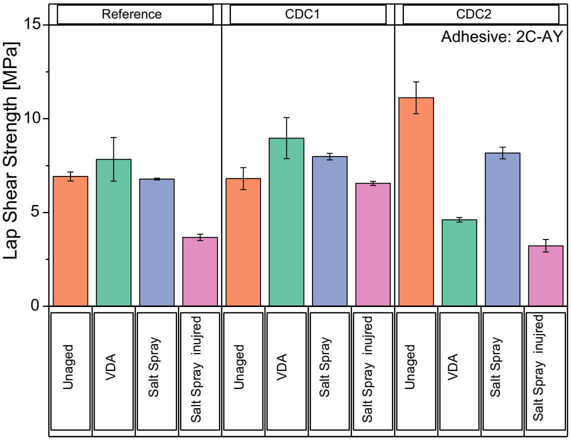

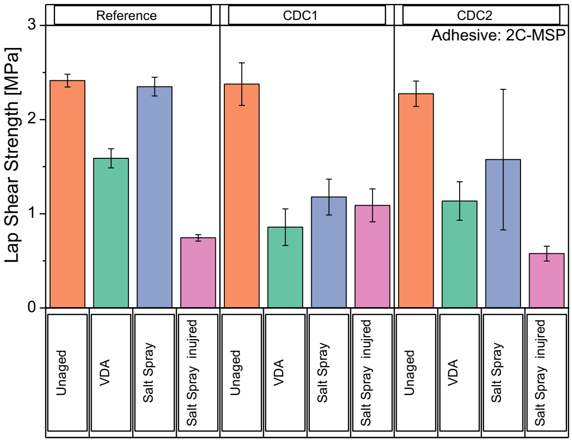

Fig. 10 Tensile shear strength with focus on VDA and salt spray injured specimens, 2C-MSP

CDC1 coating, there is a small increase after VDA than without ageing. The CDC2-coated specimens show a rigorous decrease of the lap shear strength after VDA than unaged. Also the specimens, which have been injured near the bond line, show a decrease in the lap shear strength even more than the specimens, which have not been injured. The decrease with the CDC1 is lower than on the other two coatings. Similar results have been achieved with the 2C-MSP adhesive. The fracture pattern of an injured specimen after ageing is shown in Fig. 7.

4 Summary and Conclusion

The results showed that the AY CDC coatings perform equal as EP CDC with the respective adhesives in the unaged state. However, after ageing processes, adhesive delamination of the adhesive to the AY CDC may occur. The paint adhesion on the steel substrate is brought to its limits by the 2C-EP adhesive on AY CDC coatings, which is not always the case on the EP CDC. The targeted damaging of the sample sheets near the bond shows that a corrosive infiltration weakens the bond further. In a comparison of the tensile shear strengths of the EP CDC (reference) and the CDC2, the weakening is approximately the same, and the CDC1 coating performs significantly better. In the case of the adhesive failure of the adhesives, appropriate pre-treatments must be carried out in further tests before bonding. Possible methods of pre-treatment are, for example, treatment of the surface with atmospheric pressure plasma or flame treatment. Also, the combination with adhesion promoters has to be considered in further steps.

Acknowledgements The research project was carried out in the framework of the industrial collective research programme (IGF no. 19463 N). It was supported by the Federal Ministry for Economic Affairs and Energy (BMWi) through the AiF (German Federation of Industrial Research Associations eV) based on a decision taken by the German Bundestag.

References

1. Hays, G. F.: Now is the Time. WCO http://corrosion.org/Corrosion+Resources/Publications-p-220.html, (last checked: 22.11.2019) (unknown)
2. Groß, E.: Die KTL hat sich durchgesetzt. Korrosions-Verhinderer Kataphorese. Cataphoresis stops corrosion J. **20**(1), 28–31 (1980)
3. Unknown: Zuverlässiger Schutz bis in kleinste Hohlräume: Neue Generation der kathodischen Tauchlackierung erfüllt höchste Ansprüche an Ökoeffizienz. J mo. **69**(9), 28–29 (2015)
4. Schiel, M., Stammen, E., Dilger, K.: Mechanische Eigenschaften im Vergleich. J adhäsion **58**(5), 42–46 (2014)
5. Unger, C., Schiel, M., Dilger, K.: Structural adhesive bonding on painted surfaces. J Welding and Cutting **13**(4), 226–228 (2014)
6. Möllmann, A., Gerwert, K.D.: Schwerer Korrosionsschutz auf Stahl für höchste Anforderungen: Vorstellung neuer Beschichtungssysteme. J JOT **7**, 24–28 (2013)
7. Entenmann, M., Koch, M., Schauer, T.: Schicht für Schicht wirksam. Ein Korrosionsschutz- und mechanische Eigenschaften in Automobillackaufbauten. J Farbe und Lack **117**(12), 20–23 (2011)
8. Foitzik, B.: (2003) Eine Schicht reicht. J JOT **43**(4), 28–30
9. Rennoch, K., Hildebrandt, D.: Die Lackierung von Grimme Landmaschinen mit DuPont Aqua ~ EC 5100. In: DFO Tagungsband-Erstes Deutsches Elektrotauchlack-Forum, 21–22 (2010)
10. Rembert, A.: Landmaschinen in Automobilqualität : Neue KTL-und Pulverbeschichtungsanlage für Landmaschinen-Fahrerkabinen Decklackierung mit Acrylatpulver, vollautomatische Roboterapplikation. In: Der Pulvertreff, EPS, Fachtagung Elektrostatisches Pulverbeschichten, 1–9 (2006)
11. Daniel, A., Kranz, G., Bremser, W.: Lackentwicklung und Kleben-ein Spannungsfeld? J adhäsion 5, 18–23 (2015) https://doi.org/10.1007/s35145-015-0543-0

Comparative Analysis of the Effect of Modifying Overlay Material with Selected Nanoparticles on Its Adhesion to the Substrate in Concrete Floors

Jacek Szymanowski

Abstract The article is dedicated to the comparative analysis of the effect of modifying overlay material with selected nanoparticles on its adhesion to the substrate in concrete floors. Firstly, the effect of the addition of amorphous silica nanospheres (SiO_2), tetragonal crystalline titanium oxide nanoparticles (TiO_2) and aluminum nanopowder (Al_2O_3), and the effect of their different contents on the consistency of the fresh mix (based on the Novikow cone subsidence), setting times and bulk density of the fresh mortar were compared. The effect of each type of nanoparticle and their different contents on the basic physical and mechanical properties of the hardened mortar has also been shown on the basis of previous research. Scanning electron microscope (SEM) imaging, together with the ultrasonic method and pull-off method, was used to compare and analyze the effect of the addition of SiO_2, TiO_2 and Al_2O_3 nanoparticles on the pull-off adhesion between the overlay and the concrete substrate. In addition, comparative analysis of the effect of SiO_2, TiO_2 and Al_2O_3 nanoparticles on the functional parameters of the overlay, such as abrasion resistance, subsurface tensile strength or hardness, was carried out. The analysis of the mechanical performance of all the studied mortars was also shown and was based on the mechanical performance ratio (MPR) which was calculated for each tested mortar. Based on the analysis, it has been shown that the use of the above-mentioned nanoparticles in the overlay mortar is advantageous from the point of view of adhesion as well as functional parameters.

Keywords Nanoparticles · Pull-off adhesion · Cement mortar · Overlay · Concrete floors · Functional parameters

---

J. Szymanowski (✉)
Faculty of Civil Engineering, Wroclaw University of Science and Technology, Wybrzeże Wyspiańskiego 27, 50-370 Wroclaw, Poland
e-mail: jacek.szymanowski@pwr.edu.pl

L. F. M. da Silva et al. (eds.), *Advanced Joining Processes*,
Advanced Structured Materials 125, https://doi.org/10.1007/978-981-15-2957-3_10

1 Introduction

A floor is a horizontal internal building element, which usually consists of a substrate and an overlay. The substrate is the structural support for the overlay, and it transfers the load from the overlay to either other structural elements or the ground. Depending on the type of material, floors can be divided into the following: mineral, synthetic resin floors, bituminous, plastic, ceramic, stone or steel. Floors are used in residential, civil and industrial buildings [1]. Floors made of cement composites are the most common.

If the durability of overlay mortars is taken into consideration, they should reach requirements according to the adequate level of pull-off adhesion between the overlay and the substrate [2–4]. The minimum value of pull-off adhesion for newly built overlays is equal to 0.5 MPa, and when the layer is applied as a repaired one it is equal to 1.5 MPa [5]. In order to reach the above-mentioned levels of adhesion, the following actions are used: mechanical treatment of the concrete substrate surface [6–9], increasing the effective surface area, removing the cement laitance [10–12], increasing the exposure of the aggregate on the surface of the substrate and reinforcing the surface of the substrate with bonding agents [13].

In order to increase the level of adhesion, modification of the material of the overlay with the use of additions such as carbon fibers, fly ash, metakaolin and magnesium phosphate is becoming increasingly common [14–17].

Apart from the pull-off adhesion between the overlay and the substrate, the functional and mechanical parameters of the overlay have a significant impact on the durability and defects of the overlay [18]. The above-mentioned parameters are: compressive strength, flexural strength, near-surface tensile strength, abrasion resistance and hardness. The correct values of these parameters are particularly important when the overlay also forms the finishing layer of the floor. Bearing in mind this fact, various actions are used to reach the desired level of these parameters, e.g., dispersed reinforcement, surface hardening or impregnation.

Until now in the literature, the effects of mineral powders, expanded cork, polypropylene fibers, waste ceramic, basaltic pumice, and steel and copper fibers on the level of the near-surface tensile strength and abrasion resistance of concrete and mortar have been shown [19–21].

Nanoparticles are fragments of matter that have one dimension smaller than 100 nm [22]. Since technological development has allowed nanoscale materials to be produced, more and more funds have been allocated to research that is connected with nanotechnology. A similar trend is also now visible in civil engineering [23, 24]. Nanotechnology allows for the improvement of many material properties (e.g., compressive strength, adhesion, chemical resistance, etc.) that are currently used in civil engineering and the production of new materials or composites with new properties such as those of self-cleaning or self-healing. It is predicted that the development of nanotechnology will allow many new possibilities in the field of eco-construction [25–27], the production of new materials and the modification of existing materials, as well as enable other possibilities of use in various constructions.

Based on the literature survey, it seems that the addition of nanoparticles to overlay mortar can have a positive effect on both its adhesion to concrete substrate and its functional parameters. This is indicated, for example, in papers [28–30]. However, there is still a lack of extensive research in this field. The improvement of some properties of self-compacting concrete has been described by Niewiadomski et al. [31, 32]. According to these papers, the addition of nanoparticles to self-compacting concrete can decrease its porosity. As a result of studies conducted in, among others [33–35], nanoparticles in the form of methyl silicone polymer can be used for the impregnation and hydrophobization of porous materials due to its effective filling of air pores. In turn, paper [36] shows that using nanoparticles in the form of nanocrystals and cellulose nanofibrils positively affects some physical and mechanical properties of concrete, e.g., freeze–thaw resistance.

Based on the literature survey carried out, among others, in [37–39], the application of nanoparticles as an addition to overlay mortar appears to improve the adhesion between this layer and the substrate, as well as improve its functional parameters. At the present time, these studies are incomplete and selective. There is no complete answer to the following questions: Which nanoparticles should be used? Why and in what amount should the nanoparticles be used for making overlays. Concerning this matter, there are research gaps, especially in relation to cement mortars for making overlays. The author of this article attempted to fill this gap by studying the use of amorphous silica nanospheres (SiO_2) in paper [40], tetragonal crystalline titanium oxide nanoparticles (TiO_2) in paper [41] and Al_2O_3 nanoparticles in paper [42].

The results of the research carried out in [40] indicate that modification of the composition of the overlay mortar with the addition of SiO_2 nanoparticles may increase the adhesion between the overlay and the substrate to a small extent, as well as considerably increase the values of the functional properties of the overlay. However, as was stated by the authors of paper [40], the following studies should be carried out to find an addition that could increase the adhesion between the overlay and the substrate to a greater extent. Paper [41] showed that the addition of TiO_2 nanoparticles has a positive effect on the adhesion between the overlay and the substrate (in the case of a 0.5% addition). It was also shown, especially for a 1% addition, that a significant improvement of the functional properties of the overlay (abrasion resistance, near-surface tensile strength, hardness) was observed in comparison with mortar without an addition. In turn, paper [42] reported that an addition of 0.5% Al_2O_3 nanoparticles improved the level of adhesion between the overlay and the substrate. Moreover, the highest improvement of the functional properties of the overlay in comparison with mortar without an addition was especially observed for a 1.0% addition (abrasion resistance and near-surface tensile strength).

To sum up, the article presents a comparative analysis of the effect of modifying the overlay with selected nanoparticles on its adhesion to the substrate in concrete floors. The analysis was based on the results presented in papers [40–42]. The article compares the effect of the addition of SiO_2 nanoparticles, TiO_2 nanoparticles and Al_2O_3 nanoparticles added in various amounts into the cement mortar mix on the consistency of the fresh mix (measured using the Novikow cone), the times of setting and the bulk density of the fresh mix. The effect of each type of nanoparticle and their different contents on the basic physical and mechanical parameters were compared. The effect of SiO_2, TiO_2 and Al_2O_3 on the adhesion between the overlay and the substrate was analyzed and compared based on results obtained using the pull-off method, ultrasonic method and scanning electron microscope imaging. In addition, the effect of the nanoparticles on the functional parameters of the overlay was also compared based on the results of abrasion resistance, near-surface tensile strength and hardness of the overlay.

2 Materials, Scope of Research and Methodology

2.1 Materials

In order to carry out the tests of the pull-off adhesion between the overlay and the substrate and the tests of near-surface tensile strength, as described in papers [40–42], three test elements were made. These three elements had dimensions of 80 cm × 80 cm and 60 cm × 60 cm, and a total thickness of 16.5 cm and are illustrated in Fig. 1. The elements consisted of a concrete substrate with a thickness of 12.5 cm and an overlay with a thickness of 4 cm.

Table 1 illustrates the mass composition of the fresh concrete mix used to make the substrate.

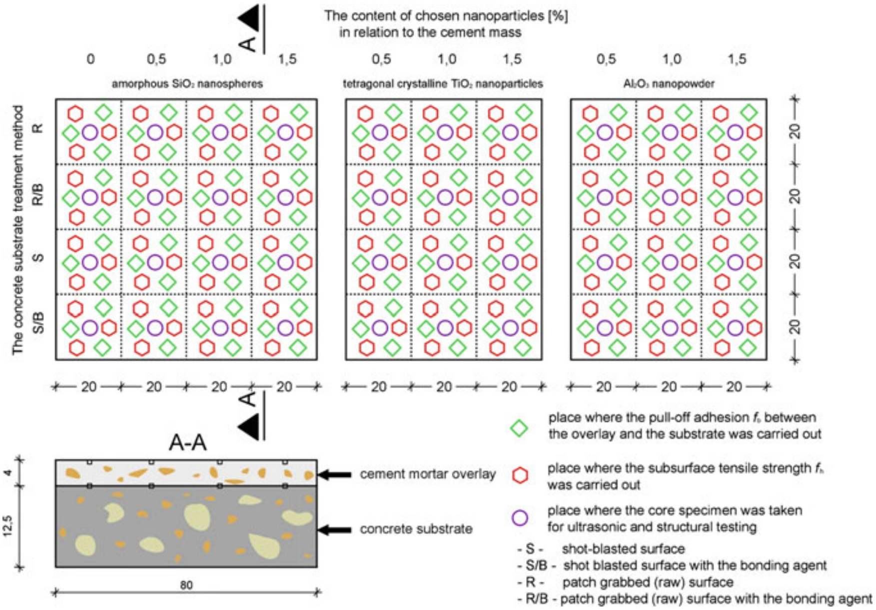

Fig. 1 Scheme of the tested elements

Table 1 Mass composition of the fresh concrete mix used to make the substrate

The element of the fresh concrete mix	[kg/m^3]
Portland cement CEM II A-LL 42.5 R	352.0
Fly ash	40
Water	165
Quartz aggregate with a grain size of up to 2 mm and a bulk density of 2620 kg/m^3	724.4
Natural coarse aggregate with a grain size of up to 8 mm with a bulk density of 2600 kg/m^3	1086.6
Polycarboxylate-based superplasticizer Sika® ViscoFlow®-6920 with a bulk density of 1070 kg/m^3	2.0

Before laying the overlay, four methods of treatment of the surface of the overlay were used. The four surfaces were marked as follows: R—raw surface, R/B—raw surface with an applied bonding agent, S—shot-blasted and S/B—shot-blasted with an applied bonding agent. The bonding agent Weber Primo was applied 4 h before laying the overlay. The product was based on the water dispersion of synthetic resin.

Then, the overlay made of cement mortars, with various amounts of nanoparticle additions (in relation to the cement mass), was applied to the four types of surfaces. In Fig. 1, the symbols of the surfaces are shown on the left. The content of nanoparticles in relation to the cement mass was 0% in the case of the reference mortar and 0.5, 1.0 and 1.5% in the case of the mortars with the addition of nanoparticles. In Table 2, the composition of cement mortars per 100 g of sand is shown.

Table 2 Composition of cement mortars per 100 g of sand

The kind of nanoparticle	Mortar series	The content of nanoparticles in relation to the cement mass [%]	Cement [g]	Nanoparticles [g]	Superplasticizer [g]	Sand [g]	Water [g]
Without nanoparticles	R-0	0	73.3	0	0.37	100	22
Amorphous silica nanospheres SiO_2	S-0.5	0.5	73.3	0.37	0.37	100	22
	S-1.0	1	73.3	0.73	0.37	100	22
	S-1.5	1.5	73.3	1.1	0.37	100	22
Tetragonal crystalline titanium oxide nanoparticles TiO_2	T-0.5	0.5	73.3	0.37	0.37	100	22
	T-1.0	1	73.3	0.73	0.37	100	22
	T-1.5	1.5	73.3	1.1	0.37	100	22
Aluminum nanopowder Al_2O_3	A-0.5	0.5	73.3	0.37	0.37	100	22
	A-1.0	1	73.3	0.73	0.37	100	22
	A-1.5	1.5	73.3	1.1	0.37	100	22

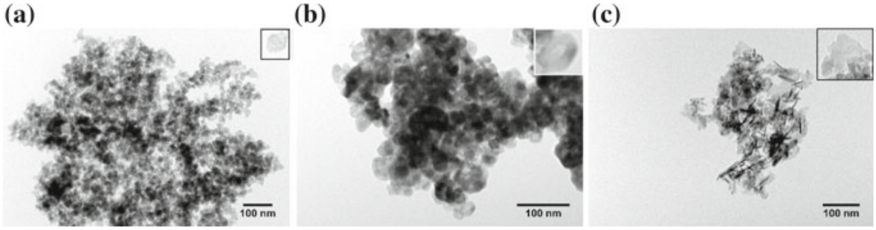

Fig. 2 Images taken with a scanning electron microscope: **a** amorphous silica nanospheres (SiO_2), **b** tetragonal crystalline titanium oxide nanoparticles (TiO_2), **c** aluminum nanopowder (Al_2O_3)

Table 3 Chosen physical properties of the used nanoparticles (based on the manufacturer's data)

The kind of nanoparticle	Molecular mass [g/mol]	Melting temperature [°C]	Boiling temperature [°C]	pH	Density in 25 °C [g/mL]	Bulk density [g/mL]	Specific surface [m^2/g]
SiO_2	60.08	1600	2230	Od 4 do 7	Od 2.2 do 2.6	0.011	300
TiO_2	79.87	1825	–	–	–	0.04–0.06	45–55
Al_2O_3	101.96	2040	2980	–	–	–	>40

In turn, the following compounds were used to make the overlay: Portland cement CEM I 42.5 R with a bulk density of 1.106 g/cm^3, dried quartz sand with a grain size of up to 2 mm and with bulk density of 1.497 g/cm^3, and superplasticizer based on polycarboxylates Sika ViscoCrete 20 HE in an amount of 0.5% of the cement mass.

As an addition to the overlay, the SiO_2 nanoparticles with 95% purity and a diameter of 19 ± 3.7 nm (Fig. 2a), TiO_2 nanoparticles with 99.7% purity and a diameter of 29 ± 7.1 nm (Fig. 2b), and Al_2O_3 nanoparticles with 99.8% purity and a diameter below 50 nm (Fig. 2c) were used (Table 3).

2.2 *The Scope of the Research and Methodology*

The procedure of preparing the fresh mortar mix consisted of adding and mixing nanoparticles, together with mixing the water and the superplasticizer. Next, cement was added and mixed for 45 s with an automatic mixer at a speed of 140 rpm. Then, the sand was added and mixed for another 45 s at 140 rpm. Everything was mixed for 18 s at 285 rpm. The concrete of the substrate and the cement mortar of the overlay were matured at a temperature of +20 °C (±3 °C) and at a relative air humidity of 60% (±5%).

Figure 3 illustrates the scope of research.

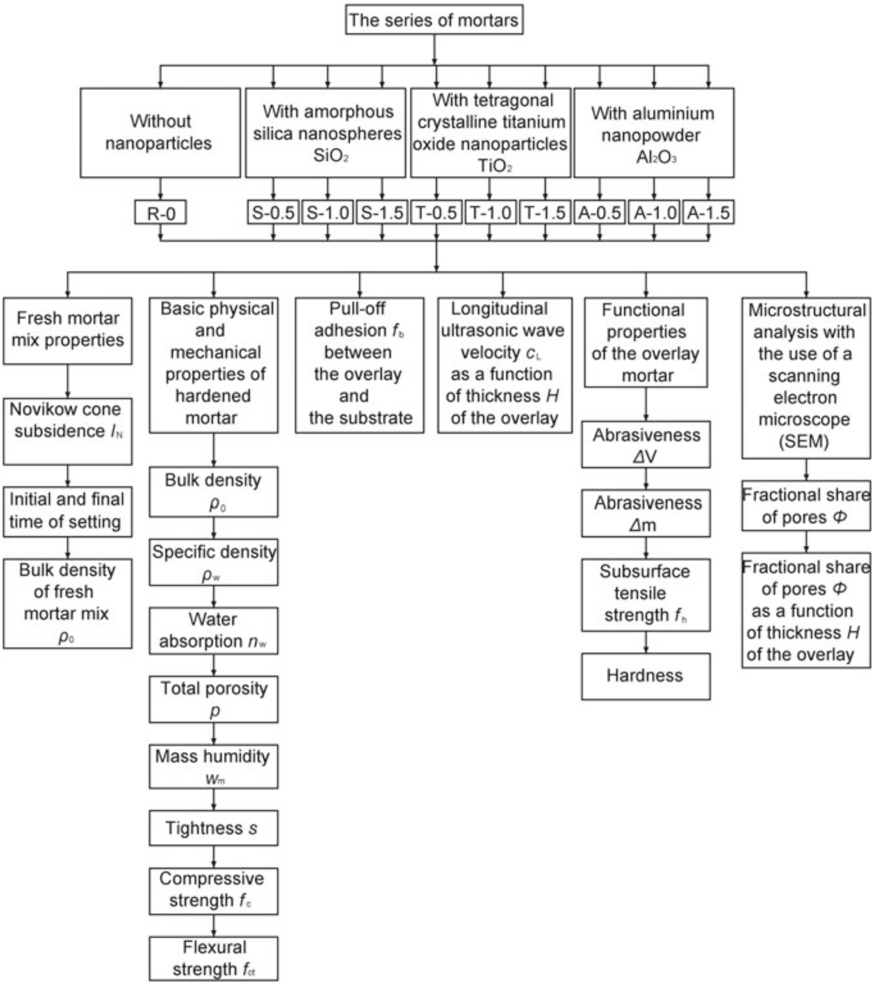

Fig. 3 Scope of research

The tests of the fresh mortar mix properties included the determination of consistency using a Novikow cone according to PN-B-04500 [43], determination of the bulk density of the fresh mix according to PN-EN 1015-6 [44], as well as the times of setting using Vicat apparatus according to PN-EN 196-1 [45].

The tests of the physical properties of the hardened mortars included determination of: the bulk density ρ_0, the specific density ρ_w, the water absorption n_w, the total porosity p, the mass humidity w_m and the tightness s. In turn, the tests of the mechanical properties included determination of: compressive strength f_c and flexural strength f_{ct} based on samples with dimensions of 40 mm × 40 mm × 160 mm according to EN 13892-2 standard [46].

The pull-off adhesion tests between the concrete substrate and the overlay, and tests of the near-surface tensile strength (also called near-surface tensile strength) were carried out according to standard EN 1542 [47] 28 days after casting the overlay. At the same time, the tests of abrasion resistance on the Boehme wheel according to EN 13892 [48] and the tests of hardness with the use of the sclerometric method according to EN 12504 [49] were carried out. In order to estimate the relations between the ultrasonic longitudinal wave speed and the thickness of the overlay, the core samples with a diameter of 50 mm were used. Point contact ultrasonic heads with a frequency of 40 Hz were used to perform the tests.

Cubic samples with dimension of 11 mm were taken from the interphase zone and from the surface of the overlay for microstructural imaging with the use of a scanning electron microscope. The images were used to determine the fractional share of pores Φ and the fractional share of pores Φ as a function of the thickness *H* of the overlay.

3 Comparative Analysis of Research Results

3.1 Results of Fresh Mortar Mix Properties

Figure 4 presents a comparative analysis of the fresh mortar mix property results

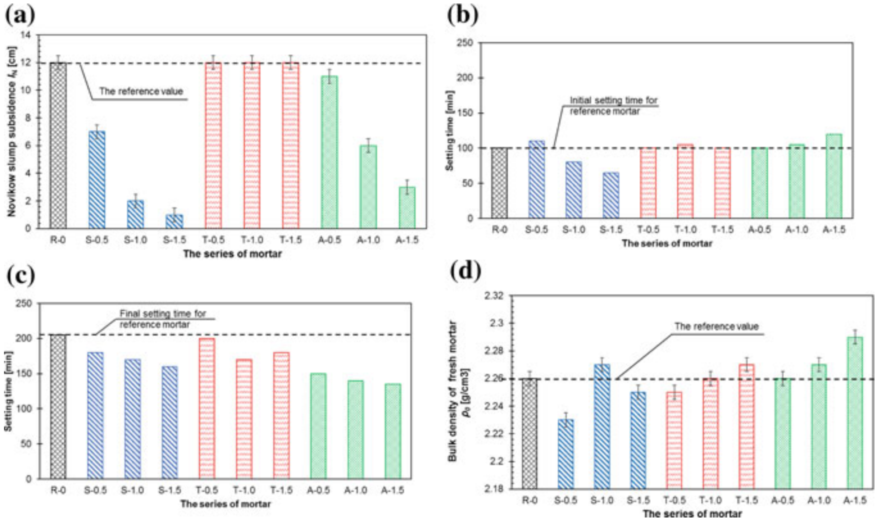

Fig. 4 Comparative analysis of the fresh mortar mix (modified with the addition of nanoparticles) properties: **a** Novikow cone subsidence (l_N), **b** initial time of setting, **c** final time of setting, **d** bulk density ρ_0 (based on the research results obtained in [40–42])

obtained in [40–42]: (a) consistency by Novikow cone subsidence, (b) initial time of setting, (c) final time of setting, (d) bulk density.

Figure 4 shows that as the content (in relation to the cement mass) of SiO_2 nanospheres and Al_2O_3 nanoparticles increases, the consistency assessed using Novikow cone subsidence decreases. This is not the case for the 0.5% addition (in relation to the cement mass), for which the consistency of the fresh mortar mix is slightly lower in comparison with the mortar without Al_2O_3 nanoparticles in their composition. Moreover, Fig. 4a illustrates that with an increasing content of TiO_2 nanoparticles in relation to the cement mass, the consistency does not change.

In addition, Fig. 4a, b illustrates that the increase in the content of SiO_2 nanospheres causes a shortening of the initial time of setting (except for the 0.5% addition) and the final time of setting. In turn, the increase in the content of TiO_2 nanoparticles does not influence the initial time of setting, but does shorten the final time of setting. Moreover, the increase in the content of Al_2O_3 nanoparticles in comparison with the mortar without the addition of Al_2O_3 nanoparticles causes a shortening of the initial time of setting and a longer final time of setting.

Figure 4c illustrates that the bulk density of fresh mortar does not depend on the addition of different contents of SiO_2 nanospheres and TiO_2 nanoparticles used to make the mix.

In the case of Al_2O_3 nanoparticles, it was found that as its content increases in relation to the cement mass, the fresh mortar's bulk density increases (except for the addition of 0.5%, for which the fresh mortar's bulk density is at the same level in comparison with the mortar without Al_2O_3 nanoparticles).

3.2 Results of the Basic Physical and Mechanical Properties of Hardened Mortars

Table 4 summarizes the results of the tests on the basic physical properties of cement mortars obtained in [47, 50], such as bulk density ρ_0, specific density ρ_w, water absorption n_w, total porosity p, mass humidity w_m and tightness s.

Table 4 illustrates that the addition of SiO_2 nanoparticles (regardless of the amount) and the addition of Al_2O_3 nanoparticles have a slight impact on the physical and mechanical properties of the hardened mortar. However, it should be noted that the addition of Al_2O_3 nanoparticles in the amount of 0.5% reduces the total porosity in relation to the reference mortar. In turn, the addition of TiO_2 nanoparticles affects the physical properties of the mortar and reduces the total porosity of the mortar by up to about 12.5% in comparison with the reference mortar.

Figure 5 presents a comparative analysis of the results of tests obtained in [40–42] on the basic mechanical properties of cement mortars, such as compressive strength f_c (Fig. 5a) and flexural strength f_{ct} (Fig. 5b).

Figure 5a illustrates that the use of each of the nanoparticles results in a slight decrease in compressive strength in comparison with the reference mortar. However,

Table 4 Basic physical properties of the tested mortars

Type of nanoparticle	Series of mortar	Bulk density ρ_0 [g/cm^3]	Specific density ρ_w [g/cm^3]	Water absorption n_w [%]	Porosity p [%]	Mass humidity w_m [%]	Tightness s [%]
Without nanoparticles	R-0	2.15	2.55	8.11	15.55	7.46	84.45
Amorphous silica nanospheres SiO_2	S-0.5	2.13	2.51	8.21	15.32	7.44	84.68
	S-1.0	2.12	2.51	8.27	15.51	7.37	84.49
	S-1.5	2.12	2.51	8.10	15.50	7.40	84.50
Tetragonal crystalline titanium oxide nanoparticles TiO_2	T-0.5	2.15	2.50	7.86	13.84	7.14	86.16
	T-1.0	2.16	2.50	7.90	13.62	7.21	86.38
	T-1.5	2.14	2.50	8.05	14.26	7.27	85.74
Aluminum nanopowder Al_2O_3	A-0.5	2.15	2.51	8.12	14.36	7.26	85.64
	A-1.0	2.13	2.51	8.22	15.25	7.50	84.75
	A-1.5	2.12	2.51	8.17	15.34	7.34	84.66

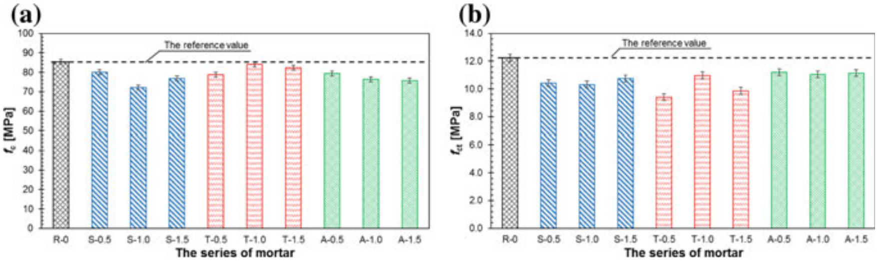

Fig. 5 Comparative analysis of the results of the basic mechanical properties of cement mortars modified with the addition of nanoparticles: **a** compressive strength f_{cm} and **b** flexural strength f_{ct} (based on the research results obtained in [40–42])

Fig. 5b illustrates that regardless of the addition content and the type of nanoparticle, the flexural strength values for the mortar are reduced.

3.3 Results of Pull-off Adhesion f_b Between the Overlay and the Concrete Substrate

Figure 6 shows a comparative analysis of the results of pull-off adhesion f_b between the overlay and the concrete substrate obtained in [40–42] in relation to the content

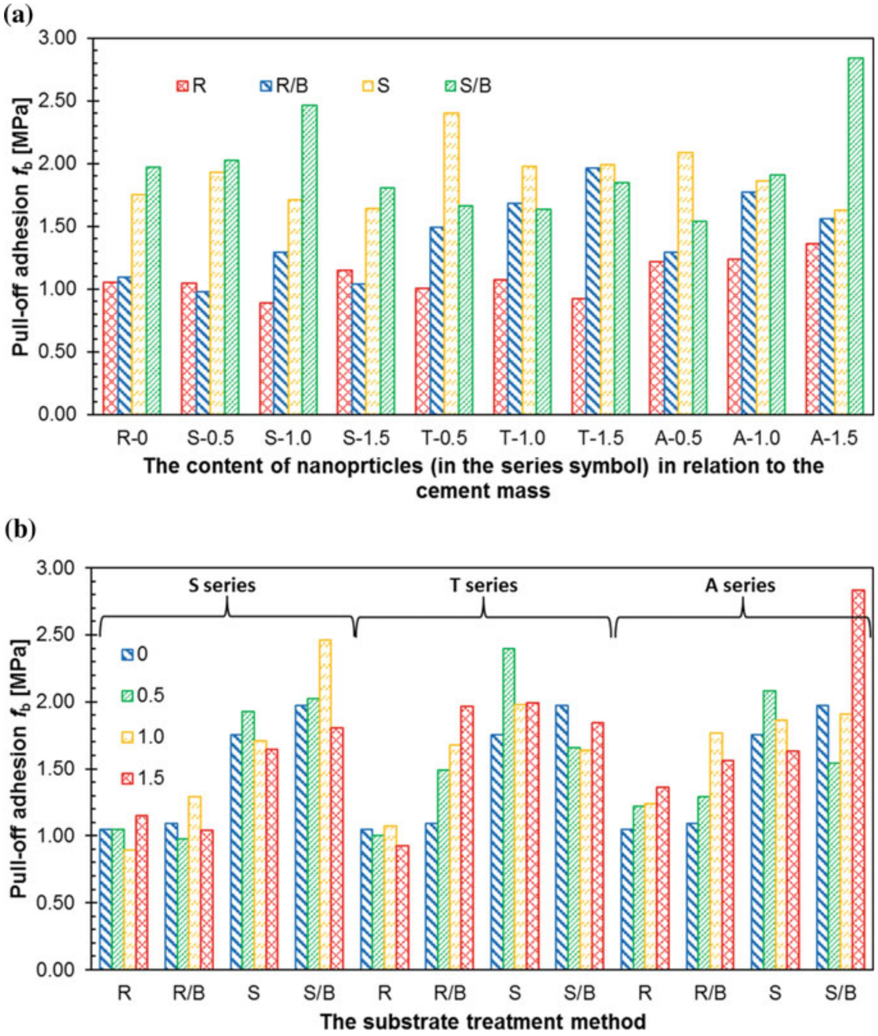

Fig. 6 Comparative analysis of the results of pull-off adhesion f_b between the overlay and the concrete substrate in relation to: **a** the content of nanoparticles in relation to the cement mass and **b** the substrate treatment method (based on the research results obtained in [40–42])

of nanoparticles in the mortar (Fig. 6a) and the method of treatment of the surface of the concrete substrate (Fig. 6b).

Figure 6a, b illustrates that the addition of 0.5% SiO_2 nanoparticles (in relation to the cement mass) has a positive effect on the pull-off f_b between the overlay and the concrete substrate. The mortar with the addition of 0.5% SiO_2 nanoparticles has a slightly higher pull-off adhesion f_b value than the reference mortar (for shot-blasted surfaces, without a bonding agent). The figures also illustrate that the addition of 0.5%

TiO_2 nanoparticles has a very positive effect on the pull-off adhesion f_b between the overlay and the concrete substrate. The values of pull-off adhesion (for shot-blasted surfaces) in this case are significantly higher than the values for the reference mortar (an increase of about 37%). This is confirmed by the SEM analysis of the samples that were taken from the interphase between the overlay and the substrate [41]. They show that the decrease in the fractional share of pores in the interphase zone of the overlay mortar containing 0.5% TiO_2 nanoparticles was about 40% in comparison with the overlay made of the reference mortar. The reduction of the fractional share of pores can be considered as one of the most important reasons for increasing the level of pull-off adhesion f_b between the overlay and the concrete substrate. In the case of the addition of 0.5% Al_2O_3 nanoparticles, a beneficial effect on the pull-off adhesion f_b is also visible. The value of pull-off adhesion f_b (for the shot-blasted surface) is about 20% higher than the value for the reference mortar. According to the SEM analysis described in [42], the reason for the improvement in the adhesion is the fact that the mortar with the addition of Al_2O_3 nanoparticles in an amount of 0.5% of cement mass has a lower fractional share of pores in the interphase zone by about 18% in relation to the reference mortar.

Figure 7 illustrates how the relationship of the average values of pull-off adhesion f_b between the overlay and the concrete substrate on the average values of compressive strength f_{cm} of the cement mortar from which the surface layer was made is formed.

Figure 7a–c illustrates that regardless of the method of substrate treatment, the value of pull-off adhesion f_b between the overlay and the concrete substrate does not depend on the compressive strength f_{cm} of the mortars with the addition of SiO_2 nanoparticles, TiO_2 nanoparticles and Al_2O_3 nanoparticles. In addition, a significant effect of the method of treatment of the concrete surface is visible because the highest values of adhesion were obtained for the shot-blasted surface with the bonding agent and the shot-blasted surface, and the lowest values were obtained for the patch-grabbed surface with the applied bonding agent and patch-grabbed surface.

On the other hand, Fig. 8 illustrates the relationship of the average pull-off adhe-

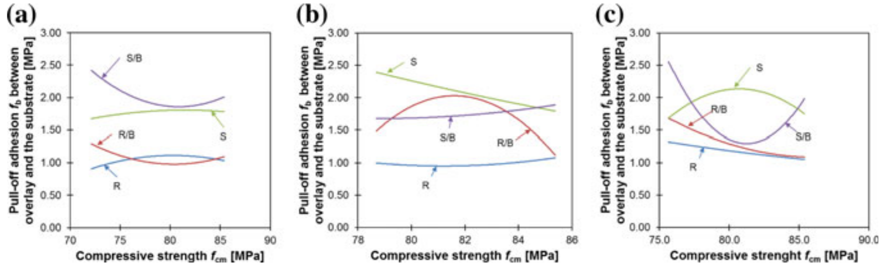

Fig. 7 Relationship of the average values of pull-off adhesion f_b between the overlay and the concrete substrate on the average values of compressive strength f_{cm} for the mortars with the addition of the following nanoparticles: **a** SiO_2, **b** TiO_2, **c** Al_2O_3 (based on the research results obtained in [40–42])

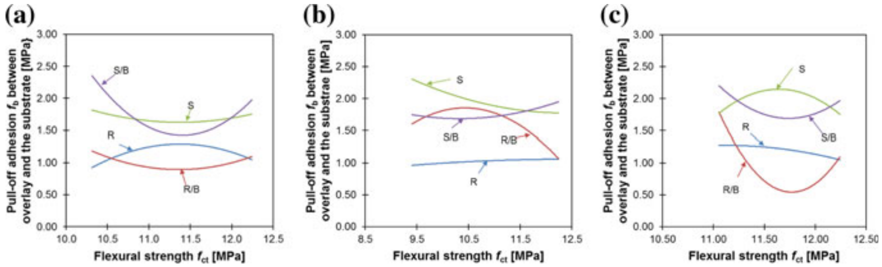

Fig. 8 Relationship of the average pull-off adhesion f_b between the overlay and the concrete substrate and the average values of the flexural strength f_{ct} of cement mortars modified with selected nanoparticles: **a** SiO_2, **b** TiO_2, **c** Al_2O_3 (based on the research results obtained in [40–42])

sion f_b between the overlay and the concrete substrate and the average values of the flexural strength f_{ct} of the cement mortar from which the surface layer was made.

Figure 8a–c shows that regardless of the substrate treatment method, the pull-off adhesion f_b between the overlay and the concrete substrate does not depend on the flexural strength of the mortars with the addition of SiO_2 nanoparticles, TiO_2 nanoparticles and Al_2O_3 nanoparticles.

3.4 Results of the Course of the Longitudinal Ultrasonic Wave Velocity c_L as a Function of Thickness H of the Overlay Mortar

Figure 9 illustrates the comparative analysis of the results (obtained in [40–42]) of longitudinal ultrasonic wave velocity c_L as a function of thickness H of the overlay mortar modified with selected nanoparticles.

Figure 9 illustrates that the addition of each of the nanoparticles positively affects the distribution of the longitudinal ultrasonic wave speed c_L. In the case of mortars

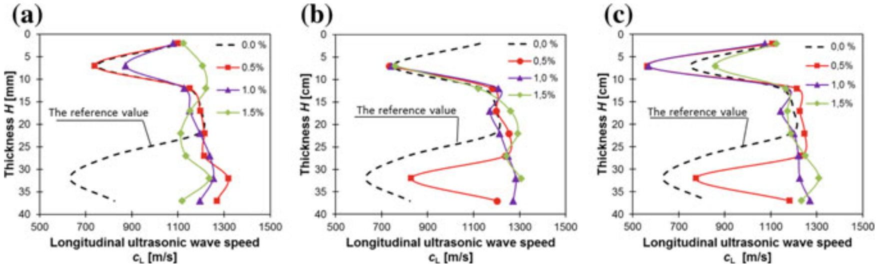

Fig. 9 Comparative analysis of the results of longitudinal ultrasonic wave velocity c_L as a function of thickness H of the overlay mortar modified with: **a** SiO_2, **b** TiO_2, **c** Al_2O_3 (based on the research results obtained in [40–42])

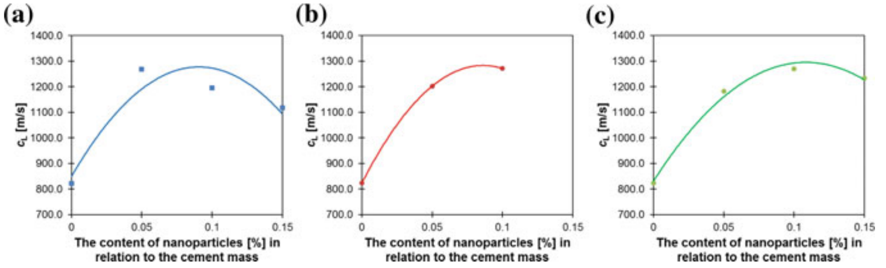

Fig. 10 Comparative analysis of the results of longitudinal ultrasonic wave velocity c_L (in a 2-mm distance from the interphase) as a function of the content of nanoparticles: **a** SiO_2, **b** TiO_2, **c** Al_2O_3 (based on the research results obtained in [40–42])

with the addition of SiO_2 nanoparticles and with a thickness of 2.5 cm (at a distance of up to 1.5 cm from the interphase zone), the velocity of the longitudinal ultrasonic wave c_L is higher than in the case of the reference mortar. For mortars with the addition of TiO_2 nanoparticles and Al_2O_3 nanoparticles with a thickness of about 2.5 cm, a more favorable distribution of the velocity of the longitudinal ultrasonic wave in relation to the reference value is also visible. In the case of the addition of each of the nanoparticles, a significant reduction in the coefficient of variation of the obtained values of pull-off adhesion f_b between the overlay and the concrete substrate was observed in relation to the reference mortar [40–42]. This is confirmed by the study of the longitudinal ultrasonic wave presented above.

Figure 10 illustrates the comparative analysis of the results of longitudinal ultrasonic wave velocity c_L (in a 2-mm distance from the interphase) as a function of the content of nanoparticles.

From Fig. 10a–c, it can be seen that the mortars, in the case of adding each of the nanoparticles, have a higher ultrasonic wave velocity in the 2-mm zone from the interphase in comparison with the mortar without the addition. It can also be concluded from the figures that the optimal amount of addition from the point of view of the longitudinal ultrasonic wave velocity in this zone is the amount between 0.5 and 1%.

3.5 *Results of the Functional Parameters of the Overlay*

Figure 11 illustrates a comparative analysis of the results of abrasiveness tests of the cement mortars (obtained in [40–42]) depending on the content of nanoparticles in relation to the cement mass.

Figure 11 illustrates that the mortar with the addition of SiO_2 nanoparticles and the mortar with the addition of TiO_2 nanoparticles in each quantity used in the tests are characterized by lower abrasiveness in comparison with the reference mortar. In

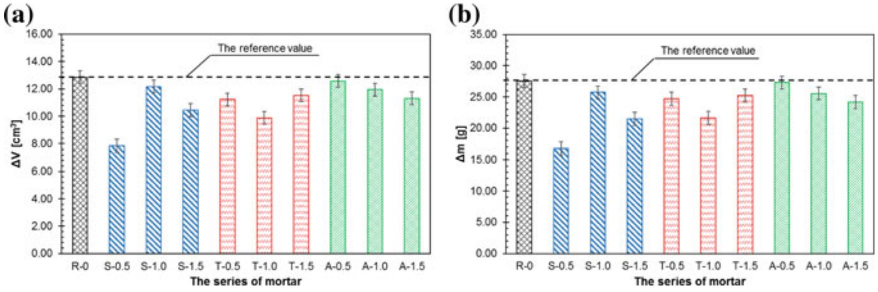

Fig. 11 Comparative analysis of the results of abrasiveness tests of the cement mortars depending on the content of nanoparticles in relation to the cement mass as: **a** volume loss ΔV and **b** mass loss Δm (based on the research results obtained in [40–42])

the case of the 1 and 1.5% addition of Al_2O_3 nanoparticles, the mortar abrasiveness is reduced when compared to the reference mortar.

Figure 12 presents a comparative analysis of the results (obtained in [40–42]) of the near-surface tensile strength f_h and hardness (examined by the sclerometric method) of the cement mortars regarding the content of nanoparticles in relation to the cement mass.

Figure 12a illustrates that in the case of the addition of 0.5 and 1% SiO_2 nanoparticles, the near-surface tensile strength of the overlay mortar increases. This is confirmed by SEM analysis of the mortar samples taken from the reference mortar surface zone and the surface zone of the mortar with the addition of 0.5% SiO_2 nanoparticles. The study presented in [40] confirmed that the reason for the improvement of surface tensile strength and abrasion resistance comes from the fact that the mortar with the addition of SiO_2 nanoparticles has a smaller fractional share of pores in the range from 0.83 to 7.50 μm in relation to the reference mortar. In the case of the addition of TiO_2 nanoparticles and Al_2O_3 nanoparticles in each of the tested quantities (0.5, 1, 1.5%), there is an increase in the near-surface tensile strength in comparison with the reference mortar. In [42], it was shown that the improvement

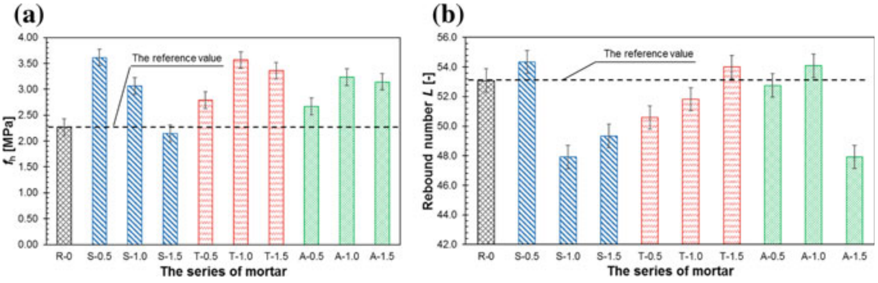

Fig. 12 Comparative analysis: **a** near-surface tensile strength f_h examined by the pull-off method and **b** subsurface hardness examined by the sclerometric method and shown as rebound number L (based on the research results obtained in [40–42])

of abrasion resistance and near-surface tensile strength of the overlay in the case of the addition of Al_2O_3 nanoparticles is associated with a smaller fractional share of pores in the range from 0.83 to 10 μm in the near-surface zone of the overlay (a decrease of about 39%). In turn, Fig. 12b illustrates that the mortar with the addition of 0.5% SiO_2 nanoparticles obtained a slightly higher value of subsurface hardness. The value of the subsurface hardness does not depend on the content of TiO_2 nanoparticles and Al_2O_3 nanoparticles in the mortar composition (except for the addition of 1.5% Al_2O_3 nanoparticles).

4 Mechanical Performance Analysis of Overlay Mortars Modified with Selected Nanoparticles

For the analysis of the mechanical performance of the overlays modified with selected nanoparticles, the test results obtained in [40–42] covering the basic mechanical properties of cement mortars modified with the addition of nanoparticles (compressive strength f_{cm} and flexural strength f_{ct}), the pull-off adhesion f_{b} between the overlay and the concrete substrate, the abrasiveness of the cement mortars (volume loss ΔV), the near-surface tensile strength f_{h} of the cement mortars using the pull-off method and the subsurface hardness assessed using the sclerometric method (described by the rebound number L) were used.

Based on the proposal given in [51], the mechanical performance ratio (MPR) was used. This ratio allows estimation of the mechanical performance of overlays modified with selected nanoparticles in relation to the reference mortar. Weights were assigned to individual properties in order to determine the mechanical performance ratio for the overlays modified with selected nanoparticles. The most important parameter characterizing the analyzed overlays was the pull-off adhesion f_{b} between the overlay and the concrete substrate, and its weight was assigned as 3. The abrasiveness of the cement mortars (volume loss ΔV) and the near-surface tensile strength f_{h} of the cement mortar, to which a weight of 2 was assigned, were considered less important. In turn, for compressive strength f_{cm} and bending strength f_{ct}, a weight of 1 was used. Therefore, the mechanical performance ratio of the overlays modified with selected nanoparticles can be defined as:

$$\mathrm{MPR} = \left(\frac{\begin{array}{c} \left(1 \cdot \left(\frac{f_{\mathrm{c}}}{f_{\mathrm{c(R-0)}}}\right)\right) + \left(1 \cdot \left(\frac{f_{\mathrm{ct}}}{f_{\mathrm{ct(R-0)}}}\right)\right) + \left(3 \cdot \left(\frac{f_{\mathrm{b}}}{f_{\mathrm{b(R-0)}}}\right)\right) + \left(2 \cdot \left(\frac{\Delta V}{\Delta V_{\mathrm{(R-0)}}}\right)\right) \\ + \left(2 \cdot \left(\frac{f_{\mathrm{h}}}{f_{\mathrm{h(R-0)}}}\right)\right) + \left(1 \cdot \left(\frac{L}{L_{\mathrm{(R-0)}}}\right)\right) \end{array}}{10} \right)$$

Table 5 summarizes all the tested parameters in relation to the reference mortar R-

Table 5 Compressive strength f_c, flexural strength f_{ct}, pull-off adhesion between the overlay and the concrete substrate f_b, abrasiveness (assessed as volume loss) ΔV, near-surface tensile strength f_h, rebound number L, mechanical performance ratio (MPR)

Series of mortar	f_c Compressive strength	f_{ct} Flexural strength	f_b Pull-off adhesion between the overlay and the substrate	ΔV Abrasiveness	f_h Near-surface tensile strength	L Hardness	MPR (%) Mechanical performance ratio
R-0	1.00	1.00	1.00	1.00	1.00	1.00	100.0
S-0.5	0.94	0.85	1.10	1.64	1.59	1.02	125.8
S-1.0	0.79	0.84	0.97	1.06	1.35	0.90	102.7
S-1.5	0.71	0.88	0.94	1.23	0.95	0.93	96.9
T-0.5	0.66	0.77	1.37	1.15	1.23	0.95	112.4
T-1.0	0.65	0.90	1.13	1.30	1.57	0.98	116.5
T-1.5	0.63	0.81	1.14	1.12	1.48	1.02	110.6
A-0.5	0.58	0.92	1.19	1.02	1.18	0.99	104.5
A-1.0	0.52	0.90	1.06	1.08	1.43	1.02	106.4
A-1.5	0.46	0.91	0.93	1.14	1.39	0.90	101.1

0 and the mechanical performance ratio calculated according to the above formula. The absolute values for mortar R-0 are: $f_c = 85.37$ MPa, $f_{ct} = 12.2$ MPa, $f_b = 1.75$ MPa (shot-blasted surface), $\Delta V = 12.85\ \text{cm}^3$, $f_h = 2.27$ MPa, $L = 53.1$.

Table 5 basically shows that each mortar with the addition of the tested nanoparticles has a higher mechanical performance ratio (the exception is the mortar with the addition of 1.5% SiO_2 nanoparticles, where the MPR value is slightly lower). For the mortars with the addition of SiO_2 nanoparticles, the highest mechanical performance ratio was achieved for the addition of 0.5% (125.8%), and then 1.0 and 1.5%. This shows that the optimal amount of addition of SiO_2 nanoparticles regarding mechanical efficiency is 0.5% in relation to the cement mass. In the case of the addition of TiO_2 nanoparticles, the highest value of the MPR was achieved for the addition of 1% and was equal to 116.5%, and then for the addition of 0.5 and 1.5% where it was 112.4% and 110.6%, respectively. It should be stated that the optimal amount of addition in this situation is 1.0%. For the addition of Al_2O_3 nanoparticles, the highest value of the MPR was achieved for the 1.0% addition where the coefficient was 106.4%, and then for the addition of 0.5 and 1.0% where the MPR was 104.5% and 101.1%, respectively. On this basis, it can be concluded that the optimal amount of addition of Al_2O_3 nanoparticles is 1.0%.

5 Summary of Research Results and Conclusions

In the article, a comparative analysis of the effect of modification of surface layer mortar with the addition of various amounts of SiO_2 nanoparticles, TiO_2 nanoparticles (TiO_2) and Al_2O_3 nanoparticles was carried out. The comparative analysis consisted of the properties of fresh mortar mixes, hardened mortar testing and microstructure testing using SEM. In addition, analysis of the mechanical performance of all the tested mortars was carried out. The comparative analysis was carried out on the basis of the mechanical performance ratio (MPR), which was calculated for each of the tested mortars.

Based on the research, the following conclusions were formulated:

1. It is advantageous to use each of the tested nanoparticles as an addition to the overlay mortar from the point of view of adhesion as well as functional parameters.
2. In terms of the pull-off adhesion f_b between the overlay and the concrete substrate, the optimum amount of nanoparticle addition is 0.5% (for all the tested nanoparticles).
3. From the point of view of the functional parameters, the optimum amount of addition is 0.5% for SiO_2 nanoparticles and a 1% addition for TiO_2 nanoparticles and Al_2O_3 nanoparticles.

References

1. Bissonnette, B., Courard, L., Garbacz, A.: Concrete Surface Engineering. CRC Press, Boca Raton, FL, USA (2015)
2. Sadowski, Ł., Hoła, J.: New nondestructive way of identifying the values of pull-off adhesion between concrete layers in floors. J. Civ. Eng. Manag. **20**(4), 561–569 (2014). https://doi.org/10.3846/13923730.2014.897642
3. Sadowski, Ł., Nikoo, M., Nikoo, M.: Principal component analysis combined with a self organization feature map to determine the pull-off adhesion between concrete layers. Constr. Build. Mater. **78**, 386–396 (2015). https://doi.org/10.1016/j.conbuildmat.2015.01.034
4. Sadowski, Ł., Hoła, J.: ANN modeling of pull-off adhesion of concrete layers. Adv. Eng. Softw. **89**, 17–27 (2015). https://doi.org/10.1016/j.advengsoft.2015.06.013
5. Czarnecki, L., Łukowski, P., Garbacz, A.: Naprawa i ochrona konstrukcji z betonu—Komentarz do PN-EN 1504. PWN, Warszawa (2017)
6. Santos, P.M.D., Júlio, E.N.B.S., Silva, V.D.: Correlation between concrete-to-concrete bond strength and the roughness of the substrate surface. Constr. Build. Mater. **21**, 1688–1695 (2007). https://doi.org/10.1016/j.conbuildmat.2006.05.044
7. Sadowski, L., Mathia, T.G.: The metrology of ground concrete surfaces morphology with 3D laser scanner. Manage. Prod. Eng. Rev. **6**(2), 40–44 (2015). https://doi.org/10.1515/mper-2015-0015
8. Courard, L., Piotrowski, T., Garbacz, A.: Near-to-surface properties affecting bond strength in concrete repair. Cem. Concr. Compos. **46**, 73–80 (2014). https://doi.org/10.1016/j.cemconcomp.2013.11.005

9. Tayeh, B.A., Bakar, B.H.A., Johari, M.A.M., Ratnam, M.M.: The relationship between substrate roughness parameters and bond strength of ultra high-performance fiber concrete. J. Adhes. Sci. Technol. **27**, 1–21 (2013). https://doi.org/10.1080/01694243.2012.761543
10. Silfwerbrand, J., Beushausen, H., Courard, L.: Bond. In: Bissonnette, B., Courard, L., Fowler, D., Granju, J.L. (eds.) Bonded Cement-Based Material Overlays for the Repair, the Lining or the Strengthening of Slabs or Pavements. RILEM State of the Art Reports, vol. 3. Springer, Dordrecht (2011)
11. Sadowski, Ł., Stefaniuk, D., Hoła, J.: The effect of the porosity within the interfacial zone between layers on pull-off adhesion. Constr. Build. Mater. **152**, 887–897 (2017). https://doi.org/10.1016/j.conbuildmat.2017.07.080
12. Sadowski, Ł., Żak, A., Hoła, J.: Multi-sensor evaluation of the concrete within the interlayer bond with regard to pull-off adhesion. Arch. Civ. Mech. Eng. **18**, 573–582 (2018). https://doi.org/10.1016/j.acme.2017.09.008
13. Błaszczyński, T., Jasiczak, J., Ksit, B., Siewczyńska, M.: Aspects of bond layer role in concrete repairs. Arch. Civ. Mech. Eng. **6**, 75–87 (2006). https://doi.org/10.1016/S1644-9665(12)60277-5
14. Sabah, S.A., Hassan, M.H., Bunnori, N.M., Johari, M.M.: Bond strength of the interface between normal concrete substrate and GUSMRC repair material overlay. Constr. Build. Mater. **216**, 261–271 (2019). https://doi.org/10.1016/j.conbuildmat.2019.04.270
15. Nunes, V.A., Borges, P.H., Zanotti, C.: Mechanical compatibility and adhesion between alkali-activated repair mortars and Portland cement concrete substrate. Constr. Build. Mater. **215**, 569–581 (2019). https://doi.org/10.1016/j.conbuildmat.2019.04.189
16. Robayo-Salazar, R., Jesús, C., de Gutiérrez, R.M., Pacheco-Torgal, F.: Alkali-activated binary mortar based on natural volcanic pozzolan for repair applications. J. Build. Eng. 100785 (2019). https://doi.org/10.1016/j.jobe.2019.100785
17. Qin, J., Qian, J., You, C., Fan, Y., Li, Z., Wang, H.: Bond behavior and interfacial micro-characteristics of magnesium phosphate cement onto old concrete substrate. Constr. Build. Mater. **167**, 166–176 (2018). https://doi.org/10.1016/j.conbuildmat.2018.02.018
18. Hulimka, J.: Errors in design, construction and utilization of large-area reinforced concrete floors. Inżyn. Budow. **74**(3), 122–126 (2018)
19. Binici, H.: Effect of crushed ceramic and basaltic pumice as fine aggregates on concrete mortars properties. Constr. Build. Mater. **21**(6), 1191–1197 (2007). https://doi.org/10.1016/J.CONBUILDMAT.2006.06.002
20. Barnat-Hunek, D., Widomski, M., Szafraniec, M., Łagód, G.: Impact of different binders on the roughness, adhesion strength, and other properties of mortars with expanded cork. Materials **11**(3), 364 (2018). https://doi.org/10.3390/ma11030364
21. Felekoğlu, B., Türkel, S., Altuntaş, Y.: Effects of steel fiber reinforcement on surface wear resistance of self-compacting repair mortars. Cem. Concr. Compos. **29**(5), 391–396 (2007). https://doi.org/10.1016/J.CEMCONCOMP.2006.12.010
22. Sobolev, K., Gutiérrez, F.M.: How nanotechnology can change the concrete world. Am. Ceram. Soc. Bull. **84**(10), 14 (2005)
23. Czarnecki, L.: Nanotechnology in construction. Constr. Rev. **82**, 40–53 (2011)
24. Teizer, J., Venugopal, M., Teizer, W., Felkl, J.: Nanotechnology and its impact on construction: bridging the gap between researchers and industry professionals. J. Constr. Eng. Manag. **138**(5), 594–604 (2012). https://doi.org/10.1061/(ASCE)CO.1943-7862.0000467
25. Czarnecki, L.: Is nanotechnology an efficient tool in eco-construction? J. Zhejiang Univ. Sci. A **5**(20), 380–381 (2019). https://doi.org/10.1631/jzus.A19BR001
26. Pacheco-Torgal, F.: Eco-efficient construction and building materials research under the EU Framework Programme Horizon 2020. Constr. Build. Mater. **51**, 151–162 (2014). https://doi.org/10.1016/j.conbuildmat.2013.10.058
27. Czarnecki, L., van Gemert, D.: Innovation in construction materials engineering versus sustainable development. Bull. Pol. Acad. Sci. Tech. Sci. **65**(6), 765–771 (2017). https://doi.org/10.1515/bpasts-2017-0083

28. Silva, J.V., Ismael, R., Carmo, R.N.F., Lourenço, C., Soldado, E., Costa, H., Júlio, E.: Influence of nano-SiO_2 and nano-Al_2O_3 additions on the shear strength and the bending moment capacity of RC beams. Constr. Build. Mater. **123**, 35–46 (2016). https://doi.org/10.1016/j.conbuildmat.2016.06.132
29. Ghazy, A., Bassuoni, M.T.: Shrinkage of nano-modified fly ash concrete as a repair material. ACI Mater. J. **114**(6) (2017). https://doi.org/10.14359/51700891
30. Haruehansapong, S., Pulngern, T., Chucheepsakul, S.: Effect of nanosilica particle size on the water permeability, abrasion resistance, drying shrinkage, and repair work properties of cement mortar containing nano-SiO_2. Adv. Mater. Sci. Eng. (2017). https://doi.org/10.1155/2017/4213690
31. Niewiadomski, P., Hoła, J., Ćwirzeń, A.: Study on properties of self-compacting concrete modified with nanoparticles. Arch. Civ. Mech. Eng. **18**(3), 877–886 (2018). https://doi.org/10.1016/j.acme.2018.01.006
32. Niewiadomski, P., Stefaniuk, D., Hoła, J.: Microstructural analysis of self-compacting concrete modified with the addition of nanoparticles. Procedia Eng. **172**, 776–783 (2017). https://doi.org/10.1016/j.proeng.2017.02.122
33. Fic, S., Barnat-Hunek, D.: The effectiveness of hydrophobisation of porous building materials by using the polymers and nanopolymers solutions. Int. J. Mater. Sci. Eng. **2**(2), 93 (2014). https://doi.org/10.12720/ijmse.2.2.93-98
34. Barnat-Hunek, D., Guz, Ł., Łagód, G., Jarosz-Hadam, M.: Impact of roughness on the wettability of mortars with basalt fibres hydrophobised by nanopolymers solution. In: AIP Conference Proceedings, vol. 2004, no. 1, p. 030004. AIP Publishing (2018). https://doi.org/10.1063/1.5051104
35. Fic, S., Szewczak, A., Barnat-Hunek, D., Łagód, G.: Processes of fatigue destruction in nanopolymer-hydrophobised ceramic bricks. Materials **10**(1), 44 (2017). https://doi.org/10.3390/ma10010044
36. Barnat-Hunek, D., Szymańska-Chargot, M., Jarosz-Hadam, M., Łagód, G.: Effect of cellulose nanofibrils and nanocrystals on physical properties of concrete. Constr. Build. Mater. **223**, 1–11 (2019). https://doi.org/10.1016/j.conbuildmat.2019.06.145
37. Szymanowski, J.: Evaluation of the adhesion between overlays and substrates in concrete floors: literature survey, recent non-destructive and semi-destructive testing methods and research gaps. Buildings **9**(9), 203 (2019). https://doi.org/10.3390/buildings9090203
38. Sadowski, Ł.: Adhesion in Layered Cement Composites. Springer Nature Switzerland AG, Basel (2019)
39. Sadowski, Ł.: Multi-scale evaluation of the interphase zone between the overlay and concrete substrate: methods and descriptors. Appl. Sci. **7**(9), 893 (2017). https://doi.org/10.3390/app7090893
40. Szymanowski, J., Sadowski, Ł.: Functional and adhesive properties of cement-based overlays modified with amorphous silica nanospheres. J. Adhes. 1–22 (2019). https://doi.org/10.1080/00218464.2019.1663412
41. Szymanowski, J., Sadowski, Ł.: The influence of the addition of tetragonal crystalline titanium oxide nanoparticles on adhesive and functional properties of layered cementitious composites. Compos. Struct. (2019). https://doi.org/10.1016/j.compstruct.2019.111636
42. Szymanowski, J., Sadowski, Ł.: The development of nanoalumina-based cement mortars for overlay applications in concrete floors. Materials **12**(21), 3456 (2019). https://doi.org/10.3390/ma12213465
43. PN-B-04500: Zaprawy budowlane—Badania cech fizycznych i wytrzymałościowych (1985)
44. PN-EN 1015-6:2000: Metody badań zapraw do murów—Określenie gęstości objętościowej świeżej zaprawy (2000)
45. EN 196-1: Methods of Testing Cement (2016)
46. EN 13892-2: Methods of Test for Screed Materials—Part 2: Determination of Flexural and Compressive Strength (2002)
47. EN 1542: Products and Systems for the Protection and Repair of Concrete Structures—Test Methods—Measurement of Bond Strength by Pull-Off (1999)

48. EN 13892-3: Methods for Testing Materials for Undercoats—Part 3: Determination of Abrasion Resistance According to Bohme (2014)
49. EN 12504-2: Testing Concrete in Structures—Part 2: Nondestructive Testing—Determination of Rebound Number (2012)
50. Gudra, T., Stawiski, B.: Non-destructive strength characterization of concrete using surface waves. NDT & E Int. **33**(1), 1–6 (2000). https://doi.org/10.1016/S0963-8695(99)00028-6
51. Kurda, R., de Brito, J., Silvestre, J.: Combined economic and mechanical performance optimization of recycled aggregate concrete with high volume of fly ash. Appl. Sci. **8**(7), 1189 (2018). https://doi.org/10.3390/app8071189

Mechanical Characterisation of Graded Single Lap Joints Using Magnetised Cork Microparticles

Catarina I. da Silva, Ana Q. Barbosa, José B. Marques, Ricardo J. C. Carbas, Eduardo A. S. Marques, Juana Abenojar and Lucas F. M. da Silva

Abstract One of the main problems associated with adhesive joints is the existence of stress concentrations (shear and peel) at the ends of the overlap, reducing joint performance. This is especially valid for the most common joint geometry—the single lap joint (SLJ). Therefore, a main area of investigation in the field of adhesive bonding is the uniformisation of the stress distribution along with the adhesive bondline, in order to decrease those stress accumulations at its ends, achieving stronger and lighter joints. The main goal of this work was to develop a functionally modified adhesive, where the mechanical properties vary gradually along the overlap. With an adequate application of magnetic fields, using a customised apparatus, magnetised cork microparticles, initially uniformly distributed within a resin, were strategically placed along the bondline of an adhesive joint, being then nonuniformly distributed along the entire overlap area. This results in a gradual variation of the mechanical properties along the overlap, decreasing the stress concentrations and leading to a more uniform stress distribution on the overlap region. The adhesive stiffness varies along the overlap, being maximum in the middle and minimum at the edges of the overlap region. Therefore, the influence of the amount of magnetised cork microparticles was assessed. Tensile tests were performed for bulk specimens and SLJs, along with SEM analysis of the particles and the correspondent fracture surfaces of the

---

C. I. da Silva · A. Q. Barbosa (✉) · J. B. Marques · R. J. C. Carbas · E. A. S. Marques
Instituto de Ciência e Inovação em Engenharia Mecânica e Engenharia Industrial,
Rua Dr. Roberto Frias 400, 4200-465 Porto, Portugal
e-mail: aqueiros@inegi.up.pt

C. I. da Silva
e-mail: cisilva@inegi.up.pt

R. J. C. Carbas · L. F. M. da Silva
Department of Mechanical Engineering, Faculty of Engineering, University of Porto,
Rua Dr. Roberto Frias, 4200-465 Porto, Portugal
e-mail: lucas@fe.up.pt

J. Abenojar
Materials Performance Group, Materials Science and Engineering Department,
Universidad Carlos III de Madrid, Leganés, Spain
e-mail: abenojar@ing.uc3m.es

L. F. M. da Silva et al. (eds.), *Advanced Joining Processes*,
Advanced Structured Materials 125, https://doi.org/10.1007/978-981-15-2957-3_11

bulk specimens. Additionally, glass transition temperature measurements were carried out. According to experimental testing result, the inclusion of these particles enhances the joint performance for both graded joints and joints with a uniform particle distribution, when compared to joints bonded with neat resin. It was also possible to manufacture graded joints with distinct mechanical behaviour, which is dependent on the amount of magnetised particles being considered.

Keywords Epoxy adhesives · Functionally graded adhesive joints · Magnetised particles · Cork microparticles · Magnetophoresis · Numerical analysis · Stress distribution · Mechanical properties

1 Introduction

Over the years, the use of adhesive bonding as a joining method for structural applications has been the focus of intensive research and evolution, gradually replacing the classical mechanical fixing methods, not only due to its improved mechanical performance, but also due to its versatility and ability to reliably join a large range of materials. This technique is also able to effectively join dissimilar materials, which cannot be easily performed with many of the alternative joining methods [1, 2]. Another key feature of adhesive bonding is the fact that the stress distribution along the joint is more uniform than that provided by other conventional methods of fastening such as bolts or rivets [3]. Consequentially, adhesive bonding is now a key manufacturing technology to numerous industrial sectors, such as the aeronautical, aerospace, medical and civil industries [4], spurred by the constant push for lighter, stronger, more resistant and more environmentally friendly materials. These specific demands are being met either with customised materials such as composites or even with custom adhesives.

One of the most used structural adhesives is the epoxy resin (a thermoset polymer) due to its good mechanical, thermal and chemical properties. Therefore, the epoxy microstructure has a densely cross-linked molecular structure, which is very useful for structural engineering applications, since it presents high modulus of elasticity and strength, as well as low creep and good thermal resistance. However, the same microstructure that provides stiffness and strength to the epoxy resins is responsible for the inherent brittleness (low ductility and toughness) with a low resistance to the initiation of cracks and their propagation.

The single lap joint (SLJ) is the most studied joint geometry in the literature and it is also the most widely used type of joint because of its simplicity and efficiency. In a SLJ, the adhesive is usually loaded in shear, the type of loading under which adhesive joints perform best. Nevertheless, when analysing this type of joint, the main problem associated with it is the nonuniform stress distribution along the overlap, resulting in the presence of stress concentrations (peel—eccentric load path; shear—unequal axial straining of the adherends) at the ends of the overlap [5–7]. This results in lower strength bonds, leading to a premature joint failure at the ends of the overlap, especially if the adhesive is brittle, such as the epoxy resin.

Hence, in order to effectively increase the joints strength, the stress distribution must be as uniform as possible [2, 3, 8]. The development of methods for decreasing those stress concentrations and enhancement of joints' performance is an area of interest that has increasingly been researched on the field of adhesive bonding. In the literature, several methods have been proposed to improve the joint strength, such as adhesive filleting [9], adherend tapering [10], adherend rounding [11], increasing thickness of the adhesive at the end [12] and several other geometrical solutions (such as voids in the bondline, surface roughness or notches in the adherend). However, with these methods, not only the complexity of the geometry increases, making it difficult to manufacture the joint, but it is also impossible to obtain a true uniform stress distribution along the adhesive layer [2, 13]. An alternative technique used to significantly improve the stress distribution in an adhesive layer is the mixed adhesive joint (MAJ) [14–22] which uses more than one adhesive on the same overlap. These joints adopt a stiff and strong adhesive in the middle of the overlap and a flexible and ductile adhesive at the overlap ends. However, one of the main problems associated with this technique is the lack of proper adhesive separation, as even in a joint bonded with several different adhesives, stress concentrations tends to occur at the borders of adjacent adhesives [14]. That is, MAJs can only improve the bonding strength of a joint up to a certain level.

Furthermore, several studies to improve the joint strength by creating functionally graded materials (FGM) [23–25] and functionally graded adhesive (FGA) bondlines [26, 27]. More recently, Carbas et al. [28] proposed a method to relieve the high stress concentrations at the borders of the overlap which creates a continuously functionally modified adhesive along the overlap length of the joint using localised induction heating. However, the major drawback of this method is that the graded effect of these joints is lost when they are subjected to post-cure temperatures higher than the glass transition temperature, reverting the process [29].

Nowadays, micro- or nanoparticles have been used as material reinforcements in several applications. They can be inorganic (silicates, glass, alumina, etc.) [30] or organic [31]. Depending on the reinforcement material selected, the use of microparticles has the potential to be less expensive and allow for faster product development, when compared to other techniques for improving joint performance. Additionally, natural materials (i.e. cork or wood fibres) [32–34] are gaining attention as reinforcements of polymeric matrices due to their unique properties such as the thermal insulation, low density, low cost and sustainability of the raw material [35]. Natural microparticles present major competitive advantages, since two of the main concerns in several industrial sectors momentarily are the final weight of the structure and the reduction of the carbon footprint, both of which are addressed by these materials. In addition, these particles can also be dispersed and displaced in order to create custom particle distributions. This principle can thus be applied to the fabrication of functionally graded joints, where the microparticles would be strategically placed along the overlap, so that variable mechanical and physical properties distributions can be obtained along a certain direction. This results in enhanced joint resistance with minimal change in the base properties of the matrix resin [2], therefore increasing its toughness—the ability of a material to absorb energy and plastically deform without breaking. Due to the many advantages that this method can offer and the importance of using materials with high toughness in structural applications, there is a growing industrial and scientific interest in the use of natural particles to increase the toughness of brittle adhesives.

Cork is a biological material with a remarkable combination of properties. A study made by the World Wide Fund for Nature has classified it as truly sustainable product, since it is a fully renewable and obtained from a biodegradable source [36]. In a macroscopic scale, cork is light, elastic and substantially impermeable to liquid and gas; it is also a thermal and electric insulator as well as an acoustic and vibration insulation absorber; innocuous and significantly imputrescible (unaffected by microbial activity), with the ability to be compressed without lateral expansion. Microscopically, cork may be described as a homogeneous tissue of thin-walled prismatic cells, displayed in an alveolar structure similar to a honeycomb [37–43]. Larger cork reinforcement particles, with a considerable number of cells, exhibit damping capabilities and can provide increased impact absorption if added to a stiff resin [32, 44, 45].

Accordingly, these cork properties are also useful to reinforce a brittle adhesive. Cork can be used to improve the mechanical properties of an adhesive, especially its toughness, since the closed cells work to absorb actively an impact [37, 38, 41, 42]. However, the properties of an adhesive/cork composite are not only dependent on the materials' properties, but also on the interfacial adhesion properties between cork and resin, the size and amount of cork particles and the mixing conditions [35]. In this context, Barbosa et al. [32, 46–48] studied the inclusion of cork microparticles as toughness promoter in brittle epoxy adhesives. Different particle sizes and amounts of cork were added to the resin to analyse the influence of those on the behaviour of the cork/resin composite. Firstly, the authors concluded that the particles' dimensions must be above 30 μm, as below this value cork has no beneficial effect on the toughness, working instead as a defect and not as an obstacle to crack propagation. The optimal combination was found to be that the use of particles in the 125–250 μm range, considering a 1% volumetric fraction. The experimental results showed an overall improvement of the mechanical properties (i.e. increased strength and strain), against the properties of the epoxy resin itself. Additionally, it was concluded that cork is able to improve the adhesive mechanical properties without detrimental effects on the curing process and on the hydrothermal degradation of the adhesive [49]. Thereupon, a new sort of application for cork powder was proposed, a material which currently is not well exploited by the cork industry, being typically considered as an industrial waste. The use of this material provides added value to the cork industry with potential benefits, especially to the Portuguese economy, since Portugal is the world's leading market of this raw material, producing three-quarters of the total production.

Within this context, the present work has been carried out to propose a new method to smooth the stress distribution along the bondline of a SLJ, through the application of the concept of FGA to joints using magnetised cork microparticles. For this purpose, a novel apparatus was designed, enabling the application of tailored magnetic fields, achieving this using a specially shaped set of magnets arrays. Magnetised microparticles were then strategically placed along the bondline, creating a particle concentration gradient from the ends of the overlap (higher) to the middle region (lower).

2 Experimental Details

2.1 Materials

Cork powder with 125–250 µm size was employed for this work. The cork used was supplied by Amorim Cork Composites (Mozelos, Portugal), without any treatment. The magnetised cork particles were manufactured by coating the same cork powder with a thin magnetite layer, following a patented process (P201730993 [50]).

The selected adhesive was Araldite 2020®, from Huntsman Advanced Materials (Pamplona, Spain). This is a two-component adhesive (100/30 by weight), consisting of an epoxy resin (component A) and a hardener (component B), with low viscosity (150 mPa s), transparent and that cures at 100 °C, within 15 min. Young's modulus of this adhesive is 3100 MPa, and its density is 1.1 g/cm^3. This material was selected due to its brittleness so that the improvements on the tensile strength after the magnetised cork microparticles inclusion can easily be perceived.

The material used for the adherends was the AW 7075 aluminium alloy (see Table 1), supplied by Poly Lanema, LDA (Ovar, Portugal). The selection of this material was due to the nonmagnetic properties of aluminium since this research is related to the application of magnetic fields in order to displace magnetised particles. The aluminium adherends will therefore have no interference on those fields.

2.2 Manufacture of Bulk Specimens

According to the production plan shown in Fig. 1, specimens with different amounts of cork and magnetised cork particles were manufactured, with the neat classification referring to specimens which are only composed of adhesive, without any cork.

Table 1 AW 7075 mechanical properties

Young's modulus [GPa]	Yield stress [MPa]	Ultimate stress [MPa]	Poisson's ratio	Elongation (%)
71	470	540	0.3	7

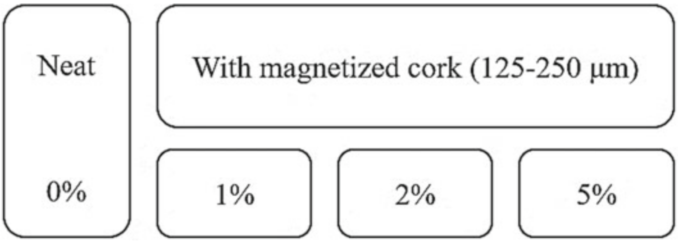

Fig. 1 Bulk specimens' production plan (% by volume)

The particles were initially mixed with the resin using a centrifugal mixing machine, model type SpeedMixer DAC 150^{TM} (Hauschild Engineering, Hamm, Germany), for 90 s at 1500 rpm. After that, hardener was added to the mixture and the resulting blend was then submitted to the same centrifugal mixing process, following the same conditions as previously mentioned. This procedure was the same for all the amounts of the particles under study. In order to ensure a better particle distribution after the mixing process, the composite was heated to 50 °C, for 10 min, to increase the adhesive viscosity. Thereafter, the composite was mixed again in the centrifugal mixing machine. By applying this sequential mixing method, particle agglomeration can be avoided in a simple, effective and reliable way [47].

After mixing the particles with the resin and hardener, the mixture was poured in a pre-heated steel mould, coated with mould release agent to ensure easy removal of the cured material. A silicone rubber frame was used to apply a hydrostatic pressure to the adhesive, which was hot pressed (2 MPa), for 15 min at 100 °C (according to the manufacturer's recommendation cure schedule), as shown in Fig. 2. Specimens were then machined from the plates manufactured with the mould [51]. This manufacturing technique was used to produce the specimens used for tensile tests and those for glass transition temperature measurements.

2.3 *Manufacture of Single Lap Joints and Graded Single Lap Joints*

In situ tests are one of the most reliable methods to characterise adhesives and adhesive joints. In this work, tests are carried out with the single lap joint (SLJ) specimen, one of the most commonly used joint configurations, being easy to manufacture and cheap to produce [2].

SLJ specimens with and without microparticles, having different amounts and distributions, were manufactured, according to the production plan presented in Fig. 3. Specimens with a uniform distribution of the particles and with a graded distribution were produced.

The geometry and dimensions of the SLJs as well as the adhesive conditions in the overlap region are summarised in Fig. 4. In order to better highlight the effect of

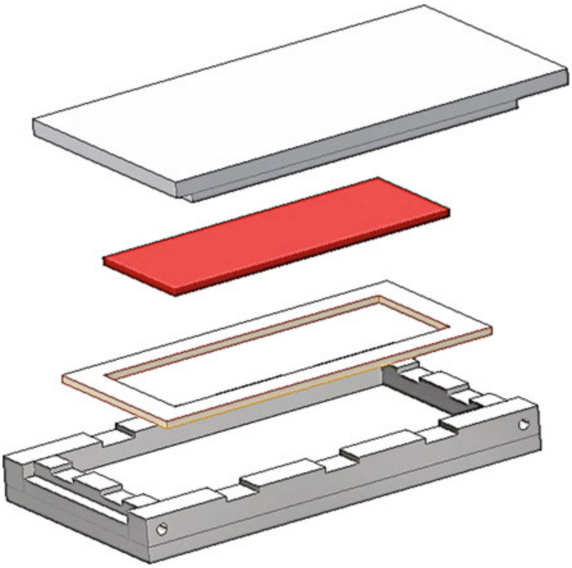

Fig. 2 Exploded view of the bulk specimens' mould: steel plates, silicone rubber frame and the adhesive plate [51]

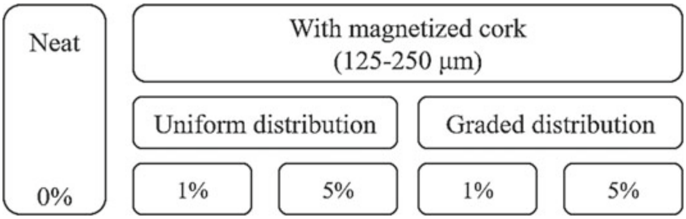

Fig. 3 SLJs' production plan (% by volume)

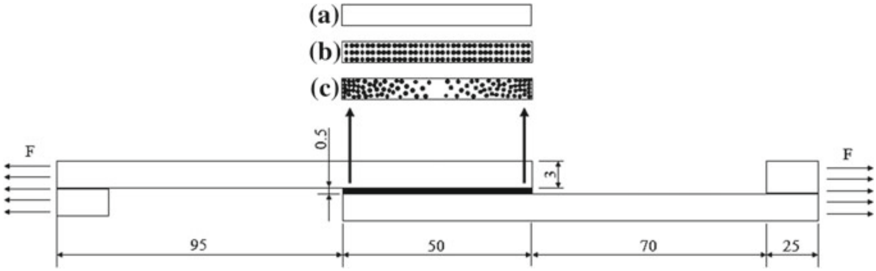

Fig. 4 Geometry of the SLJs according to ASTM D1002 (all dimensions in mm) [52]. All specimens are 15 mm wide, with the adhesive conditions: **a** neat, **b** uniform distribution and **c** graded distribution

the magnetic field gradients on the particle distribution, an overlap of 50 mm length was adopted.

To enhance the adhesion between the substrates and the adhesive, surface treatments were applied to the aluminium surface. Firstly, the surfaces of the adherends were abraded using sandpaper. Then, after cleaning with acetone (in order to remove any dust, oils or contaminants), a sol-gel anodising replacement, the 3M™ (Maplewood, MN, USA) Surface Pre-Treatment AC-130-2 was applied to the adherends. Lastly, in order to enhance the adhesion between the substrates and the resin, a primer was used, the Structural Adhesive Primer EW-5000 AS, also from 3M™.

To aid in the manufacture of this type of specimens, an annealed carbon steel mould was used (see Fig. 5). This mould ensures that the substrates' alignment is correct, restricts their movement, controls the overlap length and defines the adhesive thickness, due to its especially designed alignment pins, shims and positioner blocks. To provide an easy release of the specimens after manufacture, mould release agent was applied to all surfaces of the mould [53].

In order to manufacture graded SLJs, a novel and patented apparatus was used (PAT 20191000036260, see Fig. 6). This apparatus and respective method enables the production of adhesive joints with mechanical properties that vary gradually along the overlap, using magnetised particles, preferentially of micro- or nanosize. The adhesive layer of these joints will have then varying stiffness along the overlap. The apparatus design provides slots for an upper and a lower magnet holder; the magnet holders may contain one or two sets of magnet arrays in the form of blocks, wherein the magnetic arrays are composed by at least four neodymium block magnets.

To achieve the goal of creating a particle concentration gradient from the ends of the overlap (higher) to the middle (lower), an appropriate application of tailored

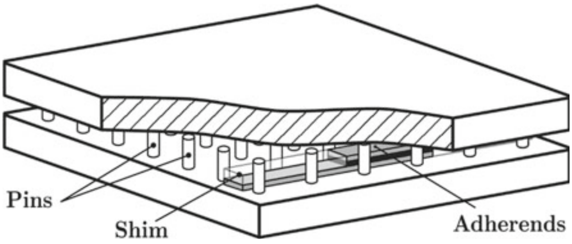

Fig. 5 Carbon steel mould for SLJs [53]

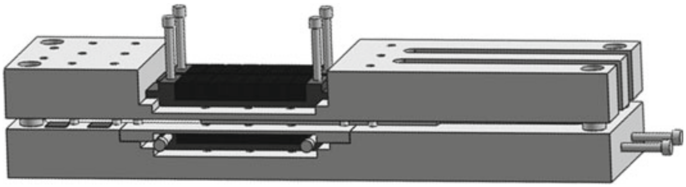

Fig. 6 Apparatus used to produce graded SLJs

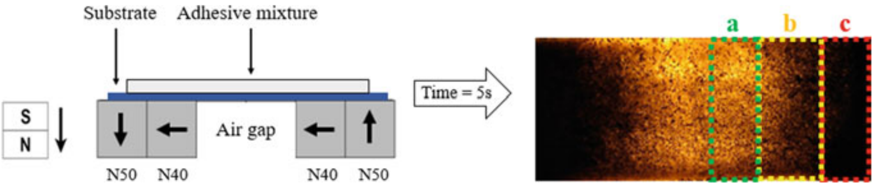

Fig. 7 Magnet set configuration and final particle distribution exhibiting three distinct zones: **a** matrix rich region, **b** transition region and **c** reinforcement particles rich region

magnetic fields is essential. Therefore, to create custom magnetic field gradients along the overlap, a set of permanent magnets (K&J Magnetics, USA) was used. Its configuration is depicted in Fig. 7, showing alternate directions of the magnetic fields. To increase the magnetic flux density slope from the middle to the edges, this magnet set features an air gap in the middle and combines magnets with different grades (N40, N50).

Taking into consideration the overlap dimensions (50 mm length, 15 mm width and 2 mm thickness), after 5 s of application of the magnetic array, the particles graded distribution was achieved, as shown in Fig. 7. Three distinct zones of particle concentration can be observed: a matrix rich region (Fig. 7a), the transition zone (Fig. 7b) and a reinforcement, particle rich, zone (Fig. 7c).

The curing process was the same as the one applied to the bulk specimens. After that, the specimens were carefully removed from the mould, separated with a saw and the excess adhesive on the side of the joint was manually removed with a file. The specimens were manufactured individually in a mould and the adhesive thickness was controlled using appropriately sized packing shims.

2.4 Particle Size Analysis

Particle size analysis is a very important step to understand how the size of the pure and magnetised cork particles is distributed in the tested specimens. In order to analyse the particle size distribution, a Malvern Mastersizer 2000 apparatus (Malvern, UK) was used. The particle size data obtained with this analysis complemented the results obtained in SEM analysis. Three tests were made for each condition.

2.5 Density Measurement

Knowledge of the particle density is essential for this study, as this information is fundamental to determine the amount of particles to be added to the epoxy resin and assess the differences between cork and magnetised cork. The density of the particles was measured using a helium pycnometer, with the reference Micromeritics AccuPyc 1330 (DataPhysics, Neurtek Instruments, Eibar, Spain).

2.6 Tensile Tests

Failure strength tests are commonly used to determine the tensile stress–strain curve of bulk specimens. This test was selected because the stress–strain curve can be used to determine the tensile strength, failure strain and Young's modulus. These mechanical properties are intrinsic to the material, being obtained under a uniform and uniaxial stress state, without the influence of adherends [53]. Therefore, for tensile tests, dog-bone specimens with 2 mm thickness were manufactured based on the specimen geometry defined by the BS 2782 standard (see Fig. 8) [54]. The tensile tests were carried out in an Instron 3367 universal testing machine (Norwood, USA), with a capacity of 30 kN, at room temperature and at test speed of 1 mm/min. Three specimens were tested for each condition.

2.7 Single Lap Joint Tests

SLJs' specimens are usually used for gathering mechanical information of adhesively bonded systems such as the lap shear strength. This test was selected since the specimens are rather simple to manufacture and resemble the geometry of many practical applications [53]. The SLJ tests were carried out in the same testing machine as the tensile tests, under the same testing conditions (room temperature and test speed of 1 mm/min). Three specimens were tested for each condition. The maximum loads were obtained from the experimental load–displacement curves. The SLJ test is standardised in ASTM D1002-99 and in ISO 4587:2003 [52, 55].

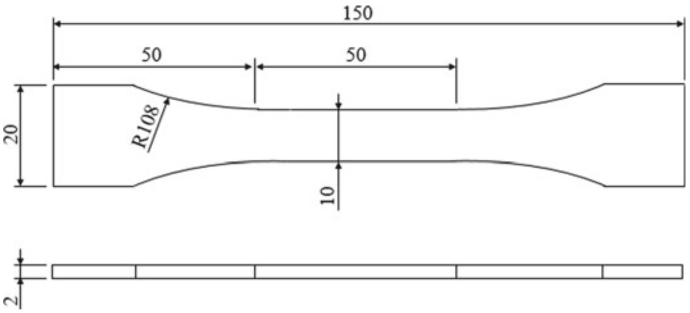

Fig. 8 Dog-bone tensile test specimens, according to the BS 2782 standard (dimensions in mm) [54]

2.8 Scanning Electron Microscopy

Scanning electron microscopy (SEM) was employed to analyse the fracture surface from dog-bone bulk specimens, to determine the particles size and geometry, analyse the magnetic coating morphology and its chemical composition as well as to confirm if random particle distributions were successfully achieved.

Scanning Electron Microscopy/Energy Dispersive X-Ray Spectroscopy (SEM/EDS) analyses were carried out in a JEOL JSM 6301F/Oxford INCA Energy 350/Gatan Alto 2500 microscope (Tokyo, Japan) at CEMUP (University of Porto, Portugal). This equipment was employed to analyse the pure and magnetised cork particles, and surface fractures from dog-bone bulk specimens. To do so, the samples were coated with a Au/Pd thin film, by sputtering, using the SPI Module Sputter Coater equipment, for 120 + 120 s, with a 15 mA current.

2.9 Glass Transition Temperature (T_g) Measurement

A dynamic mechanical type analysis method initially developed by Adams et al. [56] was used to determine the glass transition temperature (T_g) of the composite. The method involves excitation of the test specimen during both heating and cooling, thus being the T_g measured by registering the damping of the specimen as a function of the temperature, which is defined as the temperature at which the peak value of damping is observed.

This method of analysis is quite fast (19 °C/min) so that it does not alter the specimen reticulation level during heating [47, 56] and is capable of ensuring a homogeneous temperature distribution along with the specimen. The specimen consists of using a pre-cured sheet of adhesive fastened between an aluminium beam and a constraining steel sheet (Fig. 9). For the T_g measurements, the bulk adhesive was machined in the form of rectangular plates with dimensions of 30 × 10 mm and a thickness of 2.0 ± 0.1 mm.

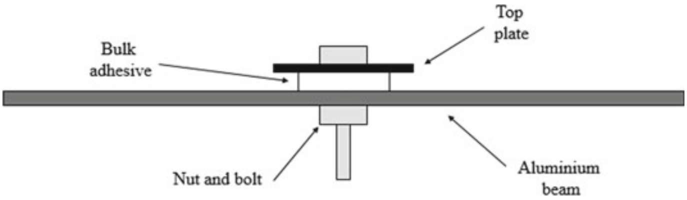

Fig. 9 Bulk specimen representation scheme for T_g measurement

3 Results and Discussion

3.1 Particle Characterisation

Particle size (Fig. 10), shape and cellular structure were analysed, for particles with and without magnetic coating. Figure 11 presents the morphological and chemical differences between the two types of particles considered in this study. Cork particles with 125–250 μm size presented a honeycomb structure composed by several cells, which include some open cells on the edges of the particles and closed cells on the particle core (see Fig. 11a, c). The number of cells existing in a particle is fundamental for ensuring good mechanical behaviour of the cork particles. Due to the milling process used to obtain these particles, some cells show damage on the cell walls. The selected particle size ensures that a sufficient number of closed cells are still present in the particles. When analysing the chemical composition of the cork particles (see Fig. 11e), it was observed that they are mostly composed of carbon (C) and oxygen (O), which is the typical composition of natural materials. The Au and Pd peaks are not from the particles, but from the fine conductive coating required for the observation of this type of material in SEM. In contrast, the magnetised cork particles do not present the typical cork cellular structure, since the ferrimagnetic coating covers the majority of cork cell (see Fig. 11b, d, f). It is possible to observe that the coating layer is rigid and not continuous, with several surface cracks being evident. These features of the coating layer may be advantageous as they increase the available interface area between the particle and the adhesive. Mapping of chemical components was performed (see Fig. 12), allowing to identify the main chemical components of the magnetised cork particles, i.e. oxygen (highlighted in green colour), iron (highlighted in blue colour) and carbon (highlighted in red colour). This chemical mapping procedure is a very useful tool, as it allows to accurately observe how these constituents are distributed. It was evident that, although the coating layer almost completely covers the cork particle (areas in blue and green), there are some uncoated areas that reveal the base cellular structure of cork (red areas in the particle). Nevertheless, the results

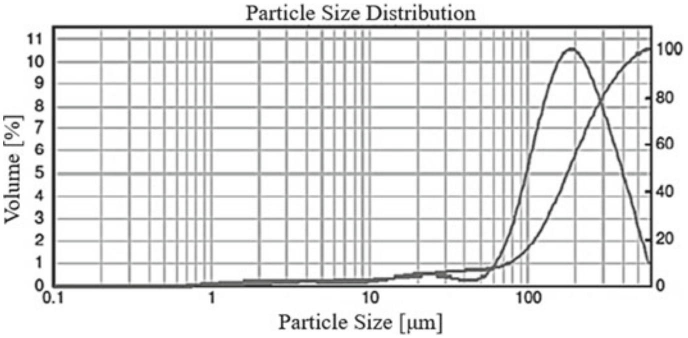

Fig. 10 Particle size distribution of cork particles with 125–250 μm size range

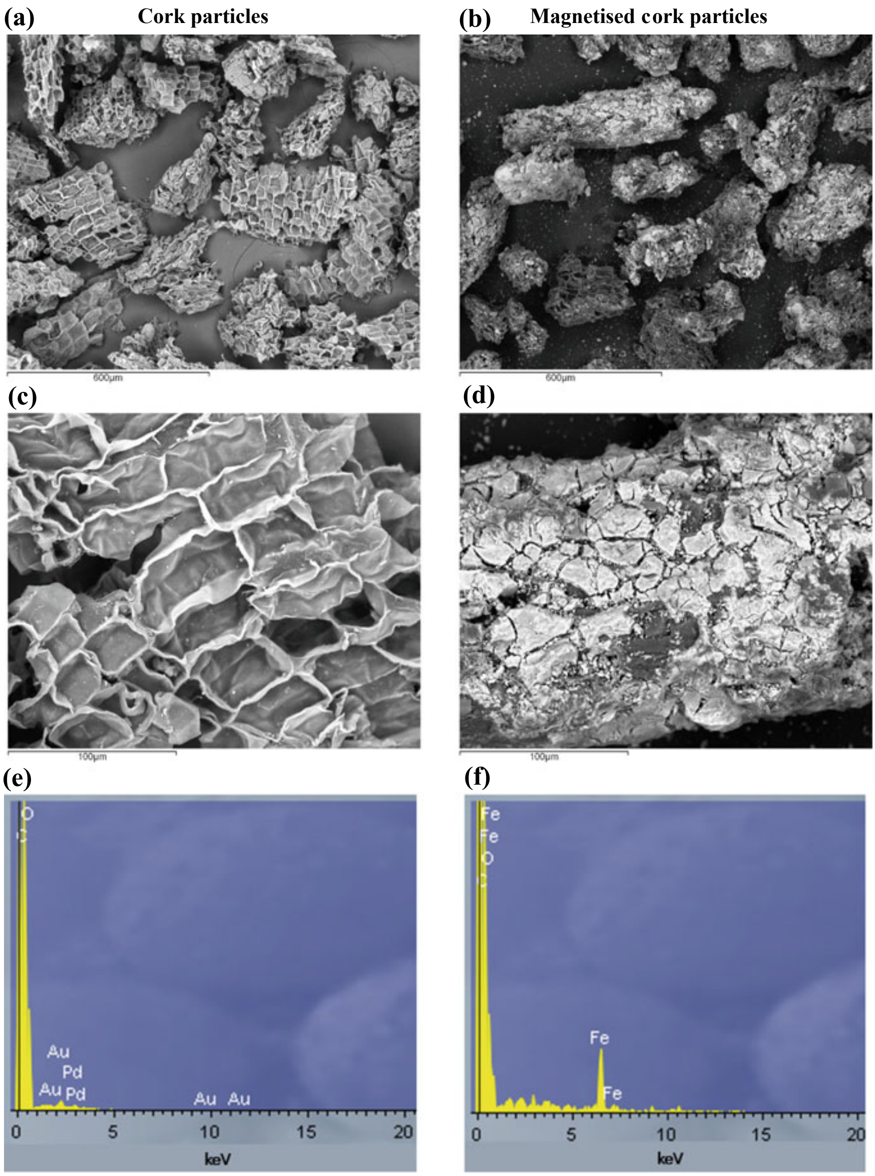

Fig. 11 Cork particles' characterisation with and without magnetic coating, 125–250 μm size: **a** shape of cork particles, **b** shape of magnetised cork particles, **c** cork cellular structure, **d** detail of magnetic coating layer, **e** spectrum EDS of a cork particle and **f** spectrum EDS of a magnetised cork particle

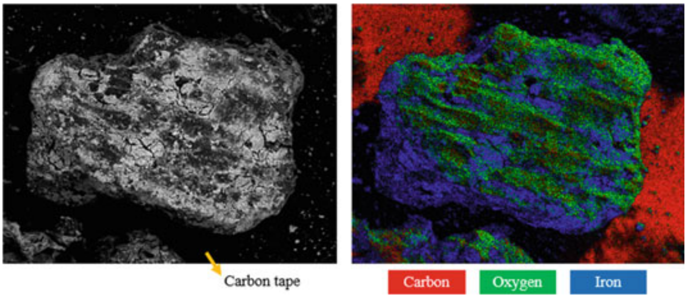

Fig. 12 Chemical distribution map of a magnetised cork microparticle

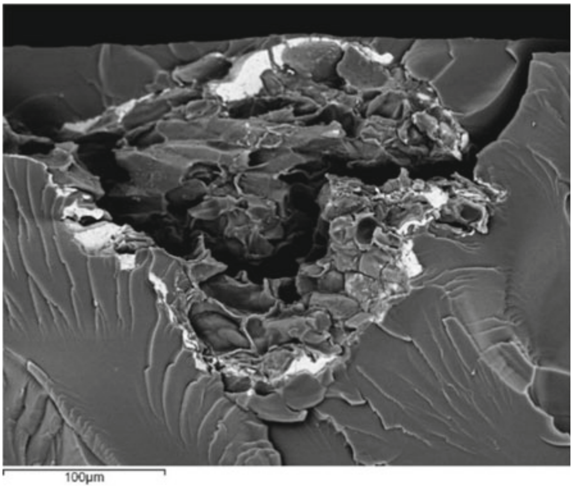

Fig. 13 Example of a magnetite coating layer in a cork particle

suggest that the coating layer covers the surface of the particles quite effectively so that they can be still displaced with the application of a magnetic field.

The magnetite coating, although very thin, as depicted in Fig. 13, is responsible for an increase in the density of the magnetised particles comparing to cork particles, as shown in Fig. 14.

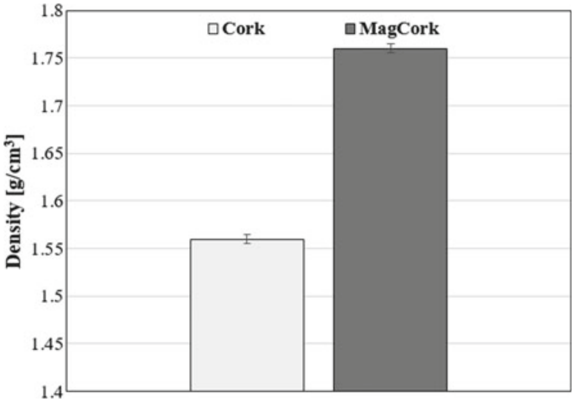

Fig. 14 Densities of pure and magnetised cork microparticles

3.2 Tensile Test Results and Fracture Surface Analysis

In order to study the influence of the amount of magnetised cork particles, tensile tests were performed. Figure 15 shows typical tensile stress–strain curves of the neat epoxy resin and of the epoxy resin with 1, 2 and 5% of magnetised cork microparticles.

Analysing these curves, it is evident that the presence of particles modifies the behaviour of the neat epoxy resin and that there are behavioural differences between the different amounts of particles under study. Therefore, for a 1% amount of magnetised particles with a random and uniform distribution among the resin, there is an increase in ductility, given by the increase in the strain, even though there is a slight decrease in the tensile stress, as expected.

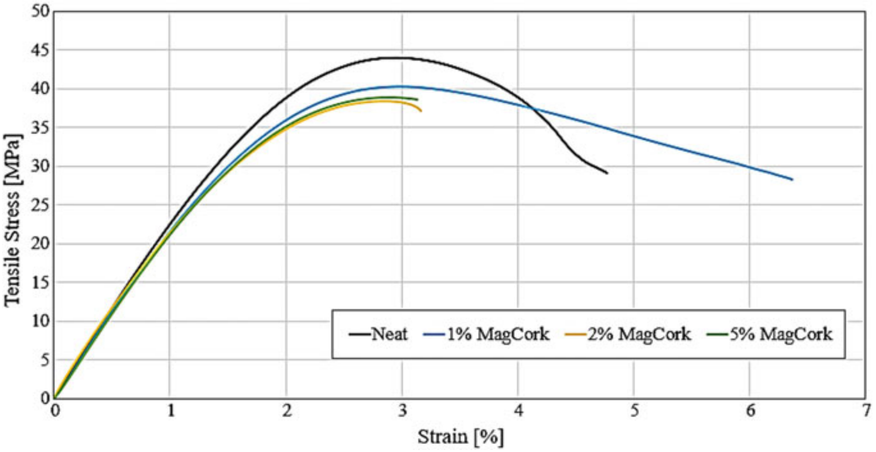

Fig. 15 Typical tensile stress–strain curves for specimens with different particles amounts

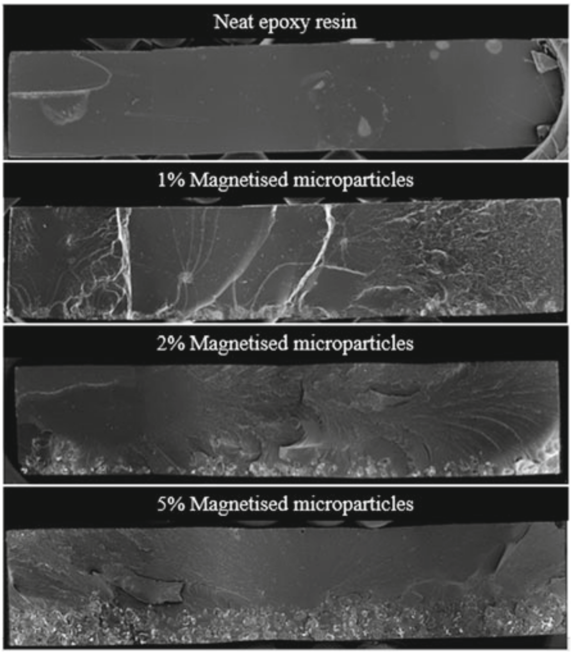

Fig. 16 Fracture surface of tensile specimens for neat and epoxy with magnetised cork microparticles (1, 2 and 5% amounts)

On the other hand, for the 2 and 5% levels, the strain and tensile stress values are lower than those presented for neat epoxy resin and 1% of magnetised particles. Therefore, with the purpose of better understanding the effect of the particle amount on the fracture mechanisms, fractographic studies of the tensile bulk specimens fracture surfaces were carried out using SEM.

Figure 16 shows the fracture surface of the tensile bulk specimens for neat resin and for resin with 1, 2 and 5% of magnetised cork microparticles. Accordingly, the results for the tensile stress–strain curves regarding 2 and 5% particle amounts are explained by the occurrence of particle deposition, as depicted in the SEM analysis, which tends to be more significant with the increase in the particle amount. As shown in Fig. 14, the magnetised particles are heavier than pure cork particles, having higher density than the adhesive. Thus, this deposition is due to the high density of the magnetised particles, compounded by the fact that by increasing their amount in the resin, their ferrimagnetic nature becomes more relevant, making them attract each other. This way, instead of showing a uniform and random particle distribution, the specimens exhibit two layers, one with mostly neat resin and another rich with the deposited particles. Such particle deposition can be avoided mainly by the increasing of the adhesive's viscosity.

The crack propagation was also analysed with SEM analysis performed previously (Fig. 16) to evaluate the particles' distribution. Therefore, regarding the specimen with the neat adhesive, known to be a very brittle epoxy, the fracture is shown to be a rapid crack growth zone, where the instability criterion for crack growth is met with the continuously increased loading.

Comparing the images of the neat epoxy resin and the epoxy resin with 1% of particles, considerable differences can be drawn. Firstly, the neat epoxy resin presents a relatively smooth fracture surface. For specimens with 1% of particles, a slow crack zone is noted at the beginning of the crack growth area (left) and a rapid crack growth zone (right) that led to the loss of material. As expected, the slow crack zone is near the crack initiation point and the rapid crack growth zone is away from the crack initiation point.

With the increase in the amount of particles from 1% on, a deposition layer is progressively more perceptible, being more severe for 5% of particle amount. The associated fracture is smoother on the layer composed by the adhesive, consistent to what succeeds to the neat epoxy specimen. However, in the deposition layer, the exact opposite occurs, with a less brittle fracture occurring. Besides, for an amount of 5% it is evident that the particles now act as defects and not as crack propagation stopping agents.

Furthermore, as depicted in Fig. 17, with the introduction of particles in the neat epoxy resin, Young's modulus decreases, as expected due to the low stiffness of cork. However, for the various amounts of magnetised particles, Young's modulus variation is not that significant, assuming a nearly constant value. Similarly, the maximum tensile stress also decreases with the addition of these particles to the epoxy resin. However, even though it is not that significant, from 2 to 5% of particles, there is a very slight recovery in both properties.

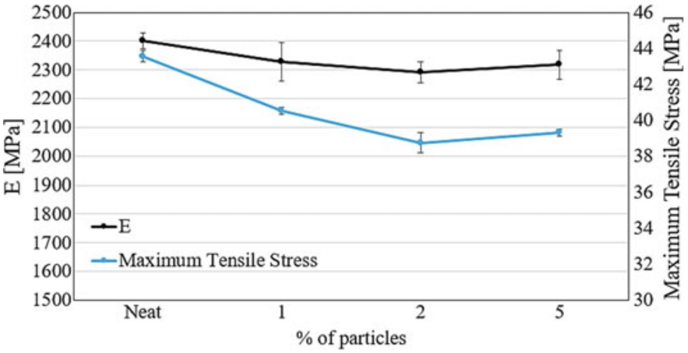

Fig. 17 Young's modulus and maximum tensile stress of specimens in function of the different particles amounts

3.3 Glass Transition Temperature Measurements (T_g)

Figure 18 shows the influence of particle inclusion in the neat epoxy resin on the T_g and the maximum strain values obtained using bulk tensile testing, in an attempt to correlate changes in the T_g with material ductility. The data shows that specimens with particles present a lower T_g in relation to neat resin specimens, these results being explained by the low T_g of the cork particles (approximately, 16.5 °C [47]).

The T_g values obtained for specimens with neat epoxy resin and 1% of particles are in line with the tensile test results, showing that as the T_g decreases, there is an increase in ductility of the adhesive [57]. However, for specimens with 2 and 5% of magnetised particles, the correlation of ductility with the T_g values is not conclusive. This is thought to be due to the aforementioned particles deposition patterns (see Fig. 16). Thus, there is a need for a new adhesive formulation in order to better assess the effect of the magnetised particles when uniformly and randomly distributed in the epoxy resin.

3.4 Single Lap Joint Tests

Typical load–displacement curves obtained by tensile tests of the SLJs are represented in Fig. 19, for neat conditions and for both uniform and graded particle distributions. Since 2 and 5% particle amounts presented similar behaviours in the tensile stress–strain curves, SLJs were only produced for neat epoxy resin and 1 and 5% amounts.

It is evident that there was an enhancement of the mechanical properties by adding magnetised microparticles of cork to the epoxy resin. For both kinds of particle distributions and considering the 1 and 5% amounts, the SLJs presented higher performance (judged by higher failure load and larger displacement at failure), when

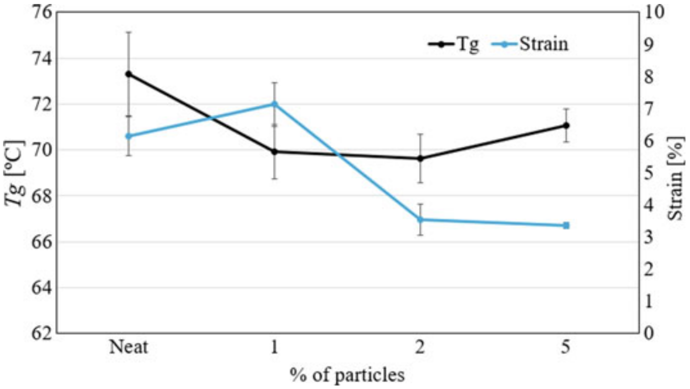

Fig. 18 Glass transition temperature and strain as a function of the amount of particles (% by volume)

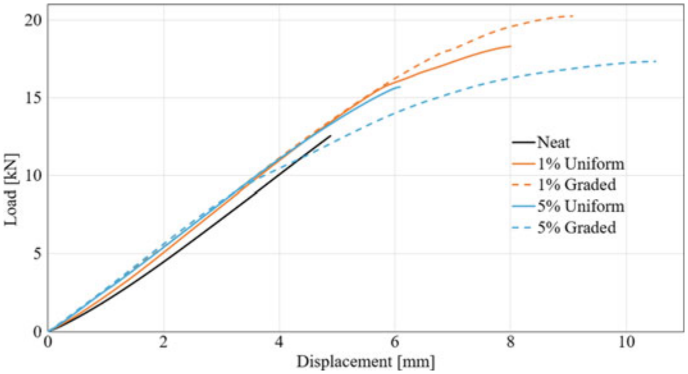

Fig. 19 Typical load–displacement curves of joints with neat epoxy resin and magnetised particles with uniform and graded distributions

compared to the results for neat conditions. In fact, this can be explained by the higher stress concentration of the neat joints at the ends of the overlap due to their high stiffness and the brittleness of the adhesive. In this case, the adhesive cannot plastically deform all over the overlap, and the failure strain of the adhesive is quickly reached at the ends of the overlap before there can be global yielding of the adhesive layer along the whole overlap [58].

Joints with 5% of uniform particle distribution exhibit higher displacement than joints with 1% of uniform particle distribution. This is the opposite of what occurs to the tensile test results. Such discrepancy can be explained by the fact that in the bulk specimens, the 2 mm thickness led to a higher particle accumulation at the lower part of the specimen; while on joints, where the thickness of the adhesive is 0.5 mm, the particles are spread more uniformly through the adhesive layer thickness.

Furthermore, graded joints with 1% particle amount were found to be stronger than those with the same particle amount but with uniform distribution, having higher failure load and larger displacement. In particular, there was a growth of 8.3 and 6.2% for the values of the failure load and the displacement, respectively. On the other hand, for graded joints with a 5% particles amount, although the failure load value slightly increased (about 5.8%), there was a substantial enhancement of the displacement at failure (about 29.6%). Thus, one can conclude that by increasing the amount of magnetised particles in the epoxy resin, the graded joints tend to be more ductile, in comparison with the equivalent ones with uniform distribution.

4 Conclusions

In this research, joints with a gradually modified adhesive, using magnetised cork microparticles, were studied and compared to the correspondent reference joints with a uniform particle distribution. The influence of the amount of magnetised cork microparticles added to a structural brittle epoxy resin was assessed by measuring tensile strength in bulk specimens, testing SLJ specimens, performing T_g measurements and carried out SEM analysis. The following conclusions can be drawn:

- The morphological analysis of cork microparticles shows that they contain a few closed cells, possibly improving the ductility of the material. From SEM analysis, the magnetised particles show a thin and mostly uniform magnetite coating layer, which enables them to be displaced in the resin when a magnetic field is applied;
- The magnetised cork microparticles can be used to enhance the mechanical properties of a brittle epoxy adhesive;
- 1% of magnetised cork particles incorporated in a brittle resin gives more ductility than other particle amounts. Different behaviour is observed for specimens above this amount, due to particle deposition;
- T_g measurements are consistent with the tensile test results for small ranges of particle amount. For a 1% of particles amount, the T_g value is lower, corresponding to a more ductile behaviour, while for values above 2% there is insufficient correlation due to the issues with particle deposition in bulk specimens;
- For SLJs, the inclusion of particles is responsible for the increasing of the failure load and displacement values, thus enhancing the joints performance (both graded joints and with a uniform distribution of particles);
- The gradation of the particle distribution is responsible for the modification of the SLJ behaviour, when compared to SLJs with a uniform particle distribution.

Acknowledgements Financial support by Foundation for Science and Technology (POCI-01-0145-FEDER-028035) is greatly acknowledged.

References

1. Chiminelli, A., Breto, R., Izquierdo, S., Bergamasco, L., Duvivier, E., Lizaranzu, M.: Analysis of mixed adhesive joints considering the compaction process. Int. J. Adhes. Adhes. **76**, 3–10 (2017)
2. da Silva, L.F.M., Öchsner, A., Adams, R.D.: Handbook of Adhesion Technology, pp. 1–7 (2011)
3. Adams, R.D., Comyn, J., Wake, W.C.: Structural Adhesive Joints in Engineering. Chapman and Hall (1997)
4. Stein, N., Rosendahl, P.L., Becker, W.: Homogenization of mechanical and thermal stresses in functionally graded adhesive joints. Compos. Part B Eng. **111**, 279–293 (2017)
5. Dillard, D.: Advances in Structural Adhesive Bonding (2010)
6. Kumarz, S.: Advances in Modeling and Design of Adhesively Bonded Systems, pp. 47–91 (2013)
7. Carver, D.R., Wooley, G.R.: Stress concentration factors for bonded lap joints. J. Aircr. **8** (1971)
8. Kinloch, A.: Adhesion and Adhesives: Science and Technology (1987)
9. Lang, T.P., Mallick, P.: Effect of spew geometry on stresses in single lap adhesive joints. Int. J. Adhes. Adhes. **18** (1998)
10. Hart-Smith, L.J.: Analysis and design of advanced composite bounded joints (1974)

11. Zhao, X., Adams, R.D., da Silva, L.F.M.: Single lap joints with rounded adherend corners: stress and strain analysis. J. Adhes. Sci. Technol. **25**, 819–836 (2011)
12. Hart-Smith, L.J.: Adhesive-bonded double-lap joints (1973)
13. Bowditch, M.R.: In: Adams, R.D. (ed.) Adhesive Bonding: Science, Technology and Applications, £135, vol. 26. CRC Press, USA and Woodhead Publishing Ltd., Cambridge, England (2005)
14. da Silva, L.F.M., Lopes, M.J.C.Q.: Joint strength optimization by the mixed-adhesive technique. Int. J. Adhes. Adhes. **29**, 509–514 (2009)
15. das Neves, P.J.C., da Silva, L.F.M., Adams, R.D.: Analysis of mixed adhesive bonded joints part I: theoretical formulation. J. Adhes. Sci. Technol. **23**, 1–34 (2009)
16. Fitton, M.D., Broughton, J.G.: Variable modulus adhesives: an approach to optimised joint performance. Int. J. Adhes. Adhes. **25**, 329–336 (2005)
17. das Neves, P.J.C., da Silva, L.F.M., Adams, R.D.: Analysis of mixed adhesive bonded joints part II: parametric study. J. Adhes. Sci. Technol. **23** (2012)
18. Marques, E.A.S., Magalhães, D.N.M., da Silva, L.F.M.: Experimental study of silicone-epoxy dual adhesive joints for high temperature aerospace applications. Materialwiss. Werkstofftech. **42**, 471–477 (2011)
19. Pires, I., Quintino, L., Durodola, J.F., Beevers, A.: Performance of bi-adhesive bonded aluminium lap joints. Int. J. Adhes. Adhes. **23**, 215–223 (2003)
20. Temiz, Ş.: Application of bi-adhesive in double-strap joints subjected to bending moment. J. Adhes. Sci. Technol. **20**, 1547–1560 (2006)
21. Marques, E.A.S., da Silva, L.F.M.: Joint strength optimization of adhesively bonded patches. J. Adhes. **84**, 915–934 (2008)
22. da Silva, L.F.M., Adams, R.D.: Techniques to reduce the peel stresses in adhesive joints with composites. Int. J. Adhes. Adhes. **4** (2006)
23. Boss, J.N., Ganesh, V.K., Lim, C.T.: Modulus grading versus geometrical grading of composite adherends in single-lap bonded joints. Compos. Struct. **62**, 113–121 (2003)
24. Ganesh, V.K., Choo, T.S.: Modulus graded composite adherends for single-lap bonded joints. J. Compos. Mater. **36** (2002)
25. Kemal Apalak, M., Gunes, R.: Elastic flexural behaviour of an adhesively bonded single lap joint with functionally graded adherends. Mater. Des. **28**, 1597–1617 (2007)
26. Sancaktar, E., Kumar, S.: Selective use of rubber toughening to optimize lap-joint strength. J. Adhes. Sci. Technol. **14** (2000)
27. Stapleton, S., Waas, A., Arnold, S.: Functionally graded adhesives for composite joints. Int. J. Adhes. Adhes. **35** (2012)
28. Carbas, R.J.C., da Silva, L.F.M., Critchlow, G.W.: Adhesively bonded functionally graded joints by induction heating. Int. J. Adhes. Adhes. **48**, 110–118 (2014)
29. Carbas, R.J.C., da Silva, L.F.M., Critchlow, G.W.: Effect of post-cure on adhesively bonded functionally graded joints by induction heating. Proc. Inst. Mech. Eng. Part L J. Mater. Des. Appl. **229**, 419–430 (2014)
30. Kinloch, A., Lee, J.H., Taylor, A., Sprenger, S., Eger, C., Egan, D.: Toughening structural adhesives via nano- and micro-phase inclusions. J. Adhes. **79** (2003)
31. Oksman, K.: Mechanical properties of natural fibre mat reinforced thermoplastic. Appl. Compos. Mater. **7**, 403–414 (2000)
32. Barbosa, A., da Silva, L.F.M., Öchsner, A., Abenojar, J., del Real, J.C.: Influence of the size and amount of cork particles on the impact toughness of a structural adhesive. J. Adhes. **88** (2012)
33. Hamza, T., Rosenstiel, S., Elhosary, M.M., Ibraheem, R.M.: The effect of fiber reinforcement on the fracture toughness and flexural strength of provisional restorative resins. J. Prosthet. Dent. **91** (2004)
34. Maddux, B., Schaffer, T.E., Viani, M., Thompson, J.B., Frederick, N.A., Kindt, J., et al.: Molecular mechanistic origin of the toughness of natural adhesives, fibres and composites. Nature **399** (1999)

35. Abdallah, F., Cheikh, R., Baklouti, M., Denchev, Z., Cunha, A.: Effect of surface treatment in cork reinforced composites. J. Polym. Res. **17** (2010)
36. WWF: WWF Mediterranean Programme Office (2019)
37. Fakirov, S., Bhattacharya, D.: Handbook of Engineering Biopolymers: Homopolymers, Blends and Composites (2007)
38. Fortes, M.A., Ferreira, P.J.: Materiais 2000. Lisbon (2003)
39. Gil, L.: Cortiça: Produção, Tecnologia e Aplicação. INETI (1998)
40. Mano, J.F.: The viscoelastic properties of cork. J. Mater. Sci. **37**, 257–263 (2002)
41. Pereira, H.: Cork: Biology, Production and Uses (2007)
42. Silva, S., Sabino, M., Fernandes, E., Correlo, V., Boesel, L., Reis, R.L.: Cork: properties, capabilities and applications. Int. Mater. Rev. **50** (2005)
43. Teles, A.: Ph.D. thesis, Universidade do Minho, Portugal (2000)
44. Anjos, O., Pereira, H., Rosa, M.: Effect of quality, porosity and density on the compression properties of cork. Holz Roh-Werkstoff **66** (2008)
45. Rosa, M., Fortes, M.A.: Rate effects on the compression and recovery of dimensions of cork. J. Mater. Sci. **23** (1988)
46. Abenojar, J., Barbosa, A.Q., Ballesteros, Y., del Real, J.C., da Silva, L.F.M., Martínez, M.A.: Effect of surface treatments on natural cork: surface energy, adhesion, and acoustic insulation. Wood Sci. Technol. **48**, 207–224 (2014)
47. Barbosa, A., da Silva, L.F.M., Öchsner, A.: Effect of the amount of cork particles on the strength and glass transition temperature of a structural adhesive. Proc. Inst. Mech. Eng. Part L J. Mater. Des. Appl. **228** (2013)
48. Barbosa, A.Q., da Silva, L.F.M., Öchsner, A., Abenojar, J., del Real, J.C.: Utilização de micro partículas de cortiça como material de reforço em adesivos estruturais frágeis. Ciênc. Tecnol. Mater. **25**, 42–49 (2013)
49. Barbosa, A., da Silva, L.F.M., Abenojar, J., del Real, J., Paiva, R., Öchsner, A.: Kinetic analysis and characterization of an epoxy/cork adhesive. Thermochim. Acta **604** (2015)
50. Abenojar, A.B.J., Martinez, M., Carbas, R., Velasco, F., Silva, L., de Real, J.: Magnetization of particles for manufacturing composite materials. Spain Patent, 2017
51. Banea, M., da Silva, L.F.M.: The effect of temperature on the mechanical properties of adhesives for the automotive industry. Proc. Inst. Mech. Eng. Part L J. Mater. Des. Appl. **224** (2010)
52. ASTM International: Standard Test Method for Apparent Shear Strength of Single-Lap-Joint Adhesively Bonded Metal Specimens by Tension Loading (Metal-to-Metal), vol. ASTM D1002-99. ASTM International, West Conshohocken, PA (2001)
53. da Silva, L.F.M., Roumagnac, P., Heuillet, P., Duncan, B., Anderson, G.L., Adams, R.D., et al.: Testing Adhesive Joints: Best Practices, pp. 79–162 (2012)
54. British Standards Institution: Methods of testing plastics. Introduction. In: BS 2782-0:2011. BSI (2011)
55. International Organization for Standardization: Adhesives—Determination of Tensile Lap-Shear Strength of Rigid-to-Rigid Bonded Assemblies, vol. ISO 4587:2003 (2003)
56. Zhang, Y., Adams, R.D., da Silva, L.F.M.: A rapid method of measuring the glass transition temperature using a novel dynamic mechanical analysis method. J. Adhes. **89** (2013)
57. Carbas, R., Marques, E.A.S., da Silva, L.F.M., Lopes, A.: Effect of cure temperature on the glass transition temperature and mechanical properties of epoxy adhesives. J.Adhes. **90** (2014)
58. da Silva, L.F.M., das Neves, P.J.C., Adams, R.D., Wang, A., Spelt, J.K.: Analytical models of adhesively bonded joints—part II: comparative study. Int. J. Adhes. Adhes. **29**, 331–341 (2009)